

Nanoparticle Conjugates and Materials through Manipulating Surface Chemistry

by

Victor R. Mann

A dissertation submitted in partial satisfaction of the requirements for the degree of

Doctor of Philosophy

in

Chemistry

in the

Graduate Division

of the

University of California, Berkeley

Committee in charge:

Doctor Bruce E. Cohen, Co-Chair

Professor Evan W. Miller, Co-Chair

Professor John T. Groves

Professor Ehud Y. Isacoff

Fall 2019

Nanoparticle Conjugates and Materials through Manipulating Surface Chemistry

Copyright © 2019

by

Victor R. Mann

Abstract
Nanoparticle Conjugates and Materials through Manipulating Surface Chemistry
by
Victor R. Mann

Doctor of Philosophy in Chemistry
University of California, Berkeley

Doctor Bruce E. Cohen, Co-Chair
Professor Evan W. Miller, Co-Chair

Chapter 1: Functionalization of nanocrystals is essential for their practical application, but synthesis on nanocrystal surfaces is limited by the available chemistries to introduce new functionality and create conjugated materials. Applications such as the development of imaging probes and hybrid materials require new methods for conjugating and interfacing nanoparticles with biological systems. The introductory chapter will present relevant background on the types of nanocrystals used in this work as well as the state and drawbacks of current nanocrystal functionalization techniques.

Chapter 2: As a basis for surface modification, the development of polymer encapsulation techniques was investigated to enable phase transfer to aqueous dispersions and to display reactive functional groups at the interface. Use of this encapsulation procedure allows for reproducible and tunable surface composition for a variety of chemistries and further modifications. Modifications can be used to display different functional groups on the nanoparticle surface for conjugation or to modulate physical properties.

Chapter 3: One surface conjugation strategy is the use of copper-catalyzed azide-alkyne cycloaddition (CuAAC). It is among the most popular methods for ligating molecules to surfaces, but as Cu(I) ions quickly and irreversibly quench semiconductor quantum dot (QD) fluorescence, development of this chemistry has been largely useless for QDs. A combinatorial fluorescence assay was developed to screen for non-quenching synthetic conditions for CuAAC on QD surfaces, and we identified conditions for complete coupling without significant quenching. Using these findings, I synthesized unquenched QD-peptidyl toxin conjugates and imaged their specific and voltage-dependent affinity for potassium channels in live cells.

Chapter 4: The use of the split domain SpyTag/SpyCatcher system forms the basis for another facet of conjugate design that can incorporate biomolecules through a small

engineered peptide tag. This peptide-protein pair is a genetically-encodable tool to incorporate specific, covalent interactions between the two components which can be included in separate materials. The reaction is traceless and agnostic to a wide range of reaction conditions, integrating a degree of modularity into our systems. With this linkage as a design rule, we generate stable biomolecule conjugates as probes for imaging and as the basis for higher order structures.

Chapter 5: Self-assembly offers a scalable and reproducible bottom-up approach to fabricate patterned nanomaterials, but they have been limited in their ability to combine high conjugation yields with programmability. We employed protein engineering to modify the bacterial S-layer proteins SbsB and RsaA to create biomolecular scaffolds for the controlled deposition of multiple types of nanoparticles. Using the isopeptide bond-forming SpyCatcher conjugation, we have enabled dense coverage of a wide range of nanoparticles on the free-floating SbsB lattice including gold nanoparticles (Au NPs), quantum dots (QDs) and upconverting nanoparticles (UCNPs). Using orthogonal conjugation strategies, we created arrays with Au NP-QD pairings that conferred plasmonic enhancement of QD radiative decay. In addition to purified sheets, we show that SpyCatcher ligation of QDs to cell surface RsaA proteins produces crosslinking into an extended 3D cellular network. Confocal and atomic force microscopies demonstrate a dense and ordered layer of QDs on the cell surface, while mechanical analysis of the supracellular material demonstrates a >30-fold enhancement of storage modulus. The modularity inherent to the design tolerates changes to the nanocrystal composition and permits regeneration of the material after damage.

Chapter 6: While the applications of nanoparticle conjugates are varied, they all stem from the central need for methods that extend the reach of synthetic chemistry on the nanocrystal surface. Development of these techniques allows the creation of hybrid materials of one or more nanocrystal types interacting with proteinaceous and cellular biomaterials. I recapitulate these findings to describe the current state of the art and the future of the nanocrystal chemistry field.

For Allison,
in return for her patience.

Table of Contents

Abstract.....	1
Table of Contents.....	ii
Table of Figures.....	iv
Acknowledgements.....	viii
1 Introduction.....	1
2 Nanocrystal Surface Functionalization <i>via</i> Encapsulation.....	7
2.1 Introduction.....	8
2.2 Results and Discussion.....	11
2.2.1 Polymer encapsulation for aqueous dispersion of nanocrystals.....	11
2.2.2 Purification of polymer-encapsulated nanocrystals.....	16
2.2.3 Chemical functionalization of polymer-displayed groups.....	20
2.3 Conclusions.....	24
2.4 Materials and Methods.....	25
3 Azide-Alkyne Click Conjugation on Quantum Dots by Selective Copper Coordination.....	30
3.1 Introduction.....	31
3.2 Results and Discussion.....	34
3.2.1 Screening for non-quenching CuAAC reaction conditions.....	34
3.2.2 Analysis of combinatorial screening data.....	40
3.2.3 Mechanisms of Cu-mediated cycloaddition and quenching.....	41
3.2.4 Cu-mediated click synthesis of QD bioconjugates.....	48
3.3 Conclusions.....	50
3.4 Materials and Methods.....	51
4 Nanoparticle Conjugates and Design Possibilities Using Engineered Isopeptide- forming Proteins.....	59
4.1 Introduction.....	60
4.2 Results and Discussion.....	65
4.2.1 Engineering SpyCatcher for nanocrystal binding.....	65
4.2.2 Nanocrystal surface display of SpyCatcher protein.....	67

4.2.3	Nanocrystal-antibody conjugates enabled by SpyCatcher conjugation	71
4.2.4	A SpyCatcher protein fusion for studying nanoparticle endocytosis..	74
4.3	Conclusions.....	80
4.4	Materials and Methods.....	81
5	Building Hybrid Materials through Nanocrystal S-layer Interactions.....	87
5.1	Introduction.....	88
5.2	Results and Discussion	92
5.2.1	Engineered S-layers for binding Au nanoparticles	92
5.2.2	S-layers incorporating protein-coupling tags can bind a versatile set of nanoparticles	95
5.2.3	Dual modified S-layers can yield nanosheets bearing two nanoparticle types at high occupancy	102
5.2.4	Plasmonic interactions between nanoparticles on dual modified SbsB sheets.....	106
5.2.5	Patterned display of nanocrystals on bacterial surfaces	107
5.2.6	Formation of QD-bacteria supracellular assemblies	111
5.2.7	Nanoparticle-mediated mechanical properties of supracellular assemblies	113
5.2.8	Expansion of hybrid materials to additional capabilities	116
5.3	Conclusions.....	118
5.4	Materials and Methods.....	119
6	Summary and Outlook.....	130
7	Appendix I: Labeling Specificity of Kv2.1 with QD-GxTX Conjugates.....	133
7.1	Introduction.....	134
7.2	Results and Discussion	135
7.2.1	Disparity in cell labeling based on location	135
7.2.2	Toxin reduction and membrane blocking modulate binding but not specificity.....	138
7.2.3	Batch variation supersedes adjustments to labeling procedure.....	140
7.3	Conclusions.....	144
	References.....	145

Table of Figures

Figure 1.1 Nanoparticle surface ligands determine material properties.....	2
Figure 1.2 Broadband absorption and narrow emission of QDs	3
Figure 1.3 Upconverting nanoparticles operate in an optical window for tissue imaging.	4
Figure 1.4 Size comparison of nanocrystal to biomolecule modifications	5
<hr/>	
Figure 2.1 Ligand exchange on nanocrystals may displace metal-terminated surface ...	8
Figure 2.2 Structures formed from amphiphilic polymers in aqueous solution.....	9
Figure 2.3 Amphiphilic encapsulation polymer structures	9
Figure 2.4 Nanocrystal polymer encapsulation workflow	11
Figure 2.5 Heterogeneity from incomplete chloroform evaporation during encapsulation	12
Figure 2.6 Maleic anhydride ring opening in PMAO	12
Figure 2.7 Heat treatment clarifies aqueous nanocrystal dispersions	13
Figure 2.8 Influence of excess coordinating ligands on surface passivation	14
Figure 2.9 Influence of post-encapsulation additives on surface passivation	15
Figure 2.10 Centrifugal dialysis enables separation of small molecules from nanocrystals.....	16
Figure 2.11 PMAO is not fully removed by centrifugal dialysis	17
Figure 2.12 Sucrose ultracentrifugation workflow for separation of excess polymer ...	18
Figure 2.13 Optical characterization of sucrose ultracentrifugation fractions	19
Figure 2.14 Sequential crosslinking of amine to thiol <i>via</i> SM(PEG) ₂	20
Figure 2.15 PMAO maleic anhydride reacts with primary amines for diversity in surface chemistry	21
Figure 2.16 Conversion of amine to activated disulfide using Traut's and Ellman's reagents	22
Figure 2.17 Pyridyldisulfide reagents for conjugation to PMAO polymer.....	23
<hr/>	
Figure 3.1 Copper-mediated click reactions on QD surfaces.....	31

Figure 3.2 Tarantula toxin GxTX bound to Kv2 potassium ion channels	32
Figure 3.3 Persistence of Cu QD quenching in the presence of Cu-coordinating ligands and Cd ²⁺	33
Figure 3.4 FRET-based screen for improved CuAAC reaction with minimal QD quenching	34
Figure 3.5 Structures of organic fluorophore azide and alkyne click reagents	36
Figure 3.6 Combinatorial fluorescence analysis of ~1200 CuAAC reaction conditions on QDs	37
Figure 3.7 Copper-free QD-Cy5 coupling	39
Figure 3.8 Reactivity of QD-PAOA surface amines	39
Figure 3.9 Emission spectra of QD compositions after CuAAC reaction with Cy5-alkyne	41
Figure 3.10 CuAAC chemistry and Cu quenching mechanisms on amphiphilic polymer-encapsulated QDs.....	42
Figure 3.11 Cy3-azide CuAAC coupling with Cy5-alkyne	42
Figure 3.12 Emission spectra from the Cy3 – Cy5 CuAAC parameter screen	43
Figure 3.13 Partial recovery of QD emission with post-CuAAC EDTA incubation	44
Figure 3.14 Effect of surface carboxylates on QD quenching and CuAAC efficiency	45
Figure 3.15 Effects of superstoichiometric Cu and Cu ligands on QD quenching and CuAAC efficiency	46
Figure 3.16 Effects of superstoichiometric Cu by QD passivating polymer.....	47
Figure 3.17 Quenching and CuAAC reaction efficiency with varying reaction parameters	47
Figure 3.18 Detection of GxTX conjugated to QD surface	48
Figure 3.19 Live cell imaging of QD-GxTX conjugates on CHO cells expressing Kv2.1 channels.....	49
—————	
Figure 4.1 SpyCatcher/SpyTag split domain conjugation system. ¹¹²	60
Figure 4.2 SpyTag-decorated fluorophores aggregate in solution	61
Figure 4.3 Antibody conjugation methods are nonideal for high-performance probes	62
Figure 4.4 Schematic design for FRET-based endocytosis probe	63
Figure 4.5 QD-fluorescent protein FRET design	64
Figure 4.6 Chimera render of Spy system crystal structure	65
Figure 4.7 SpyCatcher-nanocrystal coupling through thiol side chain	66

Figure 4.8	Screening <i>E. Coli</i> colonies for amino acid mutation	66
Figure 4.9	SDS-PAGE analysis of SpyCatcher-Ser35Cys expression	67
Figure 4.10	Hydrodynamic radius shift from QD to QD-SpyCatcher by DLS	68
Figure 4.11	Tryptophan fluorescence from SpyCatcher on QDs	69
Figure 4.12	Time trace measuring thioamide leaving group	70
Figure 4.13	Spectral detection of SpyCatcher on QDs by mTurquoise conjugation	71
Figure 4.14	SpyTag-2G10 antibody fusion retains SpyCatcher binding ability	72
Figure 4.15	Live cell imaging of QD-2G10 constructs in MDA-MB-231 cells	73
Figure 4.16	mPlum fluorescent protein spectral and structural properties	74
Figure 4.17	mPlum(Asp169Cys) spectra	75
Figure 4.18	Aeration of mPlum solution reduces green product	76
Figure 4.19	mPlum(Glu16Pro, Asp169Cys) mutant spectra show reduction in side products	76
Figure 4.20	mPlum(Glu16Pro, Asp169Cys) SDS-PAGE and Western blot	77
Figure 4.21	Arg4-mCherry(Ser131Cys, Asp132Lys)-SpyCatcher protein expression .	78
Figure 4.22	Disulfide-linked QD probe displays FRET and spectral changes under cellular reducing conditions	79
—————		
Figure 5.1	2D crystalline array of S-layer protein visualized by STEM	89
Figure 5.2	Schematic of hierarchically-ordered cell-nanoparticle hybrid material	90
Figure 5.3	Visualization of recombinant SbsB and SbsB Cys cluster constructs	93
Figure 5.4	SbsB sheets containing metal-binding Cys residues bind Au NPs	94
Figure 5.5	Conjugation of SpyCatcher protein to nanoparticles	96
Figure 5.6	SbsB nanosheets can display semiconductor quantum dots at high occupancy while preserving their optical properties <i>via</i> SpyTag/Catcher conjugation	97
Figure 5.7	Emission of QD-SpyCatcher conjugated to SbsB C-SpyTag	98
Figure 5.8	SbsB nanosheets display ceramic, upconverting nanoparticles at high occupancy while preserving their optical properties <i>via</i> SnoopTag/Catcher conjugation	99
Figure 5.9	Emission of NaGdF ₄ -SnoopCatcher bound to SbsB C-SnoopTag	100
Figure 5.10	Isopeptide conjugation allows high-occupancy, multicomponent display of nanoparticles through SbsB nanosheet scaffolds	101

Figure 5.11 Cartoon of SbsB crystal structure depicting sites of embellishment for nanoparticle binding or conjugation	102
Figure 5.12 Dual modified S-layer nanosheets can localize two types of nanocrystals at distinct locations and display plasmonic properties	104
Figure 5.13 STEM images of nanoparticle binding to dual modified sheets	105
Figure 5.14 Optical measurement of SbsB nanosheets with conjugated AuNP	107
Figure 5.15 AFM analysis of RsaA lattice and bound QDs on <i>Caulobacter</i> surface ..	108
Figure 5.16 Size determination of CdSe/ZnS QD constructs	109
Figure 5.17 Specific attachment of engineered S-layer protein RsaA-SpyTag on the <i>C. crescentus</i> cell surface to SpyCatcher-functionalized nanoparticles	110
Figure 5.18 Optimization of the binding between QD-SpyCatcher and <i>C. crescentus</i>	111
Figure 5.19 Observation of QD supracellular assemblies using confocal microscopy	112
Figure 5.20 Mechanical properties of the supracellular assemblies as measured by AFM	114
Figure 5.21 Elasticity of supracellular materials by storage modulus	115
Figure 5.22 Supracellular material can repair itself under growth conditions	116
Figure 5.23 Assembly of bacterial film mediated by NP-magnetic field interaction ..	117
—————	
Figure 7.1 QD-GxTX labeling UC Davis CHO cell line	135
Figure 7.2 Cell culture dish surface effects on QD labeling ..	136
Figure 7.3 Imaging disparity between labs	136
Figure 7.4 Nonspecific UC Davis QD batch shows specificity on LBNL cell line	137
Figure 7.5 Reduced valency of QD-GxTX constructs does not improve specificity...	138
Figure 7.6 Concentration series of QD-GxTX	139
Figure 7.7 Inclusion of nonbinding GxTX variant before and during labeling reduces overall staining	140
Figure 7.8 Batch variation dominates over biological or procedural changes	140
Figure 7.9 Dispersion additives do not disrupt QD-GxTX aggregates in labeling	141
Figure 7.10 Dissociated cells do not show increased labeling from accessibility of channels	142
Figure 7.11 Full system overhaul results in zero labeling	142
Figure 7.12 Dye-labeled GxTX shows specific labeling and K ⁺ response	143

Acknowledgements

I am thankful to a great many people for their direct and indirect contributions to this work, and I'll do my best to give them proper recognition here. This document is the culmination of an unlikely path, with appreciation due along the way.

First of all, I'd like to acknowledge my Ph.D. advisor Bruce Cohen for taking a chance on a stubborn student with trust that it would all work out in the end. You've given me the freedom and independence to be creative in my research as I see fit, and it has made me a better scientist for it. A major thank you also to Evan Miller for agreeing to serve as my advisor at times when Bruce could not. To the other Cohen group members – Cheryl Tajon, Bella Tian, David Garfield, Zeming Wang, Cassio Pedroso – thank you for all of your advice and support. I have also been a part of several years-long collaborations that have really expanded my scientific perspective. Thanks to Jon Sack, Rebecka Sepela, and Parashar Thapa of the Sack lab for your hard work and stimulating meetings. Thank you to the whole DARPA ELM team as it changed over the years, and especially to its fearless leader, Caroline Ajo-Franklin, for including me in such a bold undertaking.

I'd also like to thank the other staff and users of the Molecular Foundry for fostering an incredible environment of collaboration without competition and for concentrating so many great scientists all in one place. It was a truly unique and exceptional place to spend my time in graduate school, and there are many things I've learned here beyond the science that I take with me into the future. In particular, I'd like to thank Ron Zuckermann for showing what it means to lead by example, Dong Li for his boundless creativity, Frankie Manea for her infectious enthusiasm, and Marimikel Charrier for her eternal patience. Also to those who have contributed their advice or support: Behzad Rad, Rita Garcia, Emory Chan, Paul Ashby, Virginia Altoe, Tracy Mattox. My experience at the Foundry is something I will always truly appreciate.

To all of the students I've mentored over the years – Katie Cecil, Liz Hernandez, Alex Powers, Maya Segal, Simeon Giverts, Anna Wannemacher, Nicole Torquato, Jessica Yu – you have all made me a better advisor and teacher, and I hope my efforts have helped you in your lives and in your scientific endeavors.

A major thank you is due to the people who set me on this path before I knew where I was headed. Thank you to my undergraduate research advisors Marcel Bruchez and Saumya Saurabh for initiating me into research, and to Alison Barth for empowering me to expand into a new field of science. And of course, a huge thank you to my parents for fostering in me an intellectual curiosity that drives me even today.

Finally, I want to thank my wife Allison. This accomplishment is partly hers as well as it is mine. Her support and encouragement has helped sustain me through these long graduate school years, and I am forever grateful she took the chance to follow me out to California. This dissertation is dedicated to her, for all the patience she has showed me over the years of its development.

1 | Introduction

Colloidal nanocrystals have been a topic of great research interest for some time due to their emergent physical properties and the design capabilities of materials at the nanoscale.¹⁻⁵ Depending on the composition, these nanoparticles may exhibit strong fluorescent, luminescent, magnetic, plasmonic, or other properties due to the inherent or induced physics of the material.⁶⁻⁹ However, due to their small size and therefore large surface to volume ratio, the interaction of these devices with their environment dominates both the colloidal properties and the utility of nanocrystalline materials. Appropriate surface functionalization is essential for control of downstream applications like self-assembly or targeted delivery.¹⁰⁻¹² Precise control over the surface chemistry of nanoparticles allows for the rational design of complex and hierarchical materials driven by surface interactions.

Nanoparticles synthesized from solution typically have surfactant ligands that coordinate the nanocrystal surface during growth, which stabilize them against aggregation and play important roles in determining the reaction rate and the final size and shape of the crystals (Figure 1.1a).¹³⁻¹⁵ These native ligands are often maintained through the purification process and are used to aid in dispersion of the nanoparticles in a storage solvent. However, the coverage of these ligands is not uniform across the nanocrystal – there is a dynamic equilibrium of ligands on and off the surface,¹⁶⁻¹⁸ and certain crystal facets will more tightly coordinate ligands than others (Figure 1.1b).^{19,20} A common method of both modification of the surface as well as phase transfer is to exchange the native ligand for another surface-coordinating ligand. This is especially common in which the incoming ligand coordinates more strongly to the surface.^{21,22} For example, weakly bound citrate on gold nanoparticles may be exchanged for thiol ligands,²³⁻²⁶ and this principle is often employed on other types of nanocrystals as well.^{21,27-29} In this work, two main types of nanocrystals are explored for applications as imaging probes and as components for hybrid materials: semiconductor quantum dots and upconverting nanoparticles, which require retention of the native ligands for their effective use.^{14,21,22,30-32}

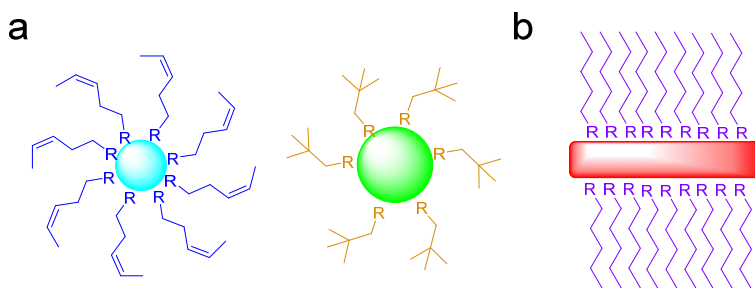


Figure 1.1 Nanoparticle surface ligands determine material properties. (a) Ligand coordination confers colloidal stability, but also dictates reaction rate and properties like final nanoparticle size during synthesis. (b) Many ligands will preferentially coordinate one crystal facet over another, leading to anisotropic growth along certain axes.

Semiconductor quantum dot nanocrystals (QDs) have an exceptional property wherein the physical size of the crystals can be reduced until an exciton is confined to a space smaller than the Bohr radius of the material, which causes the nanocrystal energy levels to become discrete compared to the continuum energy levels observed in bulk materials.^{33,34} This quantum confinement phenomenon results in a tunable energy gap, the bandgap, between the highest occupied energy level and the lowest unoccupied level. In most cases, the higher levels are pseudocontinuous such that the nanoparticles have broadband absorption of light higher energy than the bandgap. This is in contrast to their narrow emission bands from relaxation back across the bandgap due to phonon relaxation to the conduction band edge (Figure 1.2a).³⁴ Because of this disparity, QDs have high extinction coefficients in the UV or at bluer visible wavelengths with a large Stokes shift to their corresponding emission (Figure 1.2b). This large shift allows for multiple fluorophores to be excited simultaneously under the same excitation wavelength for facile multicomponent imaging. Tuning of the emission peak can be performed by adjusting the confinement through the size of the nanocrystal, but also through changes in material composition and shell type or thickness. These distinctive properties make QDs interesting candidates for research in many different fields from photovoltaics to biology.

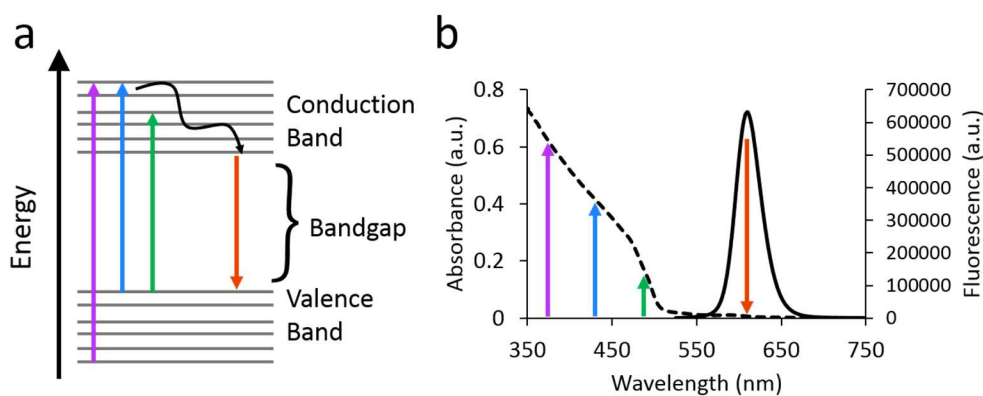


Figure 1.2 Broadband absorption and narrow emission of QDs. (a) Energy diagram for a QD system. Absorption events (purple, blue, green) need only be higher energy than the bandgap to excite the QD. Following fast phonon relaxation (black) to the conduction band edge, fluorescence emission (red) has a narrow distribution around the bandgap energy. (b) Spectral representation of data shown in (a), showing broad absorbance (dashed) and a narrow emission peak (solid).

QDs are particularly attractive to us as outstanding probes for light microscopy, with their exceptionally high photostability, large optical cross-sections, broadband excitation and large Stokes shifts, and demonstrated uses in multiplexed and single molecule experiments.^{1,6,14} Like other hydrophobic nanocrystals, though, they must be transferred to water and their surfaces functionalized to have any utility as imaging probes or biosensors.^{4,35} While a number of ligand exchange and further bioconjugation

reactions have been adapted for QDs,^{36–39} others have been found to destroy the exceptional optical properties of the nanocrystal.^{40,41} Other strategies, such as overcoating the nanocrystals in a shell of amorphous silica^{42,43} or coating in high molecular weight brush polymers^{44,45} render the final probes too large for precise biological targeting. Broadening the scope of QD surface conjugation chemistry is essential to expand the reach of QDs for imaging applications. There is also an increasing interest in the development of nanotheranostics platforms for simultaneous sensing, imaging, and therapy using nanoscale probes. QDs have great potential for such applications, with a variety of results published in the fields of sensing, drug delivery, and biomedical imaging, but uniform targeting of QDs within biological systems is still a challenge.^{1,35,41}

Likewise, luminescent lanthanide-doped upconverting nanoparticles (UCNPs) hold enormous promise as imaging probes for their nonblinking, nonbleaching, and zero background due to the anti-Stokes shift of the upconverted emission.^{7,46} Upconversion is the process of sequential absorption of two lower energy photons that results in the emission of a single higher energy photon upon relaxation (Figure 1.3a). Since the excitation wavelength for these materials is often in the near infrared (NIR) region, they also have the potential for deep penetration tissue imaging due to the decreased tissue absorbance and scattering (Figure 1.3b).^{47,48} As the excited state lifetime for the lanthanides is long, on the order of micro- to milliseconds, the energy is prone to migration to the surface of the nanocrystal and can be dissipated through interaction with vibrational modes of surface-associated oleate and nearby water molecules.^{31,32,49} Removal or exchange of the surface carboxylate ligands is common,⁵⁰ but leaves much of the nanocrystal surface available for this dissipation process through solvent interaction.

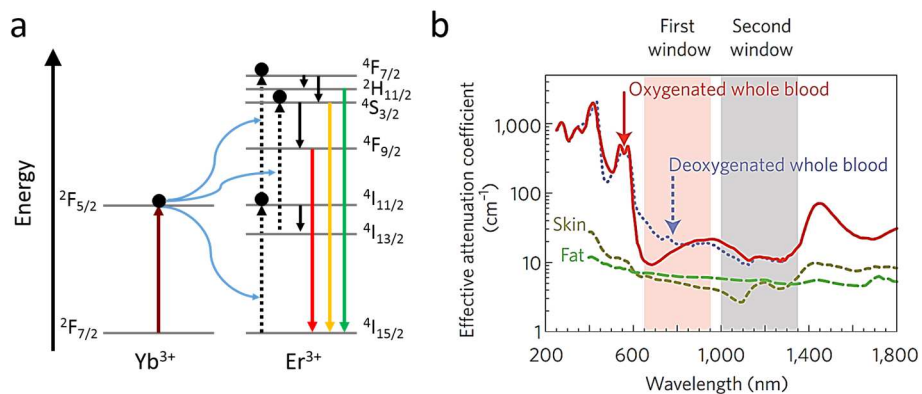


Figure 1.3 Upconverting nanoparticles operate in an optical window for tissue imaging. (a) A simplified schematic of the upconversion process. Yb^{3+} ions absorb NIR light (maroon) and sequentially transfer energy to Er^{3+} ions (blue). Phonon relaxation (solid black) yields anti-Stokes shifted emission from the Er^{3+} (red, yellow, green) into the visible spectrum. (b) Total attenuation (absorption and scattering) in common tissues⁵¹ is minimized at NIR wavelengths, allowing deeper imaging and excitation into tissue.

UCNPs offer an additional challenge in designing purification and conjugation techniques, as there is no visual indication of the nanocrystals in dispersion (no visible light absorption) and no measurement of nanoparticle concentration once they have been transferred to an aqueous dispersion. Our manipulations and methods must be careful to be high fidelity and not alter the starting concentration significantly through losses in the procedure. This is a much higher standard than for QDs, for example, wherein we could simply measure the concentration afterwards regardless if nanocrystals have been lost in the process to aggregation. Having this extra constraint leads us to create methods that are necessarily gentler and robust to changes in the exact components so that we can maximize nanocrystal dispersibility and recovery.

For both of these model systems, it is the material properties that determine the utility of the nanoparticle for an application, but the majority of a nanocrystal's interaction in a system comes from its surface. Oftentimes it is necessary to isolate the nanoparticle surface from the environment so as not to disrupt these material properties. However, the surface is also the only way to introduce functionality to the nanoparticles in order to form more complex structures. There have been numerous methods developed for bioconjugation of nanocrystals to biomolecules,³⁶⁻³⁹ but most of them fall short on some facet of design. The biotin-streptavidin system, while widely used and high affinity, does not form a permanent covalent linkage and suffers from a dramatic size increase to the nanocrystal that can hinder precise labeling and tracking in living systems.^{4,38,52} This same limitation applies to full IgG antibody-nanoparticle constructs, where the addition of 150 kDa proteins can double or triple the effective size of a nanocrystal probe, and antibody fragmentation and misorientation reduce binding efficacy (Figure 1.4).^{5,35} A new approach to conjugation that minimizes the increases to nanocrystal size is essential.

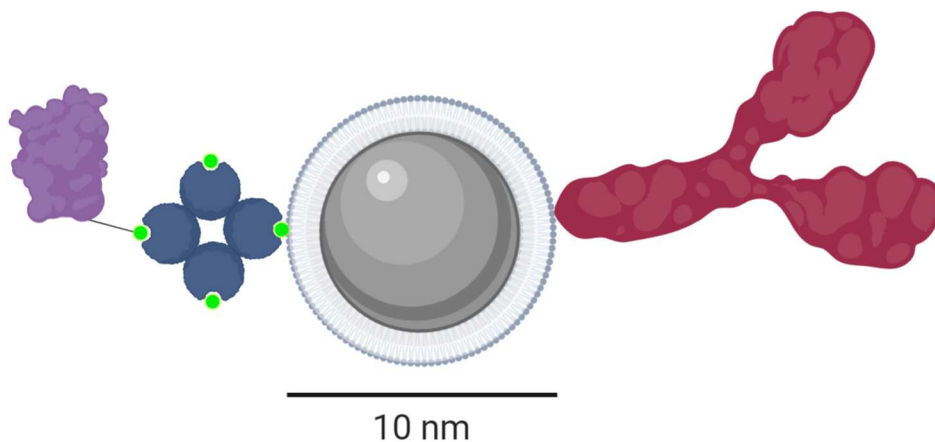


Figure 1.4 Size comparison of nanocrystal to biomolecule modifications. Addition of streptavidin (blue) or IgG antibodies (red) drastically increase the hydrodynamic radius of a nanoparticle construct.

This work will explore my efforts to use modular approaches for isolation and passivation of nanocrystal surfaces for improved optical properties and diminished batch variability, as well as novel ways to introduce functionality to the surface both chemically and through compact biomolecule linkages. I use these strategies to create complex probes of biological functions and in the design of hybrid hierarchical materials driven by the surface interactions. These improvements vastly expand our abilities in designing and synthesizing high-quality and multifunctional nanocrystal materials.

2 | Nanocrystal Surface Functionalization *via* Encapsulation

2.1 Introduction

Due to the complex nature of nanocrystal surfaces, it is desirable to design manipulations that are robust to small changes in order to mitigate the batch-to-batch variability in synthesized conjugates. By incorporating modular design principles into how we treat the nanocrystal surface, we create stable intermediates that can then be differentiated into many types of final conjugates. In engineering the surface chemistry of our nanocrystals, we accomplish this through two main avenues – polymer encapsulation and post-encapsulation chemical modifications. These two components allow us to create conjugates of many final forms and compositions from the same base starting material, and the process is largely agnostic to the type and size of the nanocrystals in question.

In order to get our nanocrystals to a target in a biological system, they must first be transferred from dispersions in organic solvent into water. It has been established that removal or displacement of the native surface ligands after synthesis is often destructive to the photoluminescence quantum yield.^{5,14,21,22} Colloidal nanocrystals are often synthesized with a metal as the terminating atom of the crystal surface (*e.g.* Cd for CdSe quantum dots) in order to promote high surface coverage of metal-coordinating surface ligands. Common ligands are comprised of a hydrophobic chain for colloidal stability in organic solvents and a head group that coordinates to the surface, often through oxygen atoms as in trioctylphosphine oxide or oleic acid.^{3,5,33} When these ligands are removed, they may remove the terminating metal atom as well, providing a surface that is less amenable to be coated in ligands, less colloiddally stable, and prone to surface traps affecting the electronic properties and decreasing quantum yield (Figure 2.1).^{21,22,53,54} Therefore, we must design ways to transfer nanocrystals to aqueous dispersions without disrupting the native ligand shell.

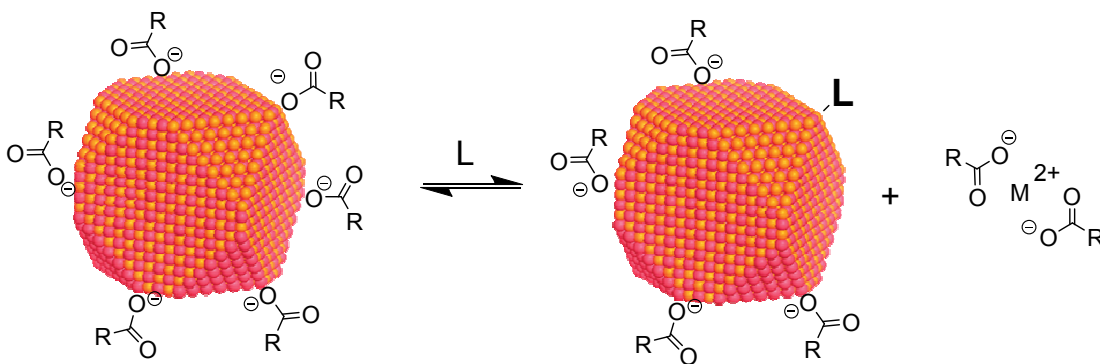


Figure 2.1 Ligand exchange on nanocrystals may displace metal-terminated surface. Excess ligands (L) that coordinate the surface may cause the release of a $M(O_2CR)_2$ complex, reducing surface metal coverage as well as surface ligand density.

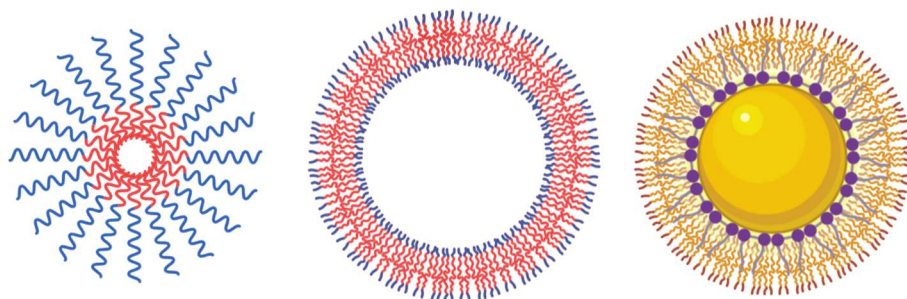


Figure 2.2 Structures formed from amphiphilic polymers in aqueous solution. Polymers in solution may form micelles (left) or liposomes (center) depending on the strand structure. By interacting with the hydrophobic ligands on nanocrystals, they may form a liposome-like structure around the nanoparticle (right).

Amphiphilic polymers are molecules with hydrophilic and hydrophobic domains, either in blocks or distributed throughout the chain. Depending on the sequence, these molecules can form larger ordered structures such as micelles or liposomes, through the hydrophobic or hydrophilic interactions between adjacent polymer strands (Figure 2.2). We exploit this capability in order to encapsulate our nanocrystals within a liposome-like structure wherein the hydrophobic portions of the polymer interact with the hydrophobic ligands stabilizing the nanocrystal, and hydrophilic groups are displayed on the polymer surface allowing the transfer into aqueous dispersions (Figure 2.2).^{8,55-58} In addition to the phase transfer, this also provides a hydrophobic barrier surrounding the nanocrystal that excludes water from reaching the surface, as well as a means to further modify the surface chemistry through reactions on the hydrophilic functional groups in the polymer. Utilizing two main polymers, poly(acrylic acid)-*co*-poly(*n*-octylacrylamide)-*co*-poly(2-aminoethylacrylamide) (PAOA)^{56,58,59} and poly(maleic anhydride-*alt*-1-octadecene) (PMAO),^{8,55,57,59} we can control surface chemistry and create conjugates for many different types of nanocrystals (Figure 2.3).

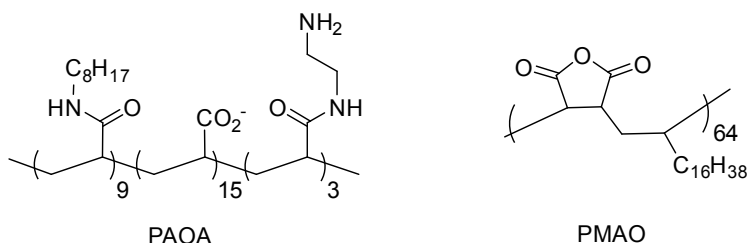


Figure 2.3 Amphiphilic encapsulation polymer structures. PAOA is a random copolymer of hydrophilic and hydrophobic side chains, while PMAO has alternating hydrophilic and hydrophobic groups. Degrees of polymerization shown are approximate for the polymers used.

Here, we show how use of the polymer encapsulation strategies and further modifications create modular conjugates that are robust to changes in nanocrystal identity, valency, and surface chemistry. The process of encapsulation is robust and repeatable, although many of the finer details have been discovered empirically as there are limited methods for probing the resulting modified nanocrystal surface. By creating reproducible surfaces with a wealth of displayable chemistries, we allow for the downstream production of high-quality nanocrystal probes and hybrid materials.

2.2 Results and Discussion

2.2.1 Polymer encapsulation for aqueous dispersion of nanocrystals

The hydrophobic native ligands must be preserved on the surface to maintain the nanocrystal's luminescence properties,^{22,53,54} so phase transfer to an aqueous dispersion is completed through conformal deposition of an amphiphilic polymer layer around the nanoparticles. This is first achieved as a dried film, followed by aqueous dispersion to form the final encapsulated structure (Figure 2.4). Depending on the surface chemistry of the nanocrystal, certain approaches must be used to avoid stripping the native ligands and forming insoluble aggregates of nanoparticles. Each of the stages in this pipeline is essential in some way to the final quality of the encapsulated nanocrystals.

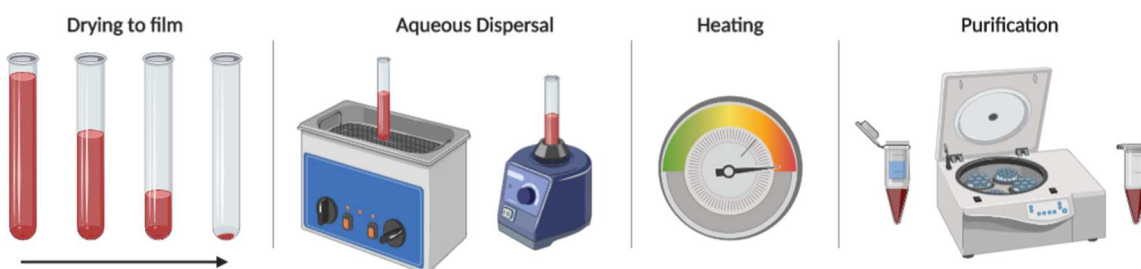


Figure 2.4 Nanocrystal polymer encapsulation workflow. Each of the encapsulation procedures follows the same basic steps, regardless of polymer or nanocrystal used. First, a film of polymer and nanocrystals is generated by evaporation from chloroform. The film is redispersed through ultrasonication and mixing in aqueous buffer and heated to homogenize the coating. Purification to remove excess polymer yields the final encapsulated nanocrystal suspension.

Due to the amphiphilic nature of these polymers, they cannot be added directly to the nanocrystals without aggregating in the hydrophobic solvent. Both nanoparticles and polymer must be well-dispersed in chloroform to allow complete surface interaction during drying (Figure 2.4). A large excess of polymer is necessary to ensure that nanoparticles are well-separated and to avoid wrapping multiple nanocrystals together.⁵⁷ The mixture is dried slowly under nitrogen with vigorous mixing to form a homogeneous film, and it is critical that no chloroform remains trapped in the material. When chloroform is not completely removed prior to dispersal of the encapsulated nanocrystals in water, several types of phase separation may occur (Figure 2.5). Each of these is inseparable back to the starting material and cannot form a homogeneous dispersion, so they must be discarded.

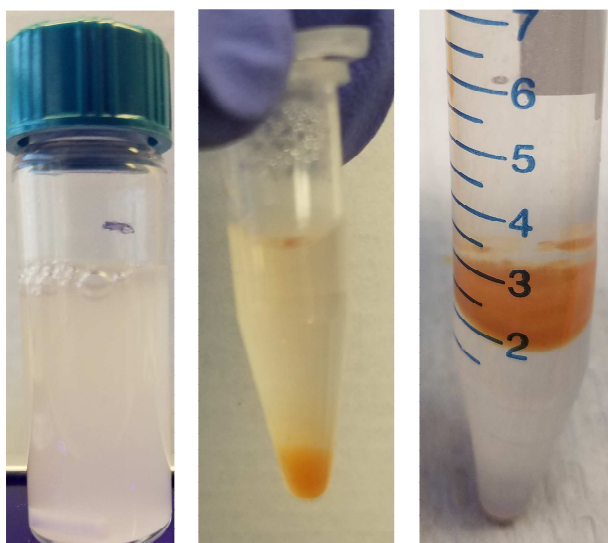


Figure 2.5 Heterogeneity from incomplete chloroform evaporation during encapsulation. Addition of water to films with chloroform may form emulsions (left), the nanocrystals may partition back to the chloroform (center), or the film may reform at the chloroform-water interface as a solid (right).

Once a dry film is obtained, it may be dispersed into a buffered solution by intermittent ultrasonication and mixing. For PAOA encapsulation, this buffered solution must be basic to ensure the nanoparticle surface coating of carboxylic acids remains deprotonated for charge repulsion between nanoparticles. In the PMAO samples, the anhydride undergoes ring opening *via* hydrolysis under basic conditions to form carboxylic acids that similarly stabilize the dispersion in water (Figure 2.6). This is also the stage that allows for further chemical reaction on PMAO *via* primary amines, as discussed in the next section. Once the nanoparticles are well-dispersed by sonication, it is likely there is extra, loosely-bound polymer on the surface due to the large excess used and the density of the dried film. Accordingly, the encapsulated nanocrystals require further purification before use, as these excess polymers can act as surfactants and disrupt biomolecules in downstream applications.

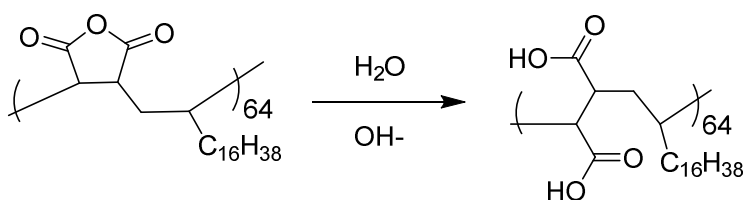


Figure 2.6 Maleic anhydride ring opening in PMAO. Hydrolysis under basic conditions after nanocrystal encapsulation yields carboxylic acid surface groups.

Heating the nanocrystal dispersion is an easy way to satisfy several means of improving the polymer surface layer – it increases the solubility of the polymer chains in the buffered solution, it provides energy for disentangling and removing partially-attached chains, and it provides thermodynamic rearrangement energy for chains to form a more conformal coating on the surface. These processes are difficult to probe, but we can observe visually from a sample before and after heating that the dispersion is clarified and more stable after the procedure (Figure 2.7). This idea of forming an unbroken polymer coating over the entire surface is very important for applications where the nanocrystal must be fully insulated from the environment to protect its optical properties. To this end, I have conducted a number of experiments designed to fill any breaks in the polymer layer that may compromise its integrity.

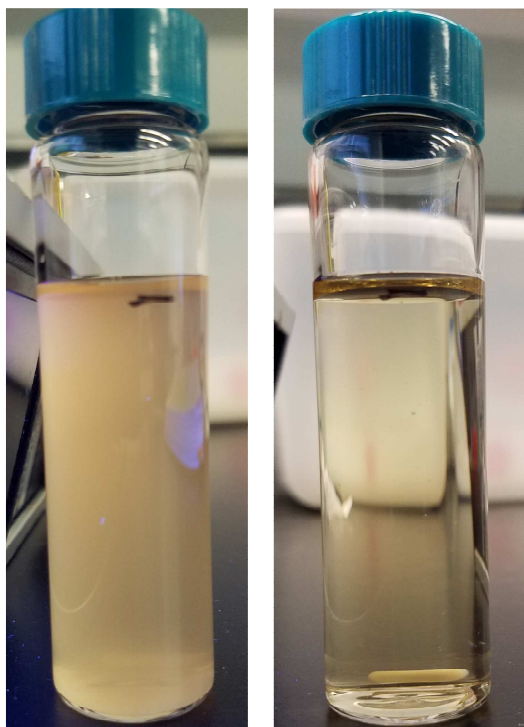


Figure 2.7 Heat treatment clarifies aqueous nanocrystal dispersions. An aqueous dispersion of PAOA-encapsulated CdSe/ZnS 585 nm quantum dots before (left) and after (right) incubation at 80°C for 1 hour.

Two approaches to tackle the issue of incomplete polymer coverage are by adding excesses of surface ligands to ensure all nanocrystal sites are coordinated or by using additives post-encapsulation to fill any gaps that remain. These experiments were conducted on CdSe/CdS core-shell quantum dots, which are stabilized during the synthesis with oleic acid ligands on the surface, but may have holdover trioctylphosphine

(TOP) or trioctylphosphine oxide (TOPO) ligands from the core synthesis (Figure 2.8a).^{6,59} In an attempt to promote higher surface coverage, excesses of each of these ligands were added prior to the encapsulation procedure. After challenging the polymer-coated QDs with Cu^+ in solution, the fluorescence was measured to see how well the coatings prevented Cu^+ -induced quenching (Figure 2.8b). Additions of TOP and TOPO on their own were mildly effective over no additives, but the combination of both presented no increased resistance at all. The addition of a large 1 vol% excess of oleic acid, the main surface ligand, resulted in nearly full attenuation of the Cu quenching (Figure 2.8b). We have also noted that this addition is essential for long term storage of the hydrophobic nanocrystals to prevent aggregation from dynamic ligand coordination of the surface, leading to a double benefit for maintaining high quality nanocrystals.

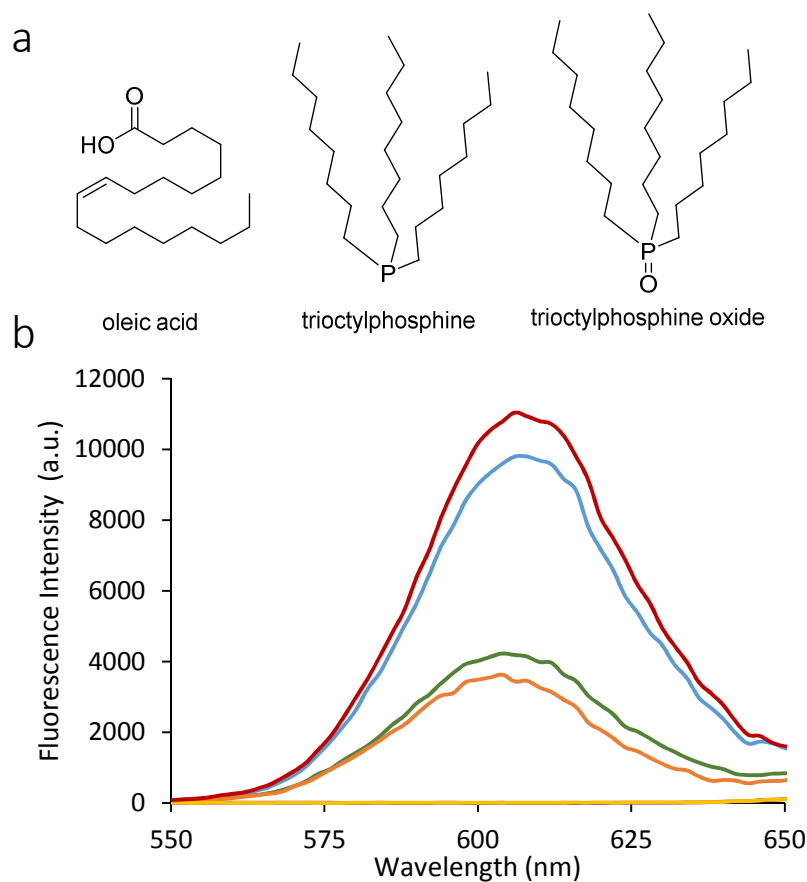


Figure 2.8 Influence of excess coordinating ligands on surface passivation. (a) Chemical structures of coordinating ligand additives. (b) Fluorescence emission of encapsulated QDs treated with: 1 vol% oleic acid (blue), 0.2 vol% TOP (green), 0.2 vol% TOPO (orange), both TOP and TOPO (yellow), or no additives and no Cu (red). Each sample was subjected to a 30 sec exposure to 50 mole equivalents of Cu^{2+} salt.

The second approach involves partitioning additives to the polymer coating after encapsulation in order to fill any gaps in the layer. For this, we want amphiphilic molecules with a hydrophobic portion or face that can insert into the ligand shell and a hydrophilic portion that can project out to stabilize the form. I've selected several small molecule and polymeric materials to put towards this goal and added them to the encapsulated nanoparticles after purification (Figure 2.9a). Three of these – CHAPS, cholesterol, and precomplexed zinc oleate – caused significant reductions in the brightness of the QDs after incubation with the additives (Figure 2.9b). No precipitate or aggregates were observed, and the mechanism of quenching is unclear in these cases. Addition of Triton X-100 and Tween 20 do not appear to affect the QD brightness, but also do not prevent infiltration of copper ions to the surface (Figure 2.9b).

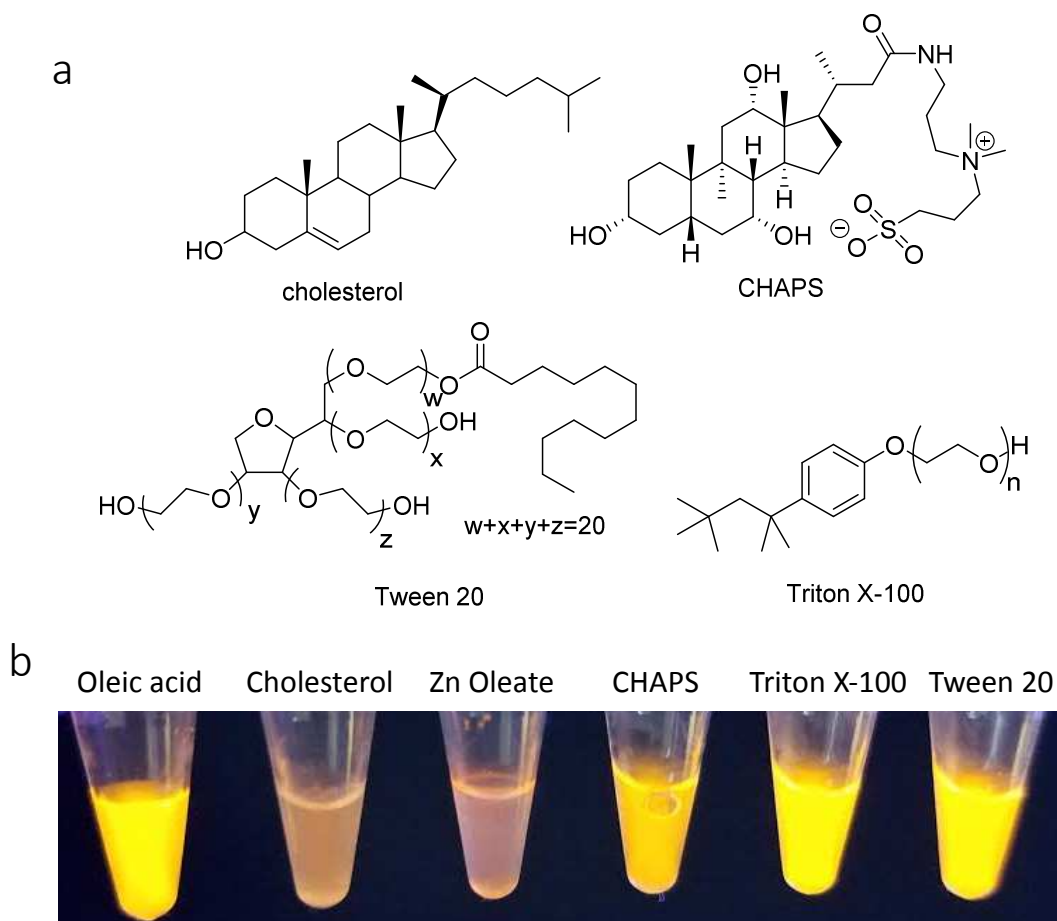


Figure 2.9 Influence of post-encapsulation additives on surface passivation. (a) Chemical structures of small molecule and polymeric additives. (b) Photograph of fluorescence from CdSe/ZnS quantum dots under UV illumination after addition and 24-hour incubation with each of the additives.

It seems the most effective approach has been to include an excess of oleic acid surface ligand in the hydrophobic nanocrystal dispersion, and to use a large excess of polymer to promote encapsulation of individual nanocrystals. However, all of these unused reagents must be removed before further chemical modifications may be made, as they will react to deplete the modification reagents. High-quality encapsulated nanocrystals can be synthesized, but they must first be rigorously purified to be useful as further building materials.

2.2.2 Purification of polymer-encapsulated nanocrystals

For the encapsulated nanocrystals to function, they must be purified of any small molecules or unbound polymer strands. For small molecules and short polymers, like PAA, this is relatively simple to do by centrifugal dialysis. The large size discrepancy between the encapsulated nanoparticles and the molecules to be removed means that the nanoparticles may be filtered on highly porous membranes without risk of transport through (Figure 2.10). For example, a 50 kDa filter has a pore size of approximately 5 nm, well below the size of our nanocrystals and much larger than the small molecules to be removed. So, several washes through these filters is all that is required to fully purify the nanocrystals.

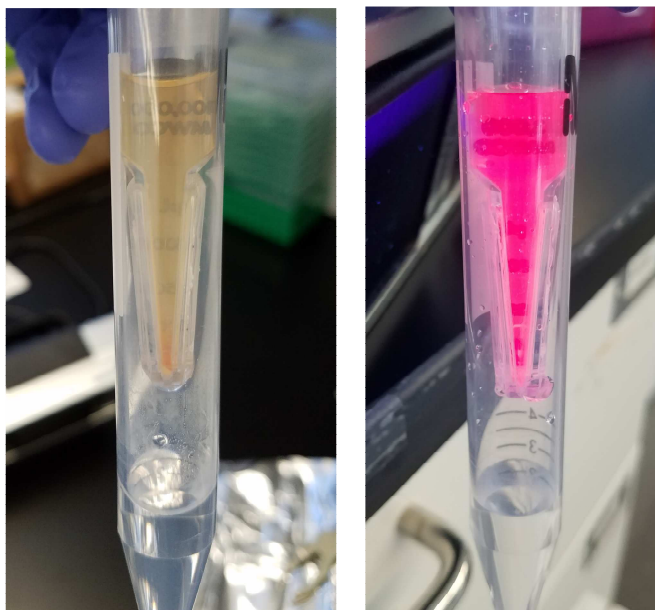


Figure 2.10 Centrifugal dialysis enables separation of small molecules from nanocrystals. A 100 kDa pore filter showing 10 nm CdSe/CdS nanocrystals (orange, red fluorescence) retained above the filter while buffer and small molecules pass through to the lower chamber.

However, this approach does not work for all separations. For the PMAO polymer encapsulation, the polymer chains are larger and have an average molecular weight of around 25,000. Despite this, we have seen evidence from DLS and fluorescence measurements that this polymer is not effectively removed even through 100 kDa filters with extensive rounds of washing (Figure 2.11). This is likely due to the amphiphilic nature of these molecules and their propensity to form supramolecular structures rather than dissolving in aqueous solution (Figure 2.2). In the DLS distribution, there is a strong contribution from < 1 nm material which is correlated with remaining excess polymer (Figure 2.11a). This can even be seen visually as fluorescence (likely from the polymerization initiator) under a handheld UV source (Figure 2.11b). The molecular weight rating for the filter assumes a globular protein for the size comparison as opposed to the extended linear chain or micellar structures of the amphiphilic polymer, so it is not a good measure of if it may pass through the membrane. Attempts to remove PMAO by traditional dialysis with membrane pore sizes as high as 600 kDa were similarly ineffective. Rather than separate based on size, we can remove the polymer based on density by using sucrose ultracentrifugation instead (Figure 2.12).^{57,60,61}

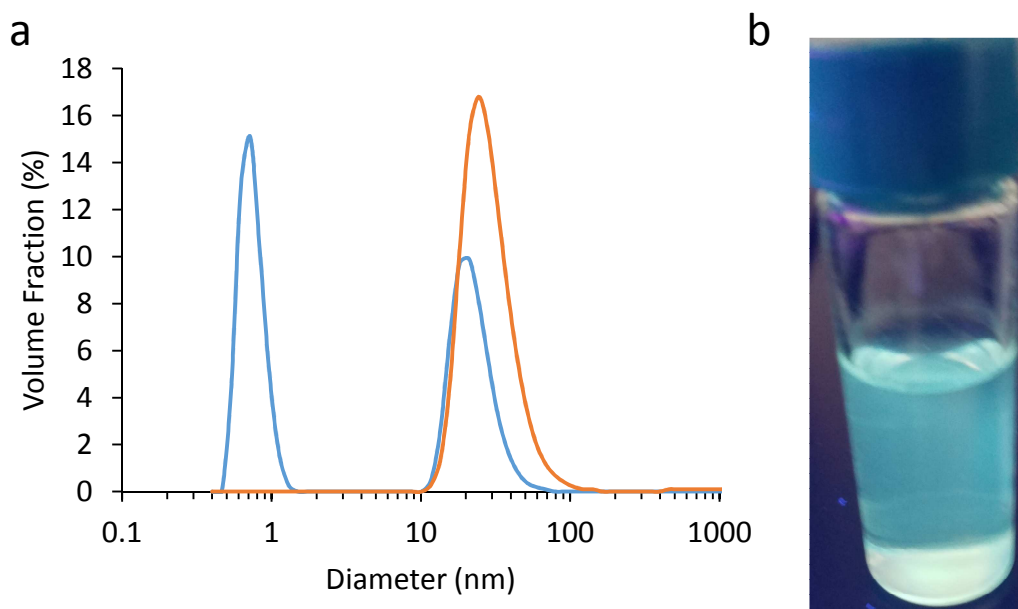


Figure 2.11 PMAO is not fully removed by centrifugal dialysis. (a) Dynamic light scattering of samples of PMAO-encapsulated (blue) and POA-encapsulated UCNP after purification by centrifugal dialysis. (b) POA-encapsulated UCNP under a UV light source, showing strong blue fluorescence.

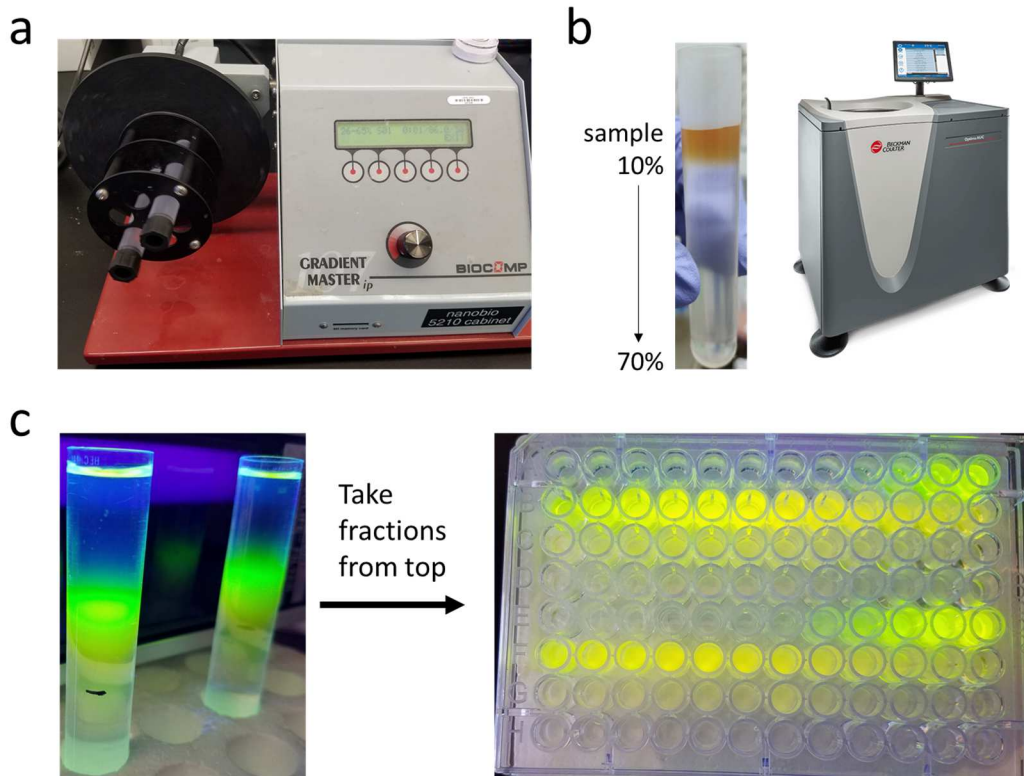


Figure 2.12 Sucrose ultracentrifugation workflow for separation of excess polymer. (a) Linear sucrose gradients are generated stepwise by rotary mixing at an oblique angle. (b) Sample is added atop the gradient (10-70 wt% sucrose in buffer) and spun in an ultracentrifuge for separation by density. (c) Once excess polymer (blue fluorescence) is separated from QDs (green fluorescence), fractions can be taken into 96 well plates and characterized to determine exactly where polymer and QDs reside.

The polymer is essentially a light hydrocarbon chain, while the nanocrystals are dense semiconductor and ceramic materials. Sucrose separation relies on building a linear gradient of sucrose solutions (*e.g.* 10-70 wt% sucrose in buffer) and centrifuging our mixture within it so that the denser components travel further into the gradient than the less dense ones. For excess PMAO separation, it largely remains at the top of the gradient as applied, while the encapsulated nanoparticles travel some distance into the sucrose dependent on centrifugation time, sucrose concentration, and nanocrystal size and composition (Figure 2.12). Typical conditions use a 500 μL sample in a 12 mL tube of 10-70 wt% sucrose solution, with 90 min of centrifugation at $150,000 \times g$. Once the components are separated, we can partition fractions from the tube and analyze their optical properties to determine which fractions contain excess polymer or nanocrystals (Figure 2.13). Fractions containing high 375 nm absorbance indicated presence of excess

PMAO polymer, and fluorescence was used to detect QD nanocrystals (Figure 2.13). Detection of fractions with encapsulated UCNPs required transfer to cuvettes for 980 nm laser-induced upconversion luminescence. After pooling of fractions and bulk dialysis to remove the sucrose, the encapsulated nanocrystals are ready for use. The encapsulated nanoparticles may be synthesized in large batches to maintain continuity for downstream products and can be stored under ambient conditions for a matter of months or years without issue. This process is also general to many nanocrystal types and sizes and to any sucrose-compatible surface chemistry, so this procedure has become a cornerstone of most of our nanocrystal preparations.

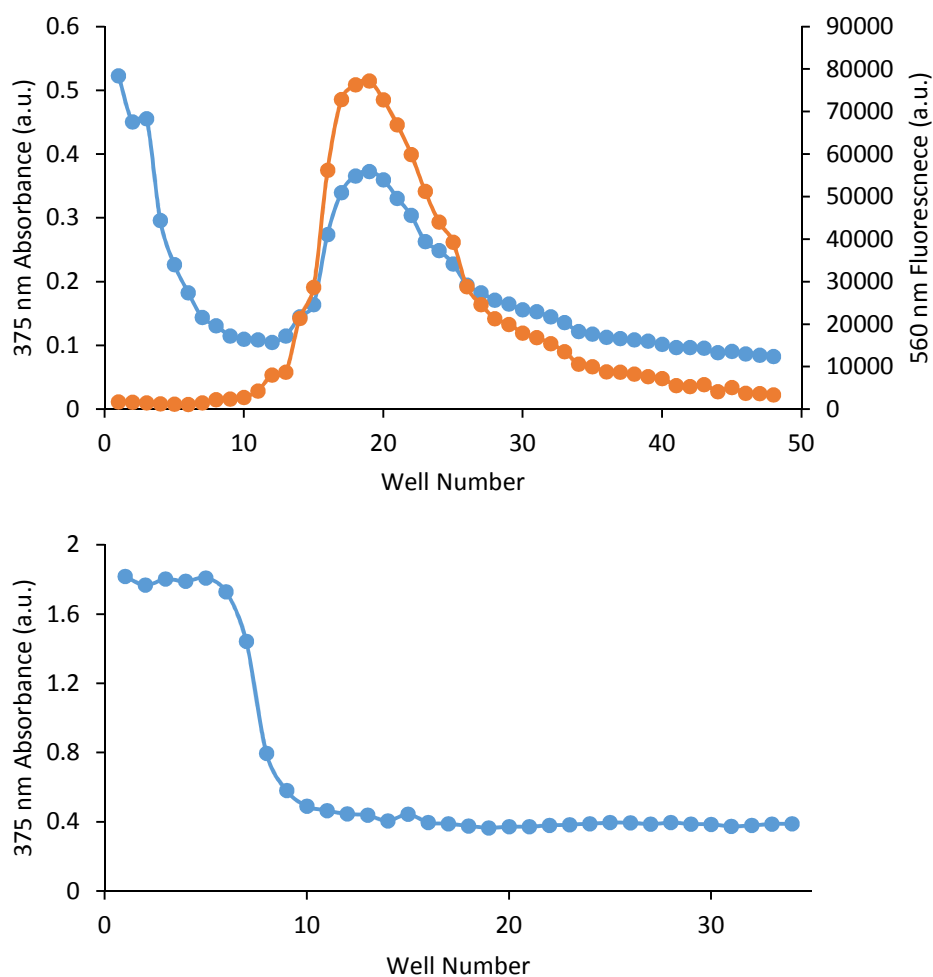


Figure 2.13 Optical characterization of sucrose ultracentrifugation fractions. (a) Absorbance at 375 nm (blue) and fluorescence emission at 560 nm (orange) for fractions from PMAO encapsulation of CdSe/CdS QDs purified by a 15-45 wt% sucrose gradient. (b) 375 nm absorbance for fractions from PMAO encapsulation of 24 nm diameter UCNPs purified by a 10-70 wt% sucrose gradient.

2.2.3 Chemical functionalization of polymer-displayed groups

Once the nanocrystals have been transferred from organic dispersions into buffered solution, the hydrophilic portions of the encapsulating polymers are exposed in solution. Depending on the polymer used, these may be further modified as means of linking a variety of functional groups to those now affixed to the nanocrystal. As carbodiimide couplings have been shown to quench QD fluorescence,⁴⁰ primary amines are the group more easily available for attachment to PAOA-modified surfaces. For this, there is a rich catalogue of available N-hydroxysuccinimidyl esters to allow facile coupling directly or the use of heterobifunctional crosslinking molecules can introduce orthogonal means of conjugation. For many of our applications using biomolecules, introduction of thiol-reactive groups is essential for well-controlled assembly.

The easiest and most straightforward way is the use of a heterobifunctional crosslinker to couple amine groups to thiols sequentially. For nanoparticles encapsulated by PAOA polymer, there are a minority of primary amine groups on the polymer surface (~50 for an 8 nm diameter QD) available for conjugation. There are a number of products on the market linking a succinimidyl ester group to a maleimide, and I have found SM(PEG)₂, one linked by a 2-unit polyethyleneglycol motif, to be the most successful (Figure 2.14). First, the succinimidyl ester reacts with the primary amines at pH 7.8 to form a stable amide bond. Excess linker can be purified away, and a thiol is then reacted with the maleimide group, which eventually undergoes hydrolysis to a stable thioether (Figure 2.14).⁶² There are many advantages to this method: it is fast, with each coupling step completing in under an hour; it forms stable covalent linkages, good for long term imaging or for structural materials; it is efficient, requiring only a small excess of reagent protein and proceeding in high yield. However, in order to tune the amine density or introduce other functional groups, a new encapsulation polymer must first be synthesized.

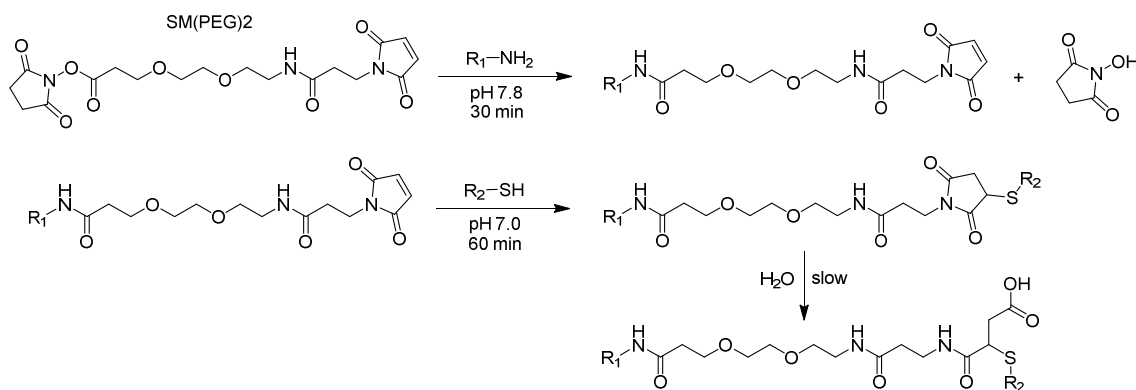


Figure 2.14 Sequential crosslinking of amine to thiol *via* SM(PEG)₂. Both reactions proceed under mild conditions and quick timescales, and eventual hydrolysis to the thioether prevents any further thiol exchange.

Use of the PMAO polymer encapsulation allows for a greater degree of flexibility in the composition of the displayed surface groups, without requiring synthesis of a dedicated polymer batch. The maleic anhydride group exposed at the nanocrystal surface is reactive to primary amines and undergoes a ring opening to form an amide bond (Figure 2.15). Like succinimidyl esters, there are a vast number of primary amines available to tune the surface chemistry through this coupling. Among the most useful is a $\text{NH}_2\text{-PEG3-N}_3$ molecule, which introduces an azide group to the surface (Figure 2.15). This makes the surface capable of copper-catalyzed click reactions, and it also may be reduced back to an amine for reactions with succinimidyl esters as above. The mixture of primary amines chosen for the phase transfer to aqueous dispersion dictate the final composition, with the caveat that 50% of the surface groups will be carboxylic acids from the maleic anhydride ring opening (Figure 2.15).

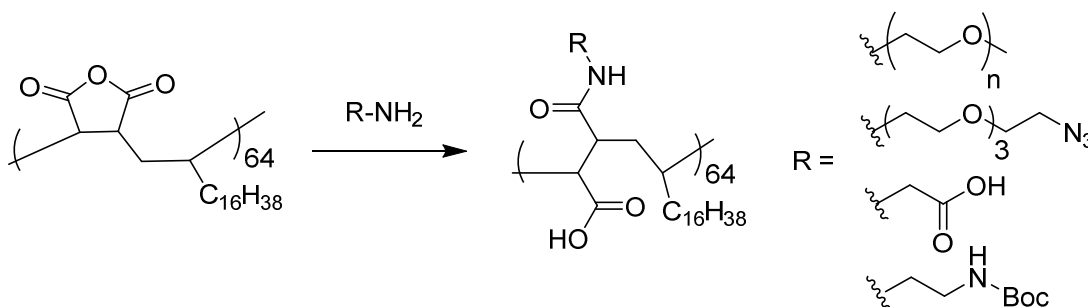


Figure 2.15 PMAO maleic anhydride reacts with primary amines for diversity in surface chemistry. Many primary amines (such as R groups shown) will function, and mixtures can be used to impart mixed functionality at the surface.

However, there are times we may not want an uncleavable linkage for the attached groups. In applications like drug delivery or for stimulus responsive probes, it is advantageous to have the design capability for a cleavage site between the nanocrystal and its cargo. Using cysteine as the attachment site for biomolecules allows the use of stable, but labile, disulfide bonds as well. These linkages can be formed from oxidized thiol groups or through disulfide exchange with a sacrificial leaving group. Once placed in a sufficiently reducing environment, the bond can be cleaved, and the two halves disassociated. To avoid crosslinking nanoparticles to each other, I have developed two disulfide conjugation strategies based on activated disulfides.^{63–65} In this way, we can incorporate disulfide groups on the nanocrystal polymer first, and then displace a leaving group with a desired thiol.

There are two distinct strategies to accomplish each based around the two encapsulation polymers. For PAOA polymer, where the surface is composed of

carboxylic acids and primary amines,⁵⁹ simultaneous reaction of the amines with 2-iminothiolane (Traut's reagent) in the presence of 5,5'-dithiobis(2-nitrobenzoic acid) (Ellman's reagent) yields conversion of the amine to amidinium chloride with a disulfide bond to nitrobenzoic acid (Figure 2.16). The Traut's reagent forms a terminal sulfhydryl group, which immediately forms a mixed disulfide with Ellman's reagent. With sufficient excess of Ellman's reagent present, crosslinking between sulfhydryl groups on adjacent nanocrystals is largely prevented. This technique preserves the positive surface charge from the amine and its progress is easily tracked by the appearance of 412 nm absorbance from the nitrobenzoic acid leaving group (Figure 2.16).

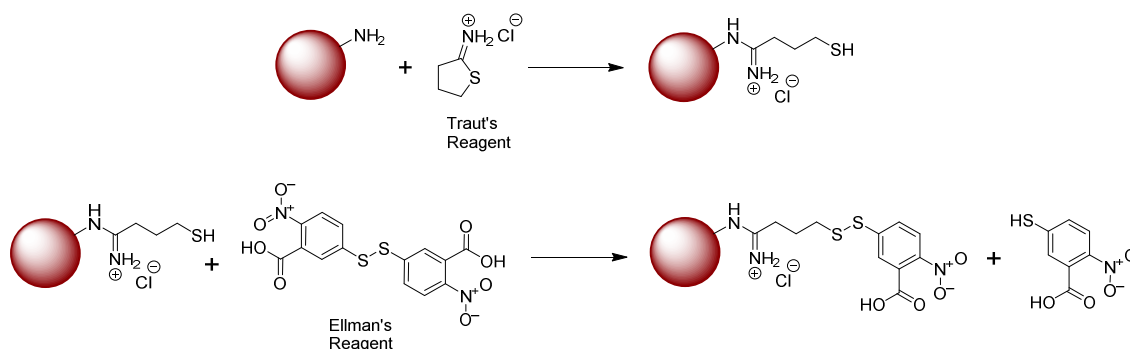


Figure 2.16 Conversion of amine to activated disulfide using Traut's and Ellman's reagents. Reaction of amines displayed on nanocrystal surface with Traut's reagent to yield surface-displayed thiols (top). *In situ* conversion of surface thiols to activated disulfides in the presence of excess Ellman's reagent (bottom).

In using the PMAO polymer, we have a bit more flexibility in how we introduce the activated disulfide group. Since the surface chemistry is decided by the amine reagents added in the encapsulation step, I designed and synthesized molecules for the incorporation of the disulfide directly. These two molecules, pyridyldisulfide-PEG-amine (PDPA) and pyridyldisulfide-ethylamine (PDEA) both contain a primary amine, a disulfide linker, and a pyridinethiol leaving group (Figure 2.17a). Once this group is cleaved from a disulfide, it quickly tautomerizes to the thioamide to prevent back reaction with other disulfides and has a trackable absorbance as well, around 343 nm (Figure 2.17b).⁶⁴⁻⁶⁶ Either of these molecules can be incorporated at encapsulation at < 5 mol% of total amines to yield a surface with disulfides ready for thiol attachment. For any of the disulfide-functionalized nanoparticles, simple overnight incubation with a cysteine-containing protein, rigorously cleaned of any residual TCEP reducing agent, results in high conjugation yield of protein-coated nanoparticles.

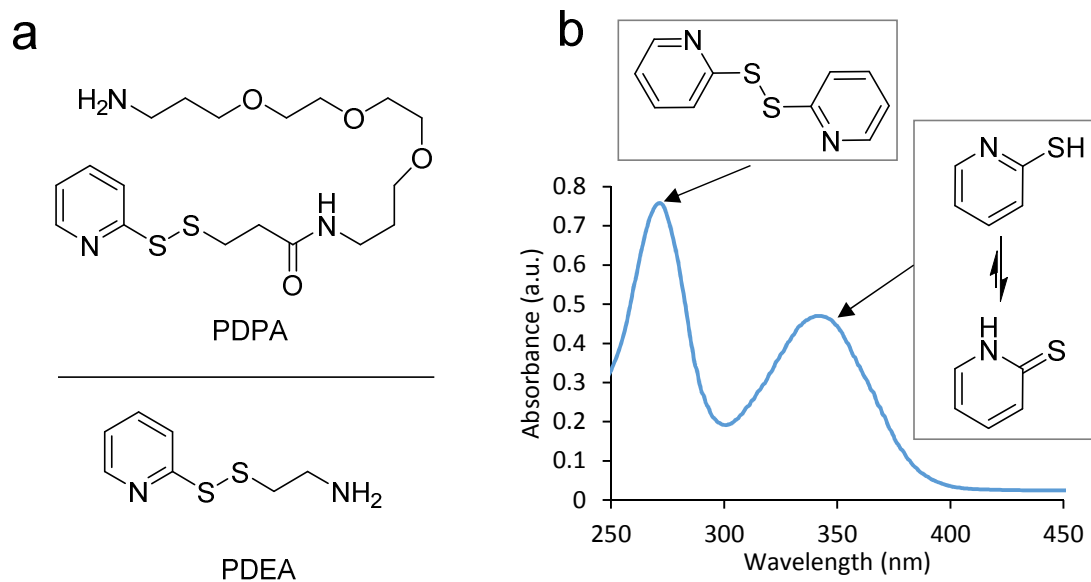


Figure 2.17 Pyridyldisulfide reagents for conjugation to PMAO polymer. (a) Structures of PDPA and PDEA amines for introduction of disulfides onto PMAO. (b) Absorbance of the leaving group tautomer from disulfide exchange on these compounds is shifted from the pyridyldisulfide starting material.

2.3 Conclusions

Tunable control over the surface chemistry of nanocrystals is the first step towards interfacing them with biological systems. By designing for modularity at each stage of manipulation of the surface, we can introduce many more ways to tune the final construct to suit an application. Through encapsulation in a high dielectric polymer coating, we can protect the native optical properties of nanocrystals as well as introduce reactive groups for further modification.

By using heterobifunctional crosslinking molecules or activated disulfide attachment, we can create precise covalent linkages between the nanocrystal surface and a wide array of cargo and biomolecules. Introduction of these functional groups expands the possibilities for chemical reactions on nanocrystal surfaces. These methods are agnostic to the nanoparticle size and identity and lay the groundwork for creating many different types of conjugates in the following Chapters.

2.4 Materials and Methods

Chemicals and materials. CdSe/ZnS nanocrystals were purchased from Ocean Nanotech. Poly(maleic anhydride-alt-1-octadecene) (PMAO) was purchased from Polysciences, Inc. NH₂-PEG4-N₃ and NH₂-PEG3 were purchased from Aurum Pharmatech. SM(PEG)2 was purchased from ThermoFisher. All other reagents and chemicals were purchased from MilliporeSigma and used without further purification.

Synthesis of poly(acrylic acid)-co-poly(*n*-octylacrylamide)-co-poly(2-aminoethylacrylamide) random amphiphilic copolymer (PAOA). Polyacrylic acid (ca. 2000 Da, 500 mg, 0.25 mmol) and *N*-hydroxysuccinimide (424 mg, 3.64 mmol) were dissolved in 20 mL of 100 mM HEPES buffer, pH 8.0. *N*-Boc-ethylenediamine (118 mg, 0.74 mmol) and *n*-octylamine (286 mg, 2.21 mmol) were dissolved in 20 mL of EtOH and added to the PAA solution. The pH was adjusted to 7.6 with 5M NaOH and then EDC (1.13 g, 5.90 mmol) was added; after 1 h, the pH was re-adjusted to 7.6, and an additional 250 mg of EDC was added. The reaction was stirred well overnight and divided into two 50-mL centrifuge tubes. EtOH was removed in a Genevac evaporator, causing the polymer to pellet. The pellets were each rinsed with 10 mL of 500 mM citrate buffer, pH 4.0, and then 10 mL of water. To remove the Boc protecting groups, the pellets were each resuspended in 5 mL of TFA with 250 μ L of H₂O. After 45 min, 10 mL of water was added to each tube and the volumes reduced to 5 mL by Genevac evaporation. To each tube were added 5 mL of EtOH and 5 mL of 0.2 M NH₄OAc buffer, pH 7.0. The solutions were dialyzed (Pierce Slide-a-Lyzer, 3.5 kDa MWCO) against 3 x 2 L of distilled water, causing much of the polymer to precipitate. The solution within the cassette was removed, and solids present in the cassette were dissolved with 10 mL of EtOH. These were combined and the EtOH was removed using a Genevac evaporator. The suspension was dissolved with ca. 20 mL of 50% CH₃CN, frozen, and lyophilized to give 608 mg of white powder with a calculated average of ~9 octyl groups, 15 carboxylates, and 3 ammonium groups per polymer.

Passivation of Core-shell CdSe/CdS Nanoparticles by poly(acrylic acid)-co-poly(*n*-octylacrylamide)-co-poly(2-aminoethylacrylamide) (PAOA) amphiphilic copolymer. CdSe/CdS QD core/shells with emission maxima of 626 nm were dispersed in hexane with 1% (v/v) oleic acid to 8 μ M; CdSe/ZnS QD core/shells (Ocean Nanotech) with emission maxima of 585 nm were diluted with hexane to 5 μ M. Concentrations were determined by first exciton absorbance. For aqueous dispersion, PAOA (20 mg, 6.25 μ mol, 3000-fold molar excess over QDs) was dissolved in 1 mL of MeOH and 19 mL of CHCl₃. QDs in hexane (*e.g.*, 250 μ L of 8 μ M 626 nm CdSe/CdS QDs, 2.0 nmol) were added with stirring, and the solvents were removed under a gentle stream of N₂ overnight.

The dry QD/polymer residue was then resuspended in 15 mL of 200 mM sodium bicarbonate buffer, pH 8.0. This suspension was sonicated for 30 minutes, heated in an 80 °C water bath for 60 minutes, slowly cooled in the bath to room temperature, and then sonicated for 30 minutes. Excess polymer was removed by spin dialysis (Amicon Ultra-15, 50 kDa MWCO), washing with 3 x 15 mL of 100 mM HEPES, pH 7.8. The retentate was diluted to 1 mL with HEPES buffer and centrifuged at 16100 x g for 5 min to remove residual polymer and insoluble aggregates. Aqueous QD dispersions were stored under ambient conditions.

Passivation of QDs by poly(maleic anhydride-*alt*-1-octadecene) (PMAO)

amphiphilic copolymer. PMAO (30 mg, 1.33 μ mol, 16 monomer units per nm² of QD surface) was dissolved in 1 mL of acetone and 14 mL of CHCl₃. QDs in hexane (*e.g.*, 250 μ L of 8 μ M 626 nm CdSe/CdS QDs, 2.0 nmol) were added with stirring, and the solvents were evaporated under a gentle stream of N₂ overnight. The QD/polymer residue was then resuspended in 15 mL of 50 mM sodium borate buffer, pH 9.0, with desired ratios of primary amines for reaction with maleic anhydrides (Figure 2.15). This suspension was sonicated for 30 minutes, heated in an 80 °C water bath for 60 minutes, slowly cooled in the bath to room temperature, and then sonicated for 30 minutes. The mixture was concentrated to 1 mL by spin dialysis (Amicon Ultra-15, 100 kDa MWCO), and excess polymer was removed by ultracentrifugation and dialysis.

Ultracentrifugation for PMAO purification. A 12 mL sucrose gradient was generated on a linear gradient maker (BioComp, Inc.), typically from 10-70 wt% sucrose dissolved in HNE buffer (20 mM HEPES, pH 7.0, 100 mM NaCl, and 1 mM EDTA). To the top of each of two tubes, 500 μ L of QDs was added gently without disturbing the gradient. The tubes were centrifuged at 150,000 x g for 90 min to separate residual polymer and insoluble aggregates from the encapsulated QDs. Fractions were taken from the tubes at 200 μ L intervals and placed into 96 well plates, then measured by fluorescence emission on a plate reader (BioTek) to detect the polymer and QD signals. Fractions with QDs were pooled and placed in a 5 mL dialysis chamber (SpectraPor Float-A-Lyzer 100 kDa pore size) and dialyzed against HNE buffer 3 x 1 L. The retentate was concentrated as above to 2 mL by centrifugal filter and stored under ambient conditions.

Ligand additive addition and quenching. Stock 610 nm CdSe/CdS QDs (500 μ L, 5.72 μ M in hexane) were washed by precipitation in 10 mL acetone followed by redispersion in hexane. Surface ligands were added to 100 μ L aliquots (*e.g.* 1 μ L oleic acid) along with 100 μ L chloroform and sonicated for 15 minutes. The nanoparticles were encapsulated in PMAO polymer and purified as above, with 50 μ L of 100mM NH₂-PEG3-N₃ and 1 mL 50 mM sodium borate, pH 9.0 to react with the maleic anhydride.

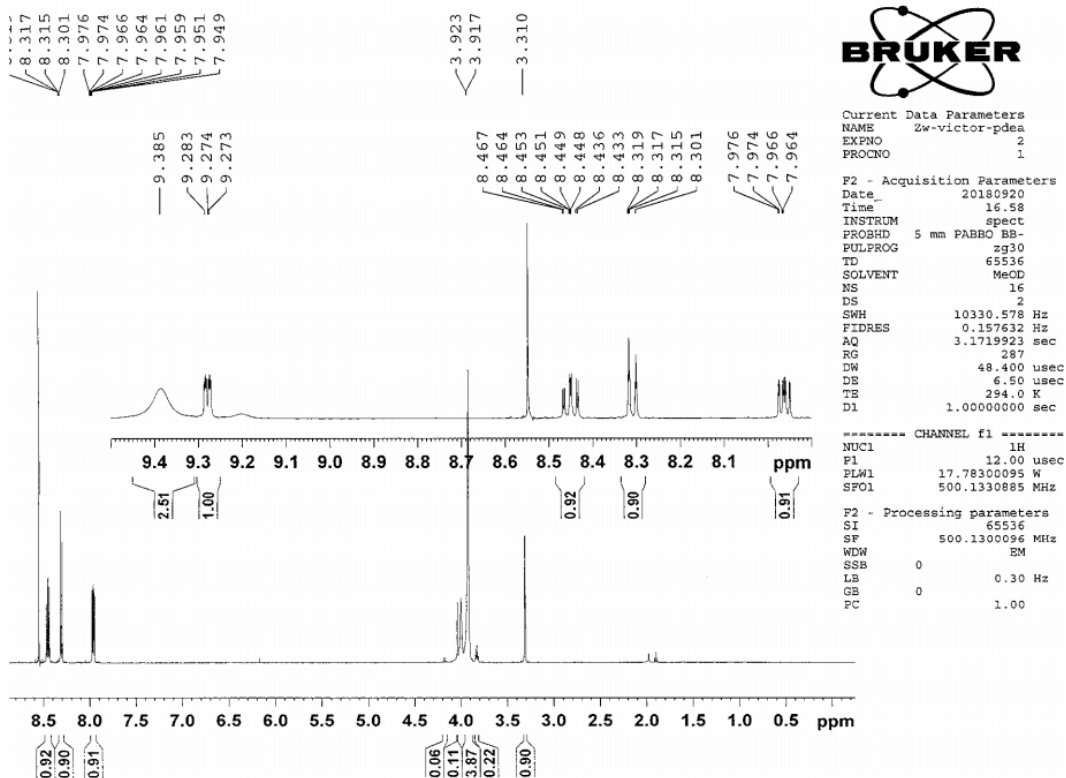
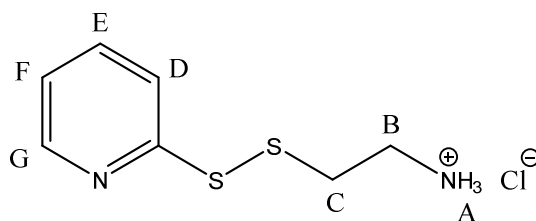
The treated QDs (40 μ L, 2 μ M, 80 pmoles) were subjected to Cu⁺ ions (8 μ L, 500 μ M, 4 nmoles), and aliquots were taken at various time points and quenched in 10 mM EDTA. Data shown were from aliquots taken 30 seconds after exposure. The fluorescence was measured on a plate reader (BioTek) under 405 nm excitation.

Gap-filling additive addition and quenching. Azide-conjugated 585 nm emission CdSe/ZnS QDs (10 μ L, 4 μ M, 40 pmoles) were mixed with the additives (cholesterol, CHAPS, Tween 20, Triton X-100; 10 μ L, 1 mM in H₂O or CHCl₃, 10 nmoles) for 10 minutes and sonicated briefly. The photo shown was taken after this incubation period, showing quenching of some of the samples. The samples were then subjected to copper-catalyzed click conditions as outlined in Chapter 3 Methods, with no successful conjugation.

Heterobifunctional linkage of polymer amines to thiols. PAOA-wrapped QDs (2 μ M, 600 μ L) in 100 mM HEPES, pH 7.8 and succinimidyl ester-PEG₂-maleimide (SM(PEG)₂, ThermoFisher, 100 mM, 100 μ L) in DMSO were combined in a 1.5-mL centrifuge tube and mixed at room temperature for 30 min on a rotary mixer. The reaction mixture was diluted to 4 mL with 100mM HEPES, pH 7.0, and excess PEG reagent was removed by centrifugal dialysis (Amicon Ultra-4, 100 kDa MWCO), washing with 3 x 4 mL of buffer. The retentate was diluted to 500 μ L in a 1.5-mL low protein binding centrifuge tube (Eppendorf), 2-fold excess of thiol (2.5 nmol) was added, and the reaction was mixed overnight at 4°C on a rotary mixer. The reaction mixture was diluted to 4 mL with 100mM HEPES, pH 7.0, and excess thiol was removed by centrifugal dialysis (Amicon Ultra-4, 100 kDa MWCO), washing with 4 x 4 mL of buffer. The retentate was diluted to 600 μ L in HEPES buffer, and the QD conjugates were stored under ambient conditions.

Synthesis of pyridyldisulfide-PEG-amine (PDPA). PEG₃-diamine (1750 μ L, 8.8 mmol, Sigma) was dissolved in 6 mL of 100 mM HEPES, pH 7.8 with 3 mL of acetonitrile and the pH was adjusted to 7.5 with 5 M HCl. The solution was mixed with 50 mg of succinimidyl 3-(2-pyridyldithio)propionate (SPDP, 0.16 mmol, ThermoFisher) dissolved in 1 mL DMSO. The pH was readjusted to 7.5 with 5 M HCl, the reaction mixture was sonicated briefly to clear, and the solution was stirred overnight for 16 hours. The product was purified on a C₁₈ HPLC column (Vydac) using a linear 2-92% CH₃CN gradient with 0.1% TFA over 45 min, with product eluting at 19 min (24% CH₃CN). MS, C₁₈H₃₂N₃O₄S₂ (MH⁺) calculated: 418.18; found: 418.4. Fractions containing the product were pooled and evaporated to 59.8 mg (90% yield) of a viscous yellow oil.

Synthesis of pyridyldisulfide-ethylamine (PDEA). 2,2'-Dipyridyldisulfide (20.0 mmol, 4.41 g, Aldrich) was dissolved in 20 mL of methanol with 0.8 mL of glacial acetic acid in a 300 mL round-bottom flask. Cysteamine HCl (10.0 mmol, 1.14 g) dissolved in 20 mL of methanol was added dropwise over 1 hour to the vigorously mixing flask and stirred for 16 hours under N₂ atmosphere. Methanol was removed by rotary evaporation, and the yellow oil product was washed twice with 50 mL dry ice-cooled diethyl ether. The oil was dissolved in 10 mL of methanol and precipitated by addition of 200mL cold diethyl ether. The flask was stored at -20°C for 36 hours to ensure full precipitation. The pale yellow solid was vacuum filtered, rinsing with 3 x 50 mL of dry ice-cold diethyl ether, and left under vacuum for 20 minutes to dry residual ether. The pale yellow solid was left to dry in a fume hood for several hours to yield 2.017 g of PDEA product (93% yield). MS, C₇H₁₁N₂S₂ (MH⁺) calculated: 187.03; found: 187.2. ¹H NMR (500 MHz, CD₃OD): δ 9.385 (broad s, A, 3H), 9.288 (d, G, 1H), 8.448 (t, E, 1H), 8.316 (d, D, 1H), 7.970 (t, F, 1H), 3.920 (m, B&C, 4H).



Conversion of polymer-displayed amines to activated disulfides. To generate UCNP-SpyCatcher conjugates, POA-encapsulated UCNPs (10 μ M, 200 μ L) in 200 mM MES, pH 5.0, were combined with 5,5'-dithiobis(2-nitrobenzoic acid) (Ellman's reagent, 10 mM, 100 μ L, Aldrich) and 2-iminothiolane HCl (Traut's reagent, 1 mM, 10 μ L, MilliporeSigma) dissolved in 100 mM MES, pH 6.0. Under vigorous stirring, 700 μ L of 200 mM CAPS buffer, pH 10.0 was added dropwise, and the mixture was allowed to react for 20 mins. The reaction mixture was diluted to 4 mL with 100 mM HEPES, pH 7.5, and excess reagents were removed by centrifugal dialysis (Amicon Ultra-4, 100 kDa MWCO), washing with 3 x 4 mL of HEPES buffer. An aliquot of SpyCatcher Ser35C protein (200 μ M, 100 μ L) was desalted on a Biospin-6 Desalting Column (Bio-Rad) and further washed by centrifugal dialysis (Amicon Ultra-4, 3 kDa MWCO), washing with 3 x 4 mL of HEPES buffer to remove all TCEP storage buffer. The retentate was diluted to 100 μ L in a 1.5-mL low protein-binding centrifuge tube, the UCNPs were added, and the reaction was mixed overnight at 4°C on a rotary mixer. The reaction mixture was diluted to 4 mL with 100 mM HEPES, pH 7.5, and excess SpyCatcher protein was removed by centrifugal dialysis (Amicon Ultra-4, 100 kDa MWCO), washing with 4 x 4 mL of buffer. The retentate was diluted to 400 μ L in HEPES buffer, and the UCNP-protein conjugate was stored under ambient conditions.

3 | Azide-Alkyne Click Conjugation on Quantum Dots by Selective Copper Coordination¹

¹ This work has been previously published in ACS Nano: Mann, V. R.; Powers, A. S.; Tilley, D. C.; Sack, J. T.; Cohen, B. E. Azide–Alkyne Click Conjugation on Quantum Dots by Selective Copper Coordination. *ACS Nano* **2018**, 12 (5), 4469–4477. Portions of this work were completed in collaboration with others: ROSETTA modeling was performed by Dr. Drew C. Tilley. Nanocrystal synthesis was performed in collaboration with Alexander S. Powers.

3.1 Introduction

In our pursuit of the development of better optical sensors of neuronal activity, we sought a method to conjugate semiconductor QDs (Figure 3.1a) to the peptidyl tarantula toxin guangxitoxin-1E (GxTX). This is a 36-amino acid cystine knot peptide that binds Kv2 channel voltage sensing domains (Figure 3.2),⁶⁷ which we have previously synthesized to contain propargylglycine alkyne sidechains for chemoselective bioconjugation.⁶⁸ We had incorporated this alkyne as the Cu-catalyzed azide-alkyne 1,3-dipolar click coupling (CuAAC) is among the most widely used reactions for both bioconjugation^{69–71} and for modification of surfaces.^{72,73} CuAAC reactions are bioorthogonal, work well in dilute aqueous conditions, and require only a Cu ion catalyst and mild reducing agent to form covalent bonds between terminal alkynes and azides.^{74–76} However, Cu ions have been found to be exceptionally strong and irreversible quenchers of QD fluorescence, even with brief exposures at nanomolar concentrations (Figure 3.1c).^{37,41,77,78}

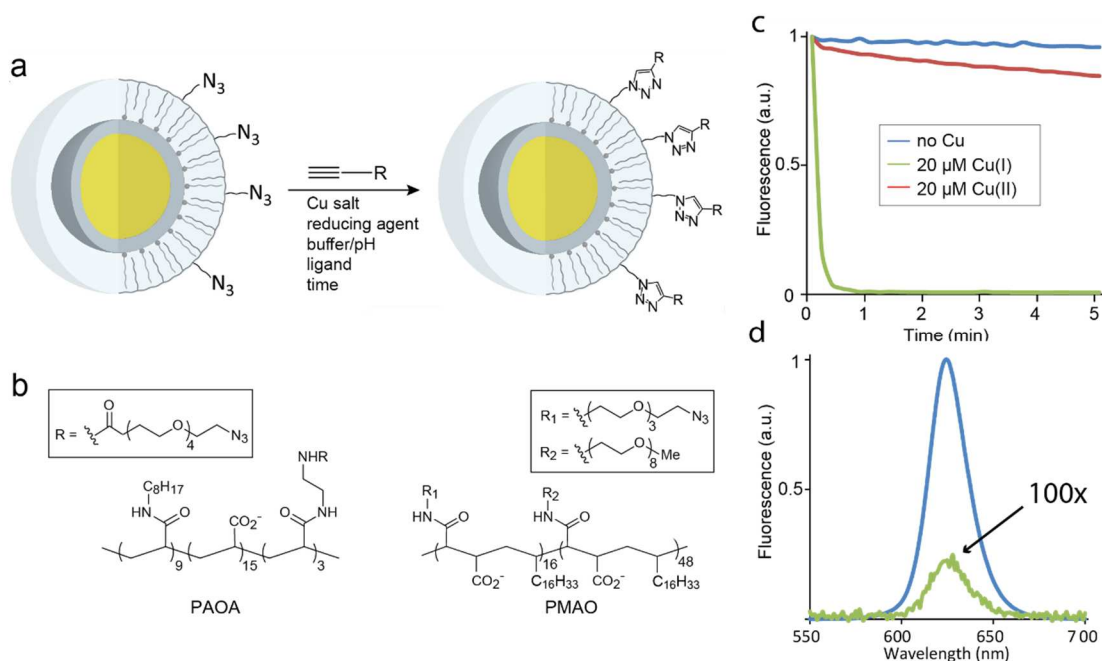


Figure 3.1 Copper-mediated click reactions on QD surfaces. (a) CuAAC reaction of alkynes with amphiphilic polymer-coated core/shell QDs, listing reaction variables tested in this study. (b) Structures of surface polymers and azide linkers. (*Left*) Polyacrylic acid-based amphiphilic random co-polymer,^{56,58} with azide PEG linker modification. (*Right*) Co-maleic anhydride-octadecene polymer^{8,55} modified with azide PEG linkers and inert PEG amines. Stoichiometries are estimates based on polymer molecular weights, and positions of monomers are random. (c) Kinetic emission of 10 nM QDs with and without exposure to Cu ions. (d) QD emission spectra before (blue) and after (green, shown magnified 100-fold) addition of 20 μM Cu⁺.

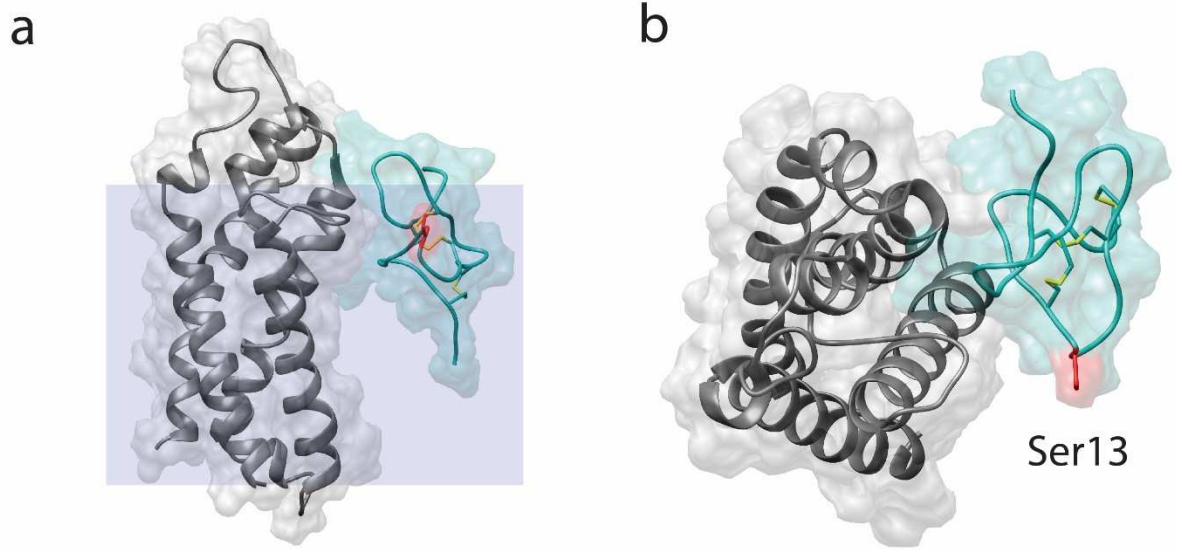


Figure 3.2 Tarantula toxin GxTX bound to Kv2 potassium ion channels. Side (a) and top (b) views of Rosetta-generated ribbon models of GxTX bound to Kv2.1 channel voltage sensor domain. Kv is gray, toxin is cyan, and Ser13 is red. Membrane dimensions are light gray.

Previous work has shown that Cu^+ is the species primarily responsible for QD quenching³⁷ and that large (> 10 nm) and heavily crosslinked polymer networks are required to prevent copper from reaching the nanocrystal surface.^{44,45} It is not clear whether this quenching is due to rapid Cu/Cd exchange⁷⁹ or the Cu ions are acting as proximal electron traps, but in our initial experiments we observed no change in QD emission wavelength maximum or line shape following Cu exposure (Figure 3.1d). Our attempts to reverse Cu quenching by exposure to high affinity Cu ligands or excess Cd^{2+} were unsuccessful, even after extended incubations (Figure 3.3). While copper-free azide-alkyne coupling methods have been successful in eliminating copper toxicity from this reaction on cells^{80,81}, the necessary strained alkynes are of limited use in certain complex structures, such as our 3-cystine knot peptides, where they must be incorporated during synthesis.⁶⁸

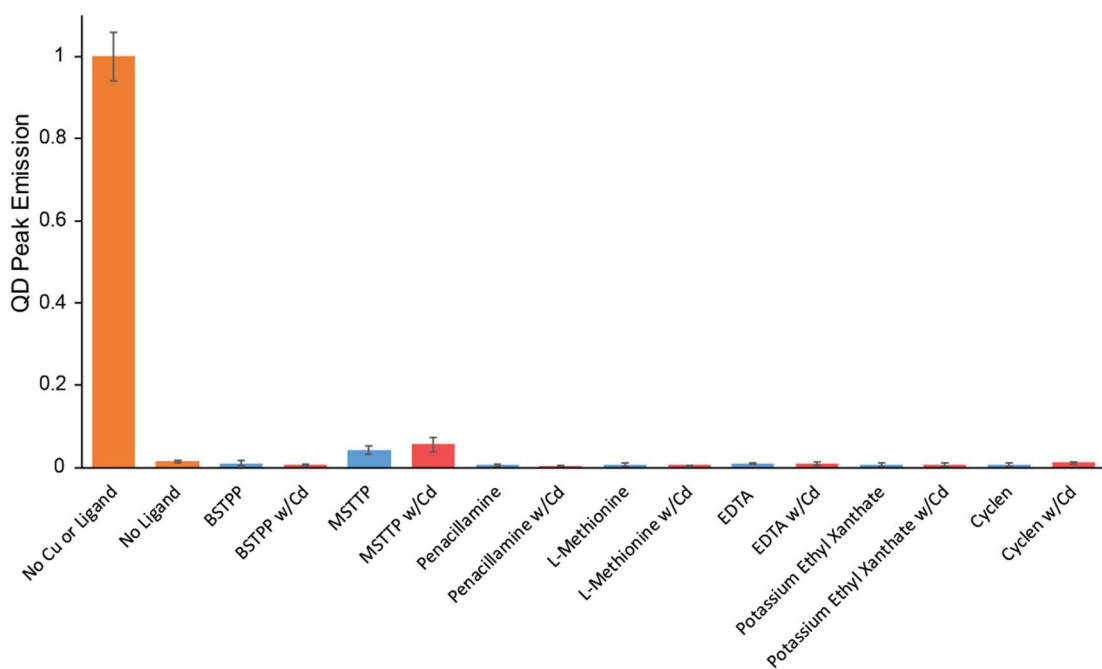


Figure 3.3 Persistence of Cu QD quenching in the presence of Cu-coordinating ligands and Cd^{2+} . Cu-treated QDs were incubated with 1000-fold excess of Cu ligand, with or without added Cd^{2+} , for 30 h. Fluorescence emission is shown scaled to the untreated QD sample. Error bars are \pm standard deviation ($n = 3$). See Table 3.1 for ligand structures.

Here, we employ a 2000-reaction combinatorial FRET-based assay to screen for suppression of the fast Cu quenching of QDs while maintaining its catalytic activity. Based on insight from this screen and mechanistic studies of copper surface coordination and quenching, we find that superstoichiometric concentrations of Cu can be used to promote full coupling if accompanied by ligands that selectively compete the Cu off the QD surface but allow it to remain catalytically active. With these conditions, we synthesize unquenched peptidyl toxin-QD conjugates and image their specific and state-dependent affinity for potassium channels in live mammalian cells.

3.2 Results and Discussion

3.2.1 Screening for non-quenching CuAAC reaction conditions

We anticipated that the amphiphilic polymer coatings commonly used to passivate QDs in water^{55,56,58} would offer a low-dielectric layer inhospitable to Cu ions, but initial CuAAC reactions with azide-bearing QDs showed only rapid quenching with no apparent conjugation (Figure 3.1). Addition of a series of Cu-coordinating ligands (Table 3.1) that have been shown to accelerate CuAAC cycloadditions^{82–85} did not measurably prevent quenching unless also completely preventing the cycloaddition. Given this poor initial reactivity, the complexity of the CuAAC mechanism,^{76,86–89} and the number of components and concentrations that can be varied, we sought a high-throughput approach to screen for synthetic conditions that might create a Cu complex able to catalyze CuAAC cycloaddition but unable to interact directly with the nanocrystal.

Previous FRET-based synthetic screens have been successful in discovery of catalysts and in improving the efficiencies of coupling reactions, including Cu⁺-mediated CuAAC couplings.^{90–94} While these screens have focused on maximizing coupling efficiencies, we faced the added challenge of optimizing the relatively slow Cu⁺-mediated coupling reaction in the presence of the rapid Cu⁺-mediated quenching of nanocrystal fluorescence. For this screen, we synthesized an alkynyl cyanine compound as a fluorescent acceptor paired with aqueous azide-coated CdSe/CdS core/shell QDs with emission maxima at 625 nm and 90% quantum yield (Figure 3.4a, and Methods).

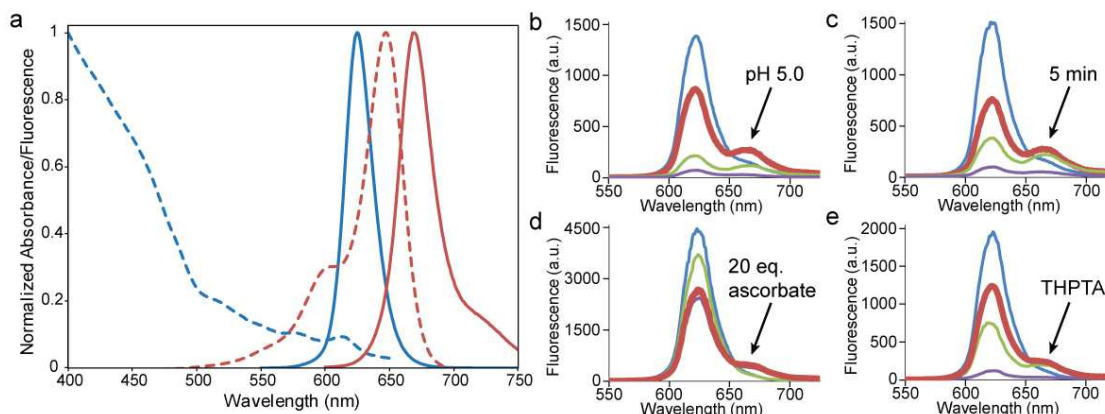


Figure 3.4 FRET-based screen for improved CuAAC reaction with minimal QD quenching.

(a) Absorbance (dashed) and emission (solid) spectra for CdSe/CdS QD donor (blue) and Cy5 acceptor (red). (b-e) Optimization of FRET emission spectra following 405-nm excitation, for reactions varying: (b) pH: 3.5 (blue), 5.0 (red), 7.5 (green), 9.0 (purple). (c) time (min): 1 (blue), 5 (red), 10 (green), 20 (purple). (d) ascorbate concentration (Cu eq.): 0 (blue), 2 (green), 20 (red), 100 (purple). (e) ligand (all 10 Cu eq.): L-cysteine (blue), THPTA (red), BTAA (green), L-methionine (purple). See Methods for reaction details. Best CuAAC conditions are highlighted.

Table 3.1 Copper-Coordinating Ligands

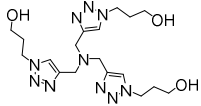
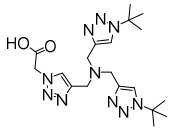
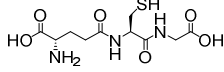
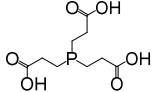
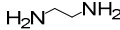
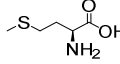
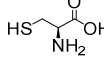
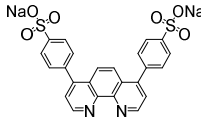
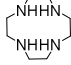
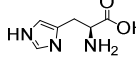
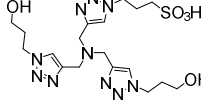
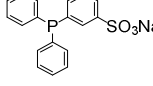
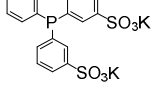
Ligand	Structure	Cu Equiv.	Relative Efficacy
THPTA		1-50	1.000
BTAA		1-50	0.958
Glutathione		1-50	0.085
TCEP		1-10	0.066
Ethylenediamine		1-10	0.058
L-Methionine		1-10	0.048
L-Cysteine		1-50	0.039
BPS		1-50	0.034
Cyclen		1-10	0.033
L-Histidine		1-50	0.022
Sulfo-THPTA		1-50	0.013
MSTPP		1-10	0.008
BSTPP		1-10	0.008

Table 3.2 Combinatorial Click Variables

Variable	Candidates	Range
Azide*	CdSe/CdS CdSe/ZnS Cy3	50 □M
Alkyne*	Cy5 Texas Red Cy3 AlexaFluor 594	1-3 azide eq
Cu source	Cu(OAc) ₂ CuSO ₄ Cu(CH ₃ CN) ₄ PF ₆	0.1-1 azide eq
Reducing agent	Sodium ascorbate	2-100 Cu eq
Ligand	See Table S1	1-50 Cu eq
Buffer	NH ₄ OAc Citrate Imidazole MES/HEPES MOPS Phosphate Phosphate-citrate	pH 3.5 - 9.0
Time		1 – 30 minutes
*see Figure 3.1, Figure 3.5, and Table 3.1 for reagent and ligand structures.		

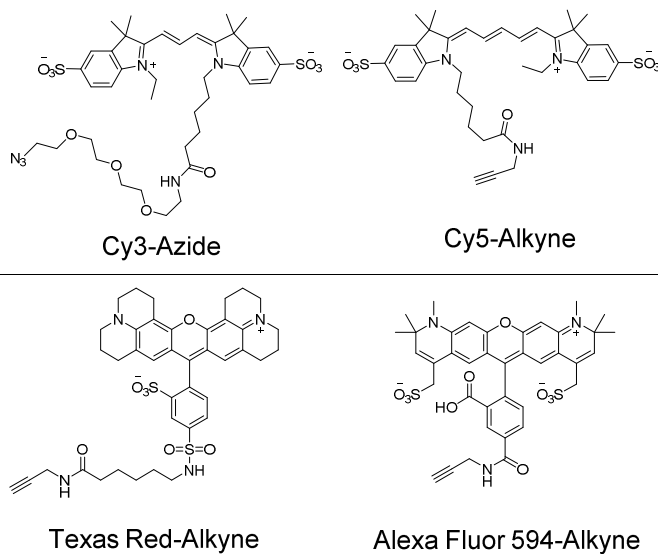


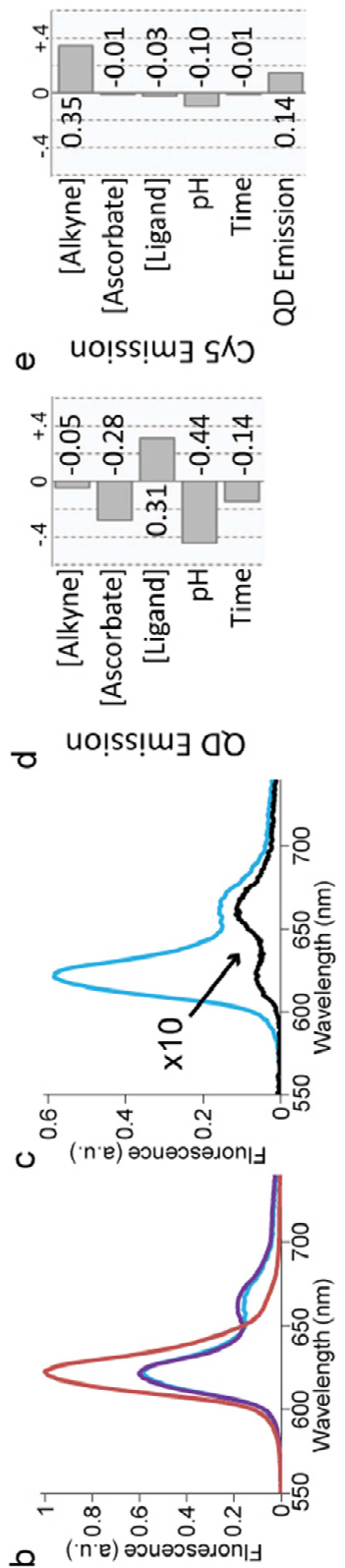
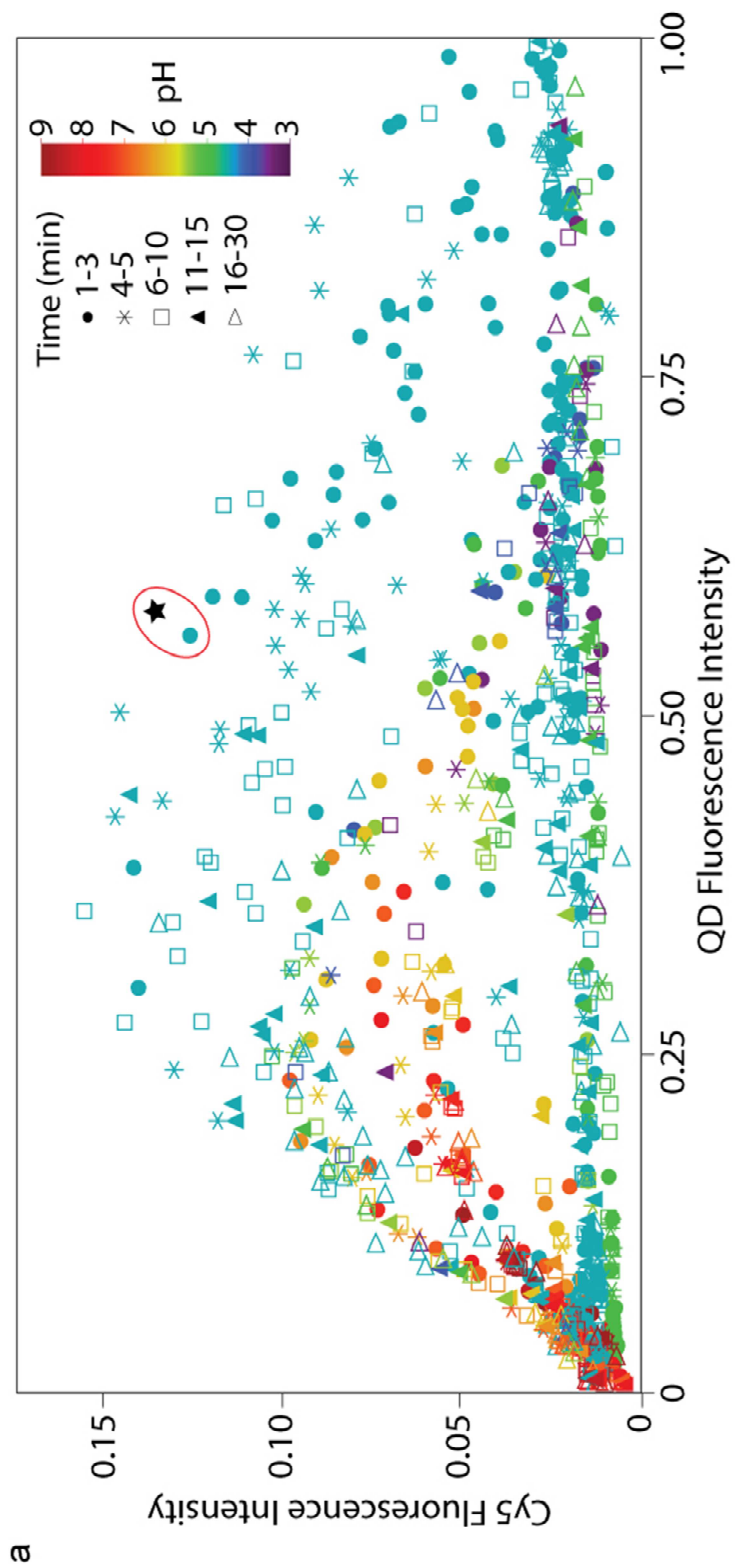
Figure 3.5 Structures of organic fluorophore azide and alkyne click reagents.

Based on previous mechanistic^{76,86-89} and empirical studies of CuAAC optimization,^{83,95} we selected a series of parameters to vary, including Cu source, alkyne/azide stoichiometry, reducing agent concentration, Cu-coordinating ligands,⁸²⁻⁸⁴ other counterions (in the form of buffer anions), and reaction time (Tables 3.1 and 3.2). Initial tests showed strong effects on both CuAAC coupling and quenching (Figure 3.4), as seen in the appearance of Cy5 acceptor emission and maintenance of QD emission beyond the ~10 s that would be required for full quenching under standard CuAAC conditions (Figure 3.1).

To expand the reach of the combinatorial screen, we carried out reactions in 96-well plates and measured spectra by plate reader. At specified time points, reactions were quenched by dilution into 10 mM EDTA solutions, and a full emission spectrum collected for each well. In a typical experiment, 8 reactions testing a single parameter were halted at 11 different time points to generate a 2-dimensional reaction series. A compilation of ~1200 such reactions (Figure 3.6a), plotting integrated QD intensity versus integrated Cy5 intensity, shows a small fraction of reaction conditions with strong emission at both wavelengths.

To determine the maximal FRET efficiency for this system, we synthesized fully Cy5-ligated QDs using a parallel Cu-free reaction on these same QDs by first reducing the azides to amines and then coupling with Cy5 succinimidyl esters (Figure 3.7). These QDs show no reactivity with alkynes through CuAAC coupling but do undergo efficient reaction with activated esters (Figure 3.8). Comparison of this emission (Figure 3.6a, black star) with the combinatorial Cu-mediated reactions, several conclusions are readily apparent. All points closest to the maximal FRET emission are at acidic pH (Figures 2.4b and 2.6a), suggestive of a surprising pH dependence. Reaction times >5 min are clustered near the axes, indicative of strong QD quenching (x-axis), minimal CuAAC coupling (y-axis), or loss of acceptor signal due to quenching of the QD donor. Low acceptor emission may arise from QD quenching, little CuAAC activity, or both. While such conditions are useless as preparative synthetic conditions, they do highlight the need to find reaction conditions that enable complete CuAAC on unusually fast timescales.

Figure 3.6 Combinatorial fluorescence analysis of ~1200 CuAAC reaction conditions on QDs. (a) Integrated Cy5 acceptor emission (670 - 700 nm) versus integrated QD emission (600 - 630 nm) for all reaction conditions. Circled data points are fully Cy5-conjugated control (black star) and closest CuAAC conditions (teal circle). (b) Emission spectra of unmodified QDs (red), control Cy5-conjugated QDs (purple), and optimized Cy5 CuAAC-conjugated QDs (teal). (c) Emission spectra of identical Cy5-QD CuAAC reactions with (teal) and without (black, shown magnified 10-fold) THPTA ligands and phosphate-citrate buffer, pH 4.5. (d-e) Pairwise correlations of reaction variables for QD emission (d) and Cy5 emission (e).



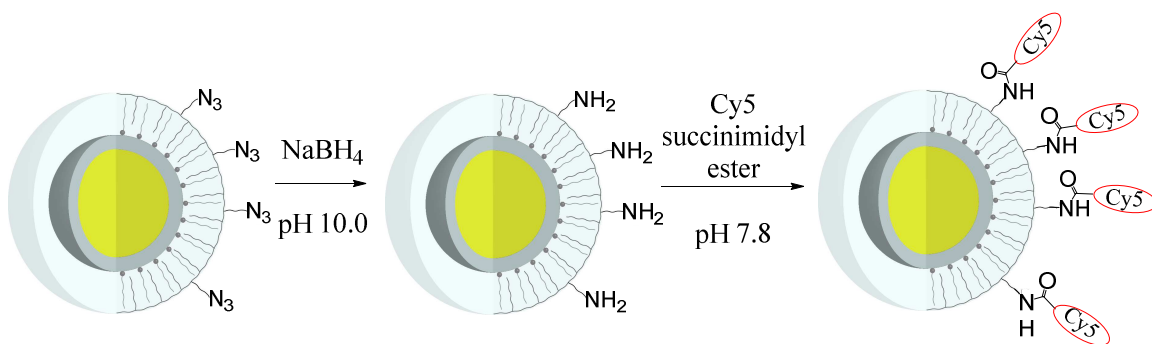


Figure 3.7 Copper-free QD-Cy5 coupling.

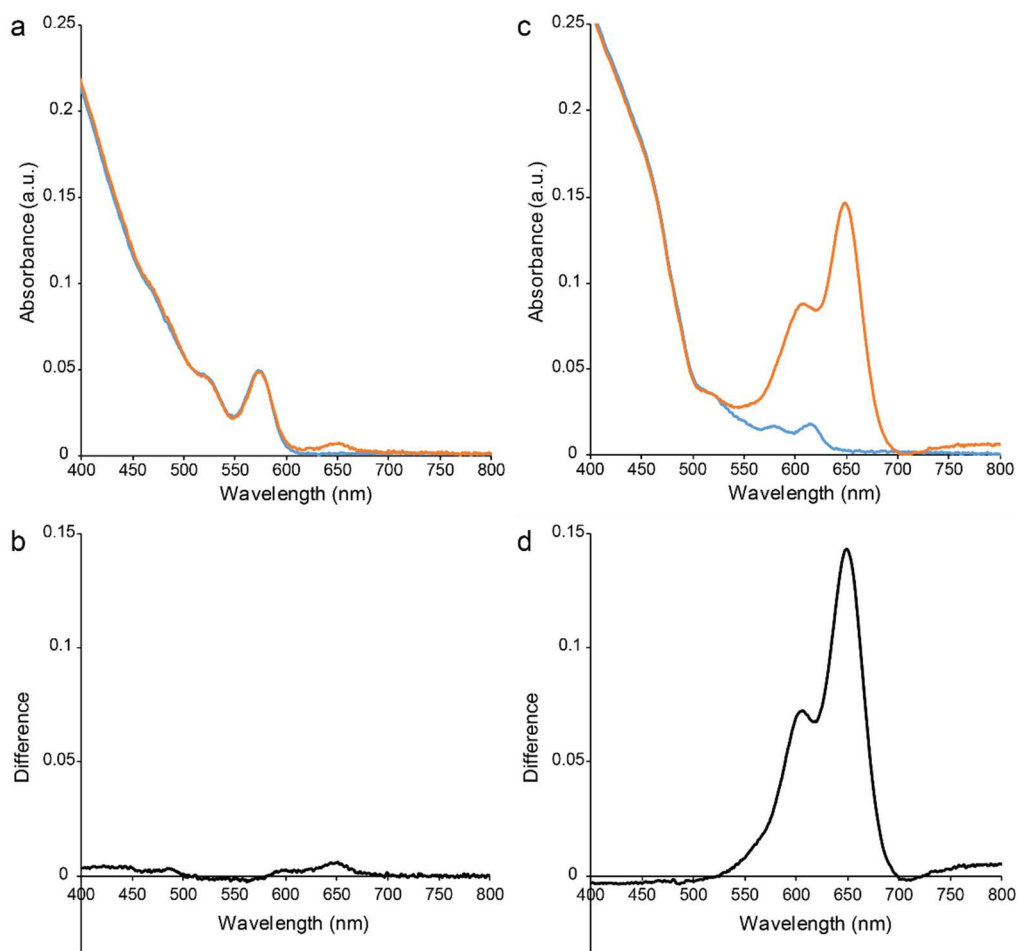


Figure 3.8 Reactivity of QD-PAOA surface amines. (a) Absorbance and (b) difference spectra of amine-coated QDs (blue) and amine-coated QDs treated with Cy5-alkyne under CuAAC conditions (orange). (c) Absorbance and (d) difference spectra of amine-coated QDs (blue) treated with Cy5-SE under amide-forming conditions (orange).

3.2.2 Analysis of combinatorial screening data

To quantify which variables have the strongest effects on QD quenching and CuAAC coupling, we analyzed this spectral data for pairwise correlations between each parameter and either QD or Cy5 emission (Figures 3.6d-e and Table 3.3). The strongest effect on QD quenching is the dependence on reaction pH, with little measured quenching below pH 4 to full and rapid quenching above pH 8. Acceptor emission is largely indifferent to reaction pH, suggesting differences between Cu quenching and catalysis that can be leveraged to optimize non-quenching CuAAC couplings.

Table 3.3 Pairwise Correlations of Reaction Parameters

1 st Variable	2 nd Variable	Correlation	Significance	-.4	0	.4
QD integrated emission	[Alkyne]	-0.049	0.12			
	[Ascorbate]	-0.276	<0.0001			
	[Ligand]	0.311	<0.0001			
	pH	-0.445	<0.0001			
	Time	-0.145	<0.0001			
Cy5 integrated emission	[Alkyne]	0.345	<0.0001			
	[Ascorbate]	-0.009	0.77			
	[Ligand]	-0.026	0.42			
	pH	-0.098	0.0021			
	Time	-0.012	0.72			
	QD emission	0.144	<0.0001			

Changes to Cu-coordinating ligand concentration did not significantly affect either reaction (Figures 3.6d-e), but we did observe major differences depending on the chemistry of the Cu coordination (Figure 3.4e and Table 3.1). Strong chelators (*e.g.*, cysteine) prevented quenching but also prevented any measurable CuAAC coupling, suggesting charged ligands can prevent Cu⁺ from reaching the nanocrystal surface but may also inhibit interaction with the alkyne.^{76,86,87} Two triazole-based ligands (THPTA and BTAA) proved most effective at generating Cy5 FRET emission while ameliorating quenching (Table 3.1), and optimization with THPTA gave us a FRET spectrum most similar to that of the QD-Cy5 conjugate synthesized without Cu (Figure 3.6b). Previous work has shown that BTAA is superior to other Cu ligands for promoting CuAAC coupling with hydrophobic substrates,^{83,95,96} while in this case the QD surfaces and Cy5 are both hydrophilic, possibly explaining the differences seen here.

3.2.3 Mechanisms of Cu-mediated cycloaddition and quenching

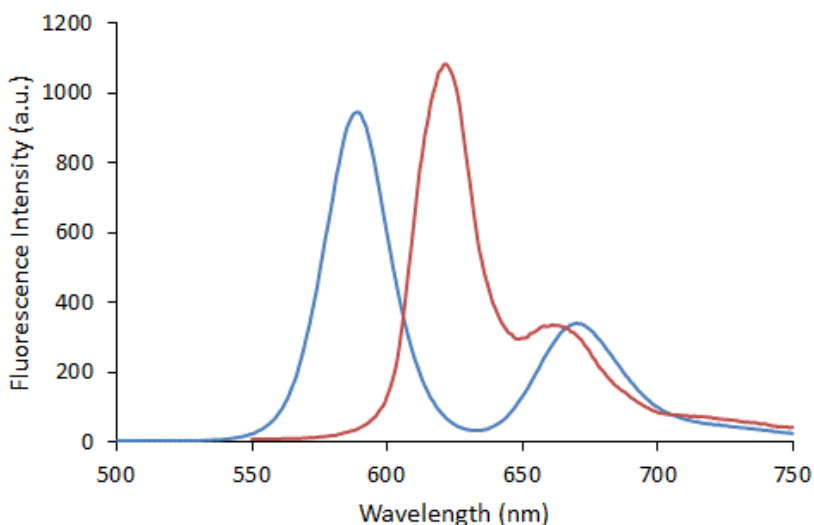


Figure 3.9 Emission spectra of QD compositions after CuAAC reaction with Cy5-alkyne. 625 nm CdSe/CdS QDs (red) and 585 nm CdSe/ZnS QDs (blue).

To understand the results of the FRET screen, we examined the reactivity of other azide and alkyne compounds, as well as other amphiphilic polymer coatings. Changing the azide inorganic nanocrystal shell from CdS to ZnS had no significant effect (Figure 3.9), but conditions for passivating QDs with amphiphilic polymer proved critical, with added surfactant (*e.g.*, oleic acid) in the hydrophobic QD dispersion essential for preparing aqueous QDs resistant to Cu quenching by diffusion to the nanocrystal surface (Figure 3.10). Changing the azide from nanocrystal to the organic fluorophore Cy3 (Figure 3.11) led to higher optimal pH and longer reaction times (Figure 3.12). This suggests the low pH optimal for QD CuAAC is needed to slow quenching but has no significant effects on the cycloaddition, corroborating analysis from the pairwise variable analysis (Figure 3.6d-e). The optimal Cy3-Cy5 CuAAC conditions square well with previous findings for small molecule coupling,^{69,94} while differences with the QD-Cy5 conditions suggest reaction conditions unique for QD substrates.

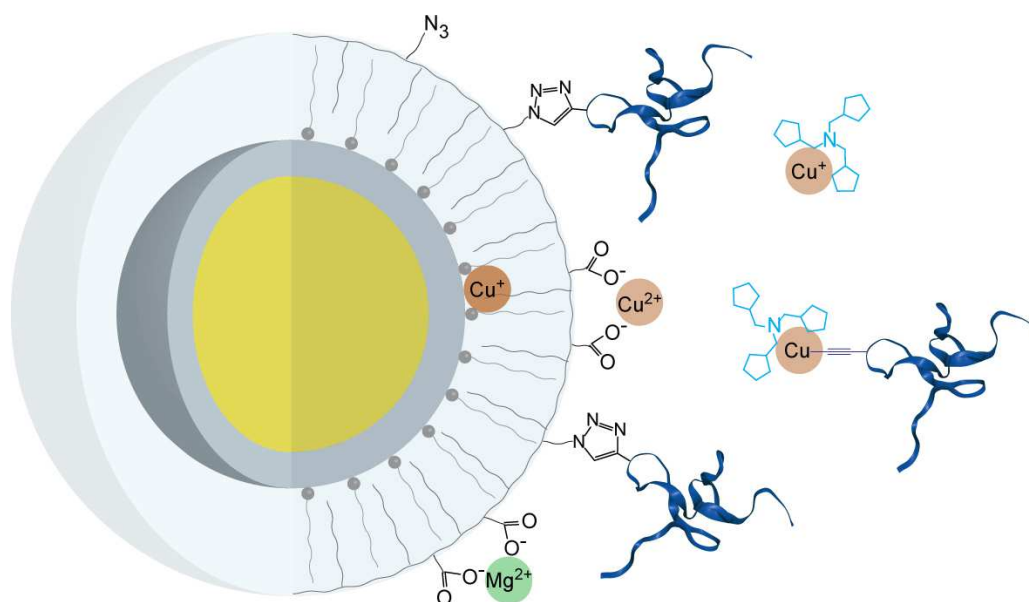


Figure 3.10 CuAAC chemistry and Cu quenching mechanisms on amphiphilic polymer-encapsulated QDs. Copper ions may quench QDs by diffusion through the hydrophobic layer to the inorganic crystal or by acting as proximal charge traps when coordinated to surface carboxylates. Peptidyl toxin is shown in dark blue; THPTA ligand in light blue; CdSe core as yellow; and ZnS or CdS shell as gray. Exact structures of Cu-ligand, Cu-QD, and M^{2+} -polymer are unknown.

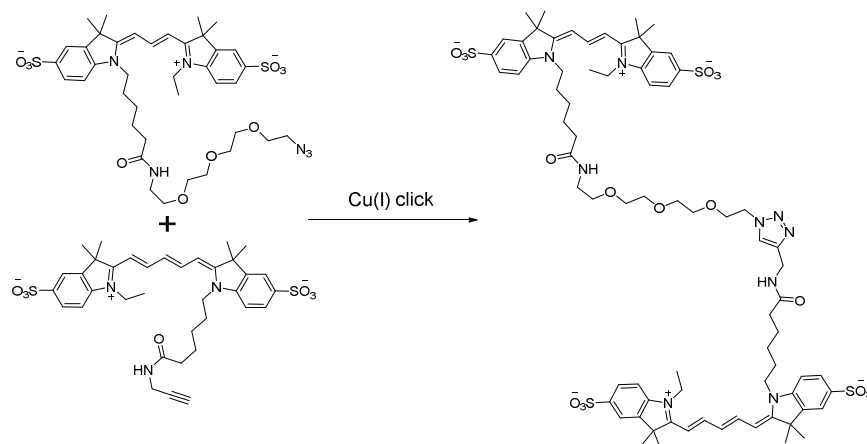


Figure 3.11 Cy3-azide CuAAC coupling with Cy5-alkyne.

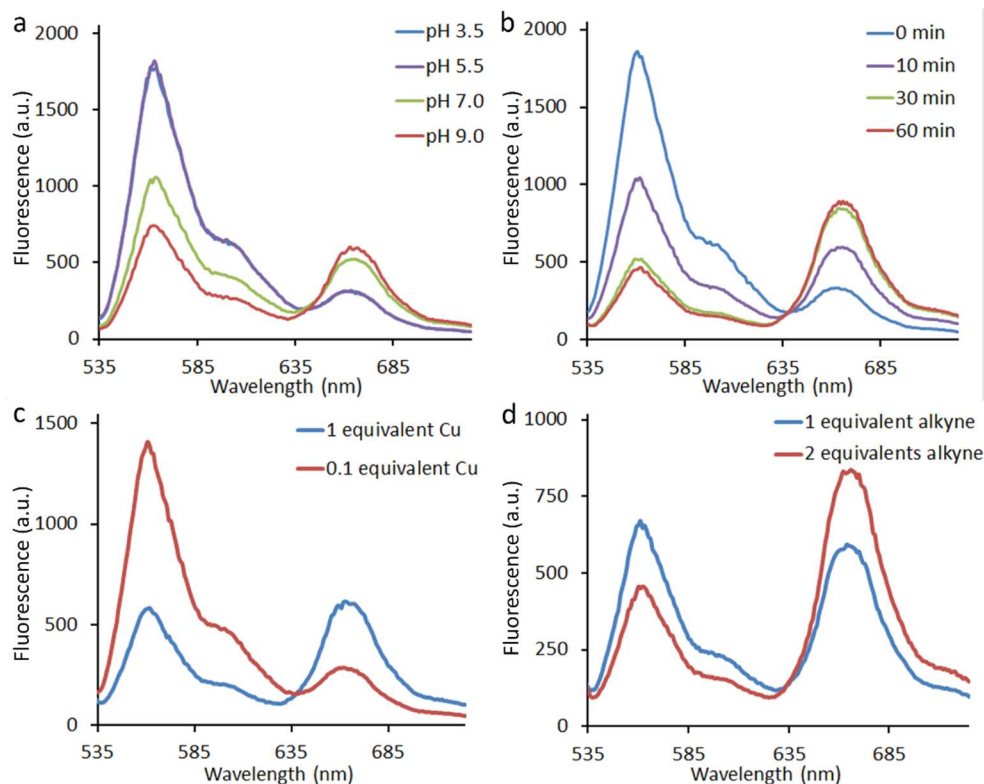


Figure 3.12 Emission spectra from the Cy3 – Cy5 CuAAC parameter screen. (A-D) Emission spectra under 515 nm excitation for reactions varying: (a) pH: 3.5 (blue), 5.5 (purple), 7.0 (green), 9.0 (red). (b) Time (min): 0 (blue), 10 (purple), 30 (green), 60 (red). (c) Cu concentration (azide equivalents): 0.1 (red), 1.0 (blue). (d) Alkyne concentration (azide equivalents): 1.0 (blue), 2.0 (red).

One explanation for these differences is that the polyacrylic acid-derived polymer passivating the QD (see Wichner *et al.* and Methods) concentrates Cu ions at the polycarboxylate surface (Figure 3.10), close enough to CuAAC substrates to speed the reaction by more than an order of magnitude compared to small molecule CuAAC. This may also explain the pH dependence, in which low pH causes increased turnover of Cu ions from surface carboxylates. Another surprising finding of the screen is that a full equivalent of Cu (50 μ M) or more is required for CuAAC with the QD, but not the organic fluorophore (Figure 3.12). This suggests a certain fraction of the Cu is either unable to react, because it is coordinated to QD surface carboxylates, or to turn over, because Cu release from the substrate is slow until the reaction is quenched by a large excess of EDTA (Figure 3.10). Indeed, we found that allowing reactions to incubate in EDTA solution for extended periods typically led to increases in acceptor emission, although without full restoration of QD emission (Figure 3.13). This suggests that Cu ions are bound to the QD surface even after initial addition of EDTA, and some are bound very tightly, possibly in or on the inorganic nanocrystal.

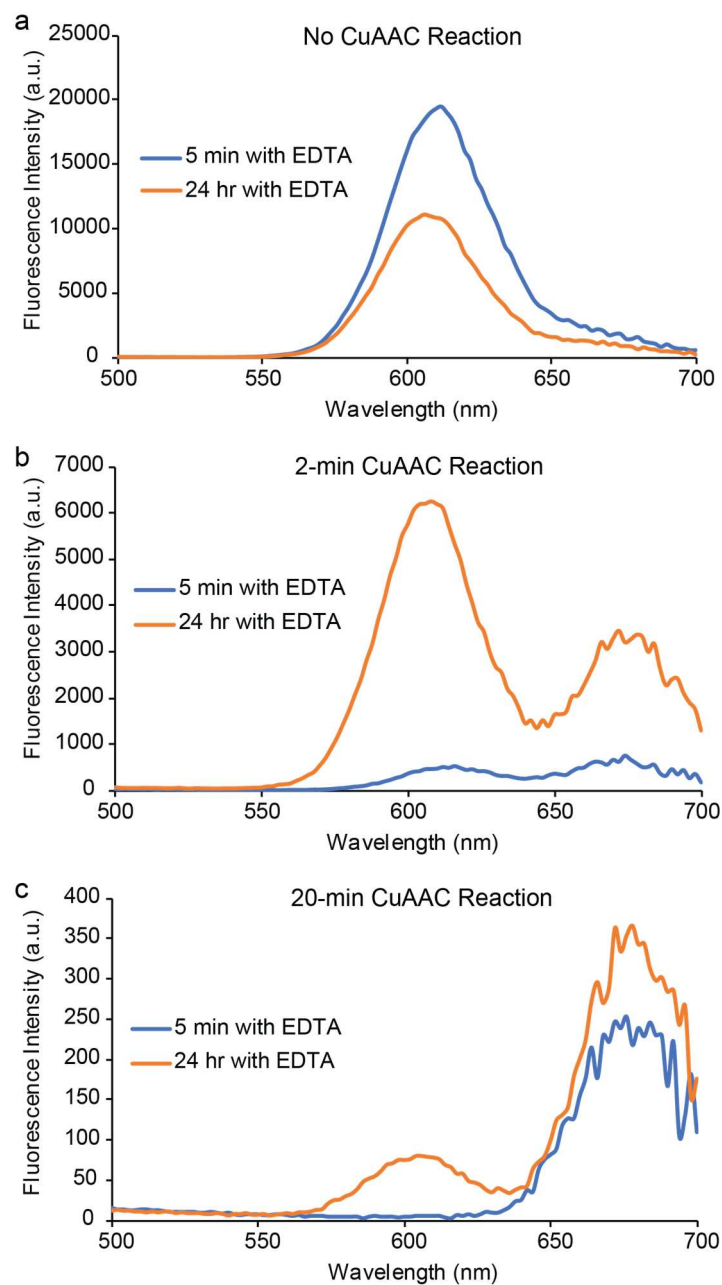


Figure 3.13 Partial recovery of QD emission with post-CuAAC EDTA incubation. Emission spectra of (a) QDs alone, (b) after 2-min CuAAC reaction with Cy5-alkyne, and (c) after 20-min CuAAC reaction with Cy5-alkyne. Spectra are immediately after quenching with EDTA (blue) or after 24 h incubation in EDTA (orange). Other reaction parameters are fixed at: 10 Cu equivalents of THPTA ligand, phosphate-citrate buffer pH 4.5, 1 azide equivalent of CuSO_4 , 100 Cu equivalents of sodium ascorbate, 0-30 min reaction time.

To test whether Cu bound to the nanoparticle surface is responsible for QD quenching during CuAAC reactions, we included a series of benign divalent metal ions (*i.e.*, Ca^{2+} , Mg^{2+} , Mn^{2+}) in the reaction mixture in addition to Cu and Cu ligands. These added ions have been shown to neither quench QDs^{41,97} nor interfere with CuAAC reactions,^{96,98} but in these reactions, all reduced quenching and increased CuAAC coupling (Figure 3.14). In addition, using common passivation polymers where the number of surface carboxylates can be varied (poly(maleic anhydride-*alt*-octadecene)⁸; Figure 3.1b), we found that the rate of quenching decreases as the number of surface carboxylates decreases, while still allowing for the CuAAC coupling to occur (Figure 3.14).

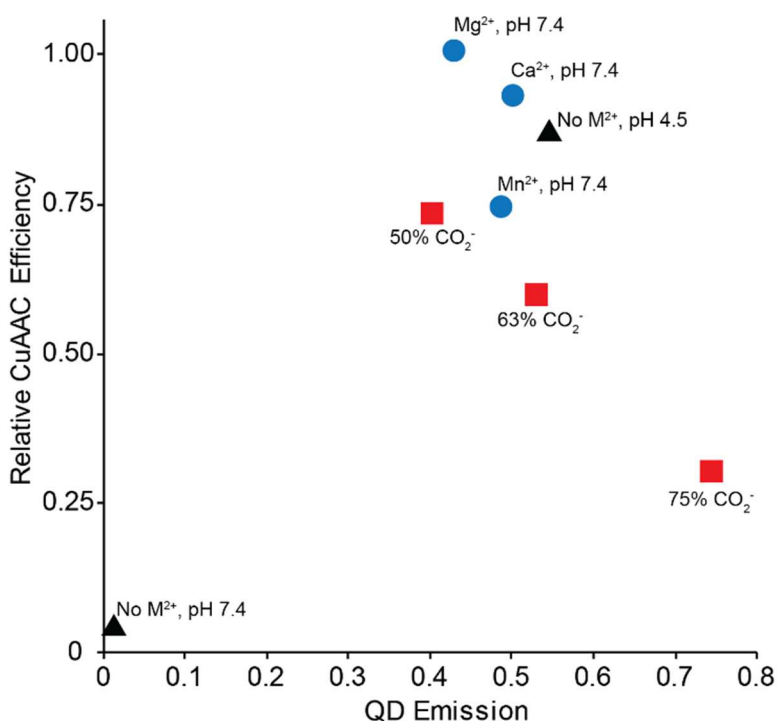


Figure 3.14 Effect of surface carboxylates on QD quenching and CuAAC efficiency. Added divalent metal ions (Mg^{2+} , Ca^{2+} , Mn^{2+} ; blue circles) or reduced density of surface carboxylates (red squares) show CuAAC efficiencies and QD emission similar to low pH reactions. M^{2+} were added in 10-fold excess over Cu in HEPES buffer, pH 7.4. Surface density of carboxylate groups of PMAO-passivated QDs was varied as in Figure 3.15 and Methods. Other reaction parameters were fixed at: 10 Cu equivalents of THPTA ligand, 1 azide equivalent of CuSO_4 , 100 Cu equivalents of sodium ascorbate, 3 min reaction time.

Compared to the PAOA surface polymer used in the high-throughput screen, for this polymer, higher Cu:QD stoichiometries are tolerated before QD quenching is

observed (Figure 3.15). Superstoichiometric quantities of Cu do not quench QDs only with an appropriate excess of triazole THPTA ligand, suggesting a complex competition for Cu between QD surface carboxylates, the triazole ligand, the QD surface, and the alkyne (Figure 3.10). Tuning the ratios of Cu to triazole and alkyne yields both high coupling and low quenching, and this phenomenon is transferable across surface passivation polymers (Figure 3.16). In contrast to most previous studies of CuAAC conditions,^{70,74,84,88} we find a 10-fold molar equivalent of Cu over the azide is most efficient (Figure 3.15), allowing for rapid (< 2 min) reactions before QD quenching begins to become apparent. Our combinatorial approach also offers a large dataset to be mined for insight into aqueous CuAAC reactions and other mechanistic questions (Figure 3.17).

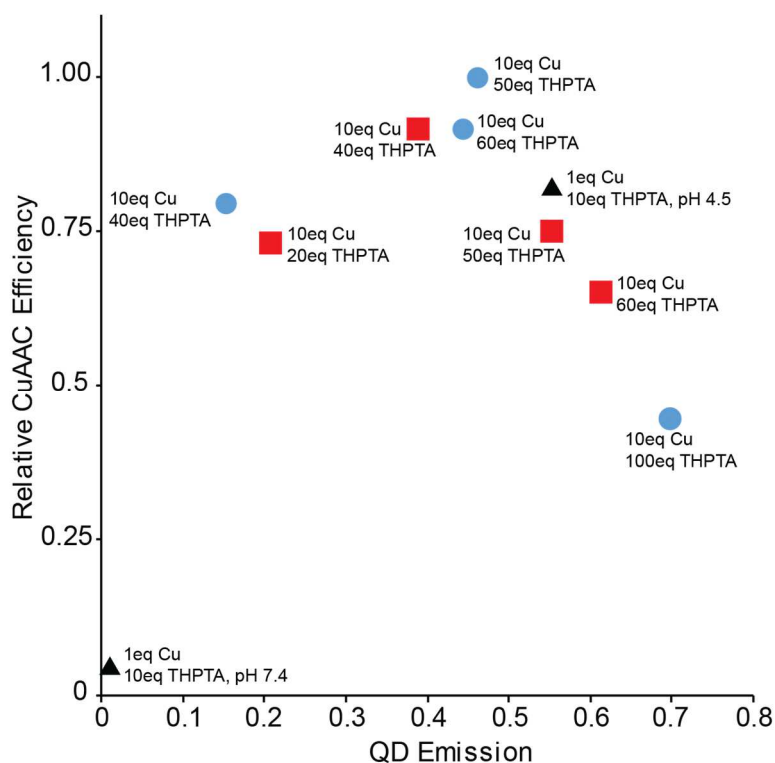


Figure 3.15 Effects of superstoichiometric Cu and Cu ligands on QD quenching and CuAAC efficiency. PAOA-passivated QDs (blue circles) with: 4-, 5-, 6- and 10-fold excess of THPTA ligand over Cu, and 10 molar azide equivalents of Cu at pH 7.4. PMAO-passivated QDs (red squares) with: 2-, 4-, 5-, and 6-fold excess of THPTA ligand over Cu, and 10 molar azide equivalents of Cu at pH 7.4. QDs with 1 equivalent of Cu (black triangles) are in either pH 4.5 or 7.4 buffer. Reaction parameters were fixed at: 100 azide equivalents of sodium ascorbate, 3 min reaction time.

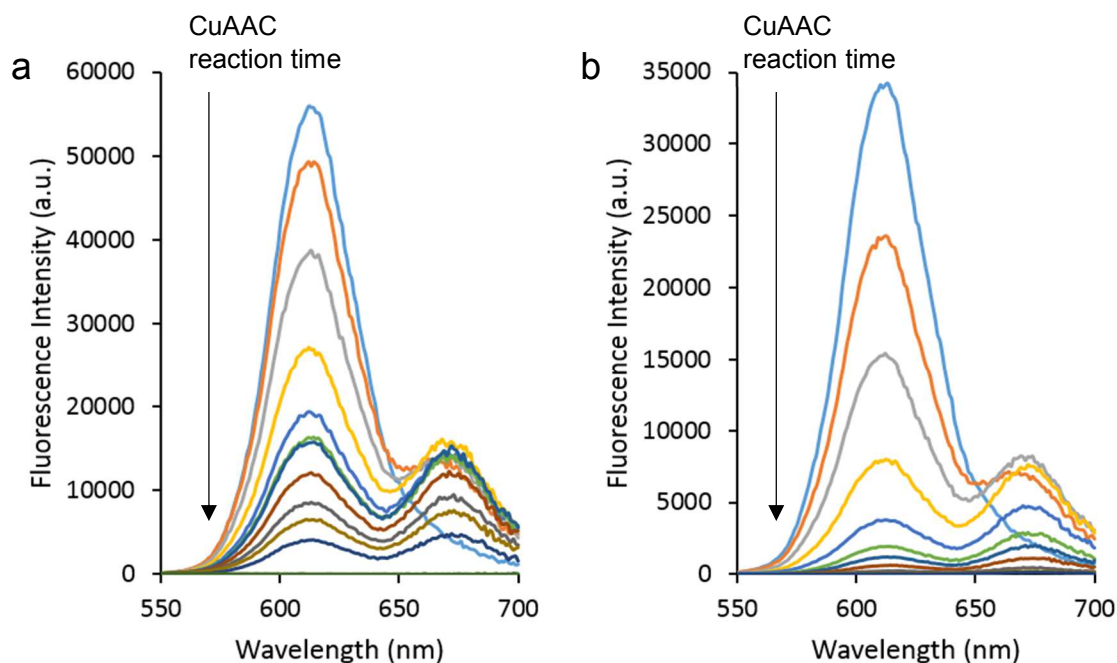


Figure 3.16 Effects of superstoichiometric Cu by QD passivating polymer. Reaction time series for (a) PMAO-passivated QDs and (b) PAOA-passivated QDs with 10 molar equivalents of Cu. Other reaction parameters are fixed at: 6 Cu equivalents of THPTA ligand, phosphate-citrate buffer pH 4.5, 100 azide equivalents of sodium ascorbate, 0-30 min reaction time.

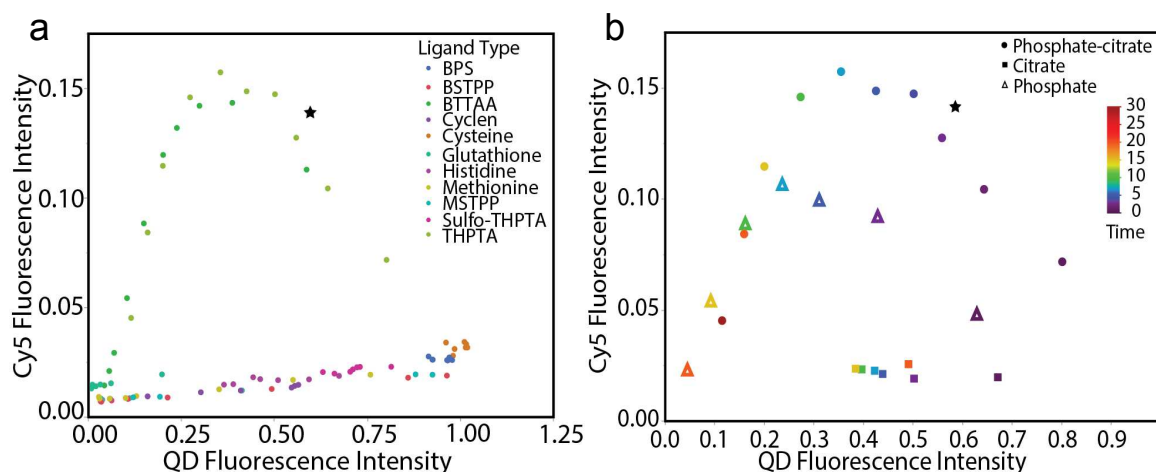


Figure 3.17 Quenching and CuAAC reaction efficiency with varying reaction parameters. (a) Ligand type. Examples of time series with largest FRET signal from each ligand are shown. Other reaction parameters are fixed at: phosphate-citrate buffer pH 4.5, 1 azide equivalent of copper sulfate, 100 Cu equivalents of sodium ascorbate. (b) Buffer anion. Other reaction parameters are fixed at: 10 Cu equivalents of THPTA ligand, pH 4.5, 1 azide equivalent of copper sulfate, 100 Cu equivalents of sodium ascorbate. Black star (★) is copper-free control emission.

3.2.4 Cu-mediated click synthesis of QD bioconjugates

To test the relevance of these non-quenching CuAAC conditions to complex biomolecules, we coupled azide-bearing CdSe/CdS QDs with the tarantula toxin GxTX, an amphiphilic 36-amino acid cysteine knot peptide.^{67,68} GxTX selectively binds to membrane-embedded voltage sensors of Kv2 channels in the resting state (Figure 3.2), and can be released by membrane depolarization.⁶⁸ We synthesized and refolded Ser13Pra GxTX, where the alkyne sidechain is predicted to extend into extracellular solution⁶⁷ and used CuAAC conditions from the combinatorial screen for conjugation. The reaction was limited to 90 s to limit the number of GxTX per QD (Figure 3.18) and minimize non-specific membrane staining. CHO cells with and without induced channel expression were incubated with QD-GxTX conjugates and imaged along with a cellular autofluorescence band outside of the QD emission (Figure 3.19).

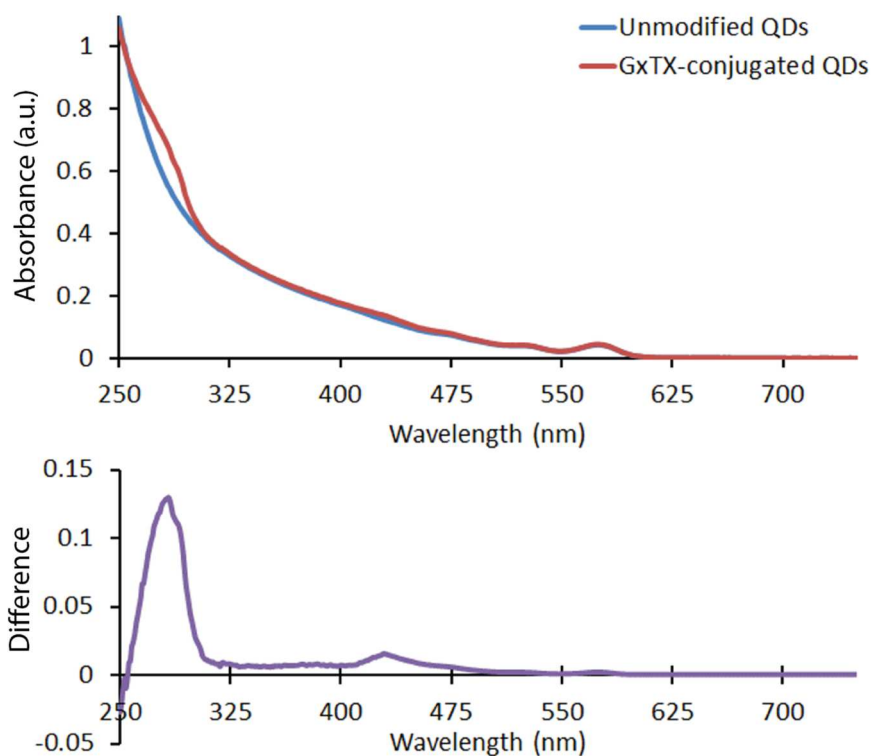


Figure 3.18 Detection of GxTX conjugated to QD surface. Absorbance (*top*) and difference (*bottom*) spectra of CdSe/ZnS QDs with (red) and without (blue) GxTX CuAAC conjugation, showing Trp absorbance of GxTX. With a molar absorptivity of $18,350 \text{ cm}^{-1} \text{ M}^{-1}$ for GxTX, this absorbance corresponds to an average of ~ 25 toxins per QD.

Cells with high levels of Kv2.1 expression show significant increases in membrane QD staining compared to cells with low Kv2.1 expression, or to cells stained with unconjugated QDs (Figure 3.19g). Membrane depolarization induced by the addition of high $[K^+]_o$ solution decreases membrane staining to background levels (Figure 3.19e-f), demonstrating that binding is dependent on the conformational state of the channel and the QD-conjugated GxTX remains physiologically active. Because of their sensitivity to changes in membrane potential, these conjugates are a first generation QD-based voltage sensor, whose sensitivity and optical properties may be refined through choice of nanoparticle and toxin.

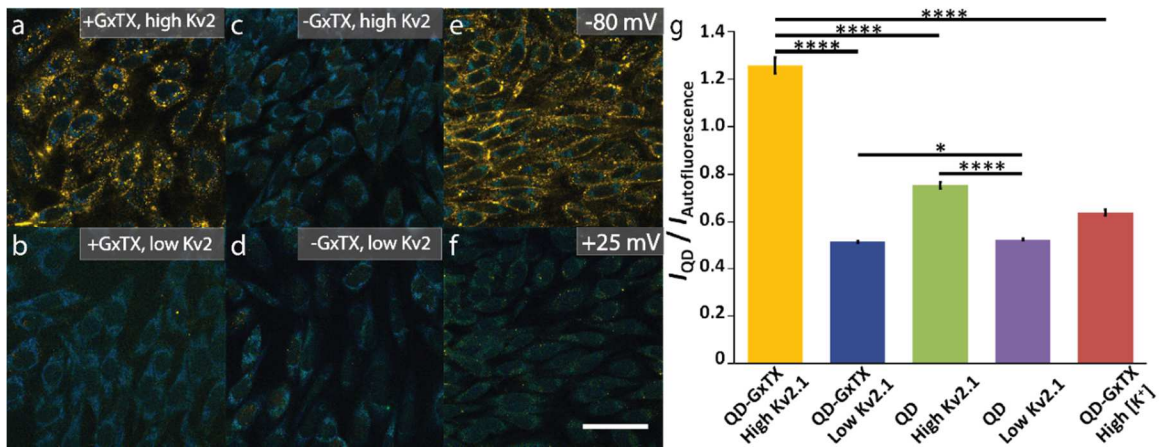


Figure 3.19 Live cell imaging of QD-GxTX conjugates on CHO cells expressing Kv2.1 channels. Representative confocal images of QD-GxTX in cells with (a) high and (b) low Kv2.1 channel expression. Yellow is QD emission and blue is cellular autofluorescence. Cells with (c) high and (d) low Kv2.1 expression show similar levels of binding for QDs without conjugated GxTX. Kv2.1-expressing cells stained with QD-GxTX (e) at resting membrane potential and (f) after K^+ -induced membrane depolarization. Scale bar is 20 μ m. (g) Statistical analysis of emission intensities in (a) – (f) using 560 - 610 nm (QD) and 450 - 500 nm (autofluorescence) integrated emissions. Error bars are standard error. P values: **** $\equiv p < 0.0001$, * $\equiv p < 0.2$ (not significant). $N = 100$ cells.

3.3 Conclusions

We have discovered rapid, non-destructive, and high-yield CuAAC reaction conditions with Cu^+ concentrations that would normally fully quench QD emission in under 10 s. As compared to previous synthetic screens, the added challenge of maintaining catalysis while suppressing a faster side-reaction is apparent in the size of the screens: about 2000 reactions in this study versus 100-200 in most others.⁹⁰⁻⁹⁴ Important discoveries from the screen include the pH dependence of QD quenching, the superiority of triazole Cu ligands for QD coupling, and the advantages for superstoichiometric concentrations of Cu. These synthetic conditions are applicable to other molecules containing simple alkynes, including peptides, oligonucleotides, lipids, and carbohydrates,⁷⁵ as well as to other imaging probes prone to Cu quenching, such as lanthanide-doped nanocrystals.^{99,100} This work demonstrates a combinatorial approach for adapting otherwise incompatible reactions to quantum dots, suggesting a more expansive view of organic synthetic possibilities on nanocrystal surfaces.

We successfully apply this conjugation strategy to the attachment of a peptidyl tarantula toxin, guanxitoxin-1E (GxTX), to the surface of QDs and image their staining of live mammalian cells. Subsequent treatment of these cells with high tonic K^+ triggers release of the QD-toxin probe from the potassium channel in the cell membrane, and the fluorescence signal can be washed away. In order to expand the reach of these probes into more complex systems like cultured neurons or acute brain slices, we first attempted to show specificity of this behavior to those cells containing high expression of the Kv2.1 potassium channel of interest. Convolved by batch variations in synthesis of the probe and changes in cell biology, we have had no consistent success in showing specific labeling of the singular cell phenotype (Appendix I). As the experimental difficulty and material scarcity are substantially increased for these future experiments, this proof of concept would be essential before moving on to more complicated biological environments.

3.4 Materials and Methods

Synthesis of CdSe QD cores. CdSe cores were synthesized as previously described.^{6,58} In an Ar glovebox, 0.058 g of Se powder (Aldrich, 99.99% trace metal basis) was added to 0.36 g of trioctylphosphine (TOP, Aldrich, 97%) in a glass vial and stirred overnight, yielding TOP-Se as a clear, colorless solution. On a Schlenk line, 0.060 g of CdO (Aldrich, 99.99% trace metal basis, 0.47 mmol), 0.28 g of octadecylphosphonic acid (ODPA, 0.84 mmol), and 3.0 g of TOP oxide were combined in a 50-mL flask fitted with a condenser and temperature probe. The flask was heated under N₂ to 150 °C and stirred under vacuum for 1 hr. The solids melted at 70 °C. The flask was purged with N₂ and heated to 320 °C until the Cd complexed with the ODPA to become clear and colorless. TOP (1.50 g) was injected into the flask drop-wise and the temperature was then raised to 370 °C. The TOP-Se precursor was then rapidly injected, and growth time was controlled to achieve the desired nanoparticle size. The flask was cooled with air and then submerged in an ice bath after the temperature cooled below 300 °C. At 110 °C, 2 mL of cold toluene was injected. The final reaction solution was removed, and the total volume of the solution was diluted with toluene to 15 mL. The nanoparticles were then precipitated with 15 mL of acetone and centrifuged at 4000 x g for 5 min. The pellet was dispersed in a minimum of CHCl₃, precipitated with 10 mL of acetone, centrifuged at 4000 x g for 5 min, dispersed in a minimum of hexane (~1 mL), and precipitated with acetone again. These cores were dispersed in 5 mL of hexane and stored in a glovebox.

Synthesis of core-shell CdSe/CdS nanoparticles. Stock solutions of 0.1 M Cd oleate in 1-octadecene (ODE) and 0.1 M octanethiol in ODE were prepared in a glovebox. On a Schlenk line, 5 mL of ODE was placed in a 3-neck flask under N₂ and 100 nmol of CdSe core nanocrystals in hexane were injected. Solvent was removed under vacuum at room temperature and then at 120 °C for 20 min. The reaction was purged with N₂ and the glovebox solutions containing 6 mL of 0.1 M Cd oleate in ODE and 6 mL of 0.1 M octanethiol in ODE were injected at 310 °C *via* 2 syringe pumps over 2 hr. After injection, 1 mL of oleic acid was quickly injected, and the reaction maintained at 310 °C for 1 hr. The reaction flask was cooled with air, the nanocrystals cleaned by repeated precipitation as above, and the nanocrystals dispersed in 5 mL of hexane with 1% oleic acid (v/v) for storage under ambient conditions.

Synthesis of poly(acrylic acid)-*co*-poly(*n*-octylacrylamide)-*co*-poly(2-aminoethylacrylamide) random amphiphilic copolymer (PAOA). Polyacrylic acid (ca. 2000 Da, 500 mg, 0.25 mmol) and *N*-hydroxysuccinimide (424 mg, 3.64 mmol) were dissolved in 20 mL of 100 mM HEPES buffer, pH 8.0. *N*-Boc-ethylenediamine (118 mg, 0.74 mmol) and *n*-octylamine (286 mg, 2.21 mmol) were dissolved in 20 mL of EtOH

and added to the PAA solution. The pH was adjusted to 7.6 with 5M NaOH and then EDC (1.13 g, 5.90 mmol) was added; after 1 h, the pH was re-adjusted to 7.6, and an additional 250 mg of EDC was added. The reaction was stirred well overnight and divided into two 50-mL centrifuge tubes. EtOH was removed in a Genevac evaporator, causing the polymer to pellet. The pellets were each rinsed with 10 mL of 500 mM citrate buffer, pH 4.0, and then 10 mL of water. To remove the Boc protecting groups, the pellets were each resuspended in 5 mL of TFA with 250 μ L of H₂O. After 45 min, 10 mL of water was added to each tube and the volumes reduced to 5 mL by Genevac evaporation. To each tube were added 5 mL of EtOH and 5 mL of 0.2 M NH₄OAc buffer, pH 7.0. The solutions were dialyzed (Pierce Slide-a-Lyzer, 3.5 kDa MWCO) against 3 x 2 L of distilled water, causing much of the polymer to precipitate. The solution within the cassette was removed, and solids present in the cassette were dissolved with 10 mL of EtOH. These were combined and the EtOH was removed using a Genevac evaporator. The suspension was dissolved with ca. 20 mL of 50% CH₃CN, frozen, and lyophilized to give 608 mg of white powder with a calculated average of ~9 octyl groups, 15 carboxylates, and 3 ammonium groups per polymer.

Peptide synthesis and folding. Alkyne-bearing guangxitoxin-1E mutants were synthesized in a background where Met35 was replaced by its isostere norleucine (Nle) to avoid complications of Met oxidation. Nle35 variants are used in all experiments, and referred to as GxTX. Linear peptides were synthesized on an AAPTEC Apex 396 peptide synthesizer using an Fmoc (*N*-(9-fluorenyl)methoxycarbonyl) methodology. Peptides were assembled stepwise on 0.1-0.3 mmol of resin (Fmoc-Pro-NovaSyn TGT, Novabiochem) in *N*-methyl-2-pyrrolidone, 0.4 M Fmoc amino acids, 0.44 M *N*-hydroxybenzotriazole, and 10% *N,N'*-diisopropylcarbodiimide (DIC). The side chain protecting groups for amino acids were triphenylmethyl for cysteine and asparagine, *tert*-butyloxycarbonyl for tryptophan and lysine, and *tert*-butyl for serine. Removal of Fmoc groups with 20% 4-methylpiperidine in dimethylformamide (DMF) preceded 2-h coupling steps. Resin was washed 5x with DMF after coupling and Fmoc removal. Linear peptides were cleaved and deprotected with trifluoroacetic acid:triisopropylsilane:1,2-ethanedithiol:thioanisole:H₂O (85:2.5:2.5:5:5 by volume) for 2-4 hours at room temperature, with removal of deprotecting groups monitored by MALDI-TOF mass spectrometry.

Cleaved peptide was separated from resin by filtration, precipitated with cold diethyl ether, the pellet washed once with ether, and dried under a stream of N₂. This peptide was dissolved in 50% acetic acid, injected onto a preparatory C₁₈ column (Vydac), and eluted with a linear gradient of ACN with 0.1% TFA. Recovered peptides were lyophilized, dissolved in 50% ACN, diluted to 50 μ M, and folded by air oxidation in: 1 M guanidinium HCl, 0.1 M NH₄OAc, 2.5 mM glutathione, 0.25 mM oxidized

glutathione, 1% ACN, and NH₄OH to adjust pH to 8.0. Oxidation was monitored by mass spectrometry (Applied Biosystems SCIEX TF4800 MALDI TOF-TOF). Upon completion (3 days), the visible aggregates that had formed in solution were removed by filtration, and 0.1% TFA added. This solution was pumped onto a C18 column, eluted as above and lyophilized. The peptide sequence of Ser13Pra GxTX is: Glu-Gly-Glu-Cys-Gly-Gly-Phe-Trp-Trp-Lys-Cys-Gly-Pra-Gly-Lys-Pro-Ala-Cys-Cys-Pro-Lys-Tyr-Val-Cys-Ser-Pro-Lys-Trp-Gly-Leu-Cys-Asn-Phe-Pro-Nle-Pro.

Reaction conditions for parameter FRET screen. For spectra in Figure 3.4b-e, reaction conditions were held constant except for the highlighted variable. For 3.4b (pH study): 10 eq. (500 μ M) THPTA, 100 eq. (5 mM) sodium ascorbate, 1 eq. (50 μ M) Cu(OAc)₂, and 5 min reaction time. For 3.4c (time series): 10 eq. (500 μ M) THPTA, 100 eq. (5 mM) sodium ascorbate, 1 eq. (50 μ M) Cu(OAc)₂, and phosphate buffer, pH 4.5. In 3.4d (ascorbate concentration): 10 eq. (500 μ M) THPTA, 1 eq. (50 μ M) CuSO₄, phosphate-citrate buffer, pH 4.5, and 7 min reaction time. In 3.4e (ligand): 100 eq. (5 mM) sodium ascorbate, 1 eq. (50 μ M) Cu(OAc)₂ or CuSO₄, and phosphate or phosphate-citrate buffer, pH 4.5, and 7 min reaction time.

Passivation of Core-shell CdSe/CdS Nanoparticles by poly(acrylic acid)-*co*-poly(*n*-octylacrylamide)-*co*-poly(2-aminoethylacrylamide) (PAOA) amphiphilic copolymer. CdSe/CdS QD core/shells with emission maxima of 626 nm were dispersed in hexane with 1% (*v/v*) oleic acid to 8 μ M; CdSe/ZnS QD core/shells (Ocean Nanotech) with emission maxima of 585 nm were diluted with hexane to 5 μ M. Concentrations were determined by first exciton absorbance. For aqueous dispersion, PAOA (20 mg, 6.25 μ mol, 3000-fold molar excess over QDs) was dissolved in 1 mL of MeOH and 19 mL of CHCl₃. QDs in hexane (*e.g.*, 250 μ L of 8 μ M 626 nm CdSe/CdS QDs, 2.0 nmol) were added with stirring, and the solvents were removed under a gentle stream of N₂ overnight. The dry QD/polymer residue was then resuspended in 15 mL of 200 mM sodium bicarbonate buffer, pH 8.0. This suspension was sonicated for 30 minutes, heated in an 80 $^{\circ}$ C water bath for 60 minutes, slowly cooled in the bath to room temperature, and then sonicated for 30 minutes. Excess polymer was removed by spin dialysis (Amicon Ultra-15, 50 kDa MWCO), washing with 3 x 15 mL of 100mM HEPES, pH 7.8. The retentate was diluted to 1 mL with HEPES buffer and centrifuged at 16100 x *g* for 5 min to remove residual polymer and insoluble aggregates. Aqueous QD dispersions were stored under ambient conditions.

Passivation of QDs by poly(maleic anhydride-*alt*-1-octadecene) (PMAO) amphiphilic copolymer. PMAO (30 mg, 1.33 μ mol, 16 monomer units per nm² of QD surface) was dissolved in 1 mL of acetone and 14 mL of CHCl₃. QDs in hexane (*e.g.*, 250 μ L of 8 μ M 626 nm CdSe/CdS QDs, 2.0 nmol) were added with stirring, and the

solvents were evaporated under a gentle stream of N₂ overnight. The QD/polymer residue was then resuspended in 15 mL of 50 mM sodium borate buffer, pH 9.0, with desired ratios of primary amines for reaction with maleic anhydrides (Figure 3.15). This suspension was sonicated for 30 minutes, heated in an 80 °C water bath for 60 minutes, slowly cooled in the bath to room temperature, and then sonicated for 30 minutes. Excess polymer was removed by spin dialysis (Amicon Ultra-15, 50 kDa MWCO), washing with 3 x 15 mL of 100 mM HEPES, pH 7.8. The retentate was diluted to 1 mL with HEPES buffer and centrifuged at 16100 x g for 5 min to remove residual polymer and insoluble aggregates. Aqueous QDs were further purified by size exclusion chromatography (HiPrep 16/60 Sephacryl S-500HR, GE Healthcare), and aqueous QD dispersions were stored under ambient conditions.

Synthesis of azide-coated QDs. PAOA-wrapped QDs (2 μM, 1 mL) in 100 mM HEPES, pH 7.8, and SE-PEG₄-N₃ (ThermoFisher, 50 mM in DMSO, 100 μL) in DMSO were combined in a 1.5-mL centrifuge tube and shaken for 1 hour on a rotary mixer. The reaction mixture was diluted to 500 μL with Milli-Q water, and excess PEG reagent was removed by spin dialysis (50 kDa MWCO), washing with 3 x 500 μL of Milli-Q water. The retentate was diluted to 1 mL with Milli-Q water and stored under ambient conditions.

Synthesis of PEG₄-amino coated QDs. Azide-coated QDs (2 μM, 100 μL) were mixed with sodium borohydride (100 mM, 100 μL) in 100 mM sodium bicarbonate buffer, pH 10.0, and stirred in a vented glass vial for 2 hours. The reaction was ended and remaining borohydride destroyed by addition of 2 mL of 100 mM phosphate buffer, pH 4.5, followed by stirring for 30 minutes. The reaction mixture was diluted to 500 μL with 100 mM HEPES, pH 7.8, and the QDs were purified by spin dialysis (50 kDa MWCO), washing with 3 x 500 μL of HEPES buffer. The retentate was diluted to 100 μL with HEPES buffer and stored under ambient conditions.

Synthesis of Cy5-alkyne. Propargylamine (0.8 μL, 12.5 μmol) was dissolved in 400 μL of 100 mM HEPES pH 7.4, which was added to 1 mg of dry Cy5 succinimidyl ester (1.26 μmol, GE Healthcare). The reaction was vortexed well, briefly centrifuged, and incubated overnight in the dark. The alkyne product was purified on a C₁₈ HPLC column (Vydac) using a linear 2-60% CH₃CN gradient with 0.1% TFA over 30 min, with product eluting at 21 min (28% CH₃CN). MS, C₃₆H₄₄N₃O₇S₂ (MH)⁺ calculated: 694.25; found: 694.8. Fractions containing product were pooled and lyophilized to 0.83 mg (94% yield) of dark blue film.

Syntheses of Texas Red-alkyne and Alexa Fluor 594-alkyne were performed under similar conditions and eluted at 49% and 37% CH₃CN respectively. MS, Texas

Red-alkyne, $C_{40}H_{45}N_4O_7S_2$ (MH)⁺ calculated: 757.27; found: 757.5; Alexa Fluor 594-alkyne, $C_{38}H_{38}N_3O_{10}S_2$ (MH)⁺ calculated: 760.18; found: 760.4.

Synthesis of Cy3-Azide. 1-Amino-11-azido-3,6,9-trioxaundecane (0.8 μ L, 4.0 μ mol, Sigma) was dissolved in 20 μ L of 200mM sodium bicarbonate pH 8.2, which was added to dry Cy3 succinimidyl ester (150 μ g, 196 nmol, GE Healthcare). The reaction was vortexed well, briefly centrifuged, and incubated overnight in the dark. The azide product was purified on a C_{18} HPLC column (Vydac) using a linear 2-60% CH_3CN gradient with 0.1% TFA over 30 min, with product eluting at 18 min (22% CH_3CN). MS, $C_{39}H_{54}N_6O_{10}S_2$ M⁺ calculated: 829.33; found: 829.5. Fractions containing product were pooled and lyophilized to 0.13 mg (79% yield) of dark pink film.

Cu-QD quenching and reversal. Emission spectra were measured on a Fluoromax fluorometer (Horiba Jobin Yvon) from 10 nM dispersions of PAOA-encapsulated CdSe/CdS QDs with 405 nm excitation. A solution of $Cu(OAc)_2$ and sodium ascorbate was quickly mixed into the QDs to give final concentrations of 10 μ M and 20 μ M, respectively. Emission at 625 nm was measured at 1-s intervals for 2000 s, and full emission spectra were recorded both before and after the kinetic experiment. For reversal tests, ligands were added to a final concentration of 10 mM, with or without 1 mM $CdCl_2$. Emission at 625 nm was measured at 5-min intervals for 30 h, with full emission spectra recorded both before and after the kinetic experiment.

Combinatorial CuAAC FRET assay. In a typical reaction, two reagent mixtures were prepared prior to reaction initiation in the following order: Tube A: 40 μ L of 2 μ M QD-PEG- N_3 (0.08 nmol), 12 μ L of 350 μ M Cy5-alkyne (4.2 nmol), and 10 μ L of 50 mM phosphate-citrate buffer, pH 4.5. Tube B: 8 μ L of 500 μ M $CuSO_4$ (4 nmol), 8 μ L of 50 mM sodium ascorbate (400 nmol), and 2 μ L of 20 mM THPTA (40 nmol) in Milli-Q water. Solution B was rapidly mixed into Solution A, and time points were taken 1, 2, 3, 4, 5, 7, 10, 15, 20, and 30 min after mixing, by removing 7 μ L aliquots and adding into 350 μ L of 10 mM EDTA solution in wells of a black wall 96-well assay plate. Fluorescence spectra were measured in a SpectraMax Gemini EM fluorescence plate reader (Molecular Devices) with 405 nm excitation and recorded with a 1-nm step size from 550 - 750 nm. Each reaction series contained an internal standard of unmodified QDs for concentration scaling. Spectra on key samples were also collected in cuvettes in a fluorometer.

Data analysis. Reaction parameters and corresponding spectral data were imported into JMP (SAS Institute, Inc.) for data manipulation and statistical analysis. All trials were scaled to QD concentration prior to cross-parameter comparisons. Each scaled spectrum was integrated from 600 – 630 nm for the QD emission value and from 670 – 700 nm for

the Cy5 emission value. The Pearson product-moment correlation coefficient and its significance were calculated for each reaction parameter paired with both the QD emission and Cy5 emission to determine the influence of each variable.^{101–103} Coefficients near zero show no dependence between variables, and values near ± 1 indicate highly correlated responses to changes in the parameters. The reaction from each ligand type that displayed maximum FRET signal was scaled for concentration, and a difference spectrum was generated by subtraction of the unmodified QD signal. The 670 – 700 nm integrated emission from the difference peak was used as a relative measure of maximum ligand efficacy (Table 3.1).

Non-quenching CuAAC reaction conditions on QDs. For reactions at acidic pH: aqueous QDs (2 μM , 40 μL) were mixed with 12 μL of 350 μM alkyne and 10 μL of 80 mM phosphate-citrate buffer pH 4.5. In a separate tube, 8 μL of 5 mM CuSO_4 , 8 μL of 50 mM sodium ascorbate, and 2 μL of 100 mM THPTA were mixed well and added to the first tube with rapid mixing. After 2 minutes, the reaction was quenched into 400 μL of 10 mM EDTA solution.

For reactions at physiological pH: aqueous QDs (2 μM , 40 μL) were mixed with 12 μL of 350 μM alkyne, 2 μL 100 mM $\text{Ca}(\text{NO}_3)_2$ or MgSO_4 , and 8 μL of 100 mM HEPES buffer pH 7.4. In a separate tube, 8 μL of 2.5 mM CuSO_4 , 8 μL of 50 mM sodium ascorbate, and 2 μL of 50 mM THPTA were mixed well and added to the first tube with rapid mixing. After 30 seconds, the reaction was quenched into 400 μL of 10 mM EDTA solution.

Reactions may be purified by spin dialysis, washing with 500 μL of 20 mM HEPES, pH 7.4, containing 500 μM EDTA, and then with 3 x 500 μL of 20 mM HEPES, pH 7.4. Yields of both reactions are estimated to be $>90\%$ based on fluorescence measurements in comparison to control QD conjugates.

Synthesis of QD-GxTX conjugates. Alkyne-bearing guangxitoxin-1E mutants were synthesized as previously described.⁶⁸ Two reagent mixtures were prepared prior to reaction initiation in the following order: Tube A: 40 μL of 2 μM QD-PEG- N_3 (0.08 nmoles), 2 μL of 2.3 mM Ser13Pra GxTX (4.6 nmoles) in 50% DMSO, 10 μL of Milli-Q water, and 10 μL of 50 mM phosphate-citrate buffer pH 4.5. Tube B: 8 μL of 500 μM CuSO_4 (4 nmoles), 8 μL of 50 mM sodium ascorbate (400 nmoles), and 2 μL of 20 mM THPTA (40 nmoles) in Milli-Q water. Tube B was rapidly mixed into tube A, allowed to react for 90 s, and then quenched in 400 μL of 10 mM EDTA. QD-GxTX conjugates were purified by spin dialysis (50 kDa MWCO, Amicon), washing with 500 μL of 20 mM HEPES, pH 7.4, containing 500 μM EDTA, and then with 3 x 500 μL of 20 mM HEPES, pH 7.4. The retentate was diluted to 160 μL with HEPES buffer and stored under ambient conditions.

Cell Culture. CHO-K1 cells were maintained in tissue culture-treated polystyrene dishes (Nunc) at 37 °C in a 5% CO₂ atmosphere in Ham's F-12 media (Sigma) containing 10% fetal bovine serum (FBS, Gibco) and 1% penicillin–streptomycin solution (Life Technologies). A CHO-K1 cell line expressing rat Kv2.1 voltage-gated potassium channels⁶⁸ was cultured with 1 µg/mL blasticidin (ThermoFisher) and 25 µg/mL zeocin (Invitrogen) to retain transfected vectors. Before experiments, 1 µg/mL minocycline was added to the cell media 2 days prior to imaging to induce Kv2.1 expression.

Live Cell Imaging. Cells were plated in 8-chamber culture slides (Ibidi) 2 days prior to imaging experiments and imaged in neuronal external solution (NES; concentration in mM: 3.5 KCl, 135 NaCl, 1.5 CaCl₂, 1 MgCl₂, 10 HEPES, pH 7.4 with NaOH). Cells were incubated in freshly prepared 5 nM QD-GxTX or 5 nM QD-PAOA in NES for 20 minutes on ice to prevent endocytosis of nanoparticles, and then washed with 3 x 400 µL of NES immediately prior to imaging under ambient conditions.

Confocal images of the focal plane at the chamber interface were obtained using an inverted Zeiss LSM710 system with a 1.4 N.A. 63x Apochromat oil immersion objective. QD emission was excited using a 405 nm diode laser with an MBS-445 main dichroic beam splitter, and emission was collected from 560 – 610 nm. Cellular autofluorescence was excited with the same 405 nm diode laser with an MBS-405 main dichroic beam splitter, and emission was collected from 450 – 500 nm. To increase K⁺ concentration for cell depolarization, NES was aspirated from the wells and replaced with NES containing 135 mM KCl and 3.5 mM NaCl. High-[K⁺] images for Figure 3.20f-g were taken 5 minutes after NES replacement.

Regions of interest (ROI) were manually drawn around 100 cells from a single well for each imaging category. Total integrated pixel intensity was calculated for both 560 – 610 nm QD fluorescence and 450 – 500 nm autofluorescence, and a ratio of the two was calculated within each ROI. The data were pooled for each imaging category and a Student's t-test was used to determine statistical differences in mean intensity ratios for each category (Figure 3.20). All cell imaging and statistics shown were taken in the same imaging session with the same reagents. Similar results were obtained for 3 separate experiments with different batches of cells and GxTX-QDs. Images and analysis in Figure 3.20 are for cells at >80% confluence coinciding with GxTX-QDs synthesized within the prior 24 h.

Molecular Docking. The model of GxTx-1E—Kv1.2-Kv2.1 chimera complex was performed using ROSETTA as described previously.⁶⁷ Briefly, the voltage sensor of a Kv1.2-Kv2.1 channel (PDB 2R9R)¹⁰⁴ was docked with a GxTx-1E NMR structure (PDB 2WH9).¹⁰⁵ After energy minimization, the lowest energy binding model most consistent

with alanine scan mutagenesis was selected for rendering. Molecular renderings were produced using the UCSF Chimera package from the Computer Graphics Laboratory, University of California, San Francisco.

4 | Nanoparticle Conjugates and Design Possibilities Using Engineered Isopeptide-forming Proteins

4.1 Introduction

In addition to chemical modifications, it is essential to have methods to interface nanocrystals with biological components. While the copper click strategy outlined previously was successful, it required the incorporation of the non-natural amino acid propargylglycine to provide one of the reactive groups. This is only possible through chemical peptide synthesis^{106–108} or difficult tRNA engineering,^{109–112} which have limitations on size and complexity. Methods that can incorporate proteins but maintain the site-specific conjugation would be advantageous for any more complex designs.

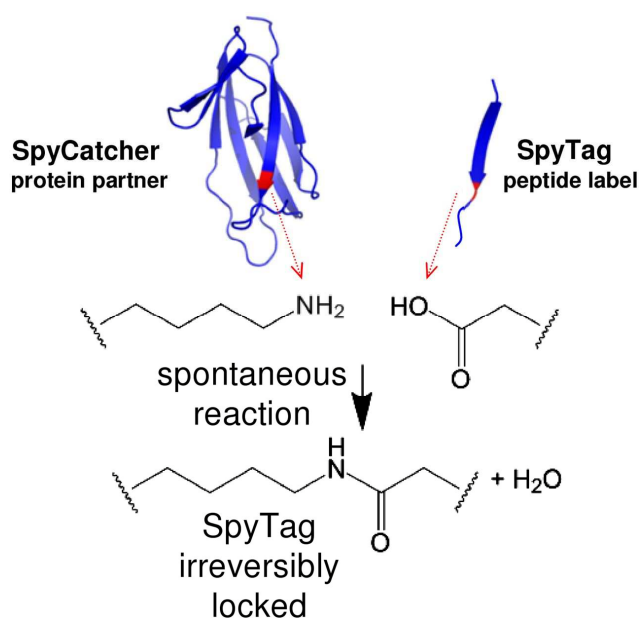


Figure 4.1 SpyCatcher/SpyTag split domain conjugation system.¹¹³ Once the peptide binds into the binding pocket of the protein, a lysine side chain in SpyCatcher and an aspartic acid side chain in SpyTag undergo a condensation to form a covalent isopeptide bond.

One such strategy is through the Spy system, which has perfused much of our nanocrystal work of the last several years. Engineering of a domain of the *Streptococcus pyogenes* fibronectin-binding protein, CnaB2, has resulted in a split peptide and protein complementary pair, SpyTag and SpyCatcher (Figure 4.1).^{113,114} When these two components bind in solution, there is an isopeptide bond formed by the condensation of a lysine side chain in the protein and an aspartic acid side chain on the peptide. Since the bond formed is in the hydrophobic core of the protein, it is not easily hydrolyzed or cleaved. The incorporation of peptides into fusions with other proteins is one of the most

common for capture or purification methods (*e.g.* His₆ or HA), but the interactions between peptide tags and protein are often labile or low affinity.¹¹⁵⁻¹¹⁹ Once made, the isopeptide bond in the SpyCatcher linkage is irreversible up to the force required to sever a covalent bond.¹¹³ So now we have two components that can be expressed as protein fusions with an intrinsic group for covalent attachment to nanocrystals decorated with the complementary component. Because the small 13 amino acid SpyTag is simpler to incorporate into expressed proteins, and the hydrophobic nature of SpyTag also seems to cause aggregation of nanocrystals once conjugated to the surface (Figure 4.2), we have focused on introducing the SpyCatcher protein onto the nanoparticle surface for further conjugation to SpyTag targets.

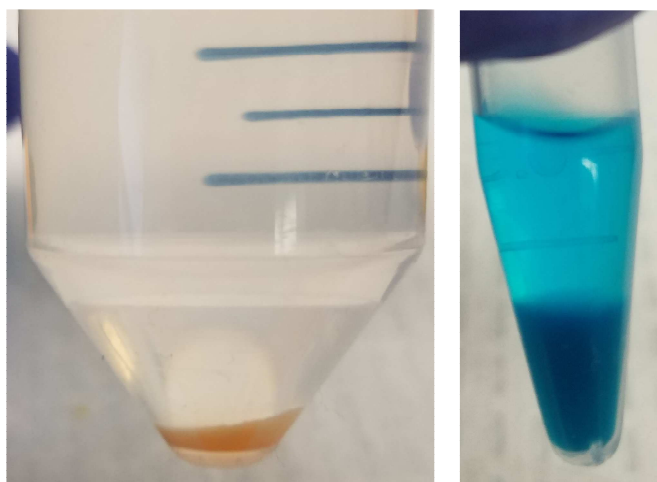


Figure 4.2 SpyTag-decorated fluorophores aggregate in solution. SpyTag-Cys coupled to CdSe/CdS QDs (left) and to Cy5-maleimide (right) precipitate out of solution and are not recoverable in aqueous mixtures. Free SpyTag-Cys peptide is also not dispersible in pure aqueous solvent and requires significant acetonitrile or DMSO as a cosolvent.

One of the main advantages of using the SpyCatcher system to form our conjugation motif, since it is an expressed protein, is that we have design control over where the cysteine linkage appears with respect to the nanocrystal and the protein orientation. This is a major boon for applications where orientation and location of conjugates dictate the activity and efficacy of the probe, such as in antibody conjugates.^{120,121} Current methods of antibody-nanocrystal conjugation often disrupt the underlying antibody protein structure^{122,123} or indiscriminately label common sidechains of the antibody in random orientation and number (Figure 4.3).¹²⁴ SpyCatcher conjugation can address both issues, modulating the number of covalently attached proteins in quantitative yield, and the orientation to the nanoparticle is fixed by the position of SpyTag in the SpyTag-antibody fusion. Genetic control of antibody

expression is required to insert the SpyTag sequence into the protein, but no chemical modifications are needed to the expressed protein. To this end, we have developed a QD-antibody probe for labeling of the urokinase-type plasminogen activator receptor (uPAR), a marker for detection of malignant tumors.¹²⁵⁻¹²⁷ The probe shows high activity for a model cell system, and results are promising as a stepping stone to *in vitro* and *in vivo* tumor studies.

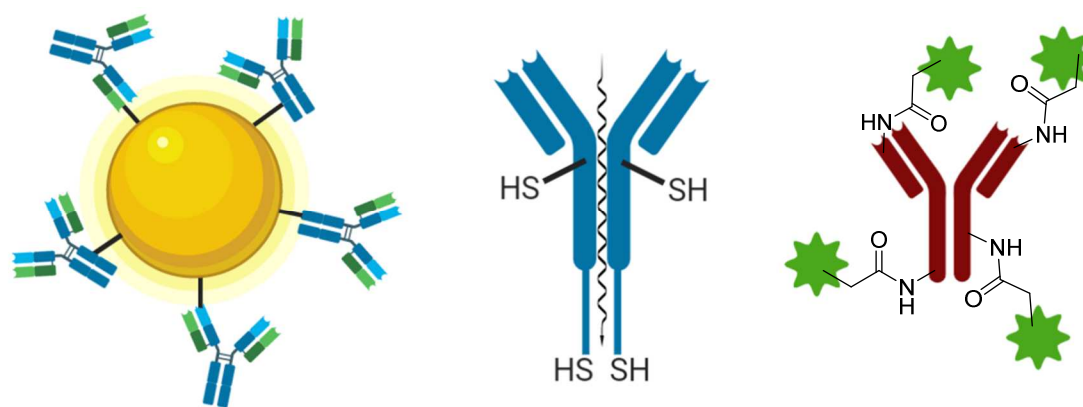


Figure 4.3 Antibody conjugation methods are nonideal for high-performance probes. (Left) Chemical crosslinking at common sidechains (*e.g.* lysine) yields a mixture of conjugation sites, orientation, and number per particle. (Center) Methods that employ cleavage of interchain disulfides can destroy the antibody structure and still generate a mixture of products. (Right) Indiscriminate labeling of sidechains such as lysine gives a distribution of number and location of labels (green).

Another advantage of the SpyCatcher system is the possibility of designing fusions with other proteins to modulate its properties. While we can use SpyCatcher to access new connections, other interesting properties can be incorporated by fusing proteins together. One application that would benefit from this design is to explore nanoparticle endocytosis into cells. Endocytosis is a process wherein a cell forms a microcompartment of pinched off cell membrane to internalize extracellular components, like nanoparticles. Nanoparticles are often trapped inside these compartments as they transform into lysosomes for degradation or are shuttled back outside the cell. When using microscopy to study nanoparticles in cells, the projected view can make it difficult to discern whether the nanoparticles are resting on the cell surface, trapped in endosomes, or in the cytosol. So, if we can design a system that changes its properties from outside to inside the cell, we could differentiate and study only those nanoparticles in the target environment. By exploiting these design possibilities and the susceptibility of the disulfide bond to reducing conditions, we can create a highly-engineered probe of nanoparticle endocytosis with new capabilities native to the protein linkage (Figure 4.4).

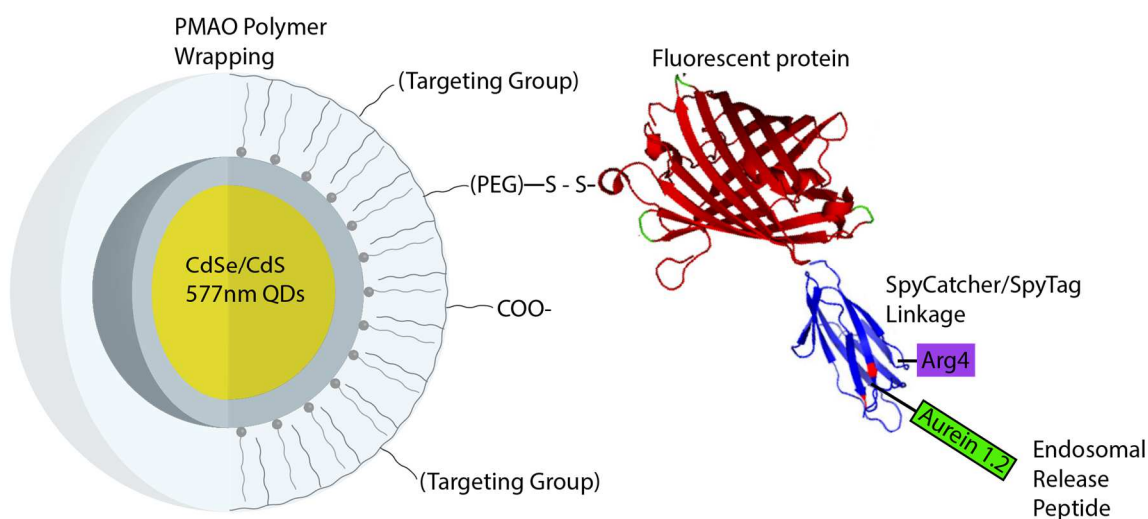


Figure 4.4 Schematic design for FRET-based endocytosis probe. Control over nanocrystal surface chemistry and protein engineering allow the design of highly complex engineered probes. Reducible bond between the nanoparticle and biomolecules yields an environment-responsive construct.

This approach is very complex, requiring the engineering of several components. The main function needed is a measurable change in the probe going from outside the cell to the cytosol. This is accomplished using a Förster resonance energy transfer (FRET) relationship between the QD nanocrystal and a fluorescent protein conjugated on the surface (Figure 4.4). While attached, when the QD is excited by incident light, some of the energy will transfer to the protein and be seen as redshifted emission in the fluorescence spectrum (Figure 4.5). Once the disulfide bond linking the protein to the QD is cleaved by the reducing environment inside the cell,^{128,129} the protein can diffuse away, disrupting FRET, and the spectrum would return to that of the unconjugated QD (Figure 4.5). The second major piece needed is a way to get the nanoparticles out of endosomes and into the cytosol. For this, we use the SpyCatcher linkage fused to the fluorescent protein as a site to incorporate SpyTag-aurein1.2. This secondary linkage is necessary, as aurein1.2 is one of a class of antimicrobial peptides^{130,131} known for their cell-penetrating properties.^{132–134} Since these disrupt bacterial cell membranes for their antimicrobial function, they cannot be expressed as a part of a protein fusion and must be added postsynthetically to the purified protein. As both aurein1.2 and SpyTag are short peptides, a fusion of them may be synthesized without cellular expression.

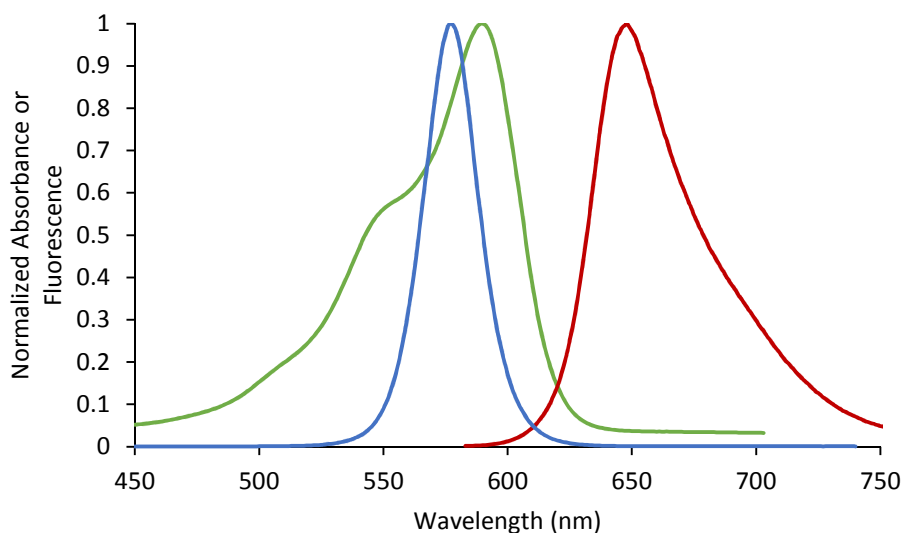


Figure 4.5 QD-fluorescent protein FRET design. QD fluorescence emission (blue) that significantly overlaps the absorbance of the fluorescent protein (green) would allow for resonant energy transfer at small enough distances between them. Excitation of the QD would then cause emission from the protein (red).

Here, we show several methods for nanoparticle surface display of SpyCatcher protein and use the linkages made to synthesize complex probes for antibody binding and tracking the stimulus of a cellular reducing environment. Cellular imaging of these constructs shows their robustness and efficacy for the design of nanocrystal probes to study cell biological processes.

4.2 Results and Discussion

4.2.1 Engineering SpyCatcher for nanocrystal binding

When choosing how to modify the SpyCatcher protein, it is important to keep in mind the significance of the molecular orientation and the specificity of the covalent attachment. While it is possible to attach biomolecules directly to the nanocrystal through chemical linkages (*e.g.* through side chain lysines or cleaved interchain disulfides in antibodies), the nonspecificity in number or location of sites often results in reduction in activity of the biomolecule.^{135–141} Instead, controlled display of SpyCatcher protein allows for specific and quantitative addition of SpyTag-fused molecules to the surface. This control comes from the introduction of a single cysteine amino acid mutation at serine 35 in a solvent-exposed unstructured region of the SpyCatcher sequence (Figure 4.6). Since the wild type protein sequence contains no cysteines, there is only one possible site for reactions, and the placement on this face of the protein exposes the SpyTag binding pocket away from the nanocrystal surface. This side chain thiol can then be reacted with a maleimide or an activated disulfide on the nanocrystal to form a stable scaffold for conjugation to further biomolecules (Figure 4.7). This nanoparticle-protein construct may be stored for a matter of months before loss in activity of the protein is observed, likely from some degradation in solution. The use of EDTA chelating agent in the storage buffer lengthens the storage period dramatically by maintaining sterility, preventing any metal ions from reducing the disulfide linkages, and perhaps by deactivating any metalloproteases.^{142,143}

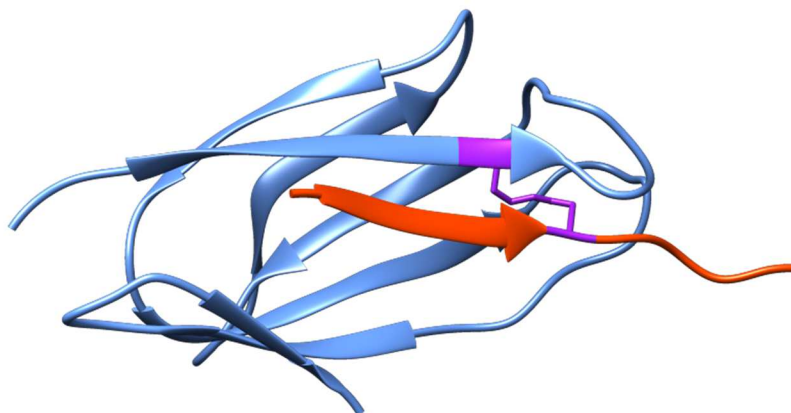


Figure 4.6 Chimera render of Spy system crystal structure. SpyTag peptide (orange) binds to SpyCatcher protein (blue) and forms an interchain isopeptide bond (purple). Serine 35 site is further upstream than the solved crystal structure, near the unstructured N-terminus. PDB ID: 4MLI.

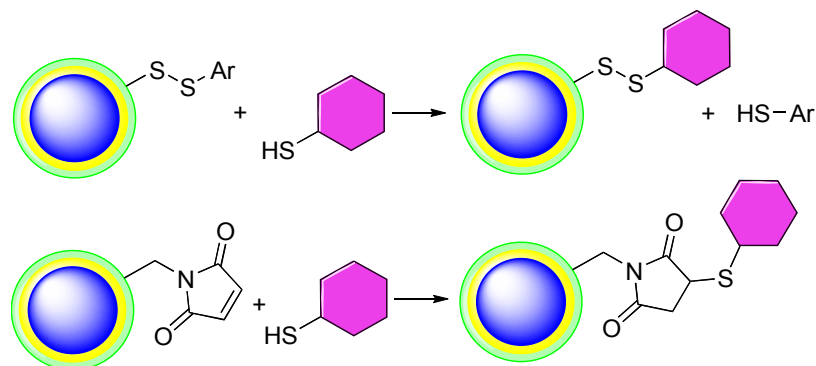


Figure 4.7 SpyCatcher-nanocrystal coupling through thiol side chain. Cys-SpyCatcher (pink) can be coupled to thiol-reactive groups (a) activated disulfide and (b) maleimide displayed on nanocrystal polymer surfaces (green). Maleimide coupling is a traceless addition, while the disulfide exchange produces a thiol side product.

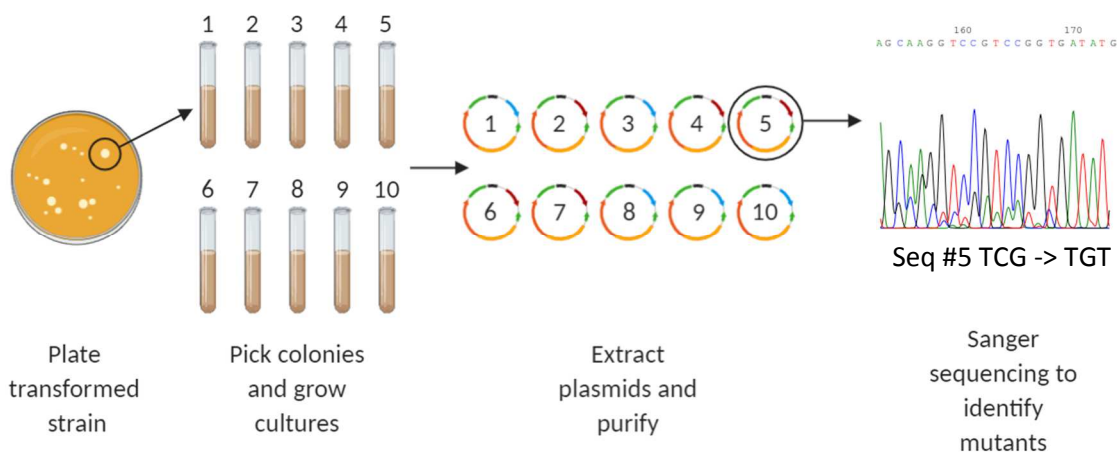


Figure 4.8 Screening *E. Coli* colonies for amino acid mutation. After mutagenesis, mutant DNA is transformed into competent cells and grown as single colonies. Cultures are grown from a selected number of colonies and the DNA is extracted and sequenced to detect that the desired mutation was conferred.

The SpyCatcher protein, as developed by the Howarth group,¹¹³ is available in a pDEST14 bacterial expression vector. As determined from the crystal structure, serine 35 is a good candidate for mutation to cysteine for its orientation and solvent exposure. Site-directed mutagenesis (SDM) was used to alter the peptide sequence,¹⁴⁴ and the new DNA was PCR amplified and recircularized into a plasmid. The DNA was transformed into a stable *Escheria coli* storage strain, DH5 α , and 10 colonies were screened for the desired

mutation (Figure 4.8). Once a positive hit was identified, the plasmid was isolated and retransformed into another *E. coli* strain, BL21 (DE3), for protein expression. Expression of this protein is straightforward, as the sequence contains an N-terminal His₆ sequence for purification *via* immobilized metal affinity chromatography. Between the His₆ tag and the SpyCatcher protein in the peptide sequence is a tobacco etch virus (TEV) cleavage sequence (ENLYFQ/G), which allows for removal of the His₆ tag after purification by a TEV-specific protease.¹⁴⁵⁻¹⁴⁷ SDS-PAGE analysis of each stage of the expression and purification shows a relatively pure band around 15 kDa due to the SpyCatcher protein (Figure 4.9).

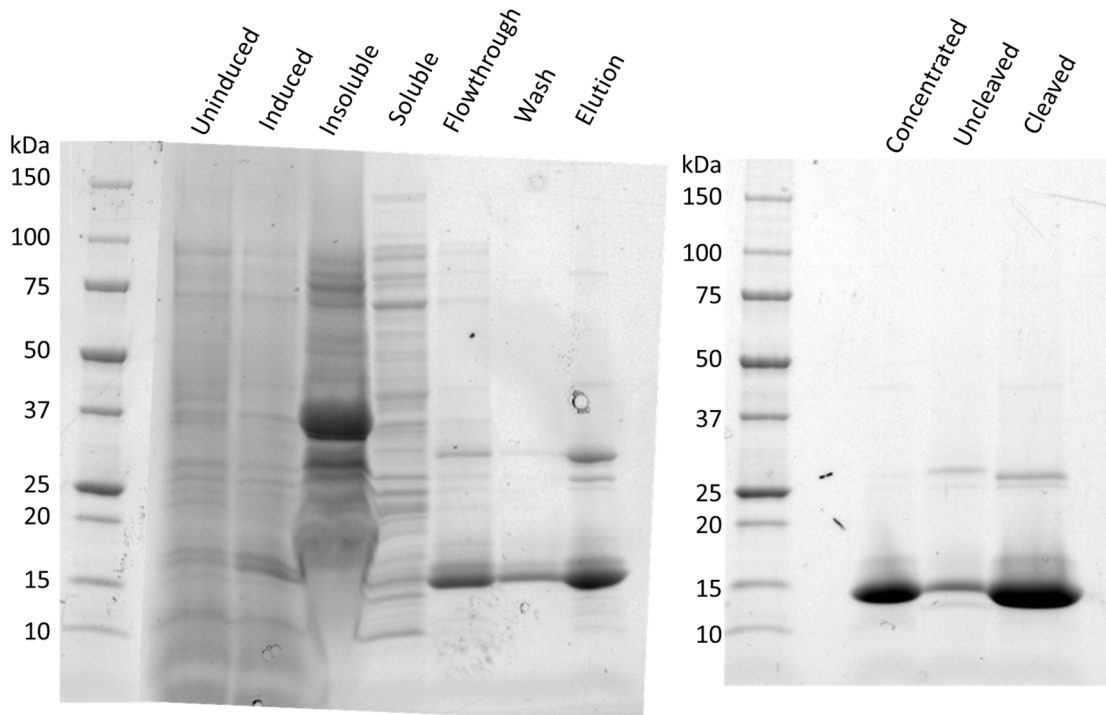


Figure 4.9 SDS-PAGE analysis of SpyCatcher-Ser35Cys expression. (Left) Affinity purification showing lanes for uninduced cells, cells induced for expression, insoluble cell lysate, soluble lysate, IMAC flowthrough, IMAC wash fraction, and eluted protein product. (Right) Cleavage of His₆ affinity tag by TEV protease and subsequent purification. The concentrated IMAC elution, remaining uncleaved product, and eluted cleaved product without His₆ tag are shown. Gels were run at 200 V for 45 mins.

4.2.2 Nanocrystal surface display of SpyCatcher protein

While there are many possible avenues for conjugating SpyCatcher onto the surface, I have focused on two main pathways – either through thiol-maleimide coupling

or through activated disulfide exchange, which both rely on the cysteine thiol introduced *via* mutagenesis. These two methods proceed through different reaction conditions and result in constructs with different properties that may be useful further downstream in processing. There are strategies presented here for each of the polymer encapsulation methods discussed in Chapter 2, so we have an increasing variety of design choices when electing how to construct a particular probe. As outlined there, once the thiol-reactive maleimide or activated disulfide is introduced to the nanoparticles, we need only mix them with SpyCatcher-Ser35Cys to form the covalent linkage (Figure 4.7).

At this point, it is important to detail how we confirm the conjugation of SpyCatcher to the nanoparticles. As discussed previously, it is difficult to probe the surface directly, but we can use several ways to measure the introduction of protein to the surface. The simplest method is through change in hydrodynamic radius as measured by dynamic light scattering (DLS). While difficult to use as an absolute measurement of size, especially for light absorbing nanoparticles like QDs, relative measurements before and after conjugation often reveal a size shift (Figure 4.10). For a protein of ~12.5 kDa like SpyCatcher, its contribution to the size would be 2-3 nm in diameter, and this is typically a large enough change to be measured by this technique.

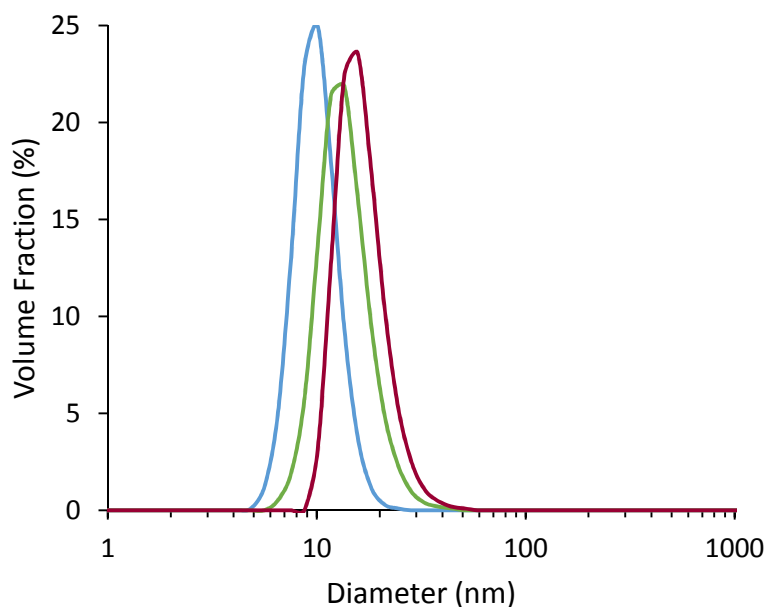


Figure 4.10 Hydrodynamic radius shift from QD to QD-SpyCatcher by DLS. Dynamic light scattering size measurements of 640 nm QD conjugates: hydrophobic (blue), PAOA-wrapped (green), and SpyCatcher-functionalized (red) QDs. Peak values found as an average of 5 runs are: 10.1 nm, 13.5 nm, and 15.7 nm, respectively.

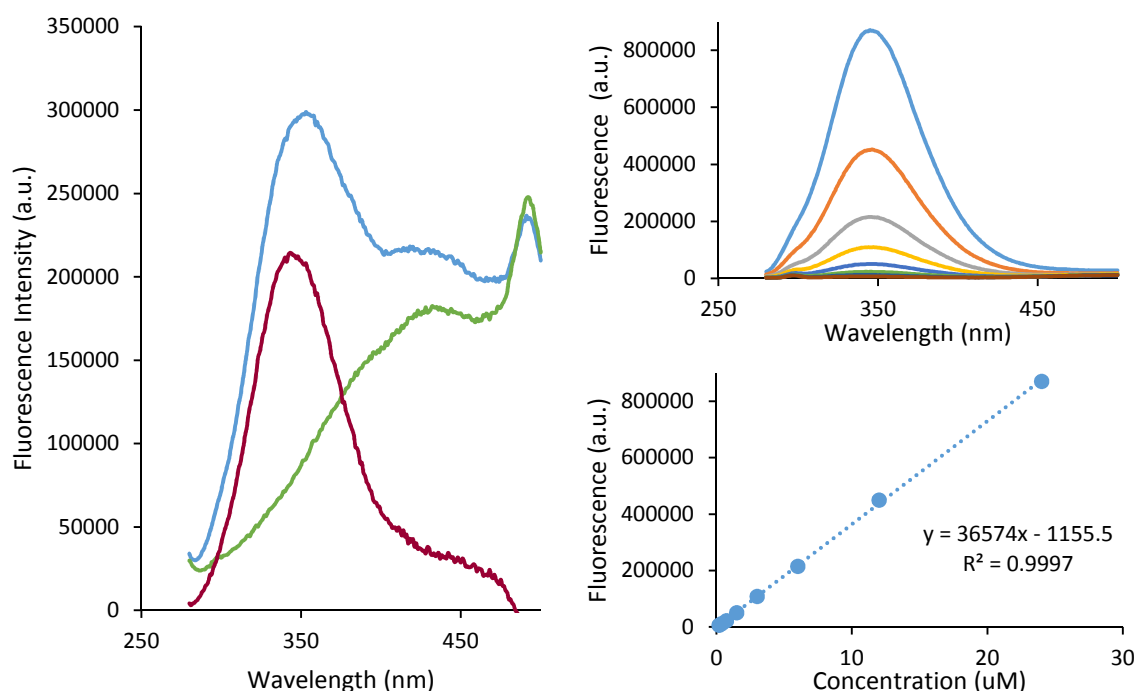


Figure 4.11 Tryptophan fluorescence from SpyCatcher on QDs. (a) Fluorescence emission from QDs conjugated to SpyCatcher (blue), QDs alone (green), and the difference (red). (b) Fluorescence emission from 2-fold dilution series of free SpyCatcher-Ser35Cys protein, starting at 24 μ M (light blue). (c) Calibration curve and linear fit of peak fluorescence values from (b). All samples were illuminated with 270 nm excitation.

While SpyCatcher contains no visible wavelength chromophore, tryptophan residues are often used to measure protein concentration from its absorbance around 280 nm. This can be difficult for samples that are highly absorbing (QDs) or highly scattering (UCNPs) in the UV region of the absorbance spectrum. There is very little background influence on the fluorescence from the tryptophan, however. By exciting nanocrystal-bound proteins around 270 nm, we can measure a fluorescence peak around 340 nm originating from the tryptophan residues (Figure 4.11a,b).^{148,149} Constructing a standard curve from known concentrations of SpyCatcher protein, we can deduce the concentration and number of proteins per nanocrystal on average based on this peak (Figure 4.11c).

If using one of the activated disulfide protocols detailed previously, we can track the progress of the reaction through absorbance measurements of the sacrificial leaving group.^{150–153} As the activated disulfide is displaced, the thioamide formed increases the 343 nm absorbance of the reaction mixture (Figure 4.12). Over a 22-hour period of incubation, this absorbance eventually saturates, indicating that the coupling is no longer

proceeding. Finally, to get a sense of the number of functional proteins on the surface, we can conjugate a SpyTag-fluorophore, like SpyTag-mTurquoise fusion protein, to the nanocrystal and measure the number of conjugated fluorophores by an optical method (Figure 4.13). By measuring the absorbance due to the attached fluorophore, we can discern the number of active conjugation sites per nanoparticle in that particular conjugate, which may prove different from the number of bound SpyCatcher proteins due to loss in activity or inaccessibility of sites. This combined evidence provides a reasonably precise prediction of the surface protein valency. Nanocrystal-SpyCatcher conjugates made in this way have been used for a variety of applications including crosslinking network nodes, assembly with biological materials, and display of targeting groups for nanocrystal imaging.

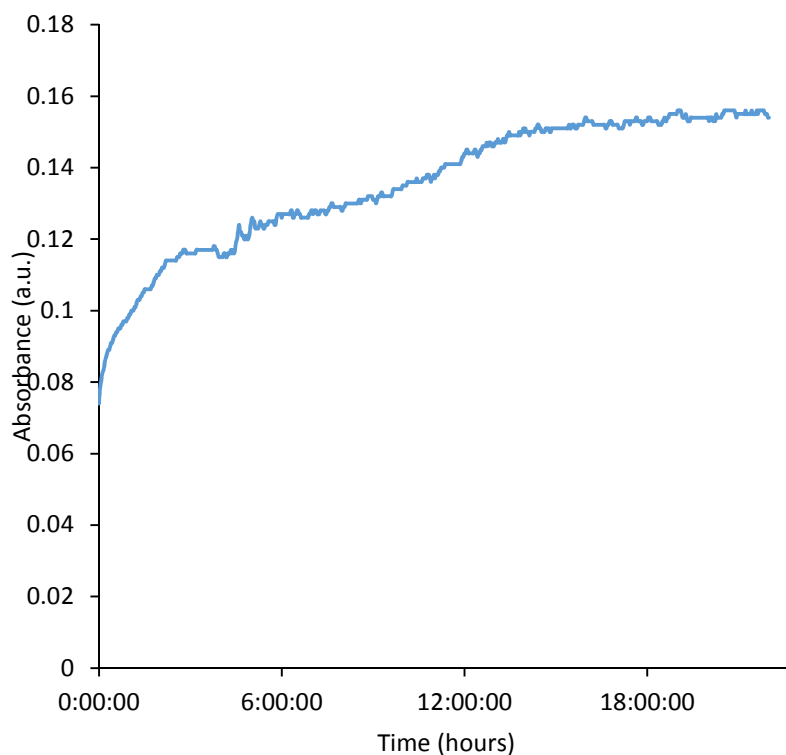


Figure 4.12 Time trace measuring thioamide leaving group. Over 22 hours of incubation, the 343 nm absorbance from the leaving group slowly saturates as binding sites are conjugated by disulfide exchange.

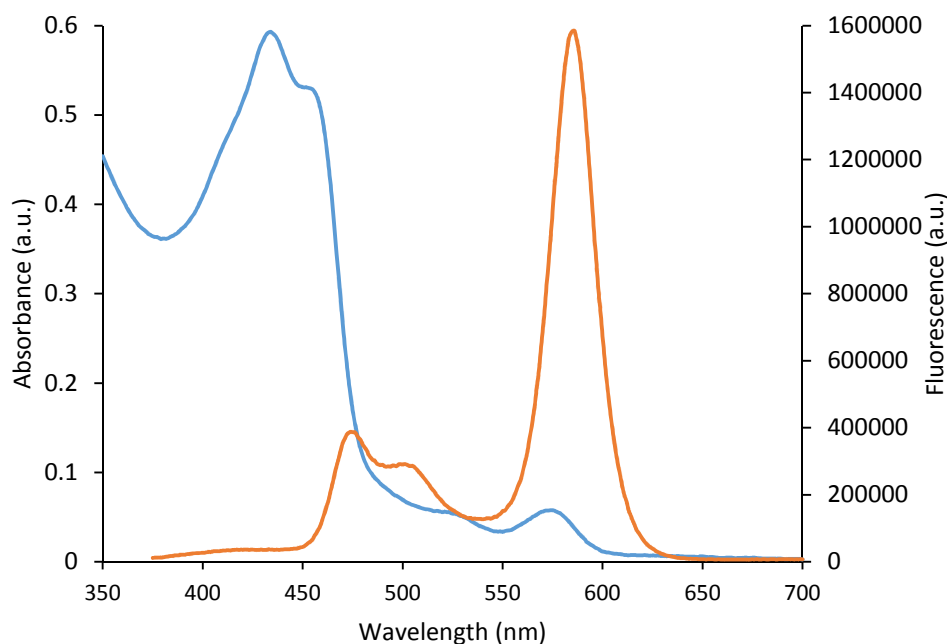


Figure 4.13 Spectral detection of SpyCatcher on QDs by mTurquoise conjugation. Absorbance (blue) and fluorescence emission (orange) of 585 nm QD-SpyCatcher/SpyTag-mTurquoise conjugates. The absorbance peak may be quantified by mTurquoise extinction coefficient, and fluorescence by calibration curve to yield two complementary measurements of conjugation number.

4.2.3 Nanocrystal-antibody conjugates enabled by SpyCatcher conjugation

As detailed previously, the controlled construction of antibody-nanoparticle conjugates is hindered by the nonspecific chemical linkages used, but this can be mitigated using single-position SpyCatcher conjugation. MDA-MB-231 is a triple-negative breast cancer cell line commonly used as a model system for a number of cancers, which express high levels of the uPAR receptor in the cell.¹⁵⁴⁻¹⁵⁷ Phage display has been used to identify anti-human-uPAR antibodies with high binding affinity, and a lead variant named 2G10 was identified.^{125,126} The antibody used in this work is an engineered short-chain variable fragment (scFv) of the full 2G10 IgG antibody, which is a section that contains the antigen binding domain but little of the overall antibody structure.^{125,126,158} Using only the scFv domain (~30kDa) means it retains its function, can be more easily bacterially expressed, and allows us to significantly reduce the size of the overall construct as compared to using a full antibody structure (Figure 1.4). The anti-

uPAR 2G10 scFv plasmid was a gift from Charly Craik, and a protein fusion with SpyTag inserted at the C-terminus was expressed for this construct.

To determine whether the expressed SpyTag was still functional, the fusion was incubated with free SpyCatcher protein and analyzed by SDS-PAGE (Figure 4.14a). Full disappearance of the starting material band shows complete conjugation of the components following overnight incubation. Following the methods outlined above, 610 nm emission QDs and 20 nm core-shell UCNPs were encapsulated by PMAO, functionalized with a 1 mol% PDEA surface, and conjugated with SpyCatcher-Ser35Cys by disulfide exchange. The SpyCatcher nanoparticles were then incubated overnight in various ratios with SpyTag-2G10, characterized for their tryptophan fluorescence, and used directly without further purification (Figure 4.14b). These methods are indifferent to the antibody structure or target, as long as the SpyTag insertion orients the binding site away from the nanocrystal surface, so they could be used for any antibody conjugations in the future.

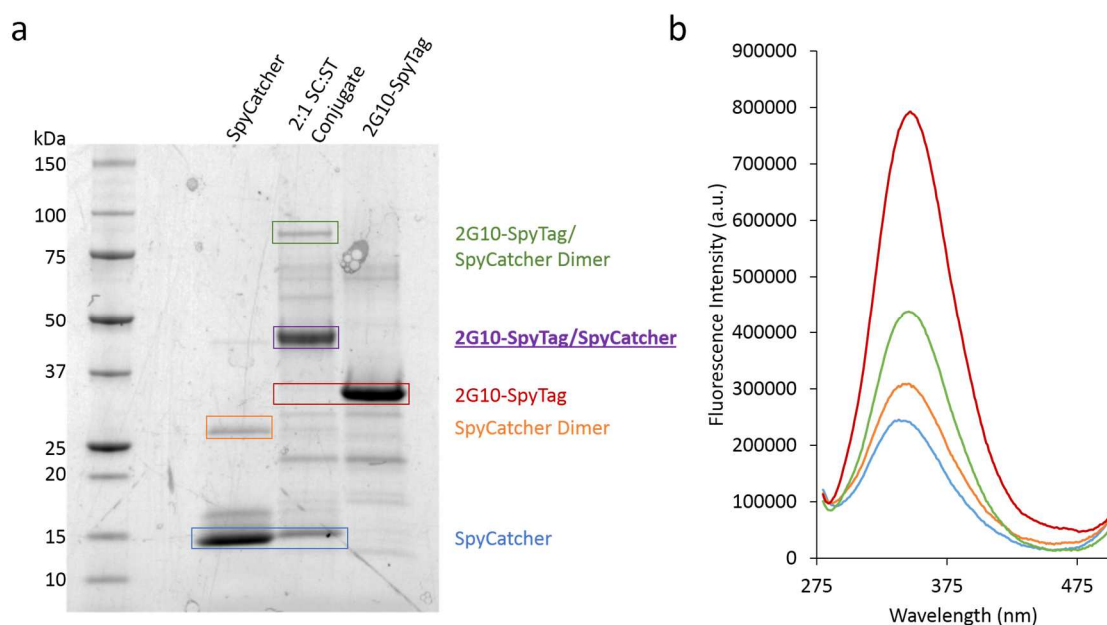


Figure 4.14 SpyTag-2G10 antibody fusion retains SpyCatcher binding ability. (a) SDS-PAGE of SpyCatcher binding to SpyTag-2G10 fusion. Disappearance of the SpyTag-2G10 band (red) and appearance of conjugate band (purple) show complete coupling in solution over 16 hours. (b) Fluorescence emission from 270 nm tryptophan excitation in UCNPs-SpyCatcher (blue) and 2-fold (orange), 5-fold (green), and 10-fold (red) conjugation ratios of SpyTag-2G10 to UCNPs.

To test the activity of the scFv construct on a nanocrystal surface, 2G10-conjugated QDs were tested to show uPAR receptor-mediated internalization in live cells.

QD-2G10 constructs were incubated with live MDA-MB-231 cells for 1 hour at 37°C in an incubator, then counterstained with AlexaFluor488-wheat germ agglutinin (WGA) for 10 minutes. The cells were washed 3 times with PBS and imaged for two-color fluorescence (Figure 4.15). Cells with high levels of uPAR expression show significant increases in internalized QD fluorescence compared to cells stained with unconjugated QDs, as well as higher membrane-associated staining (Figure 4.15). This result indicates that the 2G10-conjugated nanoparticles are preferentially internalized through the uPAR receptor-mediated pathway. These imaging experiments lay the groundwork for expansion of these probes for *in vitro* and *in vivo* studies for use in identifying cancerous cell locations as tumor resection boundaries.

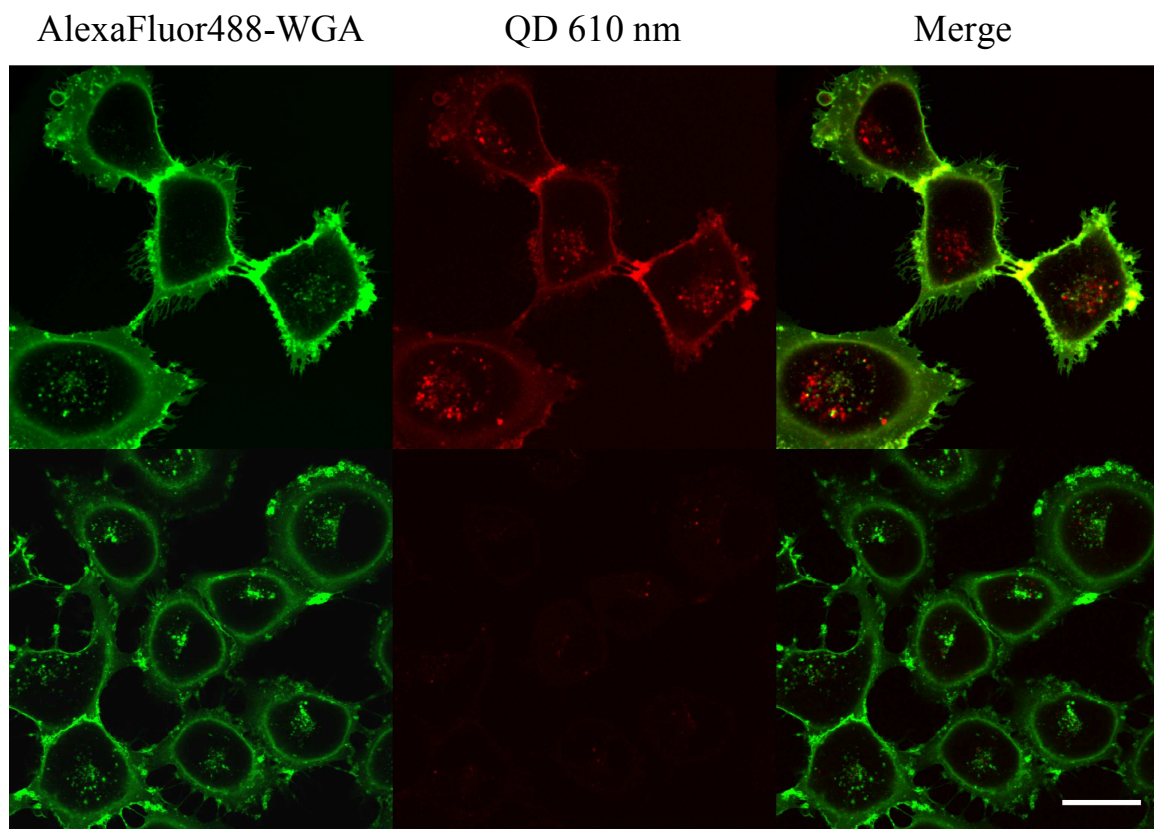


Figure 4.15 Live cell imaging of QD-2G10 constructs in MDA-MB-231 cells. Representative confocal images of QD internalization in cells with high uPAR receptor expression. Cells incubated with QD-2G10 constructs (top row) show high internalization and cell surface association of nanoparticle fluorescence (center, red), while QDs with SpyCatcher-terminated surfaces (bottom row) show much lower staining. Green fluorescence is from cell surface counterstaining with AlexaFluor488-wheat germ agglutinin. Scale bar is 30 μ m for all images.

4.2.4 A SpyCatcher protein fusion for studying nanoparticle endocytosis

In generating the intended probe for endocytosis, the first major hurdle is the construction of a SpyCatcher-fluorescent protein fusion. For applications in cell and tissue imaging, it is advantageous to use the most redshifted emission available in order to minimize scattering in the medium and absorption of the light used by water or biomolecules.^{48,51,159} Since we have high synthetic control over the QD emission wavelength, we choose the QD we'd like to use and match a protein to that wavelength for high FRET overlap. For 585 nm peak emission QDs, we chose the mPlum fluorescent protein for several advantages it brings: high overlap with the QD emission, large Stokes shift from absorbance to emission, no competing cysteines in the structure, monomeric assembly, and relatively high (10%) quantum yield (Figure 4.16).¹⁶⁰⁻¹⁶² The absorbance is well-matched to a number of QD emission peak wavelengths (e.g. 540 nm, 560 nm, 585 nm), and the emission is well-separated by its long Stokes shift.

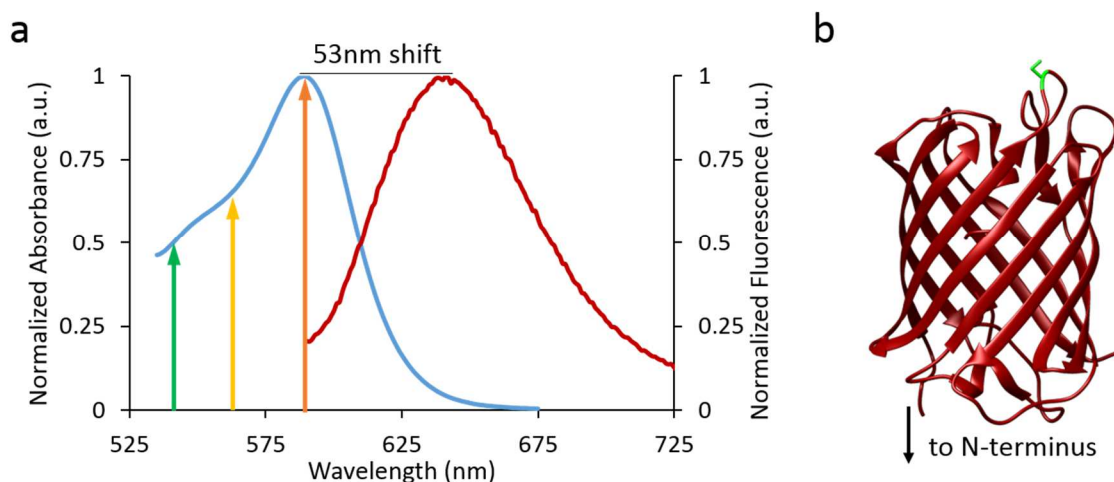


Figure 4.16 mPlum fluorescent protein spectral and structural properties. (a) Absorption (blue) and emission (red) profiles for mPlum protein. Common QD emission wavelengths 540 nm (green), 560 nm (yellow) and 585 nm (orange) are shown. Spectral overlap for energy transfer would be large for any of the above. (b) Chimera structure of mPlum protein with aspartic acid 169 highlighted (green) as a position for cysteine mutation. Its position is oriented opposite to the N-terminus where SpyCatcher would be fused. PDB ID: 2QLG.

Since we want the FRET acceptor to be as close to the nanocrystal as possible for maximum transfer, the single cysteine mutation was introduced into the mPlum sequence by site-directed mutagenesis as before, instead of into SpyCatcher. The final plasmid sequence was confirmed by Sanger sequencing, and the protein was expressed and

purified in high yield by SDS-PAGE. However, when absorbance and fluorescence spectra were taken of the protein, there were unexpected peaks in the spectrum (Figure 4.17). These spectra show 3 distinct peaks each in absorbance and fluorescence, indicative of a mixture of products present in the sample. While the desired peaks at 590 nm and 649 nm are present, they are not the majority of the material. For many of these fluorescent protein chromophores, they undergo a series of oxidation steps to form more redshifted products, so this may be the result of incomplete maturation of the protein.¹⁶³⁻¹⁶⁵ Attempts to further aerate the protein solution and give time for oxidation did increase the visual appearance of red product but did not eliminate the blue or green peaks (Figure 4.18). A deep search of the literature revealed a mechanism wherein the maturation pathway of the chromophore diverges and can terminate in either a green or red product (through a blue intermediate), so no amount of further oxidation would result in a pure product.¹⁶⁶ Since this is only a change in the chromophore, there is no difference in the molecular weight or chemistry of the overall protein that would allow separation of these two components. However, a single amino acid mutation near the chromophore, Glu16Pro, was shown to eliminate this side reaction.¹⁶⁶

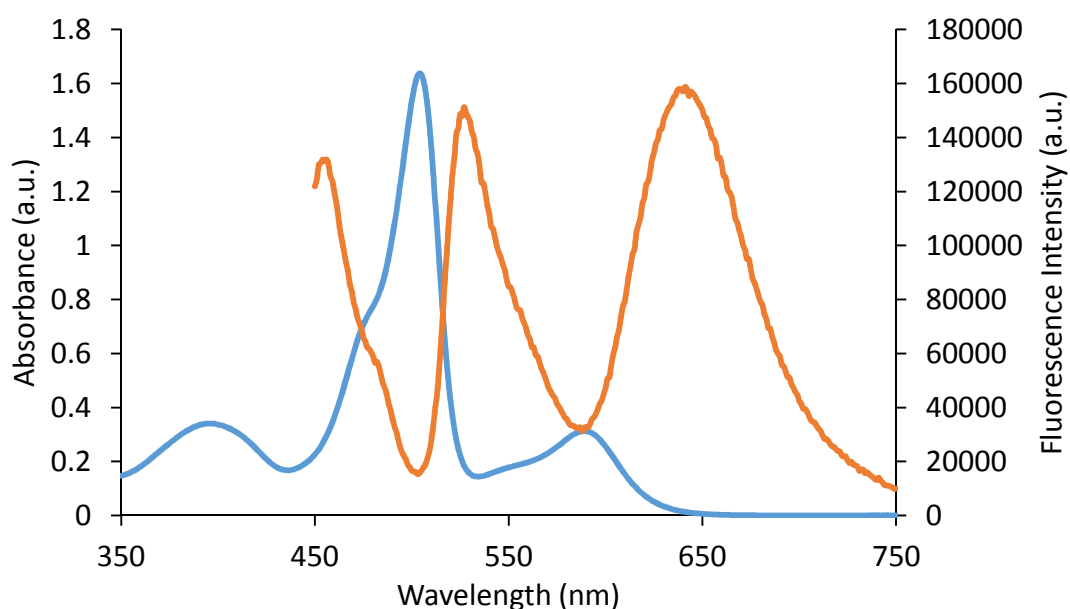


Figure 4.17 mPlum(Asp169Cys) spectra. Absorbance (blue) and fluorescence (orange) curves for expressed mPlum(Asp169Cys) protein, showing distinct peaks in the blue (460 nm), green (530 nm), and red (645 nm) regions of the emission spectrum.

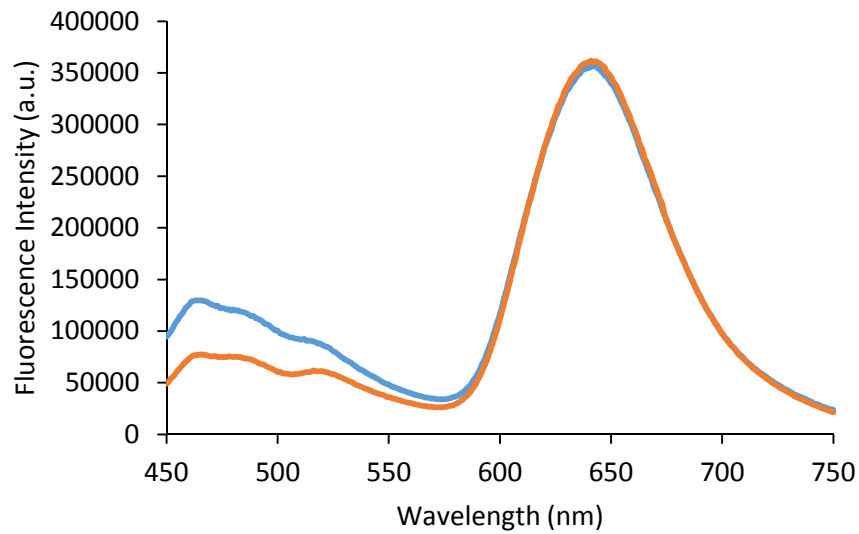


Figure 4.18 Aeration of mPlum solution reduces green product. Fluorescence spectra before (blue) and after (orange) overnight shaking in air at 4°C. Protein concentration and excitation conditions were conserved.

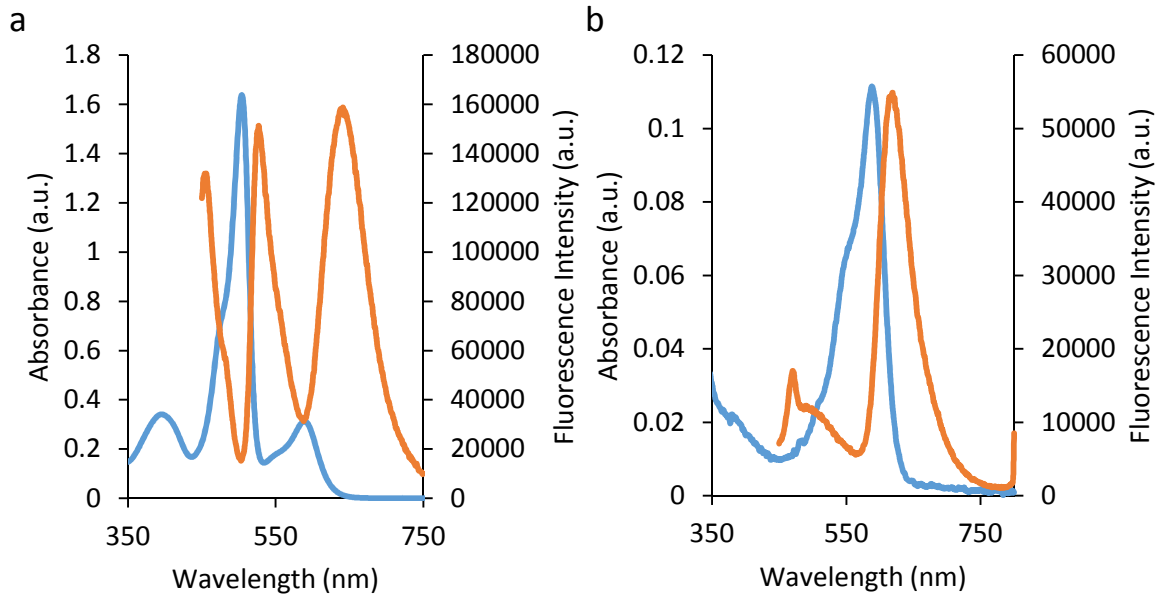


Figure 4.19 mPlum(Glu16Pro, Asp169Cys) mutant spectra show reduction in side products. (a) Absorbance (blue) and fluorescence (orange) curves for mPlum(Asp169Cys) protein, with multiple products. (b) Absorbance (blue) and fluorescence (orange) curves for mPlum(Glu16Pro, Asp169Cys) protein with predominantly red emission product.

Introduction of this second mutation proceeded similarly as above, and the protein was expressed in moderate yield. Looking at the spectra, we can see that while the side products are reduced dramatically, the green product is not eliminated entirely, and there is a slight blueshift of both spectra (Figure 4.19b). When trying to purify this construct, very little bound to a Ni-NTA column *via* the His₆ tag on the N-terminus of the protein. Because of this, it is not separable from many other cellular proteins and many bands appear in the SDS-PAGE gel (Figure 4.20). Further analysis by Western blot using anti-His₆ antibody shows none of the products contain the His₆ tag (Figure 4.20). Thus, since neither the spectra nor the purification is clean, we had to select a new protein in order to generate our FRET probe.

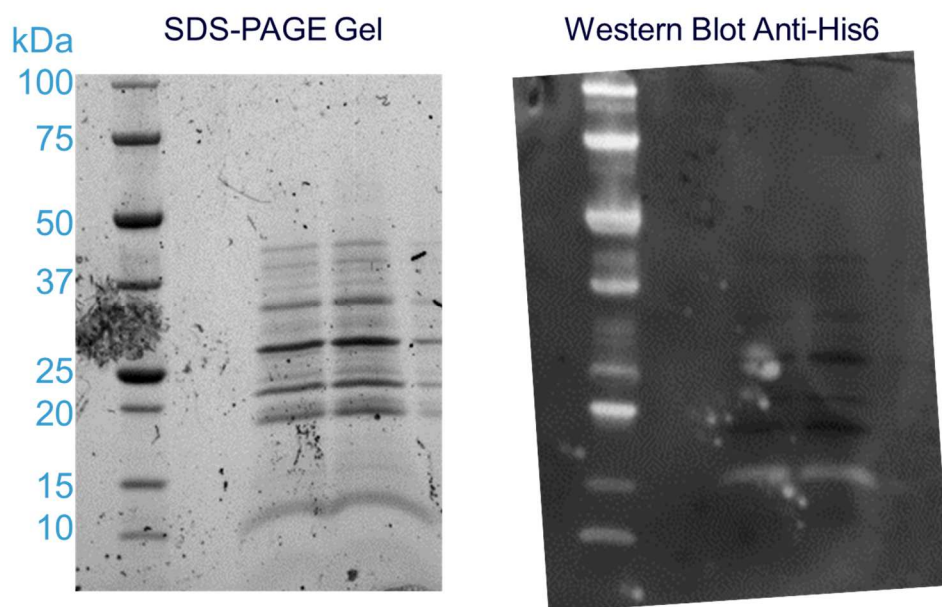


Figure 4.20 mPlum(Glu16Pro, Asp169Cys) SDS-PAGE and Western blot. Many bands in the SDS-PAGE (left) showing poor purification by Ni-NTA affinity chromatography. Western blot (right) reveals none of the high yield products contain the His₆ tag needed for isolation.

mCherry is a very well-studied and highly characterized protein from the same development line as mPlum.¹⁶⁷⁻¹⁷¹ It retains the same absorbance peak position, but its emission is not nearly as redshifted (Figure 4.21). The chromophore maturation time of mCherry is also much shorter and should present fewer issues in generating a pure product.¹⁶⁷ A single cysteine (Ser131Cys) was introduced to mCherry just as above by SDM, and several other mutations were made to improve the efficacy of the finished product: Asp132Lys to improve the reactivity of the cysteine residue, and Arg4 added at the N-terminus to aid in the uptake of the nanoparticles by endosomes. The final protein

was expressed as a fusion with SpyCatcher in high yield (Figure 4.21). The mCherry constructs express in much higher yield and are easily purified by His₆-tag and TEV cleavage to give the fusion needed as per the original design (Figure 4.4).

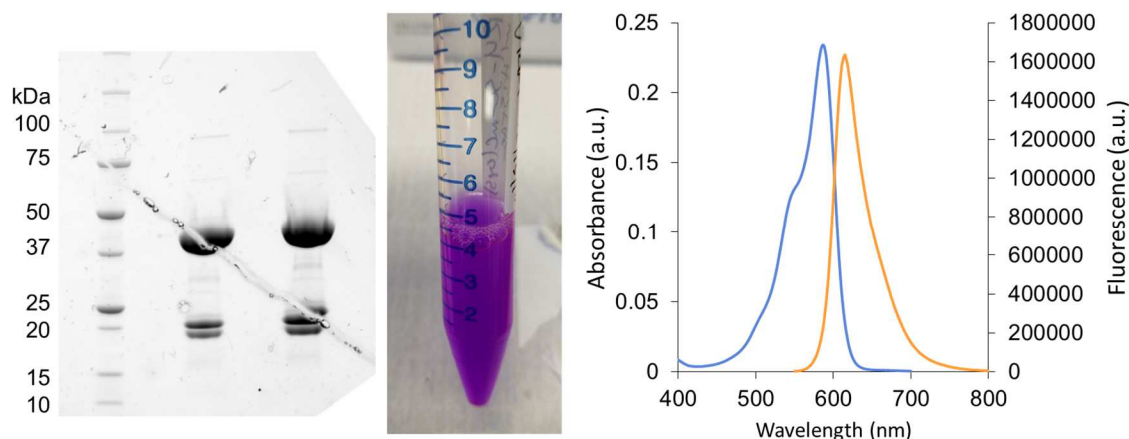


Figure 4.21 Arg4-mCherry(Ser131Cys, Asp132Lys)-SpyCatcher protein expression. Unlike mPlum, mCherry constructs are synthesized and purified in high yield. The SDS-PAGE (left) shows characteristic 3-band breakdown pattern for mCherry, and expression yield of mature purple protein (center) is much higher than mPlum. The absorption peak for mCherry (right, blue) is centered at 590 nm, and the emission peak (right, orange) has a small Stokes shift to 610 nm.

With the Arg4-mCherry(Ser131Cys, Asp132Lys)-SpyCatcher protein fusion made, we could assemble the final endocytosis product. Since we want the smallest distance between the nanocrystal and acceptor protein for maximum FRET and the highest overlap between QD emission and protein absorption, this is best achieved using 585 nm peak emission CdSe/ZnS QDs. These were encapsulated using PMAO polymer and functionalized with 1 mol% PDEA to keep the disulfide linkage close to the nanocrystal. With a simple disulfide exchange, the majority of the probe is made except for inclusion of the endosome disrupting peptide. This construct exhibits significant FRET from the QD to proteins conjugated on the surface, and the absorbance from the mCherry protein indicates there are an average of 25 proteins per nanocrystal (Figure 4.22a,b). To simulate entering the cytosol of a typical cell, this probe was subjected to a 2 mM solution of reduced glutathione in PBS buffer, causing the disulfide linkage to be cleaved. When this occurs, the FRET signal is lost and the QD brightness is restored (Figure 4.22b). This proof of concept test lays the groundwork for future *in vitro* tests under live cell imaging conditions.

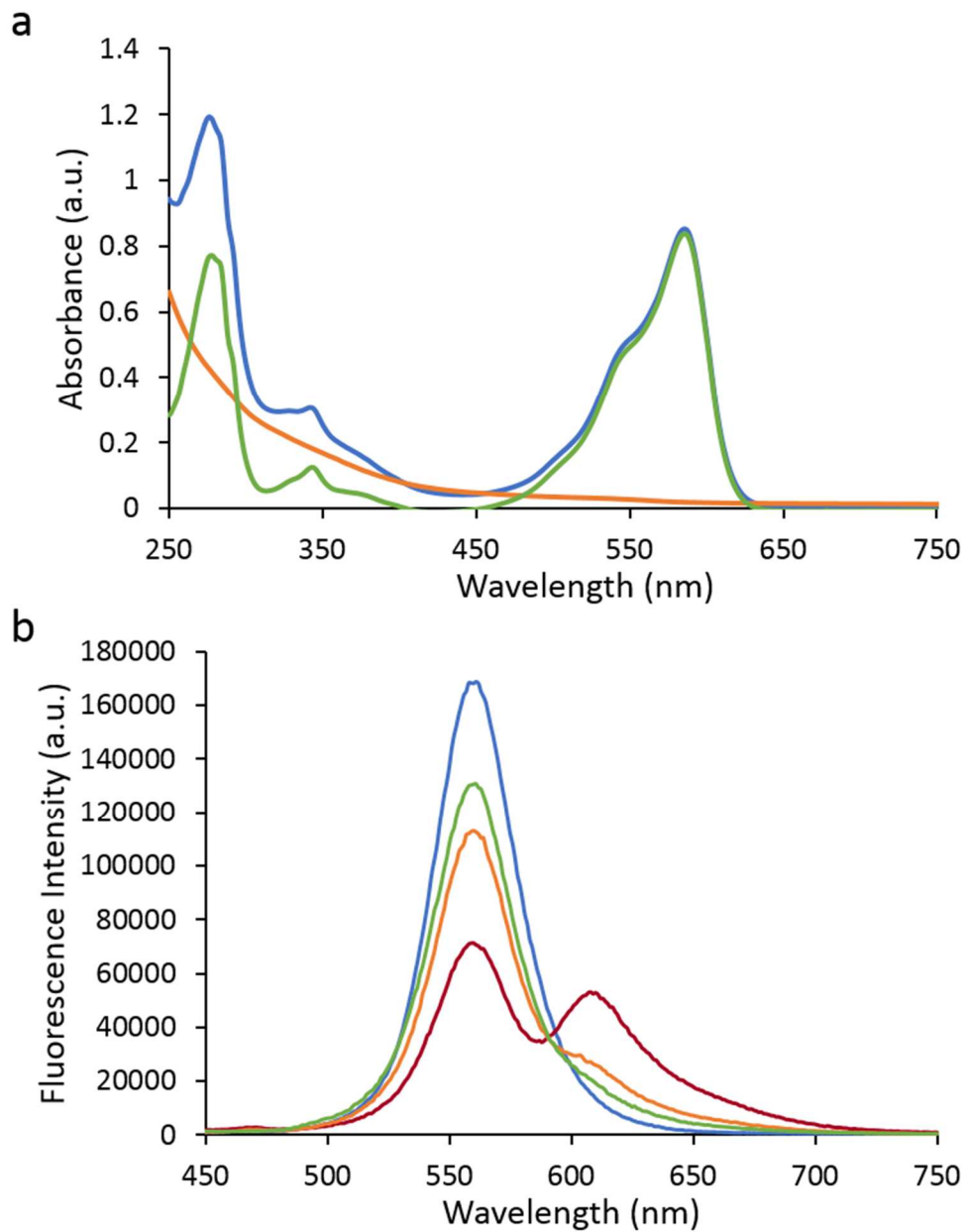


Figure 4.22 Disulfide-linked QD probe displays FRET and spectral changes under cellular reducing conditions. (a) Absorbance spectra for 560 nm QDs (orange), QD-disulfide-[Arg4-mCherry(Ser131Cys, Asp132Lys)-SpyCatcher] (blue), and the difference curve for the protein fusion (green). (b) Fluorescence emission spectra showing energy transfer from conjugation of QD (blue) to QD-disulfide-[Arg4-mCherry(Ser131Cys, Asp132Lys)-SpyCatcher] (red). Spectra after 10 min (orange) or 1 hour (green) reduction with glutathione.

4.3 Conclusions

The use of the SpyTag-SpyCatcher conjugation system represents a major shift in design for preparing nanoparticle conjugates. Through its ability for either component to be genetically-expressed and the traceless covalent linkage formed from these components, it has changed the way we think about designing surface interactions and how to incorporate biomolecules into a nanoparticle construct. Engineering of the SpyCatcher protein has allowed precise control over the placement and orientation of displayed groups, and its expressibility has led to the creation of protein fusions with unique structure and function. Novel and orthogonal peptide/protein coupling systems continue to be developed, and these may form the basis for even more complex engineering.^{114,172}

Using this system, we have created probes from antibody fragments conjugated to quantum dots for live cell labeling. While simple, this construct has been difficult to realize with the level of precision needed using other conjugation techniques. On the other end of the spectrum, the level of manipulation possible using this system has let us create complex, highly-engineered, and multifunctional probes of nanoparticle endocytosis. These constructs have unique photophysical and stimulus-responsive properties that would not be possible without the SpyTag-SpyCatcher system. For good reason, this protein has infiltrated almost all our nanoparticle conjugate designs in some way, and it has led us to expand into larger collaborations towards even more complex materials, with SpyCatcher at their core.

4.4 Materials and Methods

Chemicals and materials. CdSe/ZnS nanocrystals were purchased from Ocean Nanotech. Poly(maleic anhydride-alt-1-octadecene) (PMAO) was purchased from Polysciences, Inc. NH₂-PEG4-N₃ and NH₂-PEG3 were purchased from Aurum Pharmatech. SM(PEG)₂ was purchased from ThermoFisher. Mutagenesis kits and competent cells were purchased from New England Biolabs. Custom DNA oligos were purchased from Genscript. Plasmids were procured from Addgene, and cell lines were purchased from ATCC. All other reagents and chemicals were purchased from MilliporeSigma and used without further purification.

Site-directed mutagenesis.

PCR Amplification

A PCR amplification reaction was set up comprised of: 12.5 μ L Q5 Hot Start Hi Fidelity Master Mix, 1 μ L of template DNA to be changed (25 ng), 9 μ L MilliQ H₂O, 1.25 μ L each of the Forward and Reverse primers (see below). This mixture was PCR amplified through the following cycle:

98°C – 0:30

35 cycles of:

98°C – 0:10

66°C – 0:30

72°C – 2:50

72°C – 2:00

4°C – Hold

After PCR, agarose gel electrophoresis was used to confirm the correct size amplified product for recircularization.

Kinase, Ligase, DpnI (KLD) Digest

1 μ L of product was mixed with 5 μ L KLD Reaction buffer (NEB), 3 μ L MilliQ water, and 1 μ L 10X KLD Enzyme Mix (NEB). The mixture was incubated at room temperature for 30 minutes and transformed into NEB 5-alpha Competent *E. coli* cells.

Transformation

NEB 5-alpha Competent *E. coli* cells were thawed on ice. 5 μ L of the KLD mix were added to the cells and incubated on ice for 30 minutes. The cells were heat shocked at 42°C for 30 seconds and allowed to recover on ice for 5 minutes. 950 μ L of room temperature SOC was added into the mixture, and the cells were incubated at 37°C for 60 minutes with shaking (250 rpm). The mixture was plated on LB + ampicillin agar plates

and incubated overnight at 37°C to yield single colonies that contain the resistance plasmid.

Primers used in this work.

Mutation	Forward Sequence	Reverse Sequence
mPlum D169C	GCCACTACTGCGCCGAG GTCAAG	CGCCGTCCTTCAGC TCAGCC
R4-SpyCatcher Amplification	CGTCGGCGTCGGGCCATG GTTGATACC	GCCTGAACCTCCACCAA TATGAGCGTCACC
R4-mPlum-SpyCatcher Gibson Assembly	1: gagaacctgtacttccagggcCGT CGGCGTCGGGCCATGGTTG 2: CATATTGGTGGAGGTTT AGGCgtgagcaagggcgaggaggtc	1: CAACCATGGCCCGACGC CGACGgccctggaagtacaggttctc 2: gacctctcgcccttgctcacGCCT GAACCTCCACCAATATG
mPlum E16P	CGCTTCAAGCCGCACATG GAGG	CATGAACTCCTTGATGAC CTCCTCGC
SpyCatcher-ELP-mCherry ELP Excision	GTGAGCAAGGGCGAGGA GGAT	CTGACCCCAAATACCTTG CGGACC
mCherry S131C	CAACTTCCCCTGCGACGG CCCC	GTGCCGCGCAGCTTCACC TTGTAG
Arg4 insertion mCherry	GTCGTGGCGCCATGGTTG ATACCTTATC	GACGACGGCCCTGAAAAT ACAGGTTTTTCG
mCherry D132K	CTTCCCCTGCAAGGGCCC CGTAATG	TTGGTGCCGCGCAGCTTCACC

Recombinant protein expression. Plasmids encoding SpyCatcher or fluorescent protein variants were transformed into the *E. coli* expression cell line BL21 (DE3) (MilliporeSigma) for heterologous protein expression. Single colonies from agar plates were used to inoculate cultures of LB broth (25 mL) containing ampicillin (50 µg/mL) and grown at 37 °C overnight (250 rpm). This starter culture was then used to inoculate 2

x 500 mL LB broth containing ampicillin (50 µg/mL) at 0.05 OD600 and grown at 37 °C with shaking (250 rpm). Once cells density reached 0.4 - 0.6 (2 - 4 hr post-induction), protein expression was induced with 1 mM IPTG. Cultures were then grown 4 hours at 30 °C with shaking (250 rpm) to avoid the formation of inclusion bodies. Cells were harvested (6000 x g, 20 min, 4 °C) and the cell pellet was resuspended in 30 mL lysis buffer (20 mM Tris pH 8.0, 300 mM NaCl, 10 mM imidazole). Cell pellets were stored at -80 °C.

Recombinant protein purification. Recombinant His₆-tagged proteins were isolated *via* IMAC using a prepacked 1 mL Ni-NTA column (GE Healthcare). To remove loosely bound proteins, the column was washed with 50 mM imidazole for 20 column volumes. His₆-tagged protein was eluted utilizing a linear imidazole gradient up to 250 mM. Chromatography steps were conducted at 1 mL/min utilizing an ÄKTA Pure FPLC system (GE Healthcare).

Successful protein expression was confirmed by band shift in whole cell lysate in Laemmli buffer and 0.05% 2-mercaptoethanol on a BioRad Criterion Stain-free 4–20% SDS-PAGE. The gel was UV-activated for 2 min before imaging on a ProteinSimple FluorChem E system. As poor purification was observed for some samples, Western blot was performed for confirmation. A Bio-Rad Trans-Blot Turbo system with nitrocellulose membrane was used to transfer protein from the SDS-PAGE gel and the membrane incubated in ThermoFisher SuperBlock buffer for 1 h. The protein of interest was first labeled during a 30 min incubation with rabbit Anti-His₆ Tag polyclonal antibody (1:5000 in TBST, Tris-Buffered Saline with 0.1–0.05% Tween-20), followed by another 30 min incubation with Goat-Anti Rabbit-AlexaFluor488 (Sigma-Aldrich; 1:5000 in TBST). BioRad Precision Plus Protein Standards fluorescence was activated with Thermo-Fisher SuperSignal West Pico Chemiluminescent Substrate and imaged in chemiluminescent mode. TBST washes were performed between each incubation step.

Nanoparticle-SpyCatcher conjugation. To generate permanent QD-SpyCatcher conjugates, PAOA-encapsulated QDs (2 µM, 200 µL) in 100 mM HEPES, pH 7.8, were combined with SM(PEG)₂ (100 mM, 50 µL) in DMSO. The reaction was mixed at room temperature for 30 minutes. The mixture was diluted to 4 mL with 100 mM HEPES, pH 7.0, and excess reagents were removed by centrifugal dialysis (Amicon Ultra-4, 100 kDa MWCO), washing with 3 x 4 mL of HEPES buffer. An aliquot of SpyCatcher Ser35C protein (200 µM, 100 µL) was added to a 1.5 mL low protein-binding centrifuge tube, the QDs were added, and the reaction was mixed overnight at 4°C on a rotary mixer. The reaction mixture was diluted to 4 mL with 100 mM HEPES, pH 7.5, and excess SpyCatcher protein was removed by centrifugal dialysis (Amicon Ultra-4, 100 kDa

MWCO), washing with 4 x 4 mL of buffer. The retentate was diluted to 400 μ L in HEPES buffer, and the QD-protein conjugate was stored at 4°C.

For disulfide conjugated QD-SpyCatcher, PMAO-encapsulated QD film was taken up with 1:99 ratio of PDEA (11.14 mg, 50 μ mol) to 2-(2-(2-methoxyethoxy) ethoxy) ethylamine (818.5 μ L, 4950 μ mol) in 50 mM sodium borate, pH 8.5 and sonicated for 30 minutes at 60°C. The mixture was heated in an 80 °C water bath for 60 minutes, slowly cooled in the bath to room temperature, and then sonicated for 30 more minutes. The mixture was concentrated to 1 mL by spin dialysis (Amicon Ultra-15, 100 kDa MWCO), and excess polymer was removed by ultracentrifugation and dialysis as previously described. An aliquot of SpyCatcher Ser35C protein (200 μ M, 100 μ L) was desalted on a Biospin-6 Desalting Column (Bio-Rad) and further washed by centrifugal dialysis (Amicon Ultra-4, 3 kDa MWCO), washing with 3 x 4 mL of HEPES buffer to remove all TCEP storage buffer. The retentate was diluted to 100 μ L in a 1.5 mL low protein-binding centrifuge tube, the QDs were added, and the reaction was mixed overnight at 4°C on a rotary mixer. The reaction mixture was diluted to 4 mL with 100 mM HEPES, pH 7.5, and excess SpyCatcher protein was removed by centrifugal dialysis (Amicon Ultra-4, 100 kDa MWCO), washing with 4 x 4 mL of buffer. The retentate was diluted to 400 μ L in HEPES buffer, and the QD-disulfide-protein conjugate was stored at 4°C.

Nanoparticle-SpyCatcher characterization. To determine the size of as-synthesized nanocrystals, a dilute dispersion of nanocrystals in hexane was drop cast onto an ultrathin carbon film on lacey carbon support, 400 mesh copper TEM grid (Ted Pella) and dried in a fume hood. Images were collected on a Gemini Ultra-55 Analytical Field Emission Scanning Electron Microscope (Zeiss) in dark-field transmission mode under 30 kV accelerating voltage. Diameters for 100 random nanoparticles were manually designated in ImageJ and a distribution was plotted.

To determine the size of aqueous nanoparticles, dispersions were diluted to 20 nM in 100 mM HEPES, pH 7.8 for PAOA-encapsulated nanoparticles, and in 100 mM HEPES, pH 7.0 for PMAO-encapsulated and SpyCatcher-functionalized nanoparticles. The dispersions were sonicated for 30 minutes prior to measurement. Diameters were measured by dynamic light scattering using a Malvern Zetasizer with typical count rates of 150 kilocounts per second. Data were collected for 60 seconds each in 5 separate runs and fit using Malvern Zetasizer software to a volume-weighted size distribution of hydrodynamic diameter.

SpyCatcher calibration curve and enumeration. To confirm the presence of SpyCatcher proteins on the nanoparticle surface, fluorescence spectra were taken under

270 nm excitation prior to and after conjugation, with the difference curve showing a protein peak around 340 nm. A calibration curve was generated of known concentrations of purified SpyCatcher, and the difference curve peak was used to determine the concentration of SpyCatcher protein in the nanoparticle conjugate. A ratio made with the protein to nanoparticle concentration defined the number of proteins per nanoparticle.

SpyCatcher enumeration *via* activated disulfide exchange leaving group. To follow the disulfide exchange of SpyCatcher onto the nanoparticle surface, the absorption signature of the leaving group (pyridine-2-thione) was measured at 343 nm in a plate reader as a function of time. The concentration of pyridine-2-thione was determined from this absorbance and its extinction coefficient ($8,080 \text{ M}^{-1} \text{ cm}^{-1}$), and a ratio with the nanoparticle concentration defined the number of SpyCatcher proteins exchanged per nanoparticle.

mTurquoise-SpyTag conjugation and characterization. To confirm the activity and presence of SpyCatcher on the nanoparticle surface, an excess of SpyTag-mTurquoise fluorescent protein was added to a small sample of SpyCatcher-conjugated nanoparticles (e.g. 100 μl of 38.7 μM SpyTag-mTurquoise to 100 μl of 1 μM QD585-SpyCatcher) and incubated overnight with mixing. The excess mTurquoise was washed out with 3 x 15 mL 100 mM HEPES, pH 7.0 on a centrifugal dialysis filter (Amicon Ultra-15 100kDa pore) and taken up in 100 μl of buffer. Absorption spectra were taken prior to and after mTurquoise conjugation, showing a peak in the difference spectrum around 435 nm. The concentration of mTurquoise was determined from this absorbance and the extinction coefficient ($30,000 \text{ M}^{-1} \text{ cm}^{-1}$), and a ratio with the nanoparticle concentration defined the number of proteins per nanoparticle.

2G10 antibody conjugation and characterization. In order to generate the final QD-antibody construct, SpyCatcher-conjugated QDs (100 μl , 1 μM , 100 pmoles) and SpyTag-2G10 antibody (8.9 μl , 22.6 μM , 201 pmoles, $\sim 2\text{x}$ excess) were simply mixed overnight and used without further purification. Various ratios of antibody to nanoparticles were tested by modulating the amount of SpyTag-2G10 added. To verify the presence of antibodies on the nanoparticle surface, fluorescence spectra were taken under 270 nm excitation prior to and after conjugation, with the difference curve showing a protein peak around 340 nm. A calibration curve was generated of known concentrations of purified SpyTag-2G10, and the difference curve peak was used to determine the concentration of antibody conjugated to the nanoparticle conjugate. A ratio made with the protein to nanoparticle concentration defined the number of proteins per nanoparticle.

Cell culture. CHO-K1 cells expressing nuclear eBFP were maintained in tissue culture-treated polystyrene dishes (Corning) at 37 °C in a 5% CO₂ atmosphere in Ham's F-12 media (Sigma) containing 10% fetal bovine serum (FBS, Gibco), 1% penicillin–streptomycin solution (Life Technologies), and 100 µg/mL geneticin to maintain the eBFP expression.

MDA-MB-231 cells expressing urokinase plasminogen activation receptors (uPAR) were maintained in tissue culture-treated polystyrene dishes (Corning) at 37 °C in a 5% CO₂ atmosphere in Dulbecco's modified Eagle's medium (DMEM, Sigma) containing 10% fetal bovine serum (FBS, Gibco) and 1% penicillin–streptomycin solution (Life Technologies). Cocultures of the two cell lines were grown in DMEM containing 10% FBS, and 1% penicillin–streptomycin.

Cell antibody staining and microscopy. Cells were grown in an 8-well chamber slide to 80%+ confluency. Media was aspirated from the cells, and the wells were washed with 2 x 500 µL DMEM without phenol red. QD constructs were diluted to 10 nM concentration in DMEM without phenol red and added to the dish. Cells were incubated for 1 hour at 37°C in an incubator and washed 1 x with 500 µL PBS + 10 mM glucose. The cells were then incubated in a 5 µg/mL solution of AlexaFluor488-WGA (ThermoFisher) in PBS + glucose at room temperature for 10 minutes, and they were then washed 3 times with 500 µL PBS + glucose. Fresh PBS + glucose was added, and the cells were imaged by confocal microscopy.

Confocal images of the focal plane at the chamber interface were obtained using an inverted Zeiss LSM710 system with a 1.4 N.A. 63x Apochromat oil immersion objective. QD emission was excited using a 405 nm diode laser with an MBS-458/514 main dichroic beam splitter, and emission was collected from 605 – 690 nm. AlexaFluor488 signal at the cell membrane was excited with a 488 nm diode laser with an MBS-488/594 main dichroic beam splitter, and emission was collected from 495 – 575 nm.

5 | Building Hybrid Materials through Nanocrystal S-layer Interactions²

² Portions of this work were completed in collaboration with others: Dr. Francesca Manea, who performed the S-layer protein engineering and imaging, Dr. Nick Borys, who performed the lifetime measurements, and Dr. Dong Li who performed the cell binding studies, AFM measurements, and confocal microscopy.

5.1 Introduction

When considering the design of a nanoparticle conjugate, we often only study how to affix a certain molecule or biological component to the nanocrystal surface. But a defining feature of nanoparticle probes over a molecular dye, for example, is its multivalency – there are many points of attachment instead of the single functional site found in a molecule. While this can often act as a detriment to the final product through interactions between conjugated groups, changes in affinity or potentiation, or disruption of the colloidal stability, it also provides another facet of design to think about structures beyond two-component, binary systems.

Arranging nanoparticles in two dimensions gives rise to patterned materials with a range of applications ranging from nanoelectronics and optics^{173,174} to biochemical sensing.^{175,176} To precisely pattern nanoparticles in 2D, bottom-up approaches using self-assembling biological molecules such as DNA and proteins offer a scalable route under mild conditions. For example, DNA origami has been used to scaffold nanoparticles into arrays or wires at interparticle distances to allow modulation of optical properties of adjacent nanocrystals.^{177–179} This precise interparticle spacing has been difficult to achieve due to either inefficient bioconjugation of large, slowly-diffusing components or quantitative bioconjugation that disrupts the underlying scaffold. Inefficiencies in self-assembly become more problematic as the complexity of the material increases, as decreases in yield are compounded with each modification. Proteins are also promising scaffolds for the development of hierarchical nanomaterials as they can be engineered with angstrom precision and self-assemble into robust, complex architectures.^{180–182} However, the lack of control surrounding the assembly interaction between nanoparticles and proteins,¹⁸³ the poor ability to exploit the intrinsic structural capabilities within protein assemblies,⁹ and limited engineering strategies to create a material densely arrayed with nanomaterials have hindered progress.

Many bacteria and archaea contain a surface monolayer of highly ordered proteins or glycoproteins as their outermost cell envelope. This so-called S-layer is built *via* self-assembly of protein monomers as a two-dimensional crystalline array on the outer membrane which encapsulates the whole cell surface.^{184,185} Their controllable assembly into crystalline arrays,¹⁸⁶ well-defined lattice dimensions, and robust construction across a range of pH and temperatures make S-layers an attractive nanoparticle scaffold (Figure 5.1).¹⁸⁷ S-layers form 2D crystals rather than 3D crystals which limits X-ray crystallography and atomic resolution structures, which has hindered more complex design. Specifically, while certain S-layers have been engineered with a single nanoparticle attachment site^{188–190} they have not been explored for the simultaneous display of multiple nanomaterials. We have utilized the atomic resolution structure¹⁹¹ of

SbsB, the S-layer protein from a thermophilic bacterium *Geobacillus stearothermophilus*,¹⁹² to identify locations amenable to modification and conjugation for simultaneous display of multiple nanoparticles.

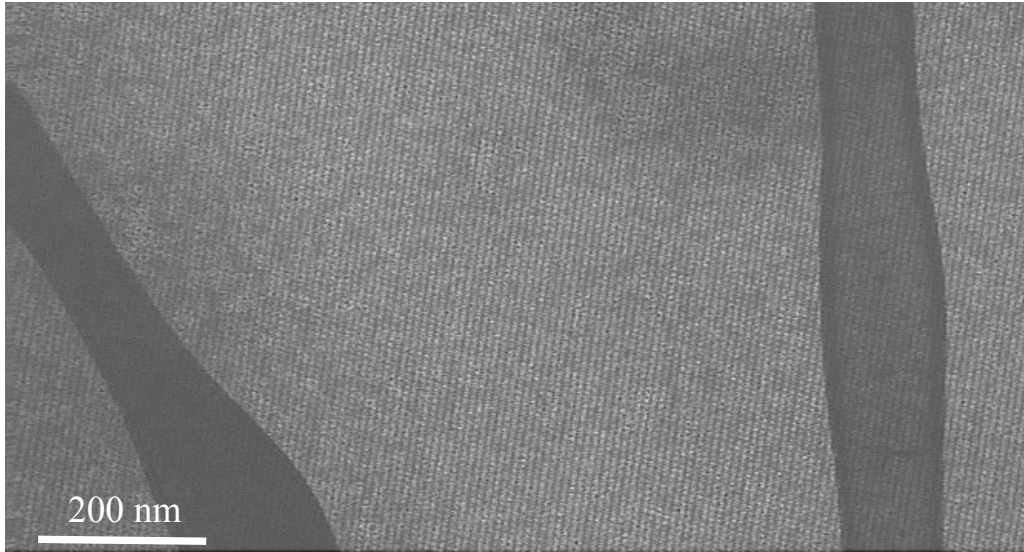


Figure 5.1 2D crystalline array of S-layer protein visualized by STEM. STEM image of a SbsB protein nanosheet, showing crystalline rows of protein monomers. Sheets can reach many microns in lateral size while just one monomer thick.

We need not be limited to the 2D crystalline morphology of S-layer sheets in solution, however. In nature, capabilities such as stimulus responsive porosity or toughness are bestowed by living organisms that control the assembly of nanoscale functional building blocks in a biocomposite.^{193,194} Engineered versions of these materials are a growing sector of research for their ability to combine the strengths of living and designed materials.^{195,196} For these engineered living materials (ELMs), the living component provides the ability to sense, adapt, and grow, while the incorporation of a non-living component expands the physical or chemical properties.^{195,197} To this end, S-layer engineering may be the pathway to achieve precise control of hybrid material properties through the incorporation of engineered nanomaterials. Depending on the species, an organism's S-layer can demonstrate unique symmetry and unit cell dimensions, with a variety of functional groups exposed in a precise repetitive manner.^{198–201} Previous efforts have already identified and manipulated S-layer proteins as templates for drug delivery, catalytic reactions, separations, and bio-sensing.^{186,188,202–211}

Caulobacter crescentus is the most genetically tractable microorganism known to possess an S-layer, and is known for forming well-ordered biofilms.^{202,212} Its S-layer

protein, RsaA, oligomerizes in the presence of Ca^{2+} into a hexameric unit that self-assembles into a two-dimensional array with 22 nm lattice spacing (Figure 5.2).^{213–215} Recent studies have identified several permissive sites for peptide insertion that do not affect RsaA self-assembly, and this allows the potential use of RsaA for biomolecular interactions and selective conjugation.^{205,216} Using the SpyCatcher attachment system developed previously, we have designed a new hybrid material comprised of nanoparticles bound to these cell membrane proteins into a synthetic biofilm (Figure 5.2). Inclusion of this inorganic component allows for tuning of mechanical or stimulus-responsive properties of the hybrid material.

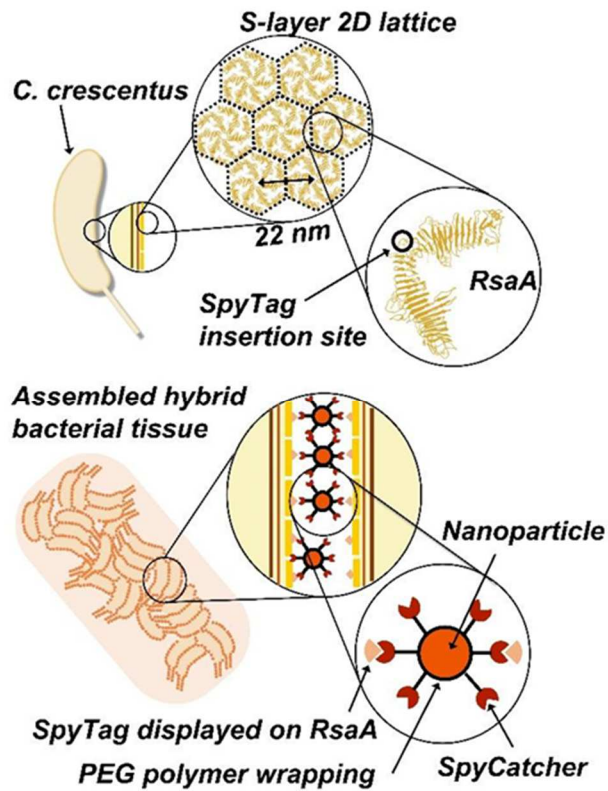


Figure 5.2 Schematic of hierarchically-ordered cell-nanoparticle hybrid material. Engineered S-layer protein RsaA of *C. crescentus* displays SpyTag peptide that covalently reacts with SpyCatcher-functionalized nanoparticles to form supracellular assemblies with enhanced mechanical properties.

Here we describe the fabrication of a new class of hybrid 2D materials comprising self-assembling protein which scaffolds plasmonically-coupled nanoparticles. This avenue is modular with respect to dimensionality and composition of the protein building

block and interparticle distances that allow energy transfer between conjugated nanoparticles. These hybrid composites allow the tailorable deposition of densely arrayed single or double species of nanoparticles through the use of protein engineering tools and protein conjugation systems. Using this, we have shown a decrease in the lifetime for quantum dots (QDs) when colocalized with gold nanoparticles (Au NPs) on the nanosheet from plasmon transfer. Taking advantage of the unique properties of *C. crescentus* and its S-layer proteins, we also report hierarchically-ordered, biotic-abiotic hybrid structures developed through engineered nanoparticle patterning and intracellular crosslinking that imparts functions like improved mechanical stiffness or magnetism in the hybrid material.

5.2 Results and Discussion

5.2.1 Engineered S-layers for binding Au nanoparticles

In the development of nanoparticle patterning, we sought a means to accurately position two different types of nanoparticles on an S-layer nanosheet. To first create S-layers that bound metallic nanoparticles, we took advantage of the ability of Au NPs to form bonds with thiols,²⁴⁻²⁶ and we introduced a cluster of cysteine residues in the SbsB monomer to produce a region for localized Au NP binding. By examining the SbsB crystal structure¹⁹¹ and identifying solvent-exposed side chains in the lattice,²¹⁷ four amino acids positioned on the surface of SbsB were chosen for mutation. The mutated residues are clustered above the intramonomer pore and were located within a 100 Å² area, where the thiol side chains would be exposed to the bulk solution. STEM and interference reflection microscopy (IRM) of engineered SbsB sheets show that modified sheets are typically rectangular ranging from 1-10 μm in length, similar to wild-type sheets (Figure 5.3). Furthermore, the nanoscale lattice dimensions of Cys-containing SbsB sheets are indistinguishable from non-engineered sheets (Figure 5.3). These observations indicate that the incorporation of the cysteine cluster does not impede SbsB crystallization or sheet formation.

To probe metallic nanoparticle binding, we incubated unmodified sheets or Cys-containing sheets with 5 nm citrate-coated Au NPs overnight with gentle rocking at room temperature. To ensure nanocrystals on the nanosheet surface were conjugated *via* thiol interactions, sheets were washed to remove excess, unbound particles. The surface of native SbsB nanosheets did not bind Au NPs, indicating low nonspecific interactions between Au NPs and the SbsB protein (Figure 5.4B). SbsB monomers that contain the incorporated Cys cluster were found to generate nanosheets that bind Au NPs (Figure 5.4C) with an overall binding site coverage of 5%. This demonstration shows that our cysteine cluster can bind metallic nanoparticles, but the efficiency of binding is insufficient to uniformly cover the nanosheet.

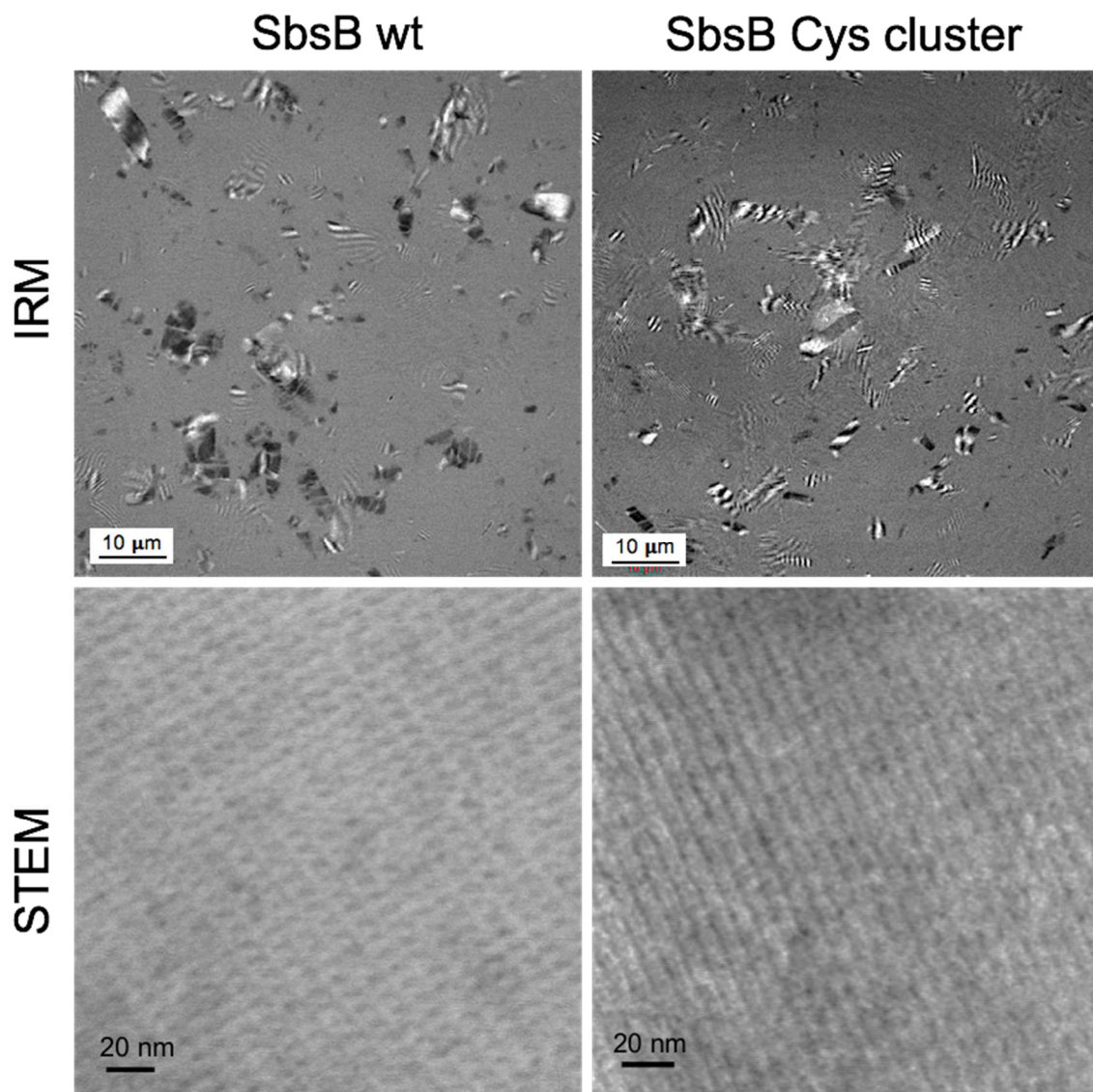


Figure 5.3 Visualization of recombinant SbsB and SbsB Cys cluster constructs. Interference reflectance microscopy (IRM) images illustrate micron-scale nanosheets, while STEM images show the nanoscale oblique array, typical for SbsB.

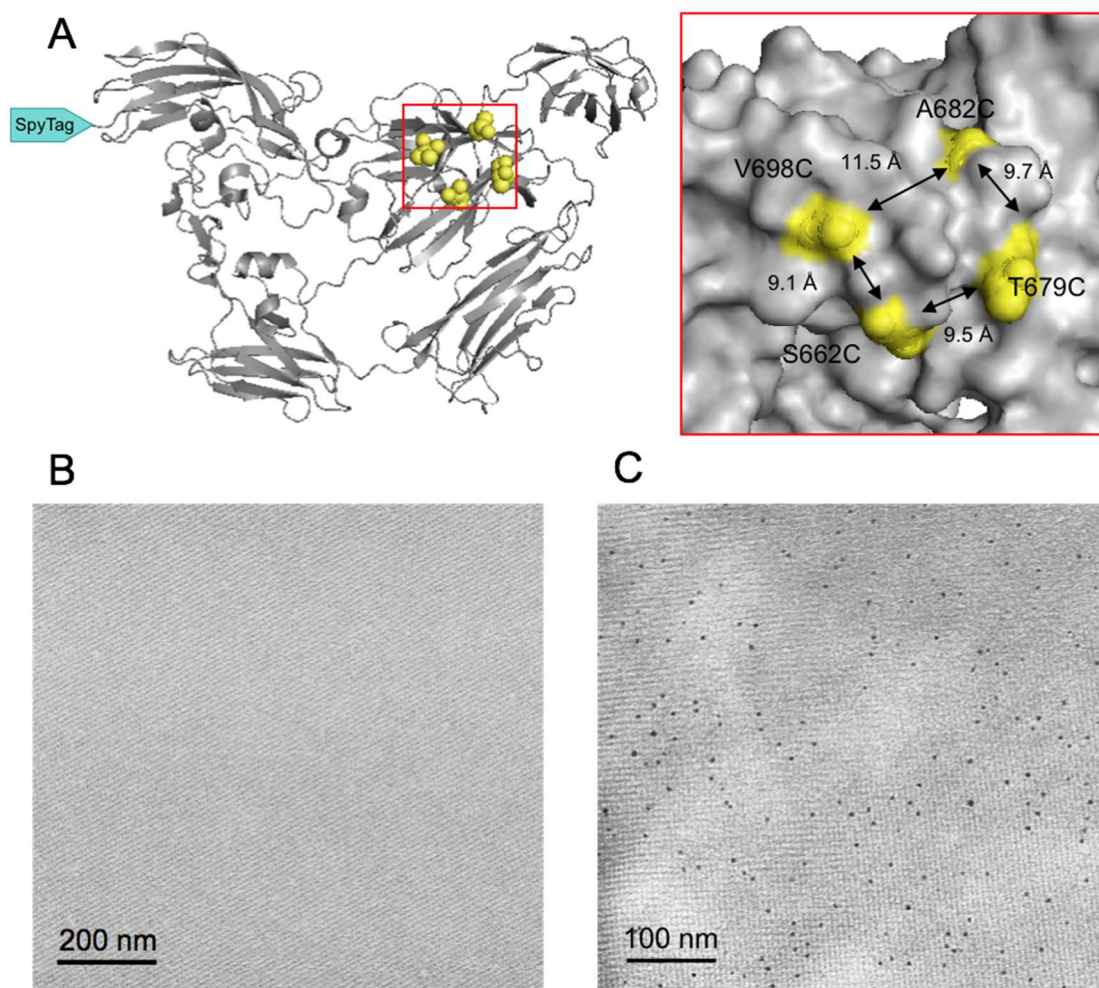


Figure 5.4 SbsB sheets containing metal-binding Cys residues bind Au NPs. (A) Cartoon depiction of SbsB crystal structure illustrating two key areas of embellishment; the C-terminal SpyTag (green) and the Cys cluster (red box). Residues that were mutated to Cys are highlighted in yellow and shown as spheres. Insert shows zoomed in surface of SbsB region containing the cysteine cluster. Changed residues are labelled and inter-Cys residue distances are shown. STEM images of wild type SbsB sheets (B) showing no nanoparticle conjugation and SbsB sheets embellished with cysteine residues (C) with 5 nm Au NPs bound.

5.2.2 S-layers incorporating protein-coupling tags can bind a versatile set of nanoparticles

To improve upon the conjugation efficiency of nanoparticles to nanosheets, we examined whether the protein-peptide coupling pairs, SpyTag/SpyCatcher,¹¹³ and an orthogonal protein-peptide coupling system, SnoopTag/SnoopCatcher,¹¹⁴ could conjugate nanoparticles to SbsB arrays more effectively. Here, we examined whether the nanoparticle size, nanoparticle surface chemistry, or protein-coupling tag type would affect nanosheet coverage. We chose the unstructured C-terminus of SbsB for SpyTag peptide insertion since we had previously utilized it as a site for embellishment amenable to modification,²¹⁸ and the SbsB crystal structure indicates the C-terminus is solvent exposed on the outward facing surface.¹⁹¹ The SbsB C-SpyTag construct displays the same expression and purification yield as wild type SbsB, and highly-ordered sheets are observed by STEM as for the wild type sheets, indicating the 13 amino acid peptide addition does not hinder self-assembly.

Next, we probed whether the SpyTag/SpyCatcher system could enable high-density attachment of inorganic nanocrystals. We examined the covalent attachment of semiconductor quantum dots (QDs)¹ and lanthanide-doped NaYF₄ upconverting nanoparticles (UCNPs)⁷ onto our nanosheets. In order to maintain colloidal stability and resistance to aggregation in aqueous media, both types of hydrophobic nanocrystals were first encapsulated in amphiphilic copolymer layers.^{58,59,219} A single cysteine mutant, SpyCatcher Ser35Cys, was expressed for conjugation to the nanocrystal polymer surface as previously discussed through heterobifunctional crosslinkers or activated disulfide exchange (Figure 5.5).

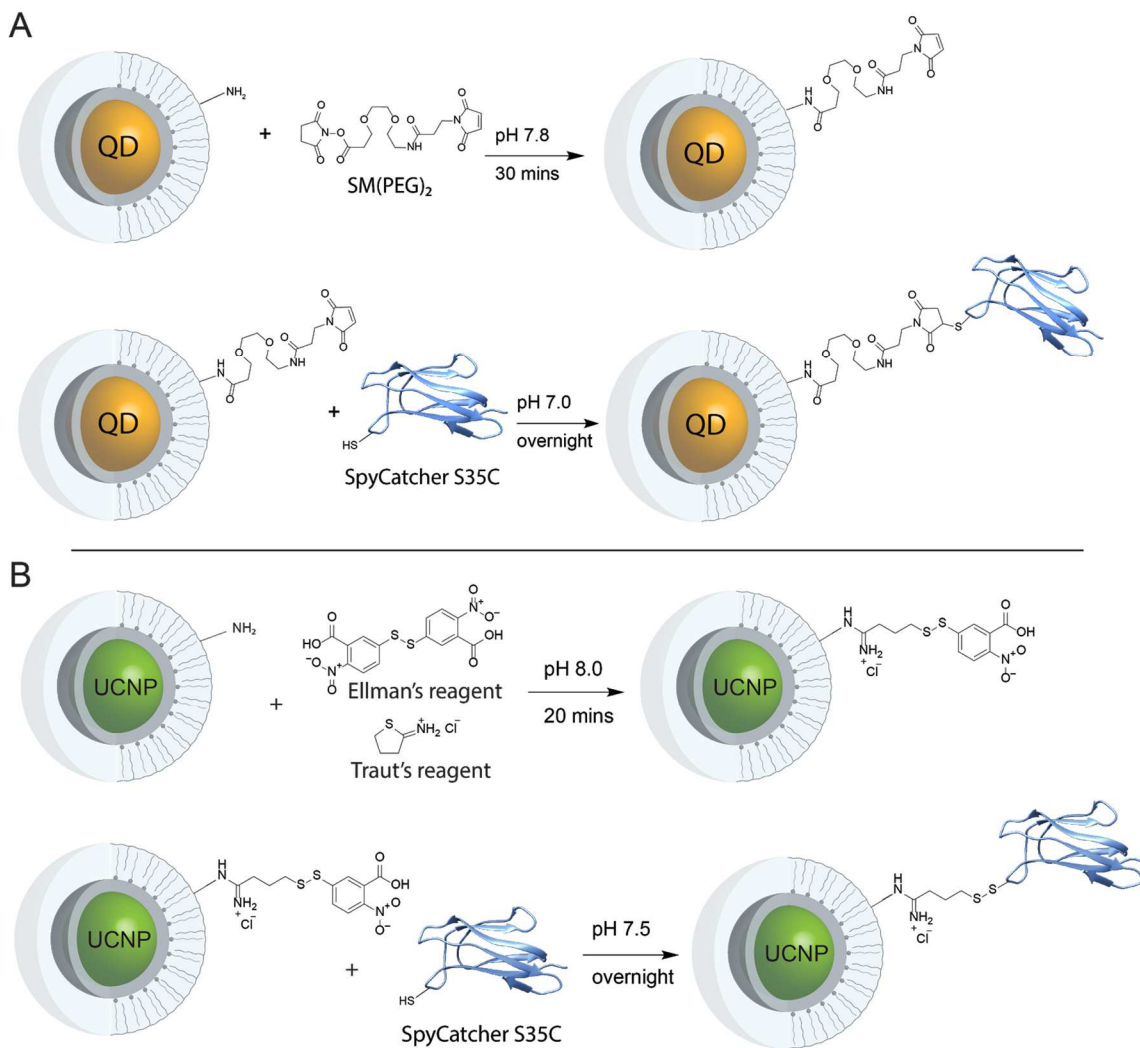


Figure 5.5 Conjugation of SpyCatcher protein to nanoparticles. Two-step conjugation of cysteine-modified SpyCatcher S35C protein to (A) PAOA-encapsulated QDs through a succinimidyl ester-PEG₂-maleimide heterobifunctional crosslinker and (B) POA-encapsulated UCNPs through generation of an activated disulfide and subsequent disulfide exchange.

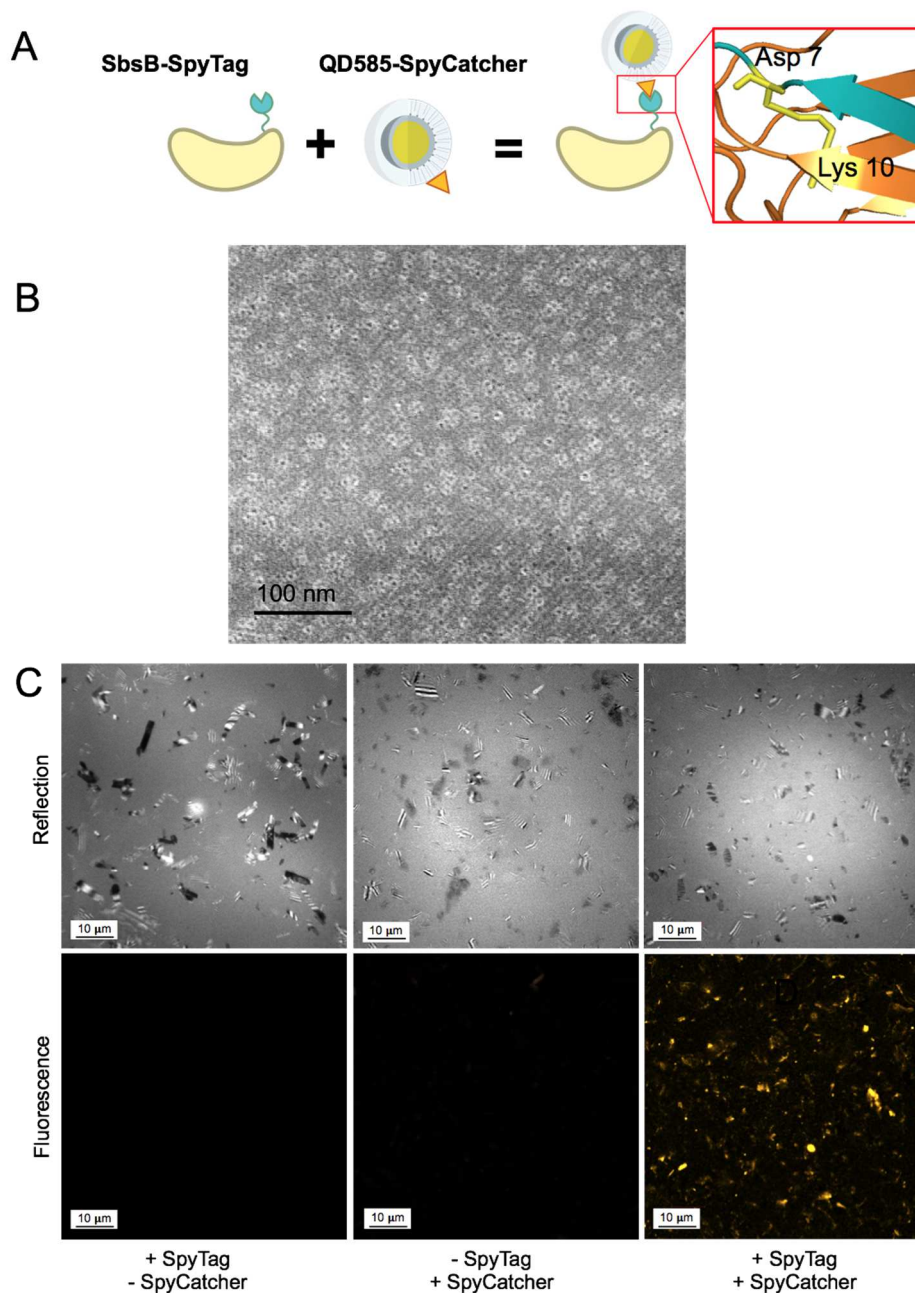


Figure 5.6 SbsB nanosheets can display semiconductor quantum dots at high occupancy while preserving their optical properties *via* SpyTag/Catcher conjugation. (A) Cartoon depicting coupling of SbsB-SpyTag to SpyCatcher-coated QDs. (B) STEM image of QD-SpyCatcher conjugated to SbsB-SpyTag nanosheets. (C) Confocal microscopy images of SbsB sheets displaying QDs. IRM images (top) showing SbsB sheets, with or without SpyTag, in the absence and presence of QD-SpyCatcher, respectively. The corresponding fluorescence images (bottom) show yellow fluorescence due to the selective conjugation of QD-SpyCatcher upon excitation at 405 nm.

The SpyCatcher-functionalized QDs were incubated with SbsB C-SpyTag sheets (Figure 5.6A) for covalent attachment and imaged by STEM and confocal microscopy. Nanoparticle-conjugated SpyCatcher maintained its affinity for SpyTag, resulting in specific conjugation to tagged SbsB nanosheets. QDs were readily visualized bound to nanosheets *via* STEM (Figure 5.6B), with a calculated sheet coverage of 18%, which is significantly higher compared to those conjugated *via* thiol sidechains. When QD-conjugated sheets were probed at 405 nm, we could clearly see emission localized to sheets (Figure 5.6C). This indicates the QDs maintain their functionality when bound to SbsB nanosheets, giving a characteristic emission peak at 585 nm (Figure 5.7).

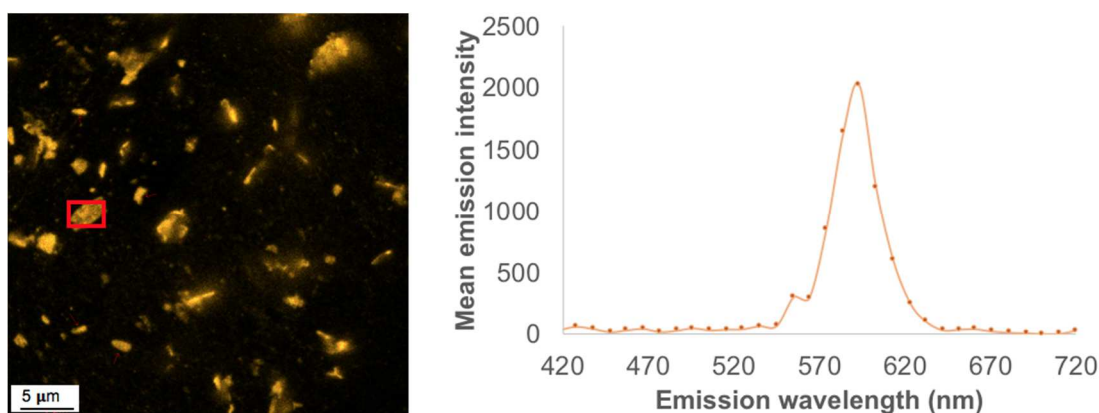


Figure 5.7 Emission of QD-SpyCatcher conjugated to SbsB C-SpyTag. Typical fluorescence image (left) of QDs localized to SbsB nanosheets. Emission profile (right) is shown for the boxed red region in the fluorescence image. An emission peak at 585 nm indicates the fluorescence signal observed is due to bound QDs.

A second protein-coupling tool, SnoopTag/SnoopCatcher,¹¹⁴ was investigated for its amenability to nanoparticle attachment and to probe whether the Spy and Snoop systems can be used orthogonally within an SbsB nanosheet, using inorganic nanoparticles. SnoopTag was inserted into the C-terminus of SbsB as previously outlined using SpyTag and incubated with SnoopCatcher-conjugated nanoparticles (Figure 5.8A). As seen with SpyTag incorporation, SnoopTag had no effect on the nanoscale lattice dimensions of SbsB, nor on the micron sized sheets. SnoopCatcher conjugated to UCNPs of different sizes was successfully bound to SnoopTag embellished nanosheets *via* isopeptide bond formation (Figure 5.8B,C).

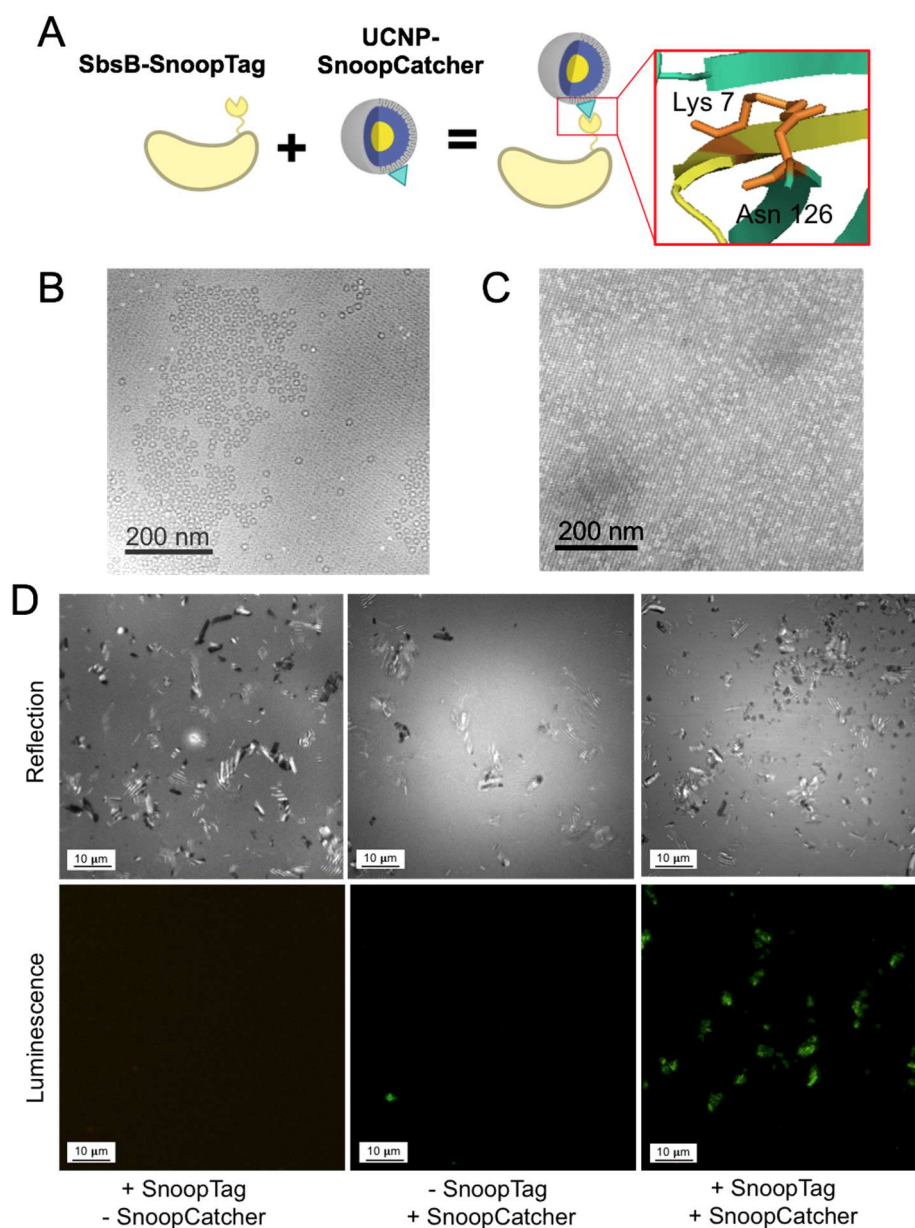


Figure 5.8 SbsB nanosheets display ceramic, upconverting nanoparticles at high occupancy while preserving their optical properties *via* SnoopTag/Catcher conjugation. A) Cartoon depicting protein coupling between SbsB-SnoopTag and UCNP-SnoopCatcher. STEM images of SbsB-SnoopTag nanosheets coupled to SnoopCatcher-conjugated 8 nm NaYF₄ (B) and 5 nm NaGdF₄ (C) UCNP. (D) Visualization of SbsB sheets bound with 8 nm NaYF₄ UCNP by confocal microscopy. IRM images (top) show SbsB sheets, with or without SnoopTag, in the absence and presence of UCNP-SnoopCatcher, respectively. The corresponding luminescence images (bottom) indicate selective conjugation of UCNP-SnoopCatcher upon excitation at 980 nm.

In addition, we found QD attachment to SbsB C-SnoopTag sheets to be similar to SbsB C-SpyTag sheets, with coverage increasing marginally from 18 to 22 %. However, SnoopCatcher-conjugated UCNPs show significantly higher attachment to nanosheets compared to their SpyCatcher counterparts. STEM images reveal uniform nanoparticle conjugation to sheets for both 8 nm NaYF₄ UCNPs and 5 nm NaGdF₄ UCNPs each doped with 20% Yb³⁺ and 2% Er³⁺ (Figure 5.8B, C). Furthermore, when excited by 980 nm light, high-occupancy bound UCNPs displayed characteristic upconversion luminescence from the dopant ions, with peaks around 540, 560, and 660 nm (Figure 5.9). Emission was localized to SbsB C-SnoopTag sheets, indicating these nanoparticles remain functional when conjugated to SbsB nanosheets *via* covalent attachment with SnoopCatcher (Figure 5.8D). The use of protein-coupling reactions to bind a range of nanoparticles demonstrates the high selectivity and programmability of these systems, which has not previously been explored for conjugation to S-layers.

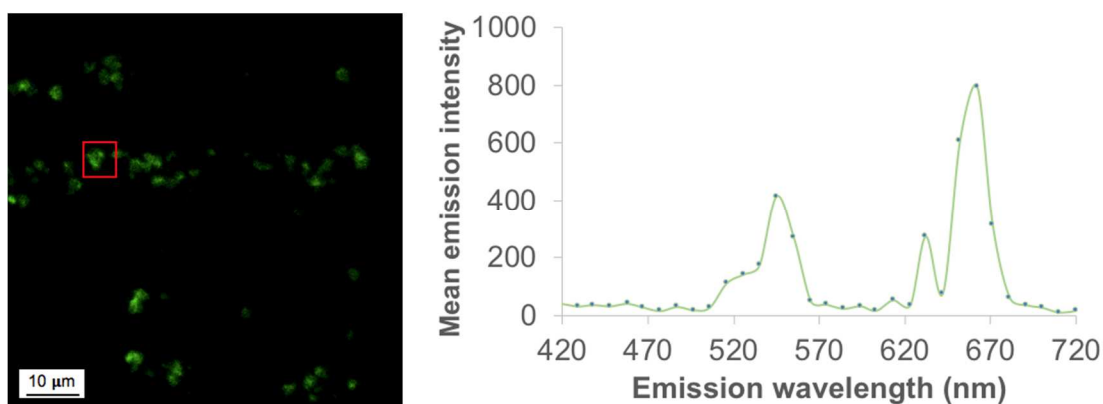


Figure 5.9 Emission of NaGdF₄-SnoopCatcher bound to SbsB C-SnoopTag. Typical luminescence image (left) of doped NaGdF₄ UCNPs localized to SbsB nanosheets. Emission profile (right) is shown for the boxed red region in the image. Emission peaks at 525, 545, and 660 nm are Er³⁺ emission from bound UCNPs.

Taken together, these experiments provide information on how nanoparticle coverage across modified SbsB sheets varies with conjugation method, protein coupling system, nanoparticle composition, and nanoparticle size (Figure 5.10). We found that thiol chemistry *via* Cys residues was the least effective route for nanoparticle conjugation. The SnoopTag/Catcher protein coupling system displayed increased coverage of nanoparticles compared to its SpyTag/Catcher counterpart. Strikingly, the coverage of NaYF₄ UCNPs increased from 2.5 % for the Spy system to dense 30.5 % for the Snoop system. While not as dramatic, a 7 % increase in coverage was observed for NaGdF₄ UCNPs when coupling was switched from the Spy system to Snoop system. Overall, these results show one of the major determinants of coupling efficiency is the

type of covalent linkage, with the covalent protein coupling systems increasing sheet coverage of nanoparticles by six-fold to ~ 30 % compared to using reactive sidechains.

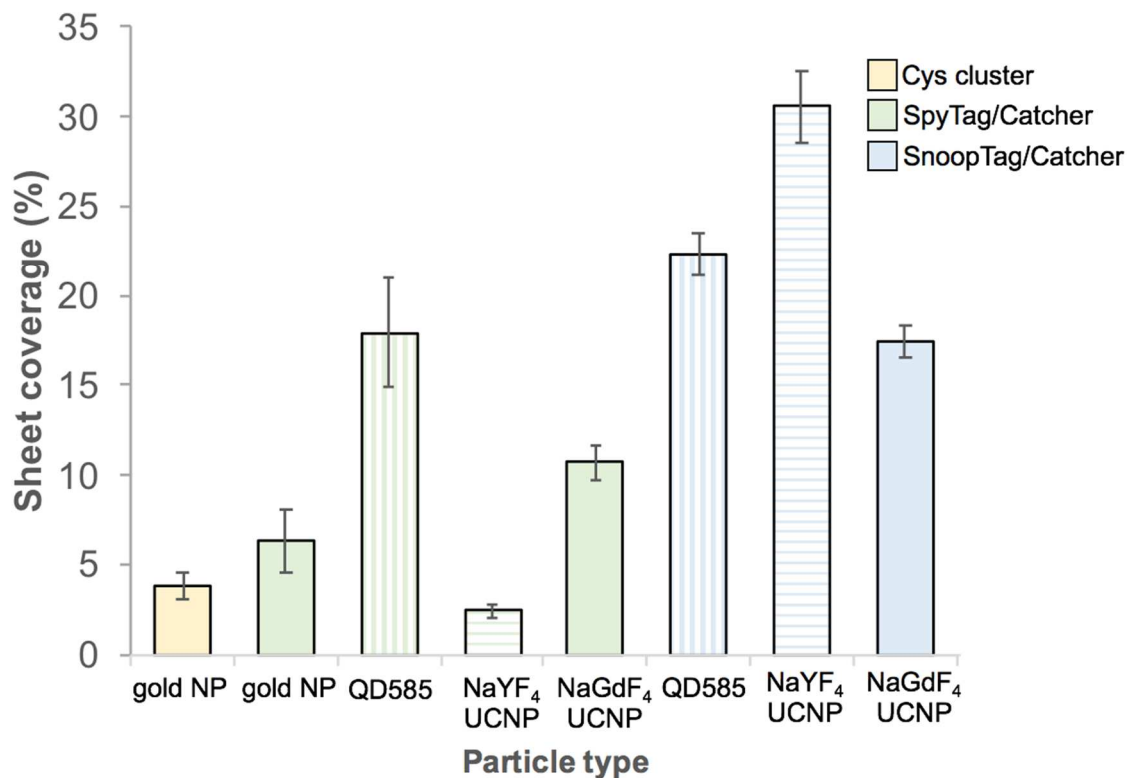


Figure 5.10 Isopeptide conjugation allows high-occupancy, multicomponent display of nanoparticles through SbsB nanosheet scaffolds. Samples are color coordinated in respect to the conjugation method used for attachment to the sheet. Particle diameter is indicated by pattern, wherein 5 nm is solid, 11 nm are vertical lines and 16 nm are horizontal lines. Error bars are \pm one standard deviation from the mean.

We observe that in particular, UCNPs have the tendency to cluster across the nanosheet. Since these wrapped particles display a strongly positive surface, it is likely that the clusters are small aggregates that arise due to pH effects. In this case, there may be nanoparticles that are not forming interactions with the underlying SbsB scaffold itself, but rather with its neighboring nanoparticle.

5.2.3 Dual modified S-layers can yield nanosheets bearing two nanoparticle types at high occupancy

To fabricate dually-embellished SbsB, several regions within the monomer were probed for the simultaneous incorporation of reactive sidechains or conjugation tags. Based on our previous work, we targeted two loop regions in addition to the C-terminus (Figure 5.11). The first loop lies between the sugar-binding domain and crystallization domain of SbsB and is referred to as the ‘mid’ loop. The second modified loop spans the inter-monomer pore and is referred to as the ‘pore’ loop.

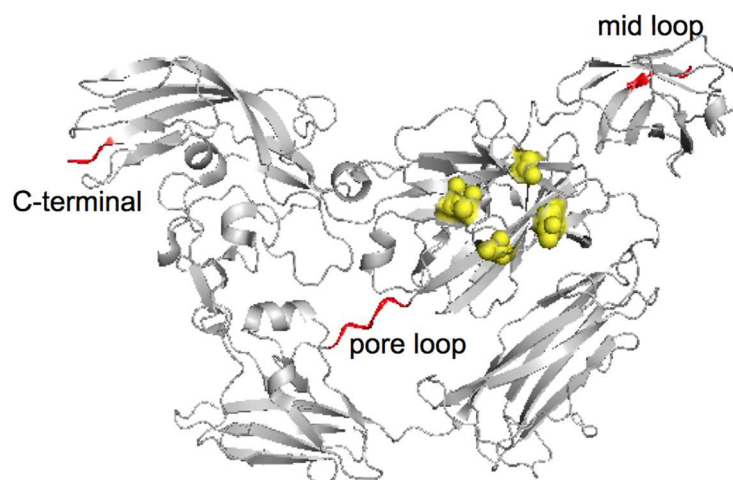


Figure 5.11 Cartoon of SbsB crystal structure depicting sites of embellishment for nanoparticle binding or conjugation. Targeted mid and pore loops and the C-terminus for SpyTag/SnoopTag incorporation are labelled and highlighted in red. Residues selected for Cys incorporation are shown as yellow spheres.

All modifications, including dual tagged constructs, result in crystalline nanosheets identical to wild type sheets upon the addition of 10 mM Ca^{2+} , as previously described.²¹⁸ Two dual modified full-length SbsB variants were investigated to determine their ability to selectively bind two distinct nanoparticles: i) SbsB mid loop (ML) SpyTag, C-terminal SnoopTag and ii) SbsB Cys cluster, C-terminal SpyTag. For each of these constructs, the dual tagged SbsB sheets displayed the capacity to bind two distinct nanoparticles (Figure 5.12A,D).

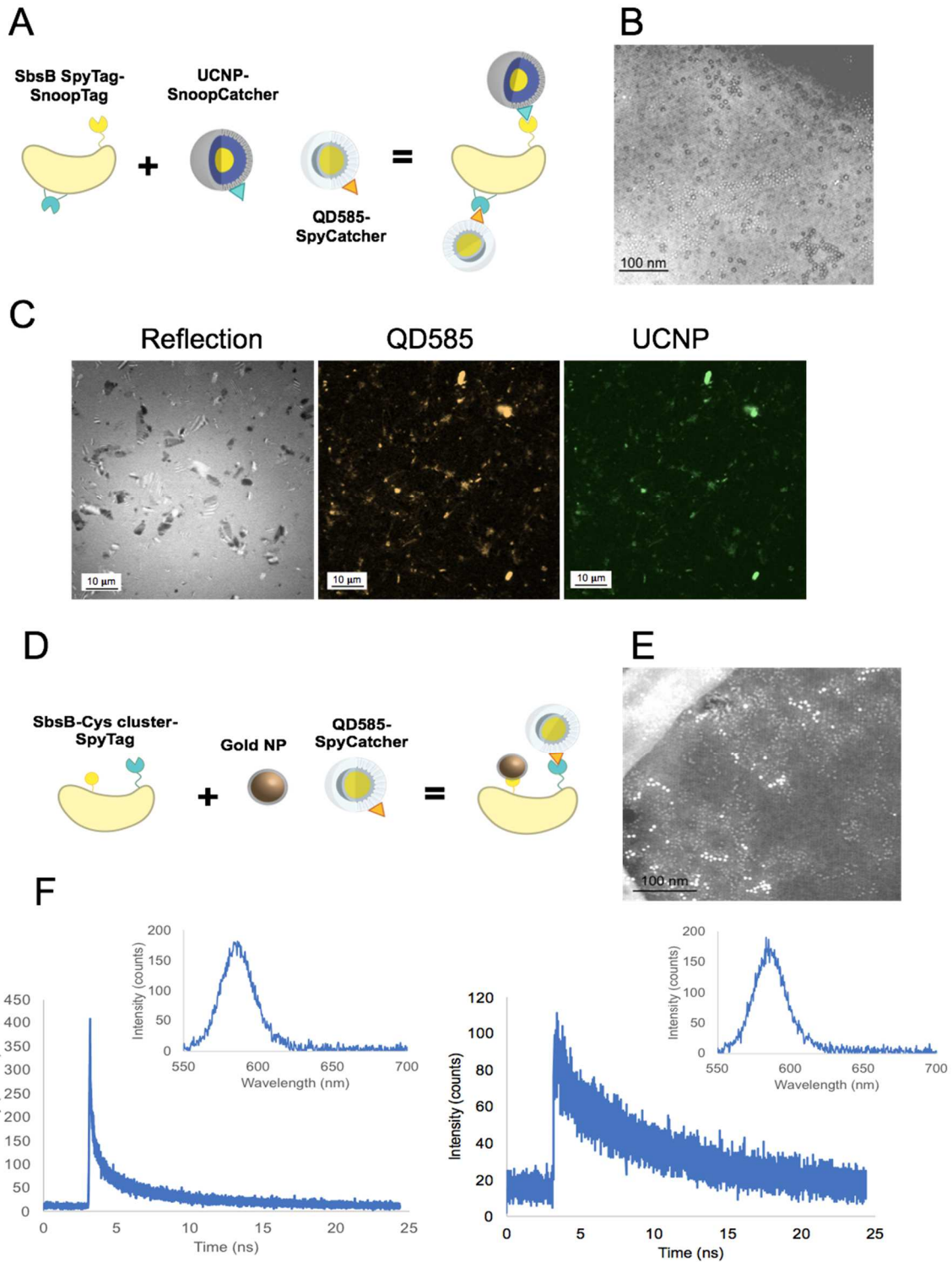


Figure 5.12 Dual modified S-layer nanosheets can localize two types of nanocrystals at distinct locations and display plasmonic properties. (A) Schematic of dual engineered SbsB system, containing both SpyTag and SnoopTag for protein coupling. (B) STEM image of SpyTAG/SnoopTag embellished SbsB sheets conjugated to both UCNPs and QDs under elevated salt conditions (500 mM NaCl). (C) Visualization of SbsB sheets bound with UCNP and QDs by confocal microscopy, displaying emission behavior expected for bound QDs and UCNPs. (D) Schematic of dual engineered SbsB system, containing a Cys cluster for thiol chemistry and SpyTag for protein coupling. (E) STEM image of Cys and SpyTag embellished SbsB sheets conjugating both AuNPs and QDs under elevated salt conditions (500 mM NaCl). (F) Fluorescence lifetime measurements of SbsB nanosheets conjugated with QDs with AuNPs (left) and QDs (right). Inserts show the corresponding emission spectra.

Two constructs were probed for dual nanoparticle attachment: SbsB ML-SpyTag, C-terminal SnoopTag and SbsB Cys cluster, C-terminal SpyTag. The first version of modified SbsB sheet could bind both semiconductor QD and ceramic UCNP sequentially through attached SpyCatcher and SnoopCatcher, respectively (Figure 5.12C). We found that aggregates were more likely to form when both types of nanoparticles were incubated with nanosheets simultaneously. Therefore, incubating sheets with one type of nanoparticle at a time yielded the greatest occupancy. We hypothesized that unfavorable electrostatic or hydrophobic interactions between the Au NPs and QDs drove this segregation, thus we probed the effect of the ionic strength, addition of detergent, and sonication on nanoparticle conjugation (Figure 5.13). We observed that an elevated ionic strength (500 mM NaCl) encourages a more dispersed coverage of the nanoparticles across the sheet without affecting occupancy, suggesting that interactions between nanoparticles can be modulated using additive reagents. The presence of low concentrations of detergent (0.5 - 1 % TWEEN/SDS), did not have a noticeable effect on nanoparticle aggregation. We also note that these detergents did not compromise the integrity of our S-layer sheets, illustrating the robust nature of our bioscaffold. Sonication resulted in aggregation of nanoparticles across the sheet, likely due to denaturation and subsequent aggregation of SpyCatcher or SnoopCatcher on the nanoparticle surface.

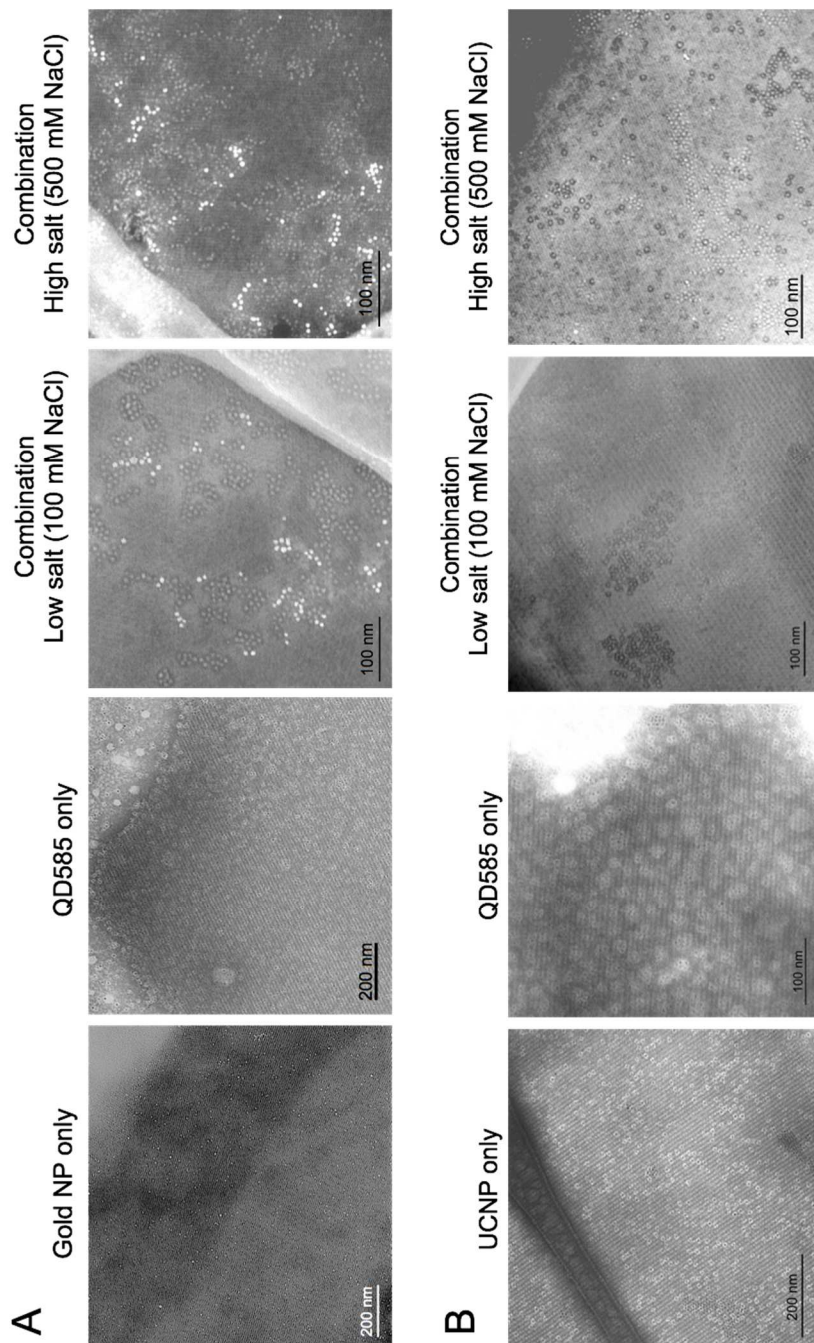


Figure 5.13 STEM images of nanoparticle conjugation to dual modified sheets. (A) Au NP and QD-SpyCatcher conjugation to SbsB Cys cluster, C-SpyTag nanosheets. (B) UCNP-SnoopCatcher and QD-SpyCatcher conjugation to SbsB ML-SpyTag, C-SnoopTag nanosheets. Nanoparticles display the capability to bind singly and as a combination across both types of dual engineered sheets. In both cases, high salt (500 mM NaCl) partially alleviated clustering of nanoparticles across the sheet.

To probe potential plasmonic materials, we focused on the construct SbsB Cys cluster, C-SpyTag for conjugation of Au NPs and QD-SpyCatcher (Figure 5.12D,E). Even with sequential nanoparticle conjugation steps, the Au NPs and QDs still had the tendency to segregate into clusters across the sheet. As observed with dual-tagged sheets, nanoparticles had the tendency to pack closely together under low salt conditions (Figure 5.13). This effect was partially alleviated with an increase in solution ionic strength, suggesting that nanoparticle clumping could be a result of electrostatic interactions between protein-conjugated nanoparticles. Despite clustering of nanoparticles across dual modified sheets, we also observed extended regions of colocalization of nanoparticles within 10-30 nm. This interparticle distance range is advantageous, as it lies within the region useful to observe plasmon transfer. Therefore, we probed the plasmonic behavior of nanosheets with bound Au NPs and QDs.

5.2.4 Plasmonic interactions between nanoparticles on dual modified SbsB sheets

One advantage of colocalizing two different nanoparticles across a 2D protein sheet is the ability to probe interactions occurring between different nanoparticles at designated spacing. We sought to determine if conjugated nanoparticles were appropriately spaced across the nanosheet to measure plasmonic enhancement of QD emission using localized lifetime measurements. For nanosheets displaying QDs alone, we observe typical QD emission with an emission peak of 585 nm and lifetime decay of 53 ns uniformly distributed over the protein sheets. In comparison, QD radiative decays are inhomogeneous in dual modified sheets with measured lifetimes as low as 15 ns (Figure 5.12F). This change in radiative lifetime of the QDs suggests that within the dual modified sheets, QDs and Au NPs are close enough for proximal Au NPs to decrease the excited state lifetime of the QDs through either radiative rate enhancement *via* the Purcell effect^{220,221} or non-radiative quenching. The localized nature of the enhanced dynamics of the QDs suggests that the interparticle distances between the Au nanoparticles and the QDs is not homogeneous, and indeed, regions of QD emission with unperturbed lifetimes were observed. Based on TEM measurements (Figures 5.3 & 5.4) and X-ray structures of the SbsB unit cell,^{190,191} we expect Au NP and QDs conjugated to the same protein sitting on opposite faces of the sheet are separated by 3 nm (edge to edge distance). Au NP and QDs on adjacent proteins would be separated by approximately 10 nm. If we could improve the precise arrangement of nanoparticles onto the two sites, these interparticle distances are ideal for plasmon transfer.

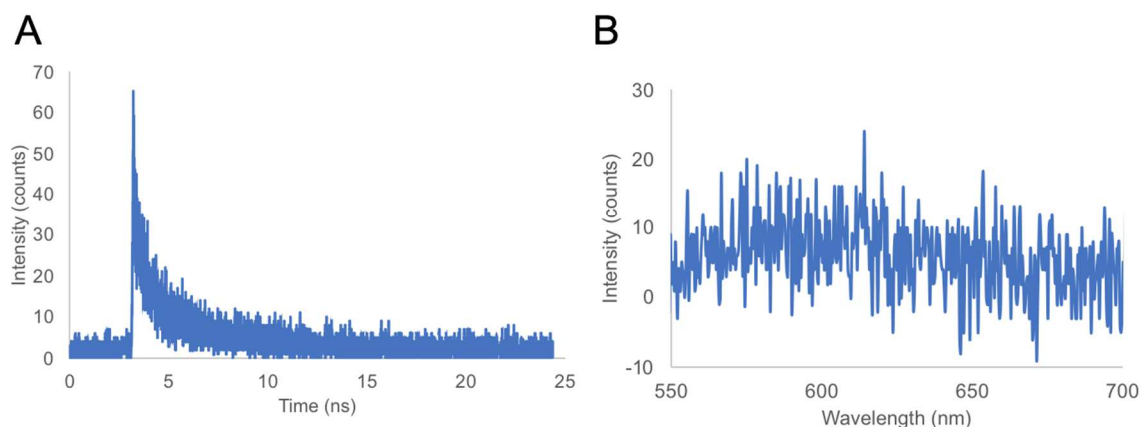


Figure 5.14 Optical measurement of SbsB nanosheets with conjugated AuNP. (A) Fluorescence lifetime measurement of SbsB sheets with bound AuNP and (B) the corresponding weak emission spectrum.

The localized nature of the observed enhancement prevented such a quantitative comparison between the QD-only and the dual modified sheets. However, regions with shorter radiative lifetimes were approximately 2 to 4 times brighter than the corresponding regions with unperturbed lifetimes in the dual modified sheets (Figure 5.12F). This observation suggests that the enhanced dynamics arise from a localized enhancement of radiative rates of the QDs due to the nearby Au NPs. Nanosheets containing only thiol-conjugated Au NPs exhibit a weak, broad emission (FWHM=60 nm) with a shorter lifetime than the QDs alone (Figure 5.14). Although this broad emission overlaps with the QD emission, it is $\sim 10\times$ weaker than any of the QD emission observed in the dual modified sheets. Nevertheless, these experiments show that photophysical properties can be affected by the nanoscale patterning of nanoparticles on S-layer sheets, and this lays the groundwork for further investigation of this scaffolded assembly.

5.2.5 Patterned display of nanocrystals on bacterial surfaces

In addition to free floating SbsB S-layer sheets, the RsaA S-layer of *C. crescentus* bacteria was also engineered to display the SpyTag peptide (Figure 5.2). The SpyTag peptide was integrated into RsaA at amino acid position 690 for solvent exposure, resulting in our engineered *rsaA690:SpyTag* strains. The *rsaA690:SpyTag* strain was immobilized on a 1.2 μm filter membrane using a filtration apparatus, and high-resolution atomic force microscopy (AFM) was used to characterize the surface morphology. The *Caulobacter* strain used has the gene for the extracellular polysaccharide layer (EPS)

deleted, which has enabled direct imaging of the S-layer, as the surface polymers no longer obscure the surface. An area scan shows many cells trapped on the filter membrane without disruption of their native shape, and the AFM height image shows long-range order of hexagonal repeating units (Figure 5.15a). The Fast Fourier Transform (FFT) of the image reveals 2D frequency peaks that are typical for a hexagonal crystalline lattice (Figure 5.15a inset). The average unit spacing found is 22 ± 1 nm, which is in agreement with the value derived from X-ray crystallography,²¹⁵ so the recombinant RsaA proteins were successfully expressed and self-assembled on the cell surface. This is the first high resolution mapping of the RsaA lattice structure on the surface of a living bacterial cell, and this technique may be used to probe the influence of other materials attached to this lattice.

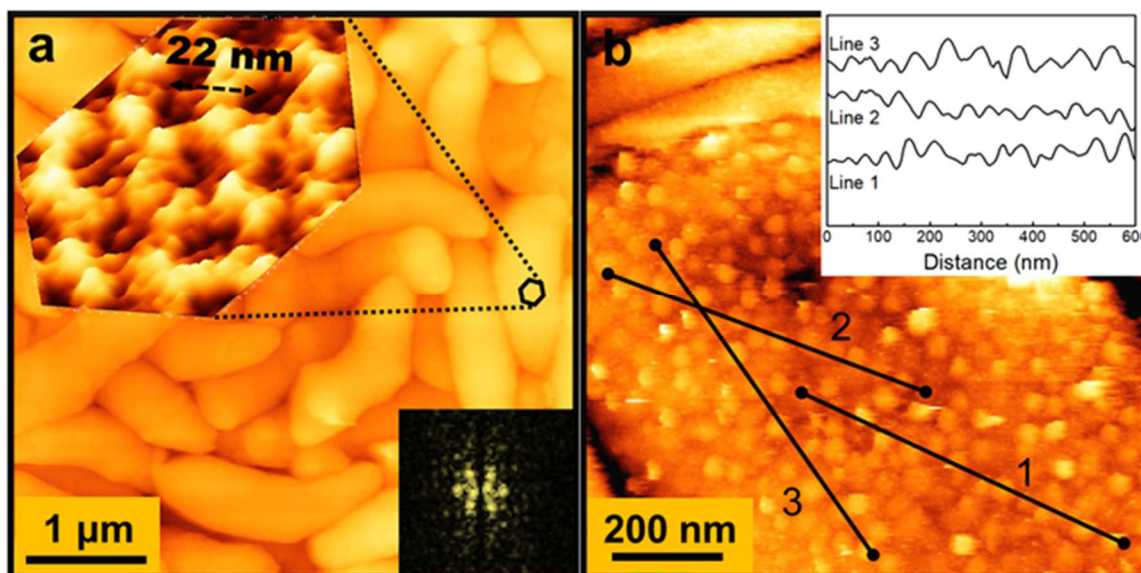


Figure 5.15 AFM analysis of RsaA lattice and bound QDs on *Caulobacter* surface. (A) High resolution AFM height image shows the 2D protein array of RsaA on a *C. crescentus* cell surface. Inset: Fast Fourier Transform of the S-layer image shows 2D frequency peaks that are typical for a hexagonal crystalline lattice with 22 nm spacing. (B) AFM height image of *C. crescentus* cells showing QDs conjugated to the surface with line profiles in the inset.

Unlike previously studied biomimetic materials, where loosely bound nanoparticles only show short-range ordering,^{222–225} the high affinity between SpyTag and SpyCatcher and the high stability of the covalent isopeptide bond can drastically increase the packing density and long-range ordering. To demonstrate the formation of densely-packed nanoparticle arrays on the RsaA S-layer lattice, we decorated the S-layer with luminescent QDs. As-synthesized CdSe/ZnS core/shell QDs were first passivated by

encapsulation with an amphiphilic copolymer, PAOA (Figure 2.3). Surface-displayed amine groups were further reacted to yield maleimide groups, which were reacted with the thiol of a SpyCatcher Ser35Cys mutant protein (Figure 5.5). The final size of the SpyCatcher-functionalized QDs (SC-PEG-QDs) was approximately 11 nm, as measured by DLS (Figure 5.16).

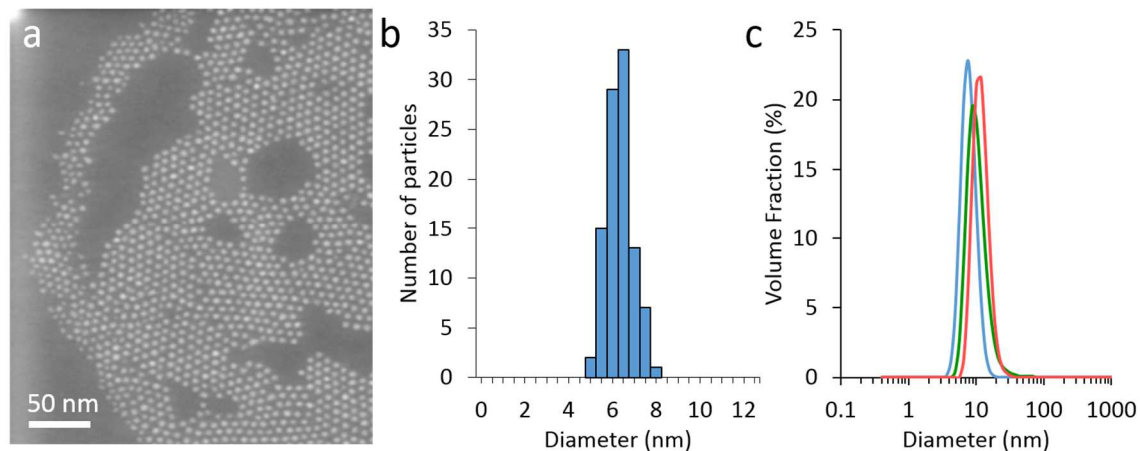


Figure 5.16 Size determination of CdSe/ZnS QD constructs. (a) STEM image of unmodified CdSe/ZnS nanoparticles. (b) Distribution of nanoparticle diameter from analyzing STEM images. Nanoparticle mean diameter is 6.1 ± 0.6 nm. $N = 100$ particles. (c) Dynamic light scattering size measurements of QD conjugates: hydrophobic (blue), PAOA-wrapped (green), and SpyCatcher-functionalized (red) QDs. Peak values found as an average of 5 runs are: 7.5 nm, 8.9 nm, and 10.9 nm, respectively.

QDs with and without the SpyCatcher motif, SC-PEG-QDs and PEG-QDs respectively, were incubated with the *C. crescentus* *rsaA690*:SpyTag overnight at room temperature, and unbound QDs were removed from the reaction through a series of wash steps. The *Caulobacter* strain without a SpyTag insertion was used as a negative control. When either SpyCatcher or SpyTag was absent from the construct, no QD luminescence signal was observed (Figure 5.17). Only when SC-PEG-QDs were mixed with the *rsaA690*:SpyTag strain did we observe bright luminescence from QDs. Furthermore, the QD emission correlated with the crescent shape of the bacterial cells, indicating they are localized at the cell surface (Figure 5.17). QD conjugation conditions were further optimized and it was found that the luminescence intensity increased with the QD concentration until saturating around 100 nM QD incubation concentration (Figure 5.18). Our recent work on the engineering of RsaA protein has identified eight locations that could be used for efficient grafting of different functional materials,²²⁶ so the amount and efficiency of conjugation may be tunable with future changes to the peptide insertion.

The cell surface morphology was probed by AFM to determine the density of bound QDs on the RsaA lattice. Closely packed, spherical objects were revealed on top of the bacterial surface, indicating the surface is covered with SC-PEG-QDs (Figure 5.15B). The average particle-to-particle spacing was found to be 43 nm by FFT, and line segments cut across the lattice have a 45 nm peak to peak distance corroborating the FFT analysis. This distance is correlated with a packing of one QD per every other lattice site, which demonstrates the ability of the SpyCatcher-decorated QDs to densely react with the SpyTag functionalized S-layer surface. These results show the first highly ordered, stable, 2D array of nanoparticles that has been assembled by the surface of a living cell and exhibit the utility of engineered biological systems in the fabrication of designed hierarchical materials.

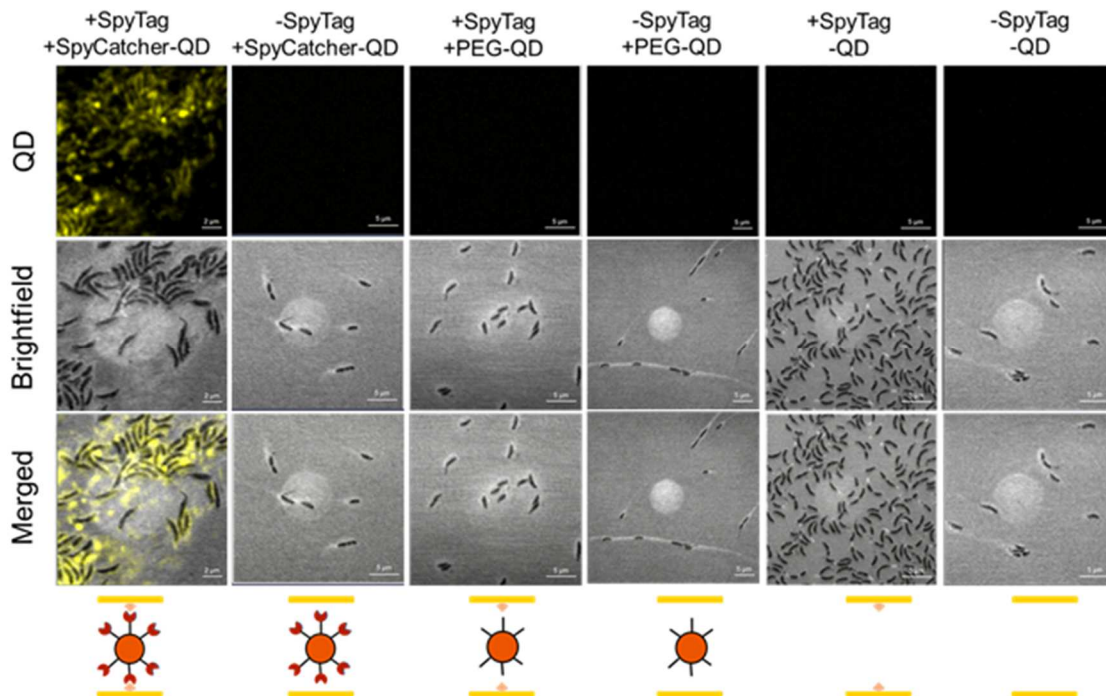


Figure 5.17 Specific attachment of engineered S-layer protein RsaA-SpyTag on the *C. crescentus* cell surface to SpyCatcher-functionalized nanoparticles. QDs, with and without conjugated SpyCatcher protein, were incubated with the engineered *C. crescentus* strains, with and without *rsaA690*:SpyTag. Only the construct with both complementary parts displays QD conjugation.

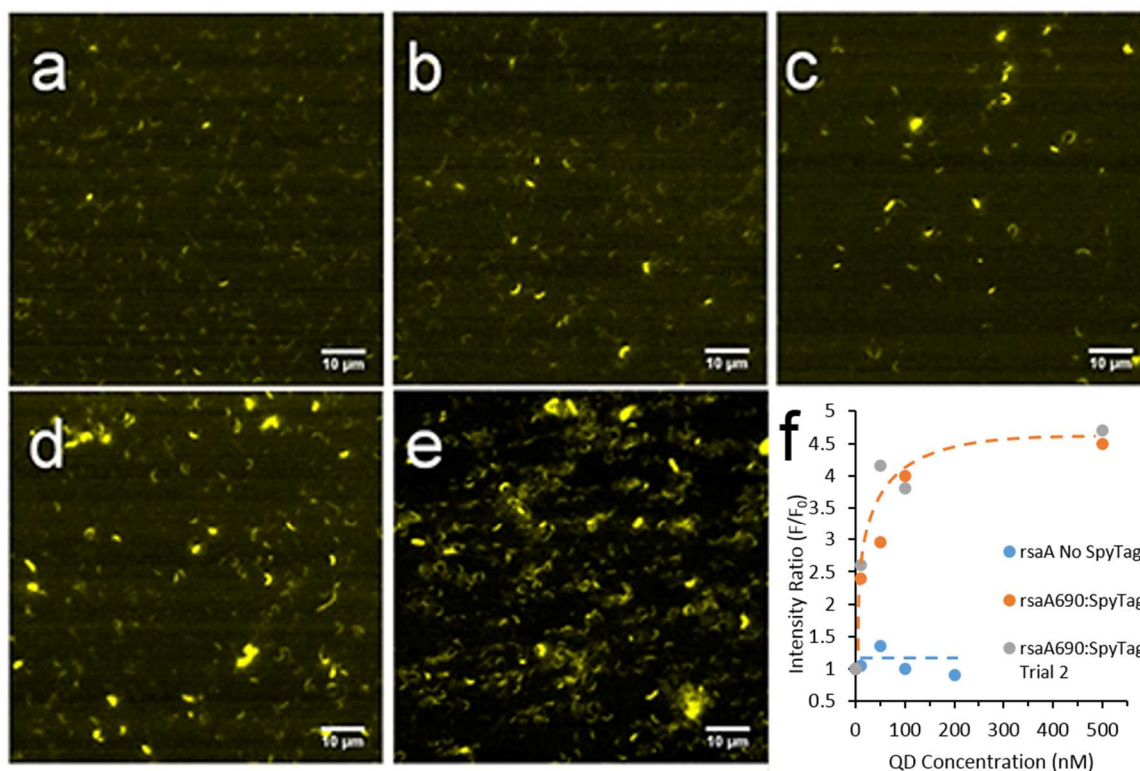


Figure 5.18 Optimization of the conjugation between QD-SpyCatcher and *C. crescentus*. Confocal fluorescence microscopy images of (a) No SpyTag negative control and (b-e) *rsaA*₆₉₀:SpyTag strain with various amount of QDs. All images (a-e) were collected under the same conditions and imaging parameters. (f) The average fluorescence intensity of individual bacterial cells as a function of QD concentration. The fluorescence intensity reaches saturation around 200 nM QDs, while the control shows no increase. All conjugation reactions were carried out for 3 hours at room temperature.

5.2.6 Formation of QD-bacteria supracellular assemblies

One aspect that separates nanocrystals from other types of materials is the property of multivalency. Since each QD is functionalized with multiple SpyCatcher proteins, this enables them to serve as crosslinking agents to connect two or more bacterial cells together through their SpyTag-coated surfaces. When the *C. crescentus* *rsaA*₆₉₀:SpyTag strain was incubated with 100 nM SC-PEG-QDs at 25°C for two days, aggregates of SC-PEG-QDs on cells appeared in the culture. These QD-incorporated aggregates, deemed supracellular assemblies, were initially small clusters of *Caulobacter* cells which eventually grew into large 3D structures ranging from 20 to 100 μm in width. Confocal imaging shows the presence of QDs throughout the volume of the bacterial assemblies,

indicating QDs played the role of a crosslinking agent. Indeed, the QDs were found sandwiched between adjacent cells, organizing bacterial cells into ordered domains within the supracellular assemblies (Figure 5.19). However, when the same strain was incubated with PEG-QDs that lack the SpyCatcher motif, only small cell aggregates were observed, indicating that QDs play a major role in the assembly process. These supracellular assemblies form within two days under both shaking and static conditions, and they can be successfully used to seed new assemblies when transferred into fresh growth conditions. Since the extracellular polysaccharide has been removed in this strain, its nonspecific interactions cannot account for the formation of the supracellular assemblies. *C. crescentus* has a lifecycle phase where the bacteria produce a protrusion with a sticky end called a holdfast. In cell culture, cells can attach at their holdfasts accumulate into a soft aggregate, and this is likely what we see in samples not crosslinked *via* nanoparticles.

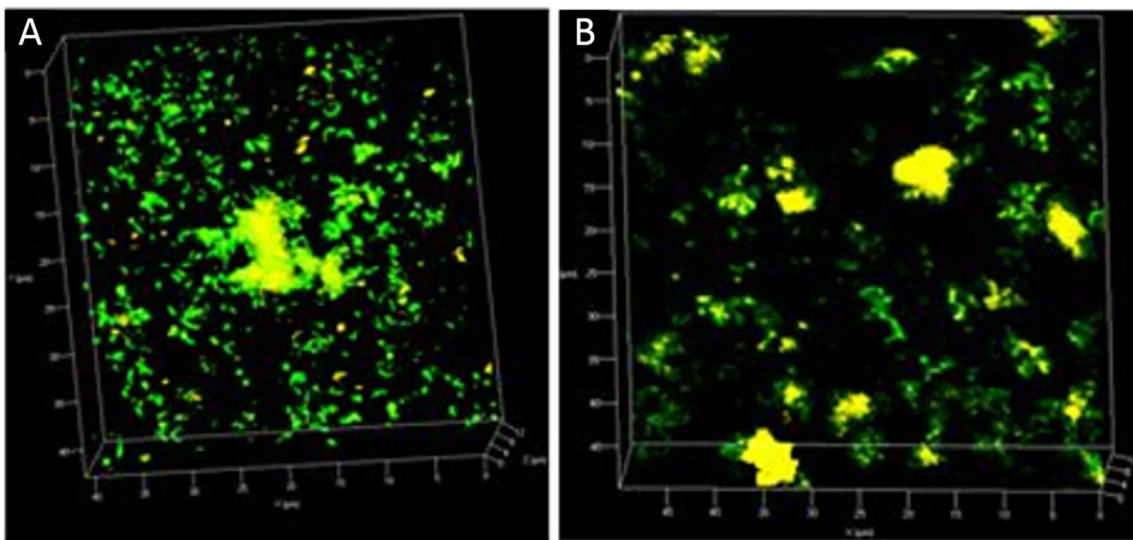


Figure 5.19 Observation of QD supracellular assemblies using confocal microscopy. Engineered *C. crescentus* strains cultured in PYE media with 100 nM SC-QD for 48 hours (A) or 30 days (B). The 3D structure of the supracellular assemblies was rendered by collecting Z-stacks of DAPI stained cells (green) bound to SC-QDs (yellow) colocalized throughout the assemblies.

5.2.7 Nanoparticle-mediated mechanical properties of supracellular assemblies

Conferring tunable mechanical properties into an ELM is challenging, where the hierarchical ordering in the complex system, the inter- and intramolecular interactions, and the long-term stability must be well controlled.^{227–230} The rapid formation of supracellular assemblies through a high density of QD crosslinkers can provide enhanced stiffness, but it is infeasible to measure their viscoelastic properties with traditional rheometry as the supracellular assemblies are still small and mobile. However, AFM-based nanoindentation is high resolution and sensitive enough to investigate the mechanical properties of the supracellular assemblies.^{231–236} To probe this, an AFM cantilever was immersed into a droplet of cell culture on top of a poly-L-lysine coated glass slide, positioned above a supracellular assembly, and compressed (Figure 5.20a). A lock-in amplifier was used to produce a sinusoidally varying load on the bacterial assembly (Figure 5.20b), and the storage modulus, G' , and loss modulus, G'' , were calculated from the amplitude of the calibrated deflection signal, piezo displacement, and contact area between the bacterial assembly and AFM cantilever (see Methods).

Dynamic mechanical analysis of the supracellular assemblies reveals that the covalent crosslinking significantly improves their viscoelastic performance. The non-crosslinked bacterial assemblies have a maximum storage modulus of 38 Pa at 100Hz (Figure 5.20b), and similarly weak values are obtained whether the assemblies are grown without QDs or with PEG-QDs as a nonbonding additive (Figure 5.21). However, when the same strain was incubated with SC-PEG-QDs, the storage modulus significantly increased from 38 Pa to 1,230 Pa at 100 Hz. This significant >30-fold enhancement in stiffness suggests that SpyCatcher-modified QDs act as a covalent crosslinking agents and the multivalent nature of those QDs promotes the close packing of the bacterial cells. Both the storage modulus and the loss modulus show a frequency dependence that is typical of gel materials,²³⁷ and as the modulation frequency increases, the material cannot relax and appears stiffer (Figure 5.20b). The substantial improvement in storage modulus upon SC-PEG-QDs addition indicates that the crosslinking density in the gel has increased.²³⁸

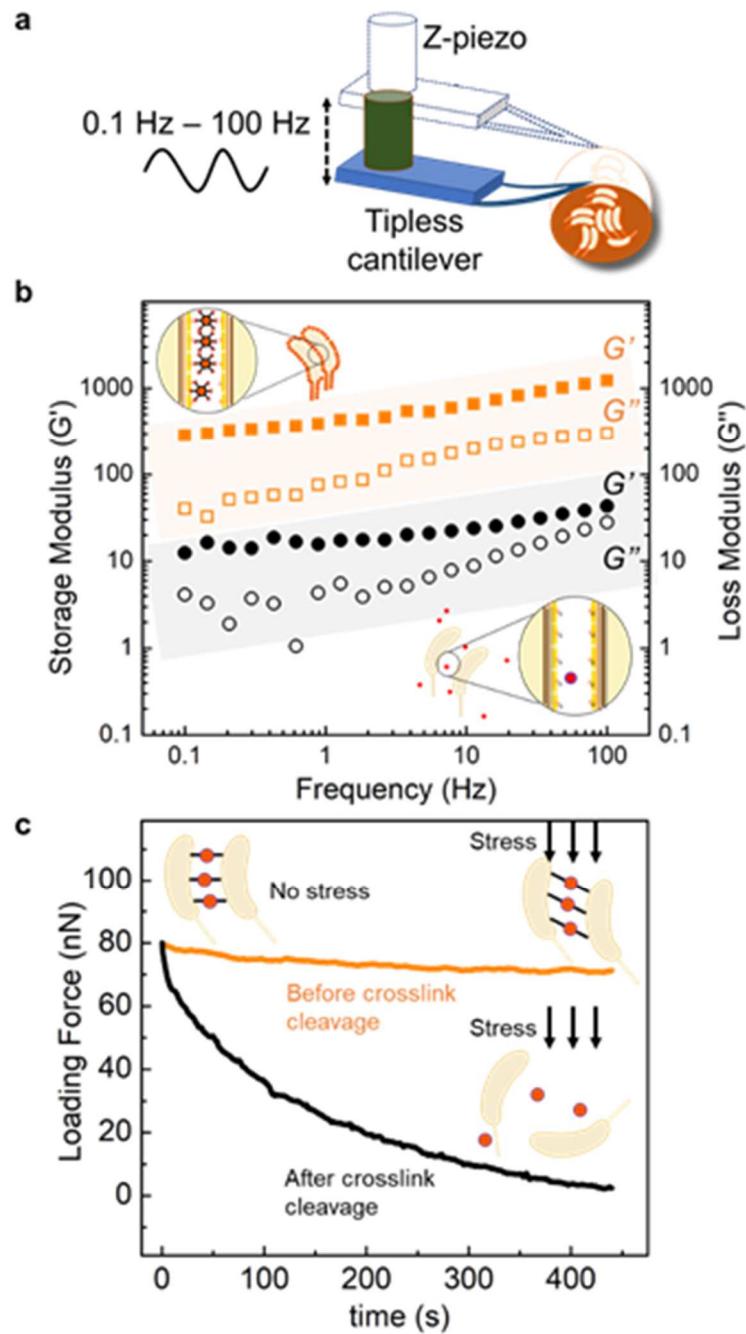


Figure 5.20 Mechanical properties of the supracellular assemblies as measured by AFM. (A) Illustration of the experimental setup. (B) The storage moduli (G' , filled) and loss moduli (G'' , open) of supracellular assemblies with SC-PEG-QDs (squares) or with PEG-QDs (circles). (C) Transient response of the supracellular assemblies to the applied stress as a function of time before (orange line) and after (black line) cleavage of the disulfide bond between the SpyCatcher motif and the polymer.

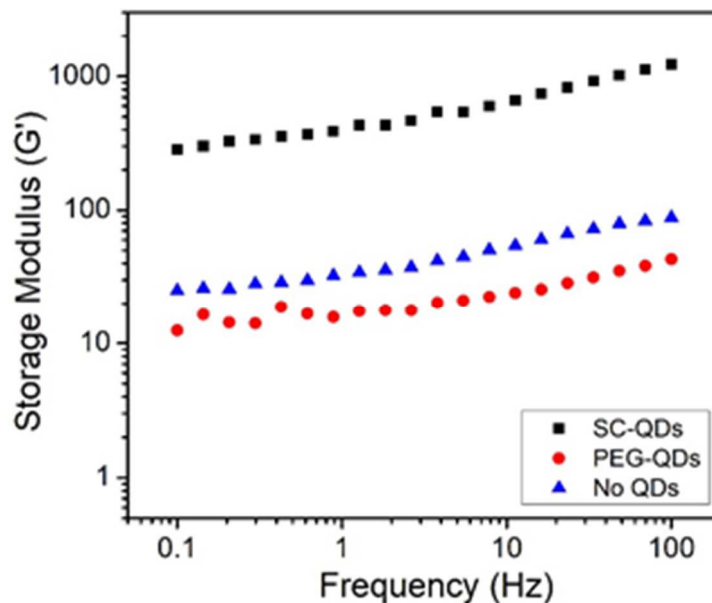


Figure 5.21 Elasticity of supracellular materials by storage modulus. The storage moduli G' of supracellular assemblies formed with SC-PEG-QDs (black squares), with PEG-QDs (red circles), and without QDs (blue triangles).

To confirm that the specific and covalent linkage between QDs and S-layer proteins is the cause of the material stiffness enhancement, a SC-S-S-PEG-QD was synthesized with a cleavable disulfide bond inserted between the SpyCatcher motif and the PEG linker. If the interaction is due to this linkage, cleaving the bond would disrupt the bacterial crosslinking and revert the material properties back to those of the weak assembly. *C. crescentus* cells were incubated with SC-S-S-PEG-QDs for 24 hours to induce the formation of supracellular assemblies, and tris(2-carboxyethyl)phosphine (TCEP) reducing agent was added to the cell culture and incubated at room temperature for 2 hours. The tipless AFM cantilever was used to deliver an initial compression force of 80 nN to the assemblies, and the response to the applied force was recorded as a function of time. For samples without TCEP addition, the supracellular assemblies showed predominantly elastic behavior and sustained the applied stress with only slight deformation. However, for samples exposed to TCEP, the applied compression force quickly dropped to zero loading force, indicating the assembly returned to predominantly liquid characteristics with cells sliding past one another (Figure 5.20c).

By controlling the bulk material through additive chemical means, we can perform manipulations such as deposition and erasure of the material through forming and dissolving of the crosslinked network. One other possibility intrinsic to this system is the

possibility of regrowth after disruption to the assembly. Since the network is comprised of living cells, if we supply the inorganic QDs, cell growth can repair damage caused to a deposited film (Figure 5.22). After 20 hours of incubation supplemented with nutrients and QDs to form new crosslinks, a 20 μm gap can be fully and autonomously repaired by the material. With this new dial for tuning the living material at the macroscale, we can imagine future applications that exploit this reconfigurability to repair damage, seal openings, or as a means of patterning on a templated surface.

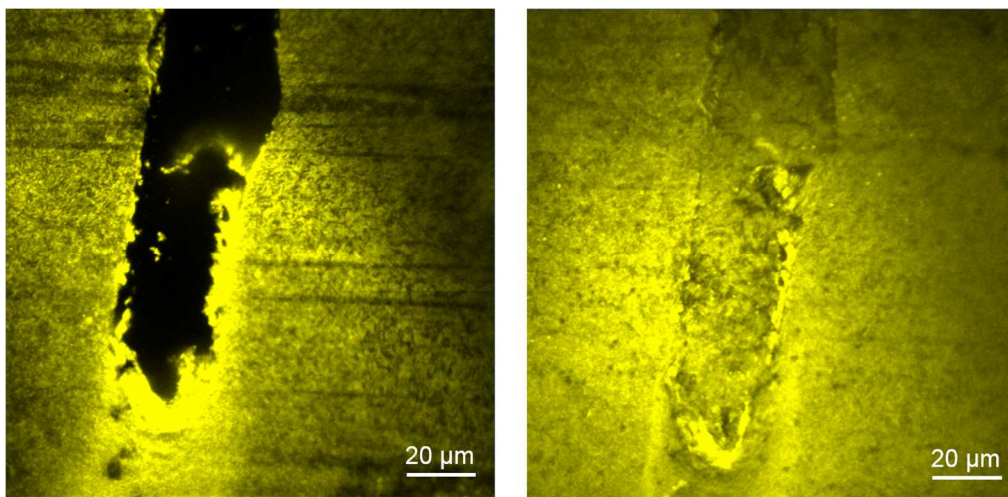


Figure 5.22 Supracellular material can repair itself under growth conditions. QD-bacterial hybrid film after a section is damaged (left) and after 20 hours of incubation (right) with growth media and supplemental QDs. Yellow fluorescence is from bound cell surface-bound QDs.

5.2.8 Expansion of hybrid materials to additional capabilities

While the SpyCatcher-decorated QDs have been shown to be essential in forming the cells into a 3D network, they fundamentally only act as nodes of multiple attachment sites, regardless of the nanoparticle inside. The luminescent properties of the QD are useful in imaging the overall structure of the assemblies, but do not impart any other interesting material properties. However, since the method of constructing the multivalent SpyCatcher nanoparticles is modular, we can use the properties of another nanoparticle type to modulate the bulk material. For example, by encapsulating and conjugating magnetic Fe_3O_4 nanoparticles instead of QDs, we lose the luminescent properties but gain magnetic control over the cell-NP network (Figure 5.23). This same concept may be expanded in the future to use other nanocrystals with unique functionality paired with living materials capable of secreting or displaying their own properties to form highly-engineered material composites.

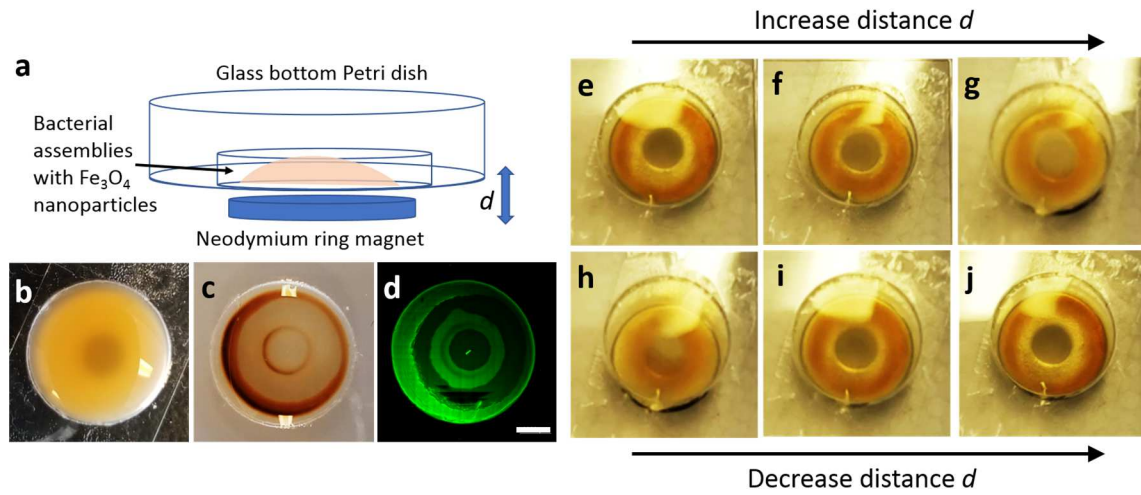


Figure 5.23 Assembly of bacterial film mediated by NP-magnetic field interaction. (a) Schematic of magnetic field templating of supracellular aggregates. Cultures of *C. crescentus* decorated with SpyCatcher-conjugated iron oxide nanoparticles before (b) and after 24 hours (c) incubation on a ring magnet. (d) Confocal microscopy of xylose-induced GFP expression (green) in the bacterial culture from (c). Disruption (e-g) and reformation (h-j) of assemblies as influenced by the distance from the inducing magnet. Scale bar for (b-d) is 2 mm.

5.3 Conclusions

Here, we demonstrate that through engineering of peptide-protein conjugation systems into the S-layers SbsB and RsaA, we can enable covalent display of multiple types of nanoparticles on free-floating protein sheets and on the surface of living cells. These hybrid materials exhibit unique properties not easily obtained through other means of synthesis.

Using the S-layer deposition platform, we have developed the first modular protein-based strategy for self-organizing hybrid composites and reveals the potential of hierarchical protein assemblies for the development of tailored plasmonic architectures. We were able to engineer the insertion of peptide tags without affecting nanosheet dimensionality or crystallization, and we observed these systems are more effective than thiol-Au interactions for nanocrystal attachment, which reflects the irreversible nature of the isopeptide bond *versus* a transient interaction. Pairing a C-terminal protein-coupling tag with a Cys cluster allowed conjugation of both Au NPs and QDs across the same face of the nanosheet, although coverage was not uniform. We observed shortened lifetimes and increased brightness for QDs colocalized with Au NPs, likely as a result of plasmon transfer. Although preliminary, this work expands the current palette of engineered hybrid materials displaying optoelectronic properties.^{9,174,179} This modular and scalable fabrication of hybrid S-layer nanosheets could benefit a range of emerging fields, including photovoltaics, electric field enhancement, and metamaterials.

In addition to engineered sheets, we have created a new hybrid living material and expressed control over its mechanical properties. The S-layer protein RsaA was also engineered to incorporate the SpyTag peptide for covalent assembly with SpyCatcher functionalized QDs. The formation of a dense layer of QDs on the cell surface serves as a multivalent node to promote the self-assembly of large 3D supracellular assemblies. The covalent crosslinking between bacterial cells significantly increases the storage and loss modulus of the assembly when compared to naturally-forming bacterial aggregates. Furthermore, reduction of a cleavable linkage disrupts the network and disassembles the material, providing a switch between a stiff gel and fluid state. So, the mechanical properties of the hybrid living supracellular assemblies can be controlled through the engineered interactions of nanoparticles in the network. As a living material, damage caused to the hybrid structure can be repaired by cellular growth supplemented with crosslinking nanoparticles. By modifying the physical properties of the nanocrystal component, we can introduce new functionality to the hybrid material, such as magnetic field-induced assembly. With all these new design possibilities, we can begin to think about other functionality that may be imparted by the inorganic component, as well as the myriad of functions and manipulations available to living systems using this novel material platform.

5.4 Materials and Methods

Generation & isolation of engineered SbsB variants for nanoparticle conjugation.

All plasmids and cell lines used in the current study are outlined in Table 5.1. The generation of recombinant SbsB protein, derived from the *G. stearothermophilus sbsB* gene, has been previously described.²¹⁸ To generate SpyTag¹¹³ and Cys-containing SbsB constructs, isolated starter plasmids were subjected to site-directed mutagenesis (Q5 Hot-Start High Fidelity mutagenesis kit, NEB), following the manufacturer's instructions, and mutagenic primers (IDT) (Table 5.2). Protein coupling tags were inserted into regions of interest within the SbsB gene as previously described.²¹⁸ Positive clones were confirmed *via* DNA sequencing. Plasmids encoding SbsB variants were transformed into the *E. coli* expression cell line HMS174(DE3) (MilliporeSigma) for heterologous protein expression.

Table 5.1 Plasmids used in this study.

Plasmid name ¹	Encodes for protein x	Strain ²
pET28A SbsB wt	SbsB	HMS174(DE3)
pET28A SbsB C-SpyTag	SbsB with C-terminal SpyTag	HMS174(DE3)
pET28A SbsB C-SnoopTag	SbsB with C-terminal SnoopTag	HMS174(DE3)
pET28A SbsB Cys cluster	SbsB with Cys quartet cluster	HMS174(DE3)
pDEST14 SpyCatcher	SpyCatcher	BL21(DE3) pLysS
pET28A SnoopCatcher	SnoopCatcher	BL21(DE3) pLysS

¹ nomenclature is given for: C-: tag insertion into the C-terminus.

² bacterial host used for protein expression

Table 5.2 Primers used in this study.

Plasmid used	Primer sequence (5 → 3) ^a	Modification
pET28A SbsB wt	i) F TAATTT <u>CGAATGTGTT</u> GAGATTTATACAC R ATAAAATCAACATCTGCAGTAG ii) F AGACGGTTACCATTAGAAT <u>G</u> CAGTGTATAAATC R AGACGGTTACCATTAGAATC iii) F TAATGGTAAT <u>G</u> TTTACAATTCAAGGGTAACGATG R ACTTCAACATAATCATTAGTACCTACAAGTGTAGTT G iv) F TTGTCCA <u>ACTTGTACT</u> ACTT <u>G</u> TAGGTAC R ACTTTTTTAAGACGGTTACCATTAGAATCGAG	incorporation of four Cys residues into SbsB ^b
pDEST14 SpyCatcher	F TGAAGAAGAT <u>TGTG</u> CTACCCATATTAATTC R ATTGTCATATCACCGGAC	substitution of serine 35 to cysteine in SpyCatcher
pET28A SnoopCatcher	F GATTGATCAGT <u>G</u> TGGGACCTATCAAATG R GCGCCATAGATATCGGGA	substitution of serine 35 to cysteine in SnoopCatcher

^a F, forward; R, reverse primers. Cys residue substitutions are underlined.

^b the following substitutions were done to create a solvent-exposed Cys cluster on the surface of SbsB i) S662C, ii) T679C, iii) V698C, iv) A682C.

Single colonies from solid media were used to inoculate cultures of LB broth (5 mL) containing kanamycin (50 µg/mL) and grown at 37 °C overnight (250 rpm). This starter culture was then used to inoculate 500 mL LB broth containing kanamycin (50 µg/mL) and grown at 37 °C with shaking (250 rpm). Once cells density reached 0.4 - 0.6 (2-4 hr post-induction), protein expression was induced with 1 mM IPTG. Cultures were then grown overnight at 18 °C with shaking (250 rpm) to avoid the formation of inclusion bodies previously described.²³⁹ Cells were harvested (6000 g, 20 min, 4 °C) and the cell

pellet was resuspended in 30 mL lysis buffer (20 mM Tris pH 8.0, 300 mM NaCl, 10 mM imidazole). Cell pellets were stored at -80 °C.

Recombinant His₆-tagged protein was isolated as previously described by gravity-flow immobilized metal-affinity chromatography (IMAC).²³⁹ Following IMAC, purified protein was dialyzed against 20 mM Tris pH 8.0 to remove imidazole. All purification steps for the isolation of SbsB Cys cluster, also included 10 mM TCEP, to avoid the formation of disulfide linkages between monomers. A TEV protease cleavage step, to remove the C-terminal His₆-tag, was carried out as previously described.²¹⁸ Protein purification and His₆-tag cleavage were confirmed by SDS-PAGE and Western blot. The addition of 10 mM CaCl₂ to our final purified protein products initiated the crystallization of SbsB monomers into nanosheets displaying oblique rectangular lattice with unit cell dimensions of 8 nm x 11 nm.

Modification and generation of protein-coupling systems. Genes encoding for SpyCatcher and SnoopCatcher were encoded within the pDEST14 and pET28A plasmids, respectively (Addgene). Both plasmids also contained an N-terminal hexa-His₆ tag for purification purposes, followed by a TEV protease cleavage site. Cys residues were incorporated into solvent exposed loops of SpyCatcher and SnoopCatcher proteins, specifically at positions S35C and N58C, respectively. Mutagenesis was carried out using a Q5 site-directed mutagenesis kit, per the manufacturer's instructions, using primers shown in Table S2. Cys-containing variants were verified by DNA sequencing. These inserted Cys side chains were required for the attachment of SpyCatcher/SnoopCatcher to the surface of nanoparticles *via* thiol chemistry.

Plasmids containing our modified SpyCatcher/SnoopCatcher were transformed into BL21(DE3) pLysS *E. coli* cells. Cell growth and recombinant protein expression were carried out following protocols as previously described.¹¹³ Following overnight protein expression, cells were harvested *via* centrifugation (6000 *g* for 20 min at 4 °C). The resulting cell pellet was resuspended in 30 mL lysis buffer (20 mM Tris pH 8.0, 300 mM NaCl, 10 mM imidazole) and stored at - 80 °C.

Recombinant His₆-tagged proteins were isolated *via* IMAC using a prepacked 1 mL His-tag column (GE Healthcare). Protein binding was carried out at 10 mM imidazole. To remove loosely bound proteins, we carried out a wash step at 40 mM imidazole for 20 column volumes. His₆-tagged protein was eluted utilizing a stepwise imidazole gradient to 250 mM. An additional purification step of preparative SEC was also carried out wherein affinity-purified samples were injected onto Superdex 200 matrix (HiLoad 16/60 column, GE Healthcare) pre-equilibrated with 20 mM Tris pH 8.0, 300 mM NaCl and 10 mM TCEP (for Cys-containing variants). All chromatography steps were conducted at 1 mL/min utilizing an ÄKTA Explorer system (GE Healthcare). Gel filtration confirmed

products were a single species with a native mass of ~ 15 kDa. SDS-PAGE analysis further confirmed solution SEC results, with a single, distinct band for purified Catcher proteins, again at approximately 15 kDa. Yields for SpyCatcher/SnoopCatcher constructs were typically between 2 - 10 mg/mL.

Nanoparticle synthesis and aqueous passivation. $\text{NaY}_{0.78}\text{Yb}_{0.2}\text{Er}_{0.02}\text{F}_4$ and $\text{NaGd}_{0.78}\text{Yb}_{0.2}\text{Er}_{0.02}\text{F}_4$ UCNPs were synthesized as described⁷ and transferred to water with poly(*n*-octylacrylamide)-*co*-poly(2-aminoethylacrylamide) (POA, 3 kDa) amphiphilic random copolymer as described previously.²¹⁹ Hydrophobic CdSe/ZnS QDs with emission maxima of 585 nm (Ocean Nanotech) were transferred to water by encapsulation in amphiphilic copolymer poly(acrylic acid)-*co*-poly(*n*-octylacrylamide)-*co*-poly(2-aminoethylacrylamide) (PAOA, 3 kDa) according to previous studies.^{58,59}

Nanoparticle-SpyCatcher conjugation. For QD-SpyCatcher conjugates, PAOA-encapsulated QDs (2 μM , 600 μL) in 100 mM HEPES, pH 7.8, were combined with the crosslinker succinimidyl ester-PEG₂-maleimide (SM(PEG)₂, (ThermoFisher, 100 mM, 100 μL) dissolved in DMSO, and mixed at room temperature for 30 min on a rotary mixer. The reaction mixture was diluted to 4 mL with 100 mM HEPES, pH 7.0, and excess PEG reagent was removed by centrifugal dialysis (Amicon Ultra-4, 100 kDa MWCO), washing with 3 x 4 mL of buffer. The retentate was diluted to 500 μL in a 1.5-mL low protein-binding centrifuge tube (Eppendorf), the SpyCatcher Ser35Cys mutant (132 μM , 200 μL) was added, and the reaction was mixed overnight at 4°C on a rotary mixer. The reaction mixture was diluted to 4 mL with 100 mM HEPES, pH 7.0, and excess SpyCatcher protein was removed by centrifugal dialysis (Amicon Ultra-4, 100 kDa MWCO), washing with 4 x 4 mL of buffer. The retentate was diluted to 600 μL in HEPES buffer, and the QD-protein conjugate was stored under ambient conditions.

To generate UCNP-SpyCatcher conjugates, POA-encapsulated UCNPs (10 μM , 200 μL) in 200 mM MES, pH 5.0, were combined with 5,5'-dithiobis(2-nitrobenzoic acid) (Ellman's reagent, 10 mM, 100 μL , Aldrich) and 2-iminothiolane HCl (Traut's reagent, 1 mM, 10 μL , Sigma) dissolved in 100 mM MES, pH 6.0. Under vigorous stirring, 700 μL of 200 mM CAPS buffer, pH 10.0 was added dropwise, and the mixture was allowed to react for 20 mins. The reaction mixture was diluted to 4 mL with 100 mM HEPES, pH 7.5, and excess reagents were removed by centrifugal dialysis (Amicon Ultra-4, 100 kDa MWCO), washing with 3 x 4 mL of HEPES buffer. An aliquot of SpyCatcher Ser35C protein (200 μM , 100 μL) was desalted on a Biospin-6 Desalting Column (Bio-rad) and further washed by centrifugal dialysis (Amicon Ultra-4, 3 kDa MWCO), washing with 3 x 4 mL of HEPES buffer to remove all TCEP storage buffer. The retentate was diluted to 100 μL in a 1.5-mL low protein-binding centrifuge tube, the

UCNPs were added, and the reaction was mixed overnight at 4°C on a rotary mixer. The reaction mixture was diluted to 4 mL with 100 mM HEPES, pH 7.5, and excess SpyCatcher protein was removed by centrifugal dialysis (Amicon Ultra-4, 100 kDa MWCO), washing with 4 x 4 mL of buffer. The retentate was diluted to 400 mL in HEPES buffer, and the UCNP-protein conjugate was stored under ambient conditions.

Nanoparticle-SpyCatcher characterization. To determine the size of as-synthesized UCNPs, a dilute dispersion of nanocrystals in hexane was drop cast onto an ultrathin carbon film on lacey carbon support, 400 mesh copper TEM grid (Ted Pella) and dried in a fume hood. Images were collected on a Gemini Ultra-55 Analytical Field Emission Scanning Electron Microscope (Zeiss) in dark-field transmission mode under 30 kV accelerating voltage. Diameters for 100 random nanoparticles were manually designated in ImageJ and a distribution was plotted.

To determine the size of aqueous UCNP and QD, dispersions were diluted to 20 nM in 100 mM HEPES, pH 7.8 for PAOA-wrapped nanoparticles, in 100 mM MES, pH 6.0 for POA-wrapped nanoparticles, and in 100 mM HEPES, pH 7.0 for SpyCatcher-functionalized nanoparticles. The dispersions were sonicated for 30 minutes prior to measurement. Diameters were measured using a Malvern Zetasizer with typical count rates of 150 kilocounts per second. Data were collected for 60 seconds each in 5 separate runs and fit using Malvern Zetasizer software to a volume-weighted size distribution of hydrodynamic diameter.

To confirm the presence of SpyCatcher on the nanoparticle surface, absorption spectra were taken prior to and after conjugation, showing a protein peak at 280 nm. The concentration of SpyCatcher was determined from this absorbance and the extinction coefficient ($10,810 \text{ M}^{-1} \text{ cm}^{-1}$), and a ratio with the nanoparticle concentration defined the number of proteins per nanoparticle.

Protein coupling reactions to SbsB nanosheets. Crystallized SbsB nanosheets (~ 1 mg/mL) with the relevant tag(s) (SpyTag/SnoopTag), were incubated in an excess of nanoparticle (1-5 μM) functionalized with their relevant protein partner (SpyCatcher/SnoopCatcher). Similarly, Au NPs (5 nm or 100 nm, citrate capped, Sigma) were kept in excess for thiol conjugation to Cys-containing SbsB sheets. All incubations were carried out overnight at room temperature with gentle rocking unless specifically stated otherwise. Prior to imaging and further analysis, unbound nanoparticles were removed *via* two centrifugation steps (16000 g, 10 min). The supernatant containing excess nanoparticles, was removed and pelleted sheets were resuspended in 20 mM Tris, pH 8.0.

Visualization of SbsB nanosheets using confocal microscopy. Interference reflection microscopy (IRM) and fluorescence microscopy were carried out on a Zeiss LSM 710 confocal microscope with an Axio Observer Z1 (Carl Zeiss Micro Imaging, Thornwood, NY). A solution of SbsB nanosheets was mounted between a glass slide and glass coverslips (No. 1.5) using a Secure Seal spacer with a 13 mm diameter, 0.12 mm thickness (ThermoFisher Scientific, Waltham, MA.) and imaged using a 100× oil immersion objective (Plan-Apochromat, 1.40 NA). A 405 nm argon ion laser was used to excite samples containing QDs and an Arroyo 980 nm continuous wave laser for samples with bound UCNPs. To collect reflection images, a 514 nm laser was reflected into the sample using a mBST80/R20 plate. The reflected light was collected and imaged onto the detector. Images were analyzed and exported using Zen Black software.

Visualization of SbsB nanosheets using scanning transmission electron microscopy (STEM). Samples for electron microscopy were prepared and visualized as previously described.¹⁸⁶ Image analysis and nanoparticle counting were carried out in Fiji V1.0.²⁴⁰ Coverage analysis was performed manually, wherein boxes corresponding to 120 SbsB monomers (100 x 100 nm) were randomly dropped on the image and nanoparticles manually counted (n = 5).

Plasmonics experiments. The experimental investigation of lifetime enhancements of the dual modified were performed using a home-built scanning confocal microscope. Pulsed laser excitation (5 ps pulse width; 40 MHz repetition rate) was provided by a supercontinuum laser source (Leukos) that was filtered using an acousto-optical tunable filter (AOTF; Gooch and Housego) to an ~5 nm-wide band centered at 520 nm. The laser excitation was focused to a diffraction-limited spot (~320 nm in diameter) by a 100X objective with an NA of 0.95 (Nikon). The CW equivalent power for all measurements reported here was ~10 nW. QD emission from the diffraction-limited excitation spot was collected by the same objective, passed through two 532 nm long-pass filters (Semrock) and focused on a single-photon counting avalanche photodiode (SC-APD; MPD) for lifetime measurements or a spectrometer (Andor) connected to a cooled scientific charge coupled device (CCD; Andor iXon) for emission spectra measurements. For the lifetime measurements, time-correlated single photon counting (TCSPC) was performed using a PicoHarp device. All transients reported in this work are significantly longer than the instrument response which exhibited a nominal full-width-at-half-max of ~70 ps.

Chemicals. Reagents were purchased from Sigma-Aldrich, VWR and used upon receipt. 1.2 μm filter membranes were purchased from Millipore. AFM cantilevers used in this study are BioLever mini BL-AC40TS (Resonance frequency at around 110 kHz in

air and 30 kHz in water with a spring constant of about 0.09 N/m) from Asylum Research and NP-O10-D triangular, tip-less cantilever (Resonance frequency at around 20 kHz in air and 4 kHz in water with a spring constant of about 0.06 N/m) from Bruker.

Engineering of *C. Crescentus* strains that produce recombinant S-layer protein

RsaA. The construction of a strain library expressing recombinant RsaA bearing Spy-Tag insertions at different locations has been previously described.²²⁶ Briefly, two *C. crescentus* background strains of CB15 (lacking EPS layer) and CB15N (expressing EPS layer) strains were created by removing *sapA*, the protease that cleaves RsaA with foreign inserts, and/or *rsaA*. Next, a library of integration strains with stable expression of engineered RsaA protein were created by integrating the SpyTag peptide into the genomic copy of the *rsaA* gene. SDS-PAGE was used to analyze the expression of engineered RsaA. As shown in Figure S1, a highly expressed protein band at 100 kD, which corresponds to the correct RsaA MW of 97kD to 102kD for both integrations can be identified. These new integration strains grow at a similar rate and have similar morphology to wild type strains and most importantly, these strains stably express RsaA-SpyTag.

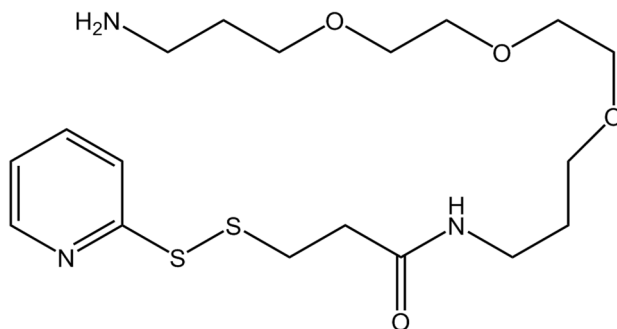
Passivation of QDs by poly(acrylic acid)-co-poly(n-octylacrylamide)-co-poly(2-aminoethylacrylamide) (PAOA) amphiphilic copolymer. CdSe/ZnS core/shell QDs (Ocean Nanotech) with emission maxima of 585 nm were passivated according to previous studies.^{58,59} Concentrations of CdSe/ZnS QDs were determined by first exciton absorbance. For aqueous dispersion of QDs, PAOA polymer (24 mg, 7.5 μ mol, 2500-fold molar excess over QDs) was dissolved in 1 mL of MeOH and 14 mL of CHCl₃ was added. QDs in toluene (200 μ L of 15 μ M, 3.0 nmol) were added with stirring, and the solvents were evaporated overnight under a gentle stream of N₂. The resulting residue was dispersed in 15 mL of 200 mM sodium bicarbonate buffer, pH 8.0 by sonication for 30 minutes. The suspension was heated in an 80 °C water bath for 60 min, slowly cooled over 2 hours in the bath to room temperature, and then sonicated again for 30 min. Excess polymer was removed using centrifugal dialysis devices (Amicon Ultra-15, 100 kDa MWCO), washing with 3 x 15 mL of 100mM HEPES, pH 7.8. To remove residual polymer and insoluble aggregates, the retentate was diluted to 1.5 mL with buffer and centrifuged at 20800 x g for 5 min. Aqueous QD dispersions were stored under ambient conditions.

Synthesis of SpyCatcher-conjugated QDs. PAOA-wrapped QDs (2 μ M, 600 μ L) in 100 mM HEPES, pH 7.8 and succinimidyl ester-PEG₂-maleimide (SM(PEG)₂, ThermoFisher, 100 mM, 100 μ L) in DMSO were combined in a 1.5-mL centrifuge tube and mixed at

room temperature for 30 min on a rotary mixer. The reaction mixture was diluted to 4 mL with 100mM HEPES, pH 7.0, and excess PEG reagent was removed by centrifugal dialysis (Amicon Ultra-4, 100 kDa MWCO), washing with 3 x 4 mL of buffer. The retentate was diluted to 500 μ L in a 1.5-mL low protein binding centrifuge tube (Eppendorf), SpyCatcher-Ser35Cys mutant protein (132 μ M, 200 μ L) was added, and the reaction was mixed overnight at 4°C on a rotary mixer. The reaction mixture was diluted to 4 mL with 100mM HEPES, pH 7.0, and excess SpyCatcher protein was removed by centrifugal dialysis (Amicon Ultra-4, 100 kDa MWCO), washing with 4 x 4 mL of buffer. The retentate was diluted to 600 μ L in HEPES buffer, and the QD-protein conjugates were stored under ambient conditions.

Synthesis of SpyCatcher-S-S-PEG-QDs. To generate activated disulfide-functionalized QDs, PAOA-wrapped QDs (2 μ M, 300 μ L) in 100 mM HEPES, pH 7.8, 5,5'-dithiobis(2-nitrobenzoic acid) (10 mM, 400 μ L), and 2-iminothiolane (1 mM, 100 μ L), were diluted into 600 μ L of 200 mM CAPS, pH 10.0 and mixed at room temperature for 1 hour. The reaction mixture was diluted to 4 mL with 100mM HEPES, pH 7.0, and excess reagents were removed by centrifugal dialysis (Amicon Ultra-4, 50 kDa MWCO), washing with 3 x 4 mL of buffer. The retentate was diluted to 600 μ L and stored under ambient conditions.

SpyCatcher-Ser35Cys mutant protein (132 μ M, 100 μ L) was treated with 1mM immobilized TCEP on agarose (ThermoFisher) for 30 minutes prior to use and centrifuged 5 min at 16,000 x g to remove beads. The treated protein was added to 100 μ L of the activated QDs, and the reaction was mixed overnight at 4°C on a rotary mixer. The reaction mixture was diluted to 4 mL with 100mM HEPES, pH 7.0, and excess SpyCatcher protein was removed by centrifugal dialysis (Amicon Ultra-4, 100 kDa MWCO), washing with 4 x 4 mL of buffer. The retentate was diluted to 200 μ L in HEPES buffer, and the QD-protein conjugates were stored under ambient conditions.



Synthesis of PDPA linker. PEG₃-diamine (1750 μ L, 8.8 mmol, Sigma) was dissolved in 6 mL of 100 mM HEPES, pH 7.8 with 3 mL of acetonitrile and the pH was adjusted to

7.5 with 5 M HCl. The solution was mixed with 50 mg of succinimidyl 3-(2-pyridyldithio)propionate (SPDP, 0.16 mmol, ThermoFisher) dissolved in 1 mL DMSO. The pH was readjusted to 7.5 with 5 M HCl, the reaction mixture was sonicated briefly to clear, and the solution was stirred overnight for 16 hours. The product was purified on a C₁₈ HPLC column (Vydac) using a linear 2-92% CH₃CN gradient with 0.1% TFA over 45 min, with product eluting at 19 min (24% CH₃CN). MS, C₁₈H₃₂N₃O₄S₂ (MH⁺) calculated: 418.18; found: 418.4. Fractions containing the product were pooled and evaporated to 59.8 mg (90% yield) of a viscous yellow oil.

Passivation of QDs by poly(maleic anhydride-alt-1-octadecene) (PMAO)

amphiphilic copolymer. For disulfide-functionalized QDs, first PMAO polymer (30 mg, 1.33 μmol, 16 monomer units per nm² of QD surface) was dissolved in 1 mL of acetone and 14 mL of CHCl₃. QDs in toluene (200 μL of 15 μM, 3.0 nmol) were added with stirring, and the solvents were evaporated under a gentle stream of N₂ overnight. The QD/polymer residue was then resuspended in 15 mL of 50 mM sodium borate, pH 9.0, with mixture of excess amines for reaction with maleic anhydrides.⁵⁹ This suspension was sonicated for 30 minutes at 60 °C, heated in an 80 °C water bath for 60 minutes, slowly cooled in the bath to room temperature, and then sonicated for 30 minutes. The sample was concentrated using centrifugal dialysis (Amicon Ultra-15, 100 kDa MWCO), and excess polymer was removed by 3 x 1 L dialysis (Spectra/Por Float-A-Lyzer G2, 100 kDa MWCO) into 100 mM HEPES, pH 7.0. The retentate was diluted to 1 mL with HEPES buffer and centrifuged at 16100 x g for 5 min to remove residual polymer and insoluble aggregates. and aqueous QD dispersions were stored under ambient conditions.

AFM imaging and nano-indentation. *In situ* force microscopy was performed on a Bruker Multimode AFM equipped with a fluid cell using soft tapping mode in liquid.^{236,241} The AFM probe consisted of a sharp silicon tip on a silicon nitride cantilever (BioLever mini). In a typical experiment, 50 μL of *C. crescentus* cells in PYE media was incubated with 100 nmol/L SpyCatcher-functionalized QDs for 1h at room temperature. The sample was fixed with 2.5% glutaraldehyde and the cells were immobilized onto a 1.2 μm filter membrane by a filtration apparatus. The sample were then washed with fresh PYE buffer to remove unbounded nanoparticles. For typical imaging conditions, AFM images were collected at scan frequencies of 0.5 - 1 Hz.

For the nano-indentation experiments, a triangular, tip-less NP-O10 AFM cantilever with a typical stiffness of 0.06 N/m was mounted onto the tip holder of an Asylum MFP-3D AFM. The sensitivity of the cantilever was calibrated by performing a deflection-distance curve on a clean glass surface in air, and the spring constant were determined using the thermal noise method. The cantilever was then immersed into a

water droplet on top of a clean glass coverslip. A Zurich Instruments' HF2LI Lock-in Amplifier was used to drive the Z-piezo in the MFP-3D scanner, which controlled the movement of the AFM cantilever. The oscillation of the Z-piezo and the cantilever generated a small, sinusoidal oscillating force, and the applied mechanical load, or stress, created a corresponding strain (deformation). The exact distance the Z-piezo travelled under a sinusoidal voltage was calibrated first, as the sensitivity of the Z-piezo is both voltage and frequency dependent. The calibration was done by pressing the tip-less cantilever onto the glass surface, and a sinusoidal voltage from the lock-in amplifier was applied to the Z-piezo. The deflection amplitude signal of the cantilever was then sent back into the lock-in amplifier to deduce the cantilever deflection voltage and the phase shift. Since the hard glass surface showed no deformation under the loading force ($d = H - h = 0$), the actual travel distance of Z-piezo H was equal to the cantilever deflection distance h . After the Z-piezo linearity calibration, the bare glass surface was switched to a 0.01 wt% PLL treated glass coverslip, and on top of which an aliquot of bacterial culture solution (ca. 100 μ L) was placed. Immersed in the cell culture, the AFM cantilever was positioned on top of a typical supracellular assemblies, and the viscoelastic properties of the supracellular assemblies were investigated as we gradually lowering the head to achieve different degree of compression of the whole material.

Under each compression, a sinusoidal driving voltage with a frequency range from 0.1 Hz to 100 Hz was used. The applied loading force F was determined by multiplying the cantilever deflection voltage with the cantilever sensitivity and spring constant. Assuming the bacterial cells that not touching cantilever does not contribute significantly to the force measurement, the applied stress σ was calculated using Equation 1, where F is the force applied to sample, A is the force applied area, K is the cantilever's spring constant, S is the cantilever's sensitivity, V_{amp} is the cantilever's deflection amplitude, a_0 is the cantilever's tip area. The strain ε was calculated using Equation 2, where D is the diameter of the supracellular assemblies. With the knowledge of stress σ , strain ε , and phase shift θ , the storage modulus (G') and the loss modulus (G'') of the supracellular assemblies were determined using Equation 3 and Equation 4, respectively. The storage modulus G' represents the stiffness of a viscoelastic material and is related to the energy stored during a loading cycle. The loss modulus G'' is related to the energy dissipated during one loading cycle.

$$\sigma = F/A = K \times S \times V_{amp} / a_0 \quad (1)$$

$$\varepsilon = d/D = (H - h)/D = (H - S \times V_{amp}) / D \quad (2)$$

$$G' = \sigma / \varepsilon \times \cos(\theta) \quad (3)$$

$$G'' = \sigma / \varepsilon \times \sin(\theta) \quad (4)$$

Optimization of QD conjugation to *C. crescentus*. Two types of QDs with and without the SpyCatcher protein (SC-PEG-QDs and PEG-QDs) were incubated overnight with *C. crescentus* CB15N Δ *sapA* *rsaA690*:SpyTag strain in PYE media at room temperature. The CB15N Δ *sapA* strain without SpyTag was used as a negative control. After the incubation, the bacterial cells were spun down, and unbound QDs were removed with the supernatant. Fresh PYE media or 1X PBS buffer was added to resuspend the cell pellet, this washing step was repeated three times before 10 μ L of the final solution was applied to a pre-cast 2% agar gel pad for confocal imaging.

To test the nanoparticle conjugation efficiency, different amounts of SpyCatcher-coated QDs were incubated with 50 μ L of *C. crescentus* JS4022 p4B-*rsaA*₆₀₀723:SpyTag strain for 3 h at room temperature. A JS4022 native strain without the SpyTag was used as the negative control. All the samples were triply washed as above prior to imaging. As shown in Figure 5.20, the population of cells with yellow luminescence increased with the nanoparticle concentration, indicating nanoparticles were bound to their surface through SpyCatcher and SpyTag. The increment of luminescence gradually reached saturation when the nanoparticle concentration was above 200 nM. At the same time, the negative control sample showed no luminescence increase as a function of nanoparticle concentration, indicating the conjugation between cells and nanoparticles is specific.

6 | Summary and Outlook

One of the biggest issues affecting the development of nanoparticle technologies is irreproducibility in both synthesis and application. Much of the work presented here has included efforts to minimize these variations in order to have more control over nanoparticle conjugate design. By encapsulating nanocrystals within polymer layers of known and designed composition, we both protect the optoelectronic properties of the nanocrystal from the environment and display chemistries on the surface that are agnostic to the nanocrystal inside. This first level of modularity allows us to use the same conjugation strategies regardless of the nanocrystal type or size. Using these surface displayed groups, I have designed chemical linkages for biomolecules and other cargo that can be controllably decorated onto the nanoparticles. Copper-catalyzed click, which was previously impossible on QD fluorophores,⁴ was achieved through a mechanistic, nanoscale understanding of these surfaces and how they can affect chemical reactions.⁵⁹ This method is now available as a choice when designing QD constructs, which expands our capabilities in fabrication.

The introduction of SpyCatcher and other covalent protein-based conjugation systems has caused a major paradigm shift in our design of nanoparticle constructs. With this compact, specific, irreversible, and expressible conjugation, we can begin to devise new conjugation techniques that take advantage of these amazing features. With SpyCatcher proteins decorating our nanocrystal surfaces, we can differentiate them into different probes depending on what SpyTag-fusion complement to add. Using this platform, we created highly-oriented conjugates of the 2G10 antibody scFv and imaged its uPAR-mediated internalization in live cell microscopy. With the inclusion of disulfide-forming chemistries for functionalization of the nanocrystal encapsulation polymers, we also introduced cleavable linkages between nanoparticles and the proteins displayed on the surface. As it is expressible as a protein fusion, we generated a SpyCatcher-fluorescent protein chimera to act as a FRET acceptor when bound to the nanoparticle that is released upon disulfide cleavage. The SpyCatcher component allows for the postsynthetic introduction of an antimicrobial peptide to the final construct. Without this specific linkage, it would be difficult to control the addition of this molecule to the probe. These applications only scratch the surface of possibilities in using these protein coupling systems for controllable fabrication, and I believe they will be a major part of nanomaterials science for years to come.

In addition to binary probes, we can also generate more complex materials using SpyCatcher-nanoparticle constructs. The simultaneous display of plasmonically-coupled nanoparticles across protein nanosheets at high density opens up new research directions in optoelectronic materials. And since these nanoparticles are covalently linked to the SbsB scaffold and thus not readily released off the nanosheet, our materials are amenable to both dry and liquid environments. This capability could allow us to study plasmonics beyond liquid crystals²⁴² and at the liquid-liquid or air-liquid interface. The S-layer array has a consistent 3 nm thickness without the roughness or defects of other fabricated

nanofilms,²⁴³ due to a single self-assembly geometry of identical subunits. The materials are robust across a range of solution-processible conditions that may otherwise disrupt inorganic thin films, but they do not require the high temperatures, pressures, or harsh conditions employed in many top-down methods.^{244,245} These factors taken together make S-layer display a very attractive platform for precise arrangement of nanomaterials beyond what we've shown in this work. With the diversity of S-layer structures known and growing numbers of orthogonal protein conjugation systems, some extraordinarily complex, yet precise structures may be realized.

This nanoscale ordering is also present in the living-nonliving hybrid materials we have generated, but now in 3 dimensions. The multivalent and cleavable nature of the nanoparticle conjugates enables tunable and dynamic mechanical properties that allow us to design advanced and responsive materials. Supracellular networks crosslinked by nanoparticle nodes exhibit novel emergent behavior, such as markedly increased material toughness, triggered assembly under magnetic field, and autonomous repair of damage. External control of biofilm formation and dissolution could allow coupling of external stimuli to cellular regulation processes and dynamic control of biosensing. Towards even more complex materials, a biomimetic nacre-like layer-by-layer structure could be assembled when supracellular bacterial networks are sandwiched between inorganic microplatelets. In the design of future ELMs, we can begin to think about other functionality that may be imparted by the inorganic component as well as the myriad of functions available *via* living systems.

While it can be very difficult to tame their shortcomings, the opportunities afforded by nanomaterials in a vast array of applications make the investigations worth pursuing. In this work, I have presented a number of attempts to control for variability and establish modular design rules for building robust nanoparticle constructs. These efforts manifest in applications from precise luminescent probes for labeling and examining cellular processes to 2D patterned arrays and 3D hybrid cellular networks. This tremendous diversity of utility is what makes nanoparticle research so captivating, and it will remain so as the field continues to mature for years to come.

7 | Appendix I: Labeling Specificity of Kv2.1 with QD-GxTX Conjugates

7.1 Introduction

One of the largest problems plaguing nanoscience research is the major disparity of seemingly identical processes. Batch to batch variability inherent to nanoparticles is compounded through each manipulation and can yield very different results by the time the final product is made. One of the major findings outlined in Chapter 3 was the proof of concept cellular imaging for a QD-GxTX probe of potassium channel activity. We were able to show that the construct bound to cells that express the targeted channel and that the probe dissociates when the channel is activated. In moving this technology closer towards neuronal imaging in acute brain slices, we wanted to show the high specificity of labeling before moving on to that more complex system.

In order to show the specificity of the QD-probe, we employed a second CHO cell line that would not express the potassium channel but would instead express eBFP fluorescent protein in the nucleus under antibiotic pressure. This would allow us to coplate the two cell lines together and differentiate them under the microscope using the blue nuclear fluorescence. What follows is a series of experiments attempting to show specificity of labeling for the QD-GxTX construct, how certain procedural changes or additives affect the labeling, and the eventual dismissal of this research avenue.

7.2 Results and Discussion

7.2.1 Disparity in cell labeling based on location

In developing this QD-GxTX probe, we have worked closely with our collaborators in the Sack Lab at UC Davis. When it initially looked like the probe was showing promise as a label that responded to tonic potassium flux (Figure 3.20), I took the QD-GxTX to the Sack Lab to test that activity by patch clamp electrophysiology. In this technique, an electrode is inserted into the cell so that the cell membrane potential can be controlled directly instead of with potassium ion concentration gradients. In our first attempt, however, we saw that the surface labeling was much patchier than previously seen, that there was a large amount of nonspecific attachment of the yellow QD fluorescence to the growth surface, and that the cells started to die very quickly under the imaging conditions (Figure 7.1).

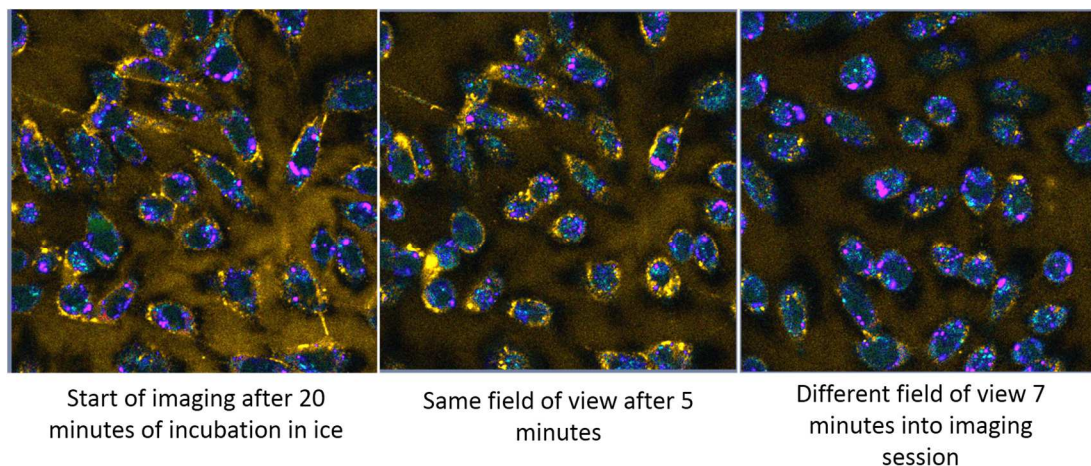


Figure 7.1 QD-GxTX labeling UC Davis CHO cell line. CHO Kv2.1 labeled with QD-GxTX at different imaging stages. Cells are purple/blue and QD staining is yellow fluorescence.

There are countless things that may be different when a preparation changes from one lab to another, and I spent time carefully eliminating possibilities until we discovered the growth was on a poly-L-lysine treated glass dish whereas the previous experiments took place on a proprietary tissue culture plastic (ibiTreat). The differences between these surfaces drastically changes the interactions with nanoparticles, and thus the labeling conditions (Figure 7.2). Unfortunately, at this time we also came to the end of a batch of nanoparticles for encapsulation and conjugation, and the replacement batch did not seem to function through the Cu-mediated click conjugation without quenching. We were forced to change nanocrystal types, and it took several trials before I was satisfied with their performance and we could try again for electrophysiology experiments.

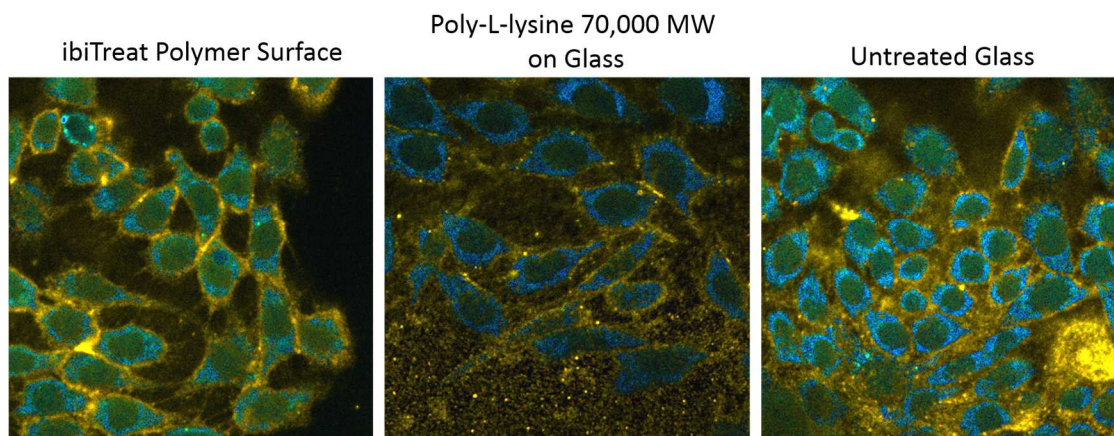


Figure 7.2 Cell culture dish surface effects on QD labeling. CHO Kv2.1 grown on various surfaces and labeled with QD-GxTX. Cells (blue) show very different QD membrane staining (yellow fluorescence) depending on the cell culture surface. QD nonspecific attachment to the surface is much higher in the glass samples as well (middle, right).

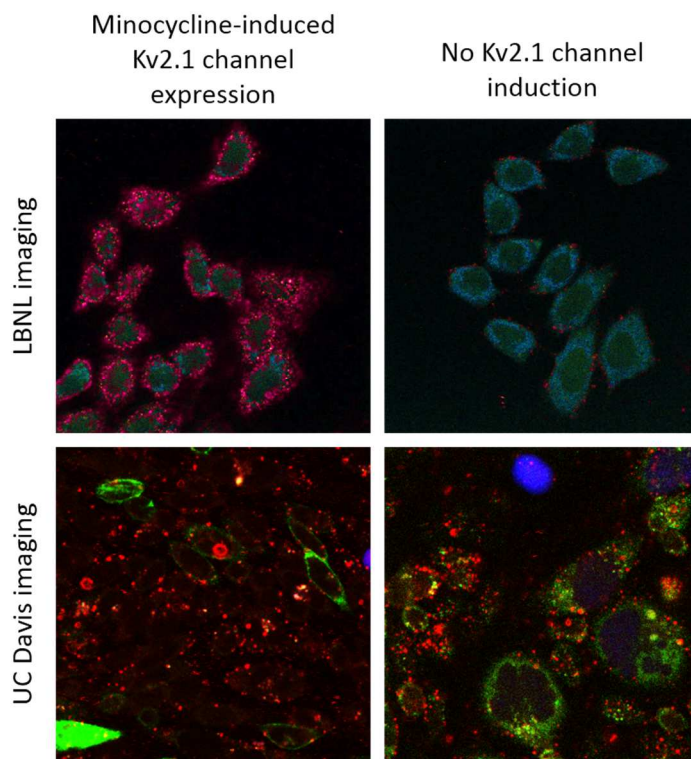


Figure 7.3 Imaging disparity between labs. In the LBNL imaging (top), the QD labeling (red) is highly membrane-associated in the sample with channels and absent in cells without. In the UC Davis imaging (bottom), showing the QD labeling (red fluorescence) found everywhere and transiently transfected GFP-tagged Kv2.1 channels (green).

Despite rigorous testing prior to transferring systems, there was still a large discrepancy between imaging in the two labs. For this new set of QD-GxTX, I had showed the high membrane specificity for cells expressing the Kv2.1 channel (Figure 7.3) on our cell line. Unfortunately, so many factors change from one lab to another: buffers and solutions, equipment, microscope setup, cell lines and treatment conditions, etc. When attempting to image a similar batch of QDs at UC Davis, we saw punctate staining of all cells regardless of channel presence, and we saw no colocalization with transiently transfected GFP-tagged Kv2.1 channels (Figure 7.3). As stated previously, batch variation in QD preparations can cause large differences in function. However, upon using the same batch of QD-GxTX on my cell line at LBNL, they perform largely as expected, with high staining on channel-expressing cells and appropriately negative controls (Figure 7.4).

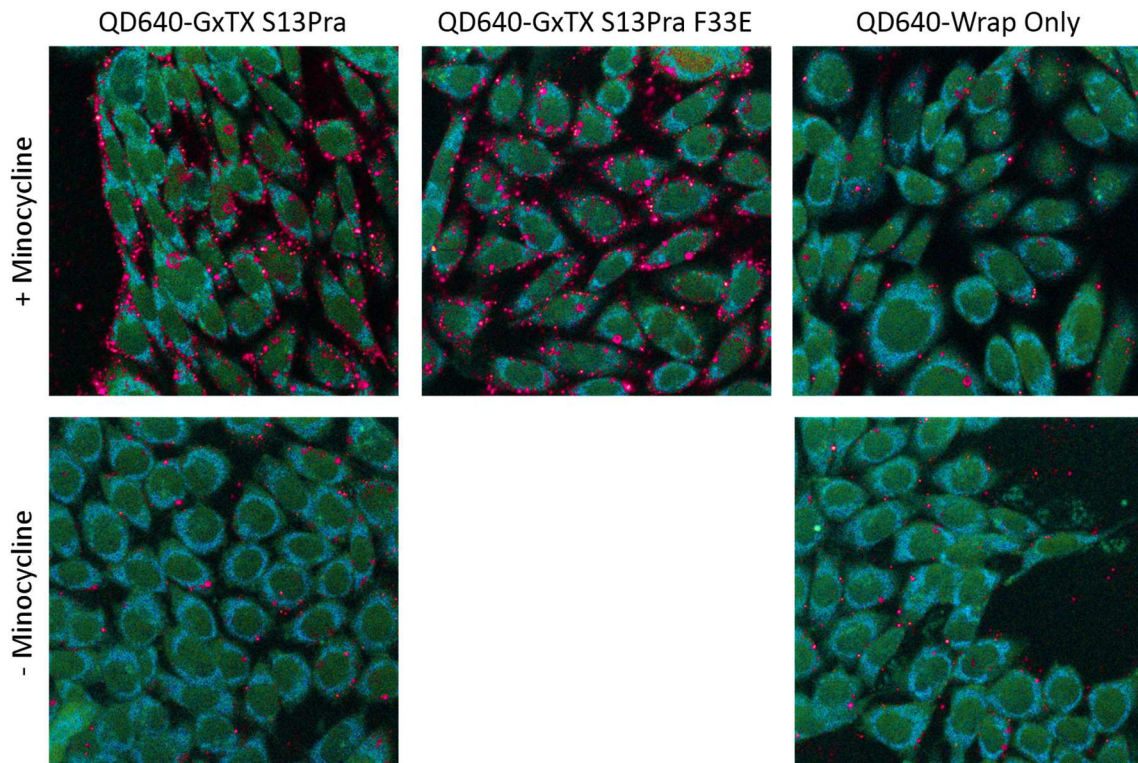


Figure 7.4 Nonspecific UC Davis QD batch shows specificity on LBNL cell line. CHO Kv2.1 labeled with various QD-GxTX constructs. While not as conformal to the membrane or uniform as previous batches, there is clear labeling of cells with the channel (top left) and no labeling without channels (bottom left) for this QD-GxTX batch. QD only samples (right) still show little nonspecific attachment. Red fluorescence is QD staining and green is cellular autofluorescence.

7.2.2 Toxin reduction and membrane blocking modulate binding but not specificity

In light of these results, we decided to reestablish our cell line using a sample from the Sack Lab so that there was at least biological continuity across the two spaces. Established alongside was another CHO-K1 cell line that did not express the Kv2.1 potassium channel, but instead expressed eBFP fluorescent protein in the cell nucleus. This way, when these two cell types are plated together in a common dish, we can look for the blue fluorescent cells as a negative control for specific labeling. In addition to newly established lines, it was discovered that QD-GxTX conjugates at that time had relatively short shelf lives and would aggregate over a period of days. The GxTX toxin, as a membrane intercalating peptide, has a face of the molecule that is quite hydrophobic. When the concentration of them is high, or there are a large number on a nanoparticle, they can trigger the precipitation out of solution. To mitigate this, I began using a small molecule, 4-pentynoic acid, in 1:1 ratio when synthesizing the QD-toxin conjugates as a way to reduce the number of toxins per nanoparticle and to impart extra colloidal stability instead. In preliminary tests, it appeared that while the aggregation was reduced, this change led to an overall decrease in cell labeling with no corresponding increase in specificity (Figure 7.5). eBFP cells without potassium channels showed similar levels of staining as the channel-induced cells, for both toxin variants.

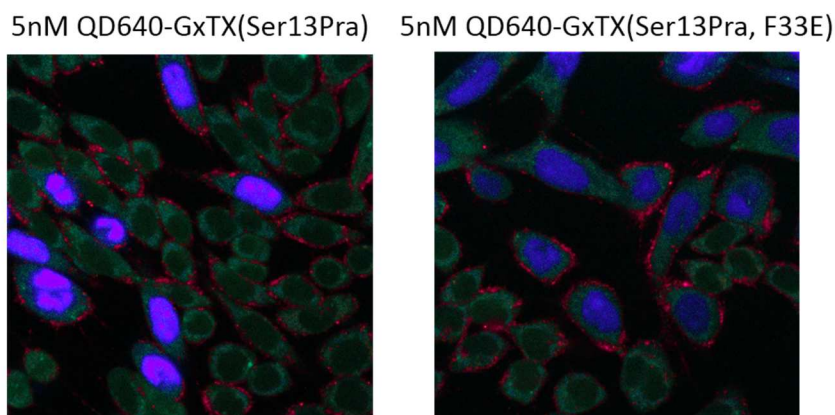


Figure 7.5 Reduced valency of QD-GxTX constructs does not improve specificity. Coplated CHO Kv2.1 and CHO eBFP labeled with QD-GxTX. For both toxin variants, the QD probes stain cells with and without (blue nuclei) channel expression roughly equally. Green is cellular autofluorescence and blue is eBFP.

In deciding how to reduce the level of nonspecific labeling, the first parameter to tune was the QD concentration. It could just be that at a lower concentration, the QDs would partition more to the intended target and we'd be able to measure a specific effect. In a series of concentration measurements, while the overall level of labeling is reduced to near zero, there is no point that shows preference for the channel-expressing cells over the eBFP cells and in some cases the eBFP cells have higher labeling. (Figure 7.6). The 5 nM sample is the only one that shows full membrane staining, so that concentration was maintained, and other factors were modulated instead.

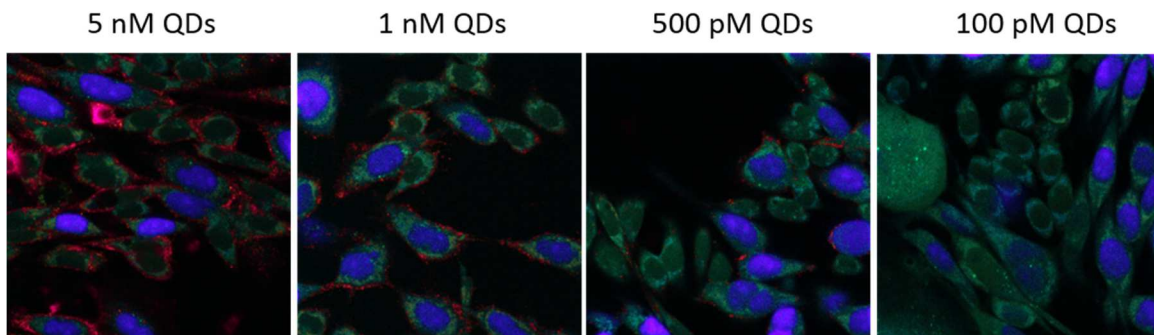


Figure 7.6 Concentration series of QD-GxTX. Coplated CHO Kv2.1 and CHO eBFP labeled with various QD-GxTX concentrations for 30 mins at 4°C. Reducing the QD concentration (left to right) reduces staining, but cell type specificity is unaffected even at the lowest concentrations.

Since it appeared that a lower number of toxins reduced the interaction of the QD probes with the membrane, it was posited that the nonspecific labeling we're seeing is from partitioning of the toxins into the cell membrane rather than actual binding at the channel sites. As a means to mitigate this, the inclusion of a toxin (GxTX(Δ C4)) that could intercalate into the membrane but is not capable of binding to the channel might effectively block this nonspecific attachment. This Δ C4 variant has had the 4 C-terminal residues removed and thus has low affinity for the potassium channel. Inclusion of this blocker during or before QD-GxTX incubation dramatically reduced all binding, but had a small, if any, effect on specificity (Figure 7.7). The blocking is effective, but we could not see labeling of the expressing cells anymore, so further optimization of concentrations and conditions was needed.

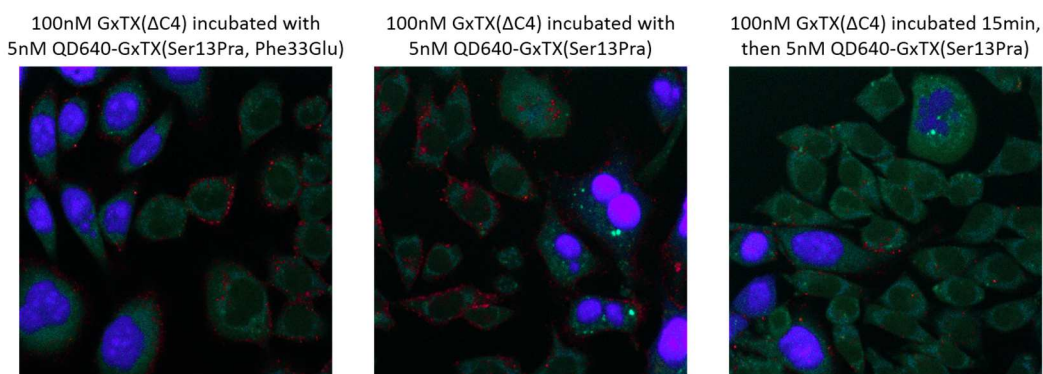


Figure 7.7 Inclusion of nonbinding GxTX variant before and during labeling reduces overall staining. Coplated CHO Kv2.1 and CHO eBFP labeled with QD-GxTX. Including GxTX(Δ C4) during (left, center) or before (right) labeling with 5 nM QD-GxTX reduces the overall level of staining, but not specifically from the negative control eBFP cells (blue nuclei).

7.2.3 Batch variation supersedes adjustments to labeling procedure

As I've experienced time and again, the batch to batch deviation for nanoparticle constructs is often larger than whatever biological or physical effect we're trying to measure. Since we are limited procedurally, and often by stability or availability, in how large of a batch of a QD conjugate we can produce, it is inevitable that we must make fresh constructs. Sometimes this can be from just one stage previous, where they end up very similar to the last batch, and some require synthesis all the way back from the nanocrystal to the finished probe. In this instance, when a new batch of QD-GxTX was synthesized to optimize the blocking behavior, the QDs showed staining in massive clumps all over all cell types and the culture dish surface even in the presence of the blocking compound (Figure 7.8). This was highly unexpected based on the previous set of experiments and it was very difficult to tell what factors may have caused such a dramatic shift.

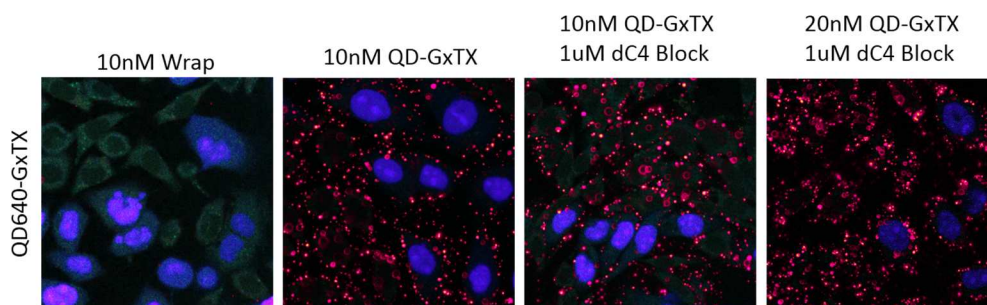


Figure 7.8 Batch variation dominates over biological or procedural changes. Coplated CHO Kv2.1 and CHO eBFP labeled with QD-GxTX. Labeling shown here (red fluorescence) is in stark contrast to previous attempts as in Figure 7.6. However, nonconjugated QDs (left) show that this issue is with GxTX nonspecific adhesion. Green is cellular autofluorescence and blue is eBFP.

In an attempt to remedy this sticking, I repeated the labeling with this same batch, but in the presence of coating compounds. Molecules like albumin found in serum and cell media should coat the nanoparticle to help avoid the nonspecific attachment, especially to the culture surface. Glycerol serves as an additive to increase the viscosity of the dispersion, hopefully to avoid aggregation of the nanoparticles. In the case of all additives, some of the nonspecific labeling was alleviated, especially at the culture dish surface, but none were effective at breaking up the large QD aggregates (Figure 7.9). The labeling was also largely unaffected by the blocking toxin, in contrast to the previous finding.

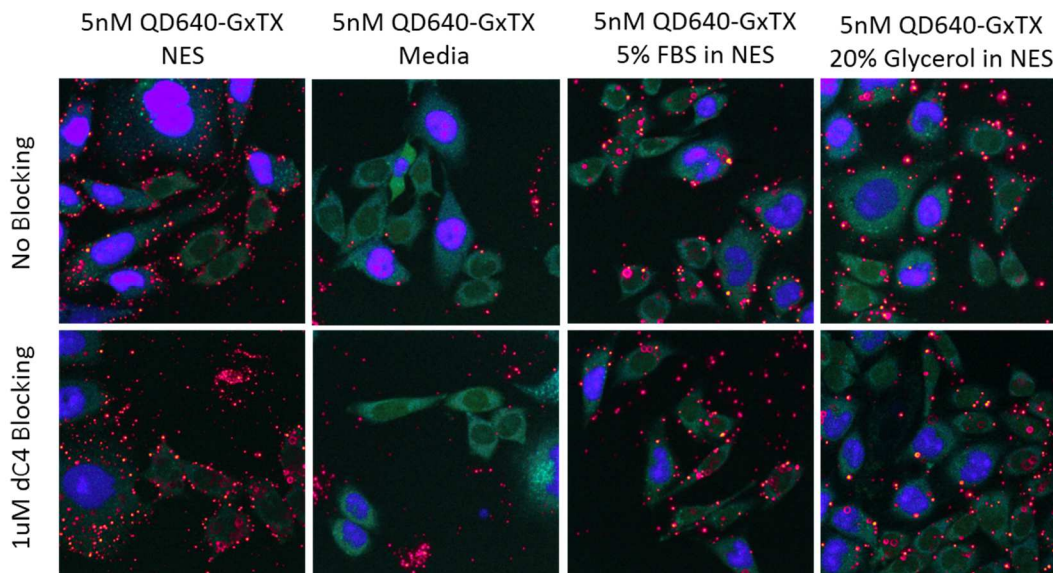


Figure 7.9 Dispersion additives do not disrupt QD-GxTX aggregates in labeling. Coplabeled CHO Kv2.1 and CHO eBFP labeled with QD-GxTX. Inclusion of additives to coat the QDs (media, FBS) or increase the viscosity (glycerol) lower the overall staining (red fluorescence), but do not reduce QD aggregation or recover the GxTX(Δ C4) blocking effect. Green is cellular autofluorescence and purple is eBFP fluorescence.

Since the QD aggregates seemed to have high affinity for the substrate surface, and we know that the majority of the Kv2.1 channels are expressed on the underside of the cell in contact with the glass, we thought it might aid our labeling to dissociate the cells off the surface and label them while suspended in solution. Then, once they have settled back down, they can be imaged at the interface. I synthesized a new batch of QD-GxTX, then labeled and imaged the dissociated cells. These showed no aggregation behavior but also no labeling of the cells or the culture surface (Figure 7.10). The incongruity of making modifications and the outcomes under the microscope made it extremely difficult to make any predictive changes from one experiment to the next.

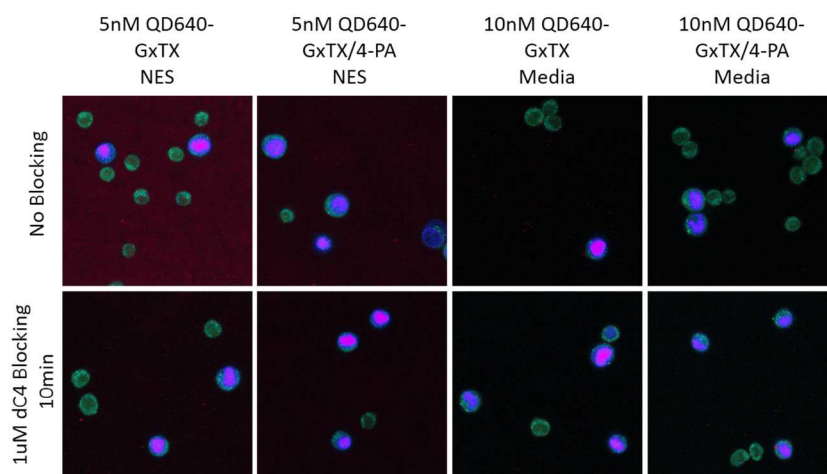


Figure 7.10 Dissociated cells do not show increased labeling from accessibility of channels. Coplated CHO Kv2.1 and CHO eBFP dissociated and labeled with various QD-GxTX concentrations. Dissociation of cells from the culture surface should expose more channels, but labeling is completely eliminated as compared to the previous trial. Green is cellular autofluorescence and purple is eBFP.

In a last attempt to remove the seemingly insurmountable issues with predictive and successful cell imaging, I completely regenerated the entire system. I established new cell lines, changed the nanocrystal type completely, and resynthesized the QD-GxTX construct from the synthesized nanocrystal to the final probe. The cell lines were healthy and the QD probes had a modest number of toxins to promote binding but avoid aggregation. And yet, there was no labeling observed for any sample (Figure 7.11).

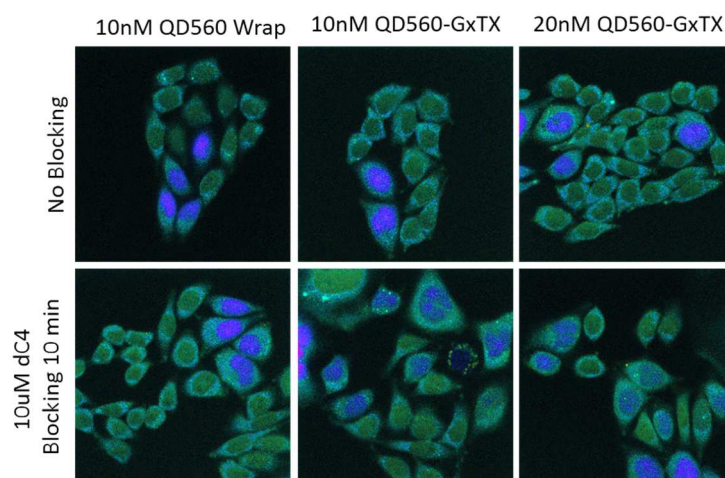
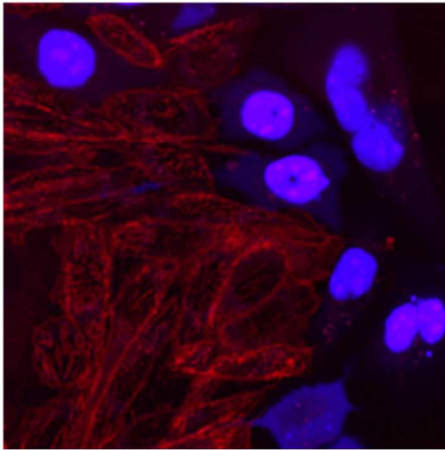


Figure 7.11 Full system overhaul results in zero labeling. Coplated CHO Kv2.1 and CHO eBFP labeled with various QD-GxTX constructs. No red QD fluorescence observed for any sample at any concentration or treatment. Green is cellular autofluorescence and blue is eBFP.

The time investment into continuing down this avenue simply became too high for no forward progress and very little understanding gained about the system. These experiments are a long, slow process (average 1 round of imaging/week) that requires the constant maintenance of cell lines as well. In this instance, it appears that the fluctuations in preparing the QD probes purely outweigh any apparent biological effects, and any signal we generate is lost in the noise. Throughout the process of eliminating as many of the confounding variables as possible, it was always important to have a positive control to ensure the cell lines were working as intended. In this case, an organic dye-labeled GxTX was used to show the specificity across cell types and its state-dependent labeling upon the addition of K^+ ions (Figure 7.12). The dye version of this probe shows high specificity for the CHO Kv2.1 membrane, especially in the striations beneath the cell, with minimal staining of the CHO eBFP cells. Upon potassium addition, the fluorescence is quickly dissociated and dissipated into solution (Figure 7.12). One of the most frustrating aspects of this work is how well the dye version functions and not being able to produce any improvements upon it with a nanocrystal probe. It may be possible to do so, but it requires further scrutiny.

10nM DyLight550-GxTX
Before K^+



10nM DyLight550-GxTX
After K^+

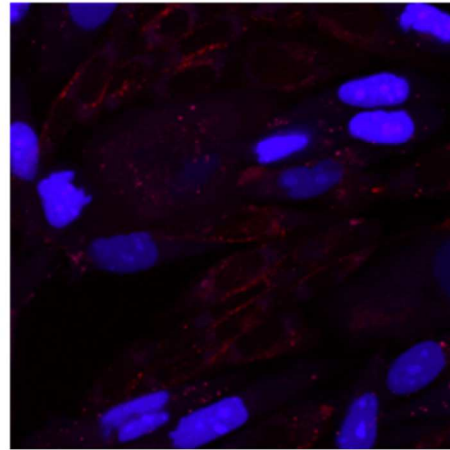


Figure 7.12 Dye-labeled GxTX shows specific labeling and K^+ response. Coplated CHO Kv2.1 and CHO eBFP labeled with DyLight550-GxTX conjugate. (Left) Labeling shows specific binarization between Kv2.1 cells (red) and eBFP cells (purple). After K^+ ion addition (right), DyLight fluorescence is drastically diminished as toxin dissociates from the membrane.

7.3 Conclusions

Without the ability to reliably make hypotheses and test them, it is impossible to make progress towards our goal of specific Kv2.1 potassium channel labeling. If we cannot meet this criterion in the model cell system, there is little chance of being able to do so in a more complex system like an acute brain slice. While some information has been gained around techniques to discourage nonspecific interactions, like blocking membranes with inactive toxin species, the effects are not reliable to all trials or batches. In a system with these many variables, the effects of batch-to-batch variation are compounded until this variation dominates any others within the system.

While I ultimately decided to abandon this direction of research, I don't think the aims presented here are impossible. We know from the organic dye example that a fluorescently-labeled probe comprised of the GxTX toxin can function in the way we intend. From other research endeavors, we also know that specific labeling with QD-based probes is also viable. I think with the right creative changes and probably a new approach to this problem, it may be possible to move forward towards neuronal QD imaging of potassium channels in the future.

References

- (1) Medintz, I. L.; Uyeda, H. T.; Goldman, E. R.; Mattoussi, H. Quantum Dot Bioconjugates for Imaging, Labelling and Sensing. *Nat Mater* **2005**, *4* (6), 435–446. <https://doi.org/10.1038/nmat1390>.
- (2) Kovalenko, M. V.; Manna, L.; Cabot, A.; Hens, Z.; Talapin, D. V.; Kagan, C. R.; Klimov, V. I.; Rogach, A. L.; Reiss, P.; Milliron, D. J.; et al. Prospects of Nanoscience with Nanocrystals. *ACS Nano* **2015**, *9* (2), 1012–1057. <https://doi.org/10.1021/nn506223h>.
- (3) Yin, Y.; Alivisatos, A. P. Colloidal Nanocrystal Synthesis and the Organic–Inorganic Interface. *Nature* **2005**, *437* (7059), 664–670. <https://doi.org/10.1038/nature04165>.
- (4) Bilan, R.; Fleury, F.; Nabiev, I.; Sukhanova, A. Quantum Dot Surface Chemistry and Functionalization for Cell Targeting and Imaging. 2015.
- (5) Sperling, R. A.; Parak, W. J. Surface Modification, Functionalization and Bioconjugation of Colloidal Inorganic Nanoparticles. *Philos. Trans. R. Soc. Math. Phys. Eng. Sci.* **2010**, *368* (1915), 1333–1383. <https://doi.org/10.1098/rsta.2009.0273>.
- (6) Chen, O.; Zhao, J.; Chauhan, V. P.; Cui, J.; Wong, C.; Harris, D. K.; Wei, H.; Han, H. S.; Fukumura, D.; Jain, R. K.; et al. Compact High-Quality CdSe–CdS Core–Shell Nanocrystals with Narrow Emission Linewidths and Suppressed Blinking. *Nat Mater* **2013**, *12* (5), 445–451. <https://doi.org/10.1038/nmat3539>.
- (7) Tian, B.; Fernandez-Bravo, A.; Najafiaghdam, H.; Torquato, N. A.; Altoe, M. V. P.; Teitelboim, A.; Tajon, C. A.; Tian, Y.; Borys, N. J.; Barnard, E. S.; et al. Low Irradiance Multiphoton Imaging with Alloyed Lanthanide Nanocrystals. *Nat. Commun.* **2018**, *9* (1), 1–8. <https://doi.org/10.1038/s41467-018-05577-8>.
- (8) Niculaes, D.; Lak, A.; Anyfantis, G. C.; Marras, S.; Laslett, O.; Avugadda, S. K.; Cassani, M.; Serantes, D.; Hovorka, O.; Chantrell, R.; et al. Asymmetric Assembling of Iron Oxide Nanocubes for Improving Magnetic Hyperthermia Performance. *ACS Nano* **2017**. <https://doi.org/10.1021/acsnano.7b05182>.
- (9) Höller, R. P. M.; Dulle, M.; Thomä, S.; Mayer, M.; Steiner, A. M.; Förster, S.; Fery, A.; Kuttner, C.; Chanana, M. Protein-Assisted Assembly of Modular 3D Plasmonic Raspberry-like Core/Satellite Nanoclusters: Correlation of Structure and Optical Properties. *ACS Nano* **2016**, *10* (6), 5740–5750. <https://doi.org/10.1021/acsnano.5b07533>.
- (10) Murray, C. B.; Sun, S.; Gaschler, W.; Doyle, H.; Betley, T. A.; Kagan, C. R. Colloidal Synthesis of Nanocrystals and Nanocrystal Superlattices. *IBM J. Res. Dev.* **2001**, *45* (1), 47–56. <https://doi.org/10.1147/rd.451.0047>.

- (11) Mirkin, C. A.; Letsinger, R. L.; Mucic, R. C.; Storhoff, J. J. A DNA-Based Method for Rationally Assembling Nanoparticles into Macroscopic Materials. *Nature* **1996**, *382* (6592), 607–609. <https://doi.org/10.1038/382607a0>.
- (12) Boles, M. A.; Engel, M.; Talapin, D. V. Self-Assembly of Colloidal Nanocrystals: From Intricate Structures to Functional Materials. *Chem. Rev.* **2016**, *116* (18), 11220–11289. <https://doi.org/10.1021/acs.chemrev.6b00196>.
- (13) Bealing, C. R.; Baumgardner, W. J.; Choi, J. J.; Hanrath, T.; Hennig, R. G. Predicting Nanocrystal Shape through Consideration of Surface-Ligand Interactions. *ACS Nano* **2012**, *6* (3), 2118–2127. <https://doi.org/10.1021/nn3000466>.
- (14) Boles, M. A.; Ling, D.; Hyeon, T.; Talapin, D. V. The Surface Science of Nanocrystals. *Nat Mater* **2016**, *15* (2), 141–153. <https://doi.org/10.1038/nmat4526>.
- (15) Morris-Cohen, A. J.; Frederick, M. T.; Lilly, G. D.; McArthur, E. A.; Weiss, E. A. Organic Surfactant-Controlled Composition of the Surfaces of CdSe Quantum Dots. *J. Phys. Chem. Lett.* **2010**, *1* (7), 1078–1081. <https://doi.org/10.1021/jz100224q>.
- (16) Fritzinger, B.; Capek, R. K.; Lambert, K.; Martins, J. C.; Hens, Z. Utilizing Self-Exchange To Address the Binding of Carboxylic Acid Ligands to CdSe Quantum Dots. *J. Am. Chem. Soc.* **2010**, *132* (29), 10195–10201. <https://doi.org/10.1021/ja104351q>.
- (17) De Roo, J.; Ibáñez, M.; Geiregat, P.; Nedelcu, G.; Walravens, W.; Maes, J.; Martins, J. C.; Van Driessche, I.; Kovalenko, M. V.; Hens, Z. Highly Dynamic Ligand Binding and Light Absorption Coefficient of Cesium Lead Bromide Perovskite Nanocrystals. *ACS Nano* **2016**, *10* (2), 2071–2081. <https://doi.org/10.1021/acsnano.5b06295>.
- (18) Hassinen, A.; Moreels, I.; de Mello Donegá, C.; Martins, J. C.; Hens, Z. Nuclear Magnetic Resonance Spectroscopy Demonstrating Dynamic Stabilization of CdSe Quantum Dots by Alkylamines. *J. Phys. Chem. Lett.* **2010**, *1* (17), 2577–2581. <https://doi.org/10.1021/jz100781h>.
- (19) Morris-Cohen, A. J.; Malicki, M.; Peterson, M. D.; Slavin, J. W. J.; Weiss, E. A. Chemical, Structural, and Quantitative Analysis of the Ligand Shells of Colloidal Quantum Dots. *Chem. Mater.* **2013**, *25* (8), 1155–1165. <https://doi.org/10.1021/cm302108j>.
- (20) Green, M. The Nature of Quantum Dot Capping Ligands. *J. Mater. Chem.* **2010**, *20* (28), 5797–5809. <https://doi.org/10.1039/C0JM00007H>.
- (21) Anderson, N. C.; Hendricks, M. P.; Choi, J. J.; Owen, J. S. Ligand Exchange and the Stoichiometry of Metal Chalcogenide Nanocrystals: Spectroscopic Observation of Facile Metal-Carboxylate Displacement and Binding. *J. Am. Chem. Soc.* **2013**, *135* (49), 18536–18548. <https://doi.org/10.1021/ja4086758>.

- (22) Owen, J. S.; Park, J.; Trudeau, P.-E.; Alivisatos, A. P. Reaction Chemistry and Ligand Exchange at Cadmium–Selenide Nanocrystal Surfaces. *J. Am. Chem. Soc.* **2008**, *130* (37), 12279–12281. <https://doi.org/10.1021/ja804414f>.
- (23) Lin, S.-Y.; Tsai, Y.-T.; Chen, C.-C.; Lin, C.-M.; Chen, C. Two-Step Functionalization of Neutral and Positively Charged Thiols onto Citrate-Stabilized Au Nanoparticles. *J. Phys. Chem. B* **2004**, *108* (7), 2134–2139. <https://doi.org/10.1021/jp036310w>.
- (24) Hinterwirth, H.; Kappel, S.; Waitz, T.; Prohaska, T.; Lindner, W.; Lämmerhofer, M. Quantifying Thiol Ligand Density of Self-Assembled Monolayers on Gold Nanoparticles by Inductively Coupled Plasma–Mass Spectrometry. *ACS Nano* **2013**, *7* (2), 1129–1136. <https://doi.org/10.1021/nn306024a>.
- (25) Woehrle, G. H.; Brown, L. O.; Hutchison, J. E. Thiol-Functionalized, 1.5-Nm Gold Nanoparticles through Ligand Exchange Reactions: Scope and Mechanism of Ligand Exchange. *J. Am. Chem. Soc.* **2005**, *127* (7), 2172–2183. <https://doi.org/10.1021/ja0457718>.
- (26) Shenoy, D.; Fu, W.; Li, J.; Crasto, C.; Jones, G.; DiMarzio, C.; Sridhar, S.; Amiji, M. Surface Functionalization of Gold Nanoparticles Using Hetero-Bifunctional Poly(Ethylene Glycol) Spacer for Intracellular Tracking and Delivery. *Int. J. Nanomedicine* **2006**, *1* (1), 51–57.
- (27) Wheeler, L. M.; Sanehira, E. M.; Marshall, A. R.; Schulz, P.; Suri, M.; Anderson, N. C.; Christians, J. A.; Nordlund, D.; Sokaras, D.; Kroll, T.; et al. Targeted Ligand-Exchange Chemistry on Cesium Lead Halide Perovskite Quantum Dots for High-Efficiency Photovoltaics. *J. Am. Chem. Soc.* **2018**, *140* (33), 10504–10513. <https://doi.org/10.1021/jacs.8b04984>.
- (28) Dong, A.; Ye, X.; Chen, J.; Kang, Y.; Gordon, T.; Kikkawa, J. M.; Murray, C. B. A Generalized Ligand-Exchange Strategy Enabling Sequential Surface Functionalization of Colloidal Nanocrystals. *J. Am. Chem. Soc.* **2011**, *133* (4), 998–1006. <https://doi.org/10.1021/ja108948z>.
- (29) J. Johnson, N. J.; M. Sangeetha, N.; Boyer, J.-C.; Veggel, F. C. J. M. van. Facile Ligand-Exchange with Polyvinylpyrrolidone and Subsequent Silica Coating of Hydrophobic Upconverting β -NaYF₄: Yb³⁺ / Er³⁺ Nanoparticles. *Nanoscale* **2010**, *2* (5), 771–777. <https://doi.org/10.1039/B9NR00379G>.
- (30) Wu, S.; Han, G.; Milliron, D. J.; Aloni, S.; Altoe, V.; Talapin, D. V.; Cohen, B. E.; Schuck, P. J. Non-Blinking and Photostable Upconverted Luminescence from Single Lanthanide-Doped Nanocrystals. *Proc. Natl. Acad. Sci.* **2009**, *106* (27), 10917–10921. <https://doi.org/10.1073/pnas.0904792106>.
- (31) Fischer, S.; Bronstein, N. D.; Swabeck, J. K.; Chan, E. M.; Alivisatos, A. P. Precise Tuning of Surface Quenching for Luminescence Enhancement in Core–Shell Lanthanide-Doped Nanocrystals. *Nano Lett.* **2016**, *16* (11), 7241–7247. <https://doi.org/10.1021/acs.nanolett.6b03683>.

- (32) Johnson, N. J. J.; He, S.; Diao, S.; Chan, E. M.; Dai, H.; Almutairi, A. Direct Evidence for Coupled Surface and Concentration Quenching Dynamics in Lanthanide-Doped Nanocrystals. *J. Am. Chem. Soc.* **2017**, *139* (8), 3275–3282. <https://doi.org/10.1021/jacs.7b00223>.
- (33) Evans, C. M.; Cass, L. C.; Knowles, K. E.; Tice, D. B.; Chang, R. P. H.; Weiss, E. A. Review of the Synthesis and Properties of Colloidal Quantum Dots: The Evolving Role of Coordinating Surface Ligands. *J. Coord. Chem.* **2012**, *65* (13), 2391–2414. <https://doi.org/10.1080/00958972.2012.695019>.
- (34) Huxter, V. M.; Scholes, G. D. Photophysics of Colloidal Semiconductor Nanocrystals: A Review. *J. Nanophotonics* **2009**, *3* (1), 032504. <https://doi.org/10.1117/1.3276902>.
- (35) Hildebrandt, N.; Spillmann, C. M.; Algar, W. R.; Pons, T.; Stewart, M. H.; Oh, E.; Susumu, K.; Daz, S. a; Delehanty, J. B.; Medintz, I. L. Energy Transfer with Semiconductor Quantum Dot Bioconjugates: A Versatile Platform for Biosensing, Energy Harvesting, and Other Developing Applications. *Chem. Rev.* **2016**, *acs.chemrev.6b00030*. <https://doi.org/10.1021/acs.chemrev.6b00030>.
- (36) Clapp, A. R.; Medintz, I. L.; Mauro, J. M.; Fisher, B. R.; Bawendi, M. G.; Mattoussi, H. Fluorescence Resonance Energy Transfer between Quantum Dot Donors and Dye-Labeled Protein Acceptors. *J. Am. Chem. Soc.* **2004**, *126* (1), 301–310. <https://doi.org/10.1021/ja037088b>.
- (37) Han, H. S.; Devaraj, N. K.; Lee, J.; Hilderbrand, S. A.; Weissleder, R.; Bawendi, M. G. Development of a Bioorthogonal and Highly Efficient Conjugation Method for Quantum Dots Using Tetrazine-Norbornene Cycloaddition. *J Am Chem Soc* **2010**, *132* (23), 7838–7839. <https://doi.org/10.1021/ja101677r>.
- (38) Goldman, E. R.; Balighian, E. D.; Mattoussi, H.; Kuno, M. K.; Mauro, J. M.; Tran, P. T.; Anderson, G. P. Avidin: A Natural Bridge for Quantum Dot-Antibody Conjugates. *J Am Chem Soc* **2002**, *124* (22), 6378–6382. <https://doi.org/10.1021/ja0125570>.
- (39) Sun, D.; Gang, O. DNA-Functionalized Quantum Dots: Fabrication, Structural, and Physicochemical Properties. *Langmuir* **2013**, *29* (23), 7038–7046. <https://doi.org/10.1021/la4000186>.
- (40) Shen, H.; Jawaid, A. M.; Snee, P. T. Poly(Ethylene Glycol) Carbodiimide Coupling Reagents for the Biological and Chemical Functionalization of Water-Soluble Nanoparticles. *ACS Nano* **2009**, *3* (4), 915–923. <https://doi.org/10.1021/nn800870r>.
- (41) Ao, Z. C.; Zheng, G. U.; Eng, J. Z.; Iu, J. L.; Eng, Q. D.; An, J. F.; Iang, J. X. A Novel Fluorescent Probe for Copper Ions Based on Polymer-Modified CdSe CdS Core Shell Quantum Dots. *Anal. Sci.* **2011**, *27* (June), 643--647.

- (42) Mulvaney, P.; Liz-Marzán, L. M.; Giersig, M.; Ung, T. Silica Encapsulation of Quantum Dots and Metal Clusters. *J. Mater. Chem.* **2000**, *10* (6), 1259–1270. <https://doi.org/10.1039/B000136H>.
- (43) Nann, T.; Mulvaney, P. Single Quantum Dots in Spherical Silica Particles. *Angew. Chem. Int. Ed.* **2004**, *43* (40), 5393–5396. <https://doi.org/10.1002/anie.200460752>.
- (44) Ostermann, J.; Merkl, J. P.; Flessau, S.; Wolter, C.; Kornowksi, A.; Schmidtke, C.; Pietsch, A.; Kloust, H.; Feld, A.; Weller, H. Controlling the Physical and Biological Properties of Highly Fluorescent Aqueous Quantum Dots Using Block Copolymers of Different Size and Shape. *ACS Nano* **2013**, *7* (10), 9156–9167. <https://doi.org/10.1021/nn4037859>.
- (45) Merkl, J. P.; Wolter, C.; Flessau, S.; Schmidtke, C.; Ostermann, J.; Feld, A.; Mews, A.; Weller, H. Investigations of Ion Transport through Nanoscale Polymer Membranes by Fluorescence Quenching of CdSe/CdS Quantum Dot/Quantum Rods. *Nanoscale* **2016**, *8* (14), 7402–7407. <https://doi.org/10.1039/c5nr08318d>.
- (46) Gargas, D. J.; Chan, E. M.; Ostrowski, A. D.; Aloni, S.; Altoe, M. V. P.; Barnard, E. S.; Sanii, B.; Urban, J. J.; Milliron, D. J.; Cohen, B. E.; et al. Engineering Bright Sub-10-Nm Upconverting Nanocrystals for Single-Molecule Imaging. *Nat. Nanotechnol.* **2014**, *9* (4), 300–305. <https://doi.org/10.1038/nnano.2014.29>.
- (47) Horton, N. G.; Wang, K.; Kobat, D.; Clark, C. G.; Wise, F. W.; Schaffer, C. B.; Xu, C. In Vivo Three-Photon Microscopy of Subcortical Structures within an Intact Mouse Brain. *Nat. Photonics* **2013**, *7* (3), 205–209. <https://doi.org/10.1038/nphoton.2012.336>.
- (48) Frangioni, J. V. In Vivo Near-Infrared Fluorescence Imaging. *Curr. Opin. Chem. Biol.* **2003**, *7* (5), 626–634. <https://doi.org/10.1016/j.cbpa.2003.08.007>.
- (49) Zuo, J.; Li, Q.; Xue, B.; Li, C.; Chang, Y.; Zhang, Y.; Liu, X.; Tu, L.; Zhang, H.; Kong, X. Employing Shells to Eliminate Concentration Quenching in Photonic Upconversion Nanostructure. *Nanoscale* **2017**, *9* (23), 7941–7946. <https://doi.org/10.1039/C7NR01403A>.
- (50) Bogdan, N.; Vetrone, F.; Ozin, G. A.; Capobianco, J. A. Synthesis of Ligand-Free Colloidally Stable Water Dispersible Brightly Luminescent Lanthanide-Doped Upconverting Nanoparticles. *Nano Lett.* **2011**, *11* (2), 835–840. <https://doi.org/10.1021/nl1041929>.
- (51) Smith, A. M.; Mancini, M. C.; Nie, S. Second Window for in Vivo Imaging. *Nat. Nanotechnol.* **2009**, *4* (11), 710–711. <https://doi.org/10.1038/nnano.2009.326>.
- (52) Abraham, L.; Lu, H. Y.; Falcão, R. C.; Scurll, J.; Jou, T.; Irwin, B.; Tafteh, R.; Gold, M. R.; Coombs, D. Limitations of Qdot Labelling Compared to Directly-Conjugated Probes for Single Particle Tracking of B Cell Receptor Mobility. *Sci. Rep.* **2017**, *7* (1), 1–13. <https://doi.org/10.1038/s41598-017-11563-9>.
- (53) Hammer, N. I.; Early, K. T.; Sill, K.; Odoi, M. Y.; Emrick, T.; Barnes, M. D. Coverage-Mediated Suppression of Blinking in Solid State Quantum Dot

- Conjugated Organic Composite Nanostructures. *J. Phys. Chem. B* **2006**, *110* (29), 14167–14171. <https://doi.org/10.1021/jp062065f>.
- (54) Yao, J.; Larson, D. R.; Vishwasrao, H. D.; Zipfel, W. R.; Webb, W. W. Blinking and Nonradiant Dark Fraction of Water-Soluble Quantum Dots in Aqueous Solution. *Proc. Natl. Acad. Sci.* **2005**, *102* (40), 14284–14289. <https://doi.org/10.1073/pnas.0506523102>.
- (55) Pellegrino, T.; Manna, L.; Kudera, S.; Liedl, T.; Koktysh, D.; Rogach, A. L.; Keller, S.; Radler, J.; Natile, G.; Parak, W. J. Hydrophobic Nanocrystals Coated with an Amphiphilic Polymer Shell: A General Route to Water Soluble Nanocrystals. *Nano Lett.* **2004**, *4* (4), 703–707. <https://doi.org/10.1021/nl035172j>.
- (56) Albers, A. E.; Chan, E. M.; McBride, P. M.; Ajo-Franklin, C. M.; Cohen, B. E.; Helms, B. A. Dual-Emitting Quantum Dot/Quantum Rod-Based Nanothermometers with Enhanced Response and Sensitivity in Live Cells. *J Am Chem Soc* **2012**, *134* (23), 9565–9568. <https://doi.org/10.1021/ja302290e>.
- (57) Corato, R. D.; Quarta, A.; Piacenza, P.; Ragusa, A.; Figuerola, A.; Buonsanti, R.; Cingolani, R.; Manna, L.; Pellegrino, T. Water Solubilization of Hydrophobic Nanocrystals by Means of Poly(Maleic Anhydride-Alt-1-Octadecene). *J. Mater. Chem.* **2008**, *18* (17), 1991–1996. <https://doi.org/10.1039/B717801H>.
- (58) Wichner, S. M.; Mann, V. R.; Powers, A. S.; Segal, M. A.; Mir, M.; Bandaria, J. N.; DeWitt, M. A.; Darzacq, X.; Yildiz, A.; Cohen, B. E. Covalent Protein Labeling and Improved Single-Molecule Optical Properties of Aqueous CdSe/CdS Quantum Dots. *ACS Nano* **2017**, *11* (7), 6773–6781. <https://doi.org/10.1021/acsnano.7b01470>.
- (59) Mann, V. R.; Powers, A. S.; Tilley, D. C.; Sack, J. T.; Cohen, B. E. Azide–Alkyne Click Conjugation on Quantum Dots by Selective Copper Coordination. *ACS Nano* **2018**, *12* (5), 4469–4477. <https://doi.org/10.1021/acsnano.8b00575>.
- (60) Prantner, A. M.; Chen, J.; Murray, C. B.; Scholler, N. Coating Evaluation and Purification of Monodisperse, Water-Soluble, Magnetic Nanoparticles Using Sucrose Density Gradient Ultracentrifugation. *Chem. Mater.* **2012**, *24* (21), 4008–4010. <https://doi.org/10.1021/cm302582z>.
- (61) Xiong, B.; Cheng, J.; Qiao, Y.; Zhou, R.; He, Y.; Yeung, E. S. Separation of Nanorods by Density Gradient Centrifugation. *J. Chromatogr. A* **2011**, *1218* (25), 3823–3829. <https://doi.org/10.1016/j.chroma.2011.04.038>.
- (62) Fontaine, S. D.; Reid, R.; Robinson, L.; Ashley, G. W.; Santi, D. V. Long-Term Stabilization of Maleimide–Thiol Conjugates. *Bioconjug. Chem.* **2015**, *26* (1), 145–152. <https://doi.org/10.1021/bc5005262>.
- (63) Vrudhula, V. M.; MacMaster, J. F.; Li, Z.; Kerr, D. E.; Senter, P. D. Reductively Activated Disulfide Prodrugs of Paclitaxel. *Bioorg. Med. Chem. Lett.* **2002**, *12* (24), 3591–3594. [https://doi.org/10.1016/S0960-894X\(02\)00784-9](https://doi.org/10.1016/S0960-894X(02)00784-9).

- (64) Vázquez-Dorbatt, V.; Tolstyka, Z. P.; Chang, C.-W.; Maynard, H. D. Synthesis of a Pyridyl Disulfide End-Functionalized Glycopolymers for Conjugation to Biomolecules and Patterning on Gold Surfaces. *Biomacromolecules* **2009**, *10* (8), 2207–2212. <https://doi.org/10.1021/bm900395h>.
- (65) Kerr, J.; Schlosser, J. L.; Griffin, D. R.; Wong, D. Y.; Kasko, A. M. Steric Effects in Peptide and Protein Exchange with Activated Disulfides. *Biomacromolecules* **2013**, *14* (8), 2822–2829. <https://doi.org/10.1021/bm400643p>.
- (66) Chong, P. C.; Hodges, R. S. A New Heterobifunctional Cross-Linking Reagent for the Study of Biological Interactions between Proteins. I. Design, Synthesis, and Characterization. *J. Biol. Chem.* **1981**, *256* (10), 5064–5070.
- (67) Gupta, K.; Zamanian, M.; Bae, C.; Milescu, M.; Krepkiy, D.; Tilley, D. C.; Sack, J. T.; Yarov-Yarovoy, V.; Kim, J. I.; Swartz, K. J. Tarantula Toxins Use Common Surfaces for Interacting with Kv and ASIC Ion Channels. *Elife* **2015**, *4*, e06774. <https://doi.org/10.7554/eLife.06774>.
- (68) Tilley, D. C.; Eum, K. S.; Fletcher-Taylor, S.; Austin, D. C.; Dupre, C.; Patron, L. A.; Garcia, R. L.; Lam, K.; Yarov-Yarovoy, V.; Cohen, B. E.; et al. Chemoselective Tarantula Toxins Report Voltage Activation of Wild-Type Ion Channels in Live Cells. *Proc Natl Acad Sci U S A* **2014**, *111* (44), E4789-96. <https://doi.org/10.1073/pnas.1406876111>.
- (69) Hong, V.; Presolski, S. I.; Ma, C.; Finn, M. G. Analysis and Optimization of Copper-Catalyzed Azide-Alkyne Cycloaddition for Bioconjugation. *Angew Chem Int Ed Engl* **2009**, *48* (52), 9879–9883. <https://doi.org/10.1002/anie.200905087>.
- (70) Lallana, E.; Riguera, R.; Fernandez-Megia, E. Reliable and Efficient Procedures for the Conjugation of Biomolecules through Huisgen Azide-Alkyne Cycloadditions. *Angew Chem Int Ed Engl* **2011**, *50* (38), 8794–8804. <https://doi.org/10.1002/anie.201101019>.
- (71) Uttamapinant, C.; Tangpeerachaikul, A.; Grecian, S.; Clarke, S.; Singh, U.; Slade, P.; Gee, K. R.; Ting, A. Y. Fast, Cell-Compatible Click Chemistry with Copper-Chelating Azides for Biomolecular Labeling. *Angew Chem Int Ed Engl* **2012**, *51* (24), 5852–5856. <https://doi.org/10.1002/anie.201108181>.
- (72) White, M. A.; Johnson, J. A.; Koberstein, J. T.; Turro, N. J. Toward the Syntheses of Universal Ligands for Metal Oxide Surfaces: Controlling Surface Functionality through Click Chemistry. *J Am Chem Soc* **2006**, *128* (35), 11356–11357. <https://doi.org/10.1021/ja064041s>.
- (73) Boisselier, E.; Salmon, L.; Ruiz, J.; Astruc, D. How to Very Efficiently Functionalize Gold Nanoparticles by “Click” Chemistry. *Chem Commun Camb* **2008**, No. 44, 5788–5790. <https://doi.org/10.1039/b812249k>.
- (74) Rostovtsev, V. V.; Green, L. G.; Fokin, V. V.; Sharpless, K. B. A Stepwise Huisgen Cycloaddition Process: Copper(I)-Catalyzed Regioselective “Ligation” of Azides and Terminal Alkynes. *Angew Chem Int Ed Engl* **2002**, *41* (14), 2596–

2599. [https://doi.org/10.1002/1521-3773\(20020715\)41:14<2596::AID-ANIE2596>3.0.CO;2-4](https://doi.org/10.1002/1521-3773(20020715)41:14<2596::AID-ANIE2596>3.0.CO;2-4).

- (75) Lutz, J. F.; Zarafshani, Z. Efficient Construction of Therapeutics, Bioconjugates, Biomaterials and Bioactive Surfaces Using Azide-Alkyne “Click” Chemistry. *Adv Drug Deliv Rev* **2008**, *60* (9), 958–970. <https://doi.org/10.1016/j.addr.2008.02.004>.
- (76) Berg, R.; Straub, B. F. Advancements in the Mechanistic Understanding of the Copper-Catalyzed Azide-Alkyne Cycloaddition. *Beilstein J Org Chem* **2013**, *9*, 2715–2750. <https://doi.org/10.3762/bjoc.9.308>.
- (77) Callan, J. F.; Mulrooney, R. C. Luminescent Detection of Cu(II) Ions in Aqueous Solution Using CdSe and CdSe-ZnS Quantum Dots Functionalised with Mercaptosuccinic Acid. *Phys. Status Solidi C* **2009**, *6* (4), 920–923. <https://doi.org/10.1002/pssc.200880571>.
- (78) Beaune, G.; Tamang, S.; Bernardin, A.; Bayle-Guillemaud, P.; Fenel, D.; Schoehn, G.; Vinet, F.; Reiss, P.; Texier, I. Luminescence of Polyethylene Glycol Coated CdSeTe/ZnS and InP/ZnS Nanoparticles in the Presence of Copper Cations. *Chemphyschem* **2011**, *12* (12), 2247–2254. <https://doi.org/10.1002/cphc.201100266>.
- (79) Li, H.; Zanella, M.; Genovese, A.; Povia, M.; Falqui, A.; Giannini, C.; Manna, L. Sequential Cation Exchange in Nanocrystals: Preservation of Crystal Phase and Formation of Metastable Phases. *Nano Lett* **2011**, *11* (11), 4964–4970. <https://doi.org/10.1021/nl202927a>.
- (80) Jewett, J. C.; Bertozzi, C. R. Cu-Free Click Cycloaddition Reactions in Chemical Biology. *Chem. Soc. Rev.* **2010**, *39* (4), 1272. <https://doi.org/10.1039/b901970g>.
- (81) Agard, N. J.; Prescher, J. A.; Bertozzi, C. R. A Strain-Promoted [3 + 2] Azide-Alkyne Cycloaddition for Covalent Modification of Biomolecules in Living Systems. *J Am Chem Soc* **2004**, *126* (46), 15046–15047. <https://doi.org/10.1021/ja044996f>.
- (82) Presolski, S. I.; Hong, V.; Cho, S. H.; Finn, M. G. Tailored Ligand Acceleration of the Cu-Catalyzed Azide-Alkyne Cycloaddition Reaction: Practical and Mechanistic Implications. *J Am Chem Soc* **2010**, *132* (41), 14570–14576. <https://doi.org/10.1021/ja105743g>.
- (83) Wang, W.; Hong, S.; Tran, A.; Jiang, H.; Triano, R.; Liu, Y.; Chen, X.; Wu, P. Sulfated Ligands for the Copper(I)-Catalyzed Azide-Alkyne Cycloaddition. *Chem Asian J* **2011**, *6* (10), 2796–2802. <https://doi.org/10.1002/asia.201100385>.
- (84) Rodionov, V. O.; Presolski, S. I.; Diaz, D. D.; Fokin, V. V.; Finn, M. G. Ligand-Accelerated Cu-Catalyzed Azide-Alkyne Cycloaddition: A Mechanistic Report. *J Am Chem Soc* **2007**, *129* (42), 12705–12712. <https://doi.org/10.1021/ja072679d>.
- (85) Rodionov, V. O.; Presolski, S. I.; Gardinier, S.; Lim, Y. H.; Finn, M. G. Benzimidazole and Related Ligands for Cu-Catalyzed Azide-Alkyne

- Cycloaddition. *J Am Chem Soc* **2007**, *129* (42), 12696–12704.
<https://doi.org/10.1021/ja072678l>.
- (86) Worrell, B. T.; Malik, J. A.; Fokin, V. V. Direct Evidence of a Dinuclear Copper Intermediate in Cu(I)-Catalyzed Azide-Alkyne Cycloadditions. *Science* **2013**, *340* (6131), 457–460. <https://doi.org/10.1126/science.1229506>.
- (87) Zhu, L.; Brassard, C. J.; Zhang, X.; Guha, P. M.; Clark, R. J. On the Mechanism of Copper(I)-Catalyzed Azide-Alkyne Cycloaddition. *Chem Rec* **2016**, *16* (3), 1501–1517. <https://doi.org/10.1002/tcr.201600002>.
- (88) Kuang, G. C.; Guha, P. M.; Brotherton, W. S.; Simmons, J. T.; Stankee, L. A.; Nguyen, B. T.; Clark, R. J.; Zhu, L. Experimental Investigation on the Mechanism of Chelation-Assisted, Copper(II) Acetate-Accelerated Azide-Alkyne Cycloaddition. *J Am Chem Soc* **2011**, *133* (35), 13984–14001.
<https://doi.org/10.1021/ja203733q>.
- (89) Ziegler, M. S.; Lakshmi, K. V.; Tilley, T. D. Dicopper Cu(I)Cu(I) and Cu(I)Cu(II) Complexes in Copper-Catalyzed Azide-Alkyne Cycloaddition. *J Am Chem Soc* **2017**. <https://doi.org/10.1021/jacs.6b13261>.
- (90) Stauffer, S. R.; Hartwig, J. F. Fluorescence Resonance Energy Transfer (FRET) as a High-Throughput Assay for Coupling Reactions. Arylation of Amines as a Case Study. *J Am Chem Soc* **2003**, *125* (23), 6977--6985.
<https://doi.org/10.1021/ja034161p>.
- (91) Scheck, R. A.; Dedeo, M. T.; Iavarone, A. T.; Francis, M. B. Optimization of a Biomimetic Transamination Reaction. *J. Am. Chem. Soc.* **2008**, *130* (20), 11762--11770.
- (92) Finbloom, J. A.; Han, K.; Slack, C. C.; Furst, A. L.; Francis, M. B. Cucurbit[6]Uril-Promoted Click Chemistry for Protein Modification. *J Am Chem Soc* **2017**. <https://doi.org/10.1021/jacs.7b05164>.
- (93) Kolodych, S.; Rasolofonjatovo, E.; Chaumontet, M.; Nevers, M. C.; Creminon, C.; Taran, F. Discovery of Chemoselective and Biocompatible Reactions Using a High-Throughput Immunoassay Screening. *Angew Chem Int Ed Engl* **2013**, *52* (46), 12056–12060. <https://doi.org/10.1002/anie.201305645>.
- (94) Lewis, W. G.; Magallon, F. G.; Fokin, V. V.; Finn, M. G. Discovery and Characterization of Catalysts for Azide-Alkyne Cycloaddition by Fluorescence Quenching. *J Am Chem Soc* **2004**, *126* (30), 9152–9153.
<https://doi.org/10.1021/ja048425z>.
- (95) Besanceney-Webler, C.; Jiang, H.; Zheng, T.; Feng, L.; Soriano del Amo, D.; Wang, W.; Klivansky, L. M.; Marlow, F. L.; Liu, Y.; Wu, P. Increasing the Efficacy of Bioorthogonal Click Reactions for Bioconjugation: A Comparative Study. *Angew Chem Int Ed Engl* **2011**, *50* (35), 8051–8056.
<https://doi.org/10.1002/anie.201101817>.

- (96) Soriano Del Amo, D.; Wang, W.; Jiang, H.; Besanceney, C.; Yan, A. C.; Levy, M.; Liu, Y.; Marlow, F. L.; Wu, P. Biocompatible Copper(I) Catalysts for in Vivo Imaging of Glycans. *J Am Chem Soc* **2010**, *132* (47), 16893–16899. <https://doi.org/10.1021/ja106553e>.
- (97) Prasuhn, D. E.; Feltz, A.; Blanco-Canosa, J. B.; Susumu, K.; Stewart, M. H.; Mei, B. C.; Yakovlev, A. V.; Loukov, C.; Mallet, J. M.; Oheim, M.; et al. Quantum Dot Peptide Biosensors for Monitoring Caspase 3 Proteolysis and Calcium Ions. *ACS Nano* **2010**, *4* (9), 5487–5497. <https://doi.org/10.1021/nm1016132>.
- (98) Hong, V.; Steinmetz, N. F.; Manchester, M.; Finn, M. G. Labeling Live Cells by Copper-Catalyzed Alkyne--Azide Click Chemistry. *Bioconjug Chem* **2010**, *21* (10), 1912–1916. <https://doi.org/10.1021/bc100272z>.
- (99) Chan, E. M.; Levy, E. S.; Cohen, B. E. Rationally Designed Energy Transfer in Upconverting Nanoparticles. *Adv Mater* **2015**, *27* (38), 5753–5761. <https://doi.org/10.1002/adma.201500248>.
- (100) Levy, E. S.; Tajon, C. A.; Bischof, T. S.; Iafrati, J.; Fernandez-Bravo, A.; Garfield, D. J.; Chamanzar, M.; Maharbiz, M. M.; Sohal, V. S.; Schuck, P. J.; et al. Energy-Looping Nanoparticles: Harnessing Excited-State Absorption for Deep-Tissue Imaging. *ACS Nano* **2016**, *10* (9), 8423–8433. <https://doi.org/10.1021/acsnano.6b03288>.
- (101) Månsson, R.; Tsapogas, P.; Åkerlund, M.; Lagergren, A.; Gisler, R.; Sigvardsson, M. Pearson Correlation Analysis of Micro-Array Data Allows for the Identification of Genetic Targets for Early B-Cell Factor. *J. Biol. Chem.* **2004**. <https://doi.org/10.1074/jbc.M400589200>.
- (102) Kao, K.-J.; Chang, K.-M.; Hsu, H.-C.; Huang, A. T. Correlation of Microarray-Based Breast Cancer Molecular Subtypes and Clinical Outcomes: Implications for Treatment Optimization. *BMC Cancer* **2011**, *11* (1), 143. <https://doi.org/10.1186/1471-2407-11-143>.
- (103) Scheiber, J.; Jenkins, J. L.; Sukuru, S. C. K.; Bender, A.; Mikhailov, D.; Milik, M.; Azzaoui, K.; Whitebread, S.; Hamon, J.; Urban, L.; et al. Mapping Adverse Drug Reactions in Chemical Space. *J. Med. Chem.* **2009**, *52* (9), 3103–3107. <https://doi.org/10.1021/jm801546k>.
- (104) Long, S. B.; Tao, X.; Campbell, E. B.; MacKinnon, R. Atomic Structure of a Voltage-Dependent K⁺ Channel in a Lipid Membrane-like Environment. *Nature* **2007**, *450* (7168), 376–382. <https://doi.org/10.1038/nature06265>.
- (105) Lee, S.; Milesescu, M.; Jung, H. H.; Lee, J. Y.; Bae, C. H.; Lee, C. W.; Kim, H. H.; Swartz, K. J.; Kim, J. I. Solution Structure of GxTX-1E, a High-Affinity Tarantula Toxin Interacting with Voltage Sensors in Kv2.1 Potassium Channels. *Biochemistry* **2010**, *49* (25), 5134–5142. <https://doi.org/10.1021/bi100246u>.

- (106) Fields, G. B.; Noble, R. L. Solid Phase Peptide Synthesis Utilizing 9-Fluorenylmethoxycarbonyl Amino Acids. *Int. J. Pept. Protein Res.* **1990**, *35* (3), 161–214. <https://doi.org/10.1111/j.1399-3011.1990.tb00939.x>.
- (107) Merrifield, R. B. Solid-Phase Peptide Synthesis. In *Advances in Enzymology and Related Areas of Molecular Biology*; John Wiley & Sons, Ltd, 2006; pp 221–296. <https://doi.org/10.1002/9780470122778.ch6>.
- (108) Palomo, J. M. Solid-Phase Peptide Synthesis: An Overview Focused on the Preparation of Biologically Relevant Peptides. *RSC Adv.* **2014**, *4* (62), 32658–32672. <https://doi.org/10.1039/C4RA02458C>.
- (109) Wang, L.; Brock, A.; Herberich, B.; Schultz, P. G. Expanding the Genetic Code of Escherichia Coli. *Science* **2001**, *292* (5516), 498–500. <https://doi.org/10.1126/science.1060077>.
- (110) Xie, J.; Schultz, P. G. Adding Amino Acids to the Genetic Repertoire. *Curr. Opin. Chem. Biol.* **2005**, *9* (6), 548–554. <https://doi.org/10.1016/j.cbpa.2005.10.011>.
- (111) Woese, C. R.; Olsen, G. J.; Ibba, M.; Söll, D. Aminoacyl-TRNA Synthetases, the Genetic Code, and the Evolutionary Process. *Microbiol. Mol. Biol. Rev.* **2000**, *64* (1), 202–236. <https://doi.org/10.1128/MMBR.64.1.202-236.2000>.
- (112) Sakamoto, K.; Hayashi, A.; Sakamoto, A.; Kiga, D.; Nakayama, H.; Soma, A.; Kobayashi, T.; Kitabatake, M.; Takio, K.; Saito, K.; et al. Site-specific Incorporation of an Unnatural Amino Acid into Proteins in Mammalian Cells. *Nucleic Acids Res.* **2002**, *30* (21), 4692–4699. <https://doi.org/10.1093/nar/gkf589>.
- (113) Zakeri, B.; Fierer, J. O.; Celik, E.; Chittock, E. C.; Schwarz-Linek, U.; Moy, V. T.; Howarth, M. Peptide Tag Forming a Rapid Covalent Bond to a Protein, through Engineering a Bacterial Adhesin. *Proc. Natl. Acad. Sci.* **2012**, *109* (12), 4347–4348.
- (114) Veggiani, G.; Nakamura, T.; Brenner, M. D.; Gayet, R. V.; Yan, J.; Robinson, C. V.; Howarth, M. Programmable Polyproteins Built Using Twin Peptide Superglues. *Proc. Natl. Acad. Sci.* **2016**, *113* (5), 1202–1207. <https://doi.org/10.1073/pnas.1519214113>.
- (115) Jarvik, J. W.; Telmer, C. A. Epitope Tagging. *Annu. Rev. Genet.* **1998**, *32* (1), 601–618. <https://doi.org/10.1146/annurev.genet.32.1.601>.
- (116) Griffin, B. A.; Adams, S. R.; Tsien, R. Y. Specific Covalent Labeling of Recombinant Protein Molecules Inside Live Cells. *Science* **1998**, *281* (5374), 269–272. <https://doi.org/10.1126/science.281.5374.269>.
- (117) Stanfield, R. L.; Wilson, I. A. Protein-Peptide Interactions. *Curr. Opin. Struct. Biol.* **1995**, *5* (1), 103–113. [https://doi.org/10.1016/0959-440X\(95\)80015-S](https://doi.org/10.1016/0959-440X(95)80015-S).
- (118) Houk, K. N.; Leach, A. G.; Kim, S. P.; Zhang, X. Binding Affinities of Host–Guest, Protein–Ligand, and Protein–Transition-State Complexes. *Angew. Chem. Int. Ed.* **2003**, *42* (40), 4872–4897. <https://doi.org/10.1002/anie.200200565>.

- (119) Allen, K. N.; Imperiali, B. Lanthanide-Tagged Proteins—an Illuminating Partnership. *Curr. Opin. Chem. Biol.* **2010**, *14* (2), 247–254. <https://doi.org/10.1016/j.cbpa.2010.01.004>.
- (120) K. Trilling, A.; Beekwilder, J.; Zuilhof, H. Antibody Orientation on Biosensor Surfaces: A Minireview. *Analyst* **2013**, *138* (6), 1619–1627. <https://doi.org/10.1039/C2AN36787D>.
- (121) Tajima, N.; Takai, M.; Ishihara, K. Significance of Antibody Orientation Unraveled: Well-Oriented Antibodies Recorded High Binding Affinity. *Anal. Chem.* **2011**, *83* (6), 1969–1976. <https://doi.org/10.1021/ac1026786>.
- (122) Wang, T.; Liu, Y. D.; Cai, B.; Huang, G.; Flynn, G. C. Investigation of Antibody Disulfide Reduction and Re-Oxidation and Impact to Biological Activities. *J. Pharm. Biomed. Anal.* **2015**, *102*, 519–528. <https://doi.org/10.1016/j.jpba.2014.10.023>.
- (123) Hutterer, K. M.; Hong, R. W.; Lull, J.; Zhao, X.; Wang, T.; Pei, R.; Le, M. E.; Borisov, O.; Piper, R.; Liu, Y. D.; et al. Monoclonal Antibody Disulfide Reduction during Manufacturing. *mAbs* **2013**, *5* (4), 608–613. <https://doi.org/10.4161/mabs.24725>.
- (124) Xing, Y.; Chaudry, Q.; Shen, C.; Kong, K. Y.; Zhau, H. E.; Chung, L. W.; Petros, J. A.; O'Regan, R. M.; Yezhelyev, M. V.; Simons, J. W.; et al. Bioconjugated Quantum Dots for Multiplexed and Quantitative Immunohistochemistry. *Nat. Protoc.* **2007**, *2* (5), 1152–1165. <https://doi.org/10.1038/nprot.2007.107>.
- (125) LeBeau, A. M.; Duriseti, S.; Murphy, S. T.; Pepin, F.; Hann, B.; Gray, J. W.; VanBrocklin, H. F.; Craik, C. S. Targeting UPAR with Antagonistic Recombinant Human Antibodies in Aggressive Breast Cancer. *Cancer Res.* **2013**, *73* (7), 2070–2081. <https://doi.org/10.1158/0008-5472.CAN-12-3526>.
- (126) LeBeau, A. M.; Sevillano, N.; King, M. L.; Duriseti, S.; Murphy, S. T.; Craik, C. S.; Murphy, L. L.; VanBrocklin, H. F. Imaging the Urokinase Plasminogen Activator Receptor in Preclinical Breast Cancer Models of Acquired Drug Resistance. *Theranostics* **2014**, *4* (3), 267–279. <https://doi.org/10.7150/thno.7323>.
- (127) Harel, E. T.; Drake, P. M.; Barfield, R. M.; Lui, I.; Farr-Jones, S.; Van't Veer, L.; Gartner, Z. J.; Green, E. M.; Lourenço, A. L.; Cheng, Y.; et al. Antibody-Drug Conjugates Targeting the Urokinase Receptor (UPAR) as a Possible Treatment of Aggressive Breast Cancer. *Antibodies* **2019**, *8* (4), 54. <https://doi.org/10.3390/antib8040054>.
- (128) López-Mirabal, H. R.; Winther, J. R. Redox Characteristics of the Eukaryotic Cytosol. *Biochim. Biophys. Acta BBA - Mol. Cell Res.* **2008**, *1783* (4), 629–640. <https://doi.org/10.1016/j.bbamcr.2007.10.013>.
- (129) Saito, G.; Swanson, J. A.; Lee, K.-D. Drug Delivery Strategy Utilizing Conjugation via Reversible Disulfide Linkages: Role and Site of Cellular Reducing

- Activities. *Adv. Drug Deliv. Rev.* **2003**, *55* (2), 199–215.
[https://doi.org/10.1016/S0169-409X\(02\)00179-5](https://doi.org/10.1016/S0169-409X(02)00179-5).
- (130) Seo, M.-D.; Won, H.-S.; Kim, J.-H.; Mishig-Ochir, T.; Lee, B.-J. Antimicrobial Peptides for Therapeutic Applications: A Review. *Molecules* **2012**, *17* (10), 12276–12286. <https://doi.org/10.3390/molecules171012276>.
- (131) Gaspar, D.; Veiga, A. S.; Castanho, M. A. R. B. From Antimicrobial to Anticancer Peptides. A Review. *Front. Microbiol.* **2013**, *4*.
<https://doi.org/10.3389/fmicb.2013.00294>.
- (132) Li, M.; Tao, Y.; Shu, Y.; LaRochelle, J. R.; Steinauer, A.; Thompson, D.; Schepartz, A.; Chen, Z.-Y.; Liu, D. R. Discovery and Characterization of a Peptide That Enhances Endosomal Escape of Delivered Proteins in Vitro and in Vivo. *J. Am. Chem. Soc.* **2015**, *137* (44), 14084–14093.
<https://doi.org/10.1021/jacs.5b05694>.
- (133) I. Fernandez, D.; Brun, A. P. L.; C. Whitwell, T.; Sani, M.-A.; James, M.; Separovic, F. The Antimicrobial Peptide Aurein 1.2 Disrupts Model Membranes via the Carpet Mechanism. *Phys. Chem. Chem. Phys.* **2012**, *14* (45), 15739–15751.
<https://doi.org/10.1039/C2CP43099A>.
- (134) Shahmiri, M.; Enciso, M.; Mechler, A. Controls and Constrains of the Membrane Disrupting Action of Aurein 1.2. *Sci. Rep.* **2015**, *5*, 16378.
<https://doi.org/10.1038/srep16378>.
- (135) Koh, I.; Wang, X.; Varughese, B.; Isaacs, L.; Ehrman, S. H.; English, D. S. Magnetic Iron Oxide Nanoparticles for Biorecognition: Evaluation of Surface Coverage and Activity. *J. Phys. Chem. B* **2006**, *110* (4), 1553–1558.
<https://doi.org/10.1021/jp0556310>.
- (136) Saha, B.; Evers, T. H.; Prins, M. W. J. How Antibody Surface Coverage on Nanoparticles Determines the Activity and Kinetics of Antigen Capturing for Biosensing. *Anal. Chem.* **2014**, *86* (16), 8158–8166.
<https://doi.org/10.1021/ac501536z>.
- (137) Jazayeri, M. H.; Amani, H.; Pourfatollah, A. A.; Pazoki-Toroudi, H.; Sedighimoghaddam, B. Various Methods of Gold Nanoparticles (GNPs) Conjugation to Antibodies. *Sens. Bio-Sens. Res.* **2016**, *9*, 17–22.
<https://doi.org/10.1016/j.sbsr.2016.04.002>.
- (138) Kim, M. T.; Chen, Y.; Marhoul, J.; Jacobson, F. Statistical Modeling of the Drug Load Distribution on Trastuzumab Emtansine (Kadcyla), a Lysine-Linked Antibody Drug Conjugate. *Bioconjug. Chem.* **2014**, *25* (7), 1223–1232.
<https://doi.org/10.1021/bc5000109>.
- (139) Phillips, G. D. L.; Li, G.; Dugger, D. L.; Crocker, L. M.; Parsons, K. L.; Mai, E.; Blättler, W. A.; Lambert, J. M.; Chari, R. V. J.; Lutz, R. J.; et al. Targeting HER2-Positive Breast Cancer with Trastuzumab-DM1, an Antibody–Cytotoxic Drug

- Conjugate. *Cancer Res.* **2008**, *68* (22), 9280–9290. <https://doi.org/10.1158/0008-5472.CAN-08-1776>.
- (140) Wang, L.; Amphlett, G.; Blättler, W. A.; Lambert, J. M.; Zhang, W. Structural Characterization of the Maytansinoid–Monoclonal Antibody Immunoconjugate, HuN901–DM1, by Mass Spectrometry. *Protein Sci.* **2005**, *14* (9), 2436–2446. <https://doi.org/10.1110/ps.051478705>.
- (141) Senter, P. D. Potent Antibody Drug Conjugates for Cancer Therapy. *Curr. Opin. Chem. Biol.* **2009**, *13* (3), 235–244. <https://doi.org/10.1016/j.cbpa.2009.03.023>.
- (142) Dean, D. D.; Martel-Pelletier, J.; Pelletier, J. P.; Howell, D. S.; Woessner, J. F. Evidence for Metalloproteinase and Metalloproteinase Inhibitor Imbalance in Human Osteoarthritic Cartilage. *J. Clin. Invest.* **1989**, *84* (2), 678–685. <https://doi.org/10.1172/JCI114215>.
- (143) Thompson, J. M.; Agee, K.; Sidow, S. J.; McNally, K.; Lindsey, K.; Borke, J.; Elsalanty, M.; Tay, F. R.; Pashley, D. H. Inhibition of Endogenous Dentin Matrix Metalloproteinases by Ethylenediaminetetraacetic Acid. *J. Endod.* **2012**, *38* (1), 62–65. <https://doi.org/10.1016/j.joen.2011.09.005>.
- (144) Ho, S. N.; Hunt, H. D.; Horton, R. M.; Pullen, J. K.; Pease, L. R. Site-Directed Mutagenesis by Overlap Extension Using the Polymerase Chain Reaction. *Gene* **1989**, *77* (1), 51–59. [https://doi.org/10.1016/0378-1119\(89\)90358-2](https://doi.org/10.1016/0378-1119(89)90358-2).
- (145) Stols, L.; Gu, M.; Dieckman, L.; Raffin, R.; Collart, F. R.; Donnelly, M. I. A New Vector for High-Throughput, Ligation-Independent Cloning Encoding a Tobacco Etch Virus Protease Cleavage Site. *Protein Expr. Purif.* **2002**, *25* (1), 8–15. <https://doi.org/10.1006/pep.2001.1603>.
- (146) Tropea, J. E.; Cherry, S.; Waugh, D. S. Expression and Purification of Soluble His6-Tagged TEV Protease. In *High Throughput Protein Expression and Purification: Methods and Protocols*; Doyle, S. A., Ed.; Methods in Molecular Biology; Humana Press: Totowa, NJ, 2009; pp 297–307. https://doi.org/10.1007/978-1-59745-196-3_19.
- (147) Waugh, D. S. An Overview of Enzymatic Reagents for the Removal of Affinity Tags. *Protein Expr. Purif.* **2011**, *80* (2), 283–293. <https://doi.org/10.1016/j.pep.2011.08.005>.
- (148) Vivian, J. T.; Callis, P. R. Mechanisms of Tryptophan Fluorescence Shifts in Proteins. *Biophys. J.* **2001**, *80* (5), 2093–2109. [https://doi.org/10.1016/S0006-3495\(01\)76183-8](https://doi.org/10.1016/S0006-3495(01)76183-8).
- (149) Ghisaidoobe, A. B. T.; Chung, S. J. Intrinsic Tryptophan Fluorescence in the Detection and Analysis of Proteins: A Focus on Förster Resonance Energy Transfer Techniques. *Int. J. Mol. Sci.* **2014**, *15* (12), 22518–22538. <https://doi.org/10.3390/ijms151222518>.

- (150) Sedlak, J.; Lindsay, R. H. Estimation of Total, Protein-Bound, and Nonprotein Sulfhydryl Groups in Tissue with Ellman's Reagent. *Anal. Biochem.* **1968**, *25*, 192–205. [https://doi.org/10.1016/0003-2697\(68\)90092-4](https://doi.org/10.1016/0003-2697(68)90092-4).
- (151) Habeeb, A. F. S. A. Reaction of Protein Sulfhydryl Groups with Ellman's Reagent. In *Methods in Enzymology*; Enzyme Structure, Part B; Academic Press, 1972; Vol. 25, pp 457–464. [https://doi.org/10.1016/S0076-6879\(72\)25041-8](https://doi.org/10.1016/S0076-6879(72)25041-8).
- (152) Egorov, T. A.; Svenson, A.; Rydén, L.; Carlsson, J. A Rapid and Specific Method for Isolation of Thiol-Containing Peptides from Large Proteins by Thiol-Disulfide Exchange on a Solid Support. *Proc. Natl. Acad. Sci.* **1975**, *72* (8), 3029–3033. <https://doi.org/10.1073/pnas.72.8.3029>.
- (153) DeCollo, T. V.; Lees, W. J. Effects of Aromatic Thiols on Thiol–Disulfide Interchange Reactions That Occur during Protein Folding. *J. Org. Chem.* **2001**, *66* (12), 4244–4249. <https://doi.org/10.1021/jo015600a>.
- (154) Cailleau, R.; Olivé, M.; Cruciger, Q. V. J. Long-Term Human Breast Carcinoma Cell Lines of Metastatic Origin: Preliminary Characterization. *In Vitro* **1978**, *14* (11), 911–915. <https://doi.org/10.1007/BF02616120>.
- (155) Holst-Hansen, C.; Johannessen, B.; Hoyer-Hansen, G.; Romer, J.; Ellis, V.; Brüner, N. Urokinase-Type Plasminogen Activation in Three Human Breast Cancer Cell Lines Correlates with Their in Vitro Invasiveness. *Clin. Exp. Metastasis* **1996**, *14* (3), 297–307. <https://doi.org/10.1007/BF00053903>.
- (156) Long, B. J.; Rose, D. P. Invasive Capacity and Regulation of Urokinase-Type Plasminogen Activator in Estrogen Receptor (ER)-Negative MDA-MB-231 Human Breast Cancer Cells, and a Transfectant (S30) Stably Expressing ER. *Cancer Lett.* **1996**, *99* (2), 209–215. [https://doi.org/10.1016/0304-3835\(95\)04066-8](https://doi.org/10.1016/0304-3835(95)04066-8).
- (157) Yoon, S. Y.; Lee, Y. J.; Seo, J. H.; Sung, H. J.; Park, K. H.; Choi, I. K.; Kim, S. J.; Oh, S. C.; Choi, C. W.; Kim, B. S.; et al. UPAR Expression under Hypoxic Conditions Depends on INOS Modulated ERK Phosphorylation in the MDA-MB-231 Breast Carcinoma Cell Line. *Cell Res.* **2006**, *16* (1), 75–81. <https://doi.org/10.1038/sj.cr.7310010>.
- (158) Ahmad, Z. A.; Yeap, S. K.; Ali, A. M.; Ho, W. Y.; Alitheen, N. B. M.; Hamid, M. scFv Antibody: Principles and Clinical Application <https://www.hindawi.com/journals/jir/2012/980250/> (accessed Oct 22, 2019). <https://doi.org/10.1155/2012/980250>.
- (159) Jacques, S.; Alter, C. A.; Prahl, S. A. Angular Dependence of HeNe Laser Light Scattering by Human Dermis. *Lasers Life Sci.* **1988**, *2* (4), 309–333.
- (160) Wang, L.; Jackson, W. C.; Steinbach, P. A.; Tsien, R. Y. Evolution of New Nonantibody Proteins via Iterative Somatic Hypermutation. *Proc. Natl. Acad. Sci.* **2004**, *101* (48), 16745–16749. <https://doi.org/10.1073/pnas.0407752101>.

- (161) Yoon, E.; Konold, P. E.; Lee, J.; Joo, T.; Jimenez, R. Far-Red Emission of MPlum Fluorescent Protein Results from Excited-State Interconversion between Chromophore Hydrogen-Bonding States. *J. Phys. Chem. Lett.* **2016**, *7* (12), 2170–2174. <https://doi.org/10.1021/acs.jpcc.6b00823>.
- (162) Faraji, S.; Krylov, A. I. On the Nature of an Extended Stokes Shift in the MPlum Fluorescent Protein. *J. Phys. Chem. B* **2015**, *119* (41), 13052–13062. <https://doi.org/10.1021/acs.jpcc.5b07724>.
- (163) Nagai, T.; Ibata, K.; Park, E. S.; Kubota, M.; Mikoshiba, K.; Miyawaki, A. A Variant of Yellow Fluorescent Protein with Fast and Efficient Maturation for Cell-Biological Applications. *Nat. Biotechnol.* **2002**, *20* (1), 87–90. <https://doi.org/10.1038/nbt0102-87>.
- (164) Stepanenko, O. V.; Stepanenko, O. V.; Shcherbakova, D. M.; Kuznetsova, I. M.; Turoverov, K. K.; Verkhusha, V. V. Modern Fluorescent Proteins: From Chromophore Formation to Novel Intracellular Applications. *BioTechniques* **2011**, *51* (5), 313–327. <https://doi.org/10.2144/000113765>.
- (165) Miyawaki, A.; Shcherbakova, D. M.; Verkhusha, V. V. Red Fluorescent Proteins: Chromophore Formation and Cellular Applications. *Curr. Opin. Struct. Biol.* **2012**, *22* (5), 679–688. <https://doi.org/10.1016/j.sbi.2012.09.002>.
- (166) Moore, M. M.; Oteng-Pabi, S. K.; Pandelieva, A. T.; Mayo, S. L.; Chica, R. A. Recovery of Red Fluorescent Protein Chromophore Maturation Deficiency through Rational Design. *PLOS ONE* **2012**, *7* (12), e52463. <https://doi.org/10.1371/journal.pone.0052463>.
- (167) Shaner, N. C.; Campbell, R. E.; Steinbach, P. A.; Giepmans, B. N. G.; Palmer, A. E.; Tsien, R. Y. Improved Monomeric Red, Orange and Yellow Fluorescent Proteins Derived from *Discosoma* Sp. Red Fluorescent Protein. *Nat. Biotechnol.* **2004**, *22* (12), 1567–1572. <https://doi.org/10.1038/nbt1037>.
- (168) Shaner, N. C.; Steinbach, P. A.; Tsien, R. Y. A Guide to Choosing Fluorescent Proteins. *Nat. Methods* **2005**, *2* (12), 905–909. <https://doi.org/10.1038/nmeth819>.
- (169) Day, R. N.; Davidson, M. W. The Fluorescent Protein Palette: Tools for Cellular Imaging. *Chem. Soc. Rev.* **2009**, *38* (10), 2887–2921. <https://doi.org/10.1039/B901966A>.
- (170) Shen, Y.; Chen, Y.; Wu, J.; Shaner, N. C.; Campbell, R. E. Engineering of MCherry Variants with Long Stokes Shift, Red-Shifted Fluorescence, and Low Cytotoxicity. *PLOS ONE* **2017**, *12* (2), e0171257. <https://doi.org/10.1371/journal.pone.0171257>.
- (171) Gebhardt, M. J.; Jacobson, R. K.; Shuman, H. A. Seeing Red; the Development of PON.MCherry, a Broad-Host Range Constitutive Expression Plasmid for Gram-Negative Bacteria. *PLOS ONE* **2017**, *12* (3), e0173116. <https://doi.org/10.1371/journal.pone.0173116>.

- (172) Tan, L. L.; Hoon, S. S.; Wong, F. T. Kinetic Controlled Tag-Catcher Interactions for Directed Covalent Protein Assembly. *PLOS ONE* **2016**, *11* (10), e0165074. <https://doi.org/10.1371/journal.pone.0165074>.
- (173) Sun, J.; Wang, Y.; Liao, J. Tailoring Two-Dimensional Nanoparticle Arrays into Various Patterns. *Nanotechnology* **2017**, *29* (4), 044003. <https://doi.org/10.1088/1361-6528/aa9ab3>.
- (174) Tian, Y.; Wang, T.; Liu, W.; Xin, H. L.; Li, H.; Ke, Y.; Shih, W. M.; Gang, O. Prescribed Nanoparticle Cluster Architectures and Low-Dimensional Arrays Built Using Octahedral DNA Origami Frames. *Nat. Nanotechnol.* **2015**, *10* (7), 637–644. <https://doi.org/10.1038/nnano.2015.105>.
- (175) Shipway, A. N.; Katz, E.; Willner, I. Nanoparticle Arrays on Surfaces for Electronic, Optical, and Sensor Applications. *ChemPhysChem* **2000**, *1* (1), 18–52. [https://doi.org/10.1002/1439-7641\(20000804\)1:1<18::AID-CPHC18>3.0.CO;2-L](https://doi.org/10.1002/1439-7641(20000804)1:1<18::AID-CPHC18>3.0.CO;2-L).
- (176) Daniel, M.-C.; Astruc, D. Gold Nanoparticles: Assembly, Supramolecular Chemistry, Quantum-Size-Related Properties, and Applications toward Biology, Catalysis, and Nanotechnology. *Chem. Rev.* **2004**, *104* (1), 293–346. <https://doi.org/10.1021/cr030698+>.
- (177) Zheng, J.; Constantinou, P. E.; Micheel, C.; Alivisatos, A. P.; Kiehl, R. A.; Seeman, N. C. Two-Dimensional Nanoparticle Arrays Show the Organizational Power of Robust DNA Motifs. *Nano Lett.* **2006**, *6* (7), 1502–1504. <https://doi.org/10.1021/nl060994c>.
- (178) Kuzyk, A.; Schreiber, R.; Fan, Z.; Pardatscher, G.; Roller, E.-M.; Högele, A.; Simmel, F. C.; Govorov, A. O.; Liedl, T. DNA-Based Self-Assembly of Chiral Plasmonic Nanostructures with Tailored Optical Response. *Nature* **2012**, *483* (7389), 311–314. <https://doi.org/10.1038/nature10889>.
- (179) Roller, E.-M.; Besteiro, L. V.; Pupp, C.; Khorashad, L. K.; Govorov, A. O.; Liedl, T. Hotspot-Mediated Non-Dissipative and Ultrafast Plasmon Passage. *Nat. Phys.* **2017**, *13* (8), 761–765. <https://doi.org/10.1038/nphys4120>.
- (180) Hong, S. H.; Hegde, M.; Kim, J.; Wang, X.; Jayaraman, A.; Wood, T. K. Synthetic Quorum-Sensing Circuit to Control Consortial Biofilm Formation and Dispersal in a Microfluidic Device. *Nat. Commun.* **2012**, *3* (1), 1–8. <https://doi.org/10.1038/ncomms1616>.
- (181) Azam, A.; Tullman-Ereck, D. Type-III Secretion Filaments as Scaffolds for Inorganic Nanostructures. *J. R. Soc. Interface* **2016**, *13* (114), 20150938. <https://doi.org/10.1098/rsif.2015.0938>.
- (182) Botyanszki, Z.; Tay, P. K. R.; Nguyen, P. Q.; Nussbaumer, M. G.; Joshi, N. S. Engineered Catalytic Biofilms: Site-Specific Enzyme Immobilization onto E. Coli Curli Nanofibers. *Biotechnol. Bioeng.* **2015**, *112* (10), 2016–2024. <https://doi.org/10.1002/bit.25638>.

- (183) Treuel, L.; Nienhaus, G. U. Toward a Molecular Understanding of Nanoparticle–Protein Interactions. *Biophys. Rev.* **2012**, *4* (2), 137–147. <https://doi.org/10.1007/s12551-012-0072-0>.
- (184) Sleytr, U. B.; Beveridge, T. J. Bacterial S-Layers. *Trends Microbiol.* **1999**, *7* (6), 253–260. [https://doi.org/10.1016/S0966-842X\(99\)01513-9](https://doi.org/10.1016/S0966-842X(99)01513-9).
- (185) Fagan, R. P.; Fairweather, N. F. Biogenesis and Functions of Bacterial S-Layers. *Nat. Rev. Microbiol.* **2014**, *12* (3), 211–222. <https://doi.org/10.1038/nrmicro3213>.
- (186) Rad, B.; Haxton, T. K.; Shon, A.; Shin, S.-H.; Whitlam, S.; Ajo-Franklin, C. M. Ion-Specific Control of the Self-Assembly Dynamics of a Nanostructured Protein Lattice. *ACS Nano* **2015**, *9* (1), 180–190. <https://doi.org/10.1021/nn502992x>.
- (187) Engelhardt, H.; Peters, J. Structural Research on Surface Layers: A Focus on Stability, Surface Layer Homology Domains, and Surface Layer–Cell Wall Interactions. *J. Struct. Biol.* **1998**, *124* (2), 276–302. <https://doi.org/10.1006/jsbi.1998.4070>.
- (188) Shenton, W.; Pum, D.; Sleytr, U. B.; Mann, S. Synthesis of Cadmium Sulphide Superlattices Using Self-Assembled Bacterial S-Layers. *Nature* **1997**, *389* (6651), 585–587. <https://doi.org/10.1038/39287>.
- (189) Hall, S. R.; Shenton, W.; Engelhardt, H.; Mann, S. Site-Specific Organization of Gold Nanoparticles by Biomolecular Templating. *ChemPhysChem* **2001**, *2* (3), 184–186. [https://doi.org/10.1002/1439-7641\(20010316\)2:3<184::AID-CPHC184>3.0.CO;2-J](https://doi.org/10.1002/1439-7641(20010316)2:3<184::AID-CPHC184>3.0.CO;2-J).
- (190) Mark, S. S.; Bergkvist, M.; Yang, X.; Teixeira, L. M.; Bhatnagar, P.; Angert, E. R.; Batt, C. A. Bionanofabrication of Metallic and Semiconductor Nanoparticle Arrays Using S-Layer Protein Lattices with Different Lateral Spacings and Geometries. *Langmuir* **2006**, *22* (8), 3763–3774. <https://doi.org/10.1021/la053115v>.
- (191) Baranova, E.; Fronzes, R.; Garcia-Pino, A.; Van Gerven, N.; Papapostolou, D.; Péhau-Arnaudet, G.; Pardon, E.; Steyaert, J.; Howorka, S.; Remaut, H. SbsB Structure and Lattice Reconstruction Unveil Ca²⁺ Triggered S-Layer Assembly. *Nature* **2012**, *487* (7405), 119–122. <https://doi.org/10.1038/nature11155>.
- (192) Sleytr, U. B.; Sára, M. Bacterial and Archaeal S-Layer Proteins: Structure-Function Relationships and Their Biotechnological Applications. *Trends Biotechnol.* **1997**, *15* (1), 20–26. [https://doi.org/10.1016/S0167-7799\(96\)10063-9](https://doi.org/10.1016/S0167-7799(96)10063-9).
- (193) Burg, K. J. L.; Porter, S.; Kellam, J. F. Biomaterial Developments for Bone Tissue Engineering. *Biomaterials* **2000**, *21* (23), 2347–2359. [https://doi.org/10.1016/S0142-9612\(00\)00102-2](https://doi.org/10.1016/S0142-9612(00)00102-2).
- (194) Sheppard, C.; Davy, S.; Pilling, G.; Graham, N. *The Biology of Coral Reefs*, Second Edition.; Biology of Habitats Series; Oxford University Press: Oxford, New York, 2018.

- (195) Nguyen, P. Q.; Courchesne, N.-M. D.; Duraj-Thatte, A.; Praveschotinunt, P.; Joshi, N. S. Engineered Living Materials: Prospects and Challenges for Using Biological Systems to Direct the Assembly of Smart Materials. *Adv. Mater.* **2018**, *30* (19), 1704847. <https://doi.org/10.1002/adma.201704847>.
- (196) Goldfield, E. C. *Bioinspired Devices*; Harvard University Press, 2018.
- (197) Chen, A. Y.; Zhong, C.; Lu, T. K. Engineering Living Functional Materials. *ACS Synth. Biol.* **2015**, *4* (1), 8–11. <https://doi.org/10.1021/sb500113b>.
- (198) Sleytr, U. B.; Schuster, B.; Egelseer, E.-M.; Pum, D. S-Layers: Principles and Applications. *FEMS Microbiol. Rev.* **2014**, *38* (5), 823–864. <https://doi.org/10.1111/1574-6976.12063>.
- (199) Madhurantakam, C.; Howorka, S.; Remaut, H. S-Layer Structure in Bacteria and Archaea. In *Nanomicrobiology*; Springer: New York, NY, 2014.
- (200) Mark, S. S.; Bergkvist, M.; Yang, X.; Angert, E. R.; Batt, C. A. Self-Assembly of Dendrimer-Encapsulated Nanoparticle Arrays Using 2-D Microbial S-Layer Protein Biotemplates. *Biomacromolecules* **2006**, *7* (6), 1884–1897. <https://doi.org/10.1021/bm0603185>.
- (201) Pum, D.; Toca-Herrera, J. L.; Sleytr, U. B. S-Layer Protein Self-Assembly. *Int. J. Mol. Sci.* **2013**, *14* (2), 2484–2501. <https://doi.org/10.3390/ijms14022484>.
- (202) Sleytr, U. B.; Schuster, B.; Egelseer, E. M.; Pum, D.; Horejs, C. M.; Tscheliessnig, R.; Ilk, N. Nanobiotechnology with S-Layer Proteins as Building Blocks. In *Progress in Molecular Biology and Translational Science*; Howorka, S., Ed.; Molecular Assembly in Natural and Engineered Systems; Academic Press, 2011; Vol. 103, pp 277–352. <https://doi.org/10.1016/B978-0-12-415906-8.00003-0>.
- (203) Chung, S.; Shin, S.-H.; Bertozzi, C. R.; Yoreo, J. J. D. Self-Catalyzed Growth of S Layers via an Amorphous-to-Crystalline Transition Limited by Folding Kinetics. *Proc. Natl. Acad. Sci.* **2010**, *107* (38), 16536–16541. <https://doi.org/10.1073/pnas.1008280107>.
- (204) Rad, B.; Haxton, T.; Shin, S.-H.; Whitelam, S.; Ajo-Franklin, C. Self Assembly Pathways of Surface-Layer Proteins. *Biophys. J.* **2012**, *102* (3), 261a. <https://doi.org/10.1016/j.bpj.2011.11.1437>.
- (205) Ilk, N.; Egelseer, E. M.; Sleytr, U. B. S-Layer Fusion Proteins--Construction Principles and Applications. *Curr. Opin. Biotechnol.* **2011**, *22* (6), 824–831. <https://doi.org/10.1016/j.copbio.2011.05.510>.
- (206) Schuster, B.; Sleytr, U. B. Biomimetic Interfaces Based on S-Layer Proteins, Lipid Membranes and Functional Biomolecules. *J. R. Soc. Interface* **2014**, *11* (96), 20140232. <https://doi.org/10.1098/rsif.2014.0232>.
- (207) Aichmayer, B.; Mertig, M.; Kirchner, A.; Paris, O.; Fratzl, P. Small-Angle Scattering of S-Layer Metallization. *Adv. Mater.* **2006**, *18* (7), 915–919. <https://doi.org/10.1002/adma.200501646>.

- (208) Shin, S. H.; Comolli, L. R.; Tscheliessnig, R.; Wang, C.; Nam, K. T.; Hexemer, A.; Siegerist, C. E.; De, J. Y.; Bertozzi, C. R. Self-Assembly of “S-Bilayers”, a Step toward Expanding the Dimensionality of S-Layer Assemblies. *ACS Nano* **2013**, *7* (6), 4946–4953. <https://doi.org/10.1021/nn400263j>.
- (209) Habibi, N.; Pastorino, L.; Soumetz, F. C.; Sbrana, F.; Raiteri, R.; Ruggiero, C. Nanoengineered Polymeric S-Layers Based Capsules with Targeting Activity. *Colloids Surf. B Biointerfaces* **2011**, *88* (1), 366–372. <https://doi.org/10.1016/j.colsurfb.2011.07.015>.
- (210) Ladenhauf, E. M.; Pum, D.; Wastl, D. S.; Toca-Herrera, J. L.; Phan, N. V. H.; Lieberzeit, P. A.; Sleytr, U. B. S-Layer Based Biomolecular Imprinting. *RSC Adv.* **2015**, *5* (102), 83558–83564. <https://doi.org/10.1039/C5RA14971A>.
- (211) Rothbauer, M.; Küpcü, S.; Sticker, D.; Sleytr, U. B.; Ertl, P. Exploitation of S-Layer Anisotropy: PH-Dependent Nanolayer Orientation for Cellular Micropatterning. *ACS Nano* **2013**, *7* (9), 8020–8030. <https://doi.org/10.1021/nn403198a>.
- (212) Bodenmiller, D.; Toh, E.; Brun, Y. V. Development of Surface Adhesion in *Caulobacter Crescentus*. *J. Bacteriol.* **2004**, *186* (5), 1438–1447. <https://doi.org/10.1128/JB.186.5.1438-1447.2004>.
- (213) Walker, S. G.; Smith, S. H.; Smit, J. Isolation and Comparison of the Paracrystalline Surface Layer Proteins of Freshwater *Caulobacters*. *J. Bacteriol.* **1992**, *174* (6), 1783–1792. <https://doi.org/10.1128/jb.174.6.1783-1792.1992>.
- (214) Herrmann, J.; Jabbarpour, F.; Bargar, P. G.; Nomellini, J. F.; Li, P.-N.; Lane, T. J.; Weiss, T. M.; Smit, J.; Shapiro, L.; Wakatsuki, S. Environmental Calcium Controls Alternate Physical States of the *Caulobacter* Surface Layer. *Biophys. J.* **2017**, *112* (9), 1841–1851. <https://doi.org/10.1016/j.bpj.2017.04.003>.
- (215) Bharat, T. A. M.; Kureisaite-Ciziene, D.; Hardy, G. G.; Yu, E. W.; Devant, J. M.; Hagen, W. J. H.; Brun, Y. V.; Briggs, J. A. G.; Löwe, J. Structure of the Hexagonal Surface Layer on *Caulobacter Crescentus* Cells. *Nat. Microbiol.* **2017**, *2* (7), 1–6. <https://doi.org/10.1038/nmicrobiol.2017.59>.
- (216) Patel, J.; Zhang, Q.; McKay, R. M. L.; Vincent, R.; Xu, Z. Genetic Engineering of *Caulobacter Crescentus* for Removal of Cadmium from Water. *Appl. Biochem. Biotechnol.* **2010**, *160* (1), 232–243. <https://doi.org/10.1007/s12010-009-8540-0>.
- (217) Howorka, S.; Sára, M.; Wang, Y.; Kuen, B.; Sleytr, U. B.; Lubitz, W.; Bayley, H. Surface-Accessible Residues in the Monomeric and Assembled Forms of a Bacterial Surface Layer Protein. *J. Biol. Chem.* **2000**, *275* (48), 37876–37886. <https://doi.org/10.1074/jbc.M003838200>.
- (218) Manea, F.; Garda, V. G.; Rad, B.; Ajo-Franklin, C. M. Programmable Assembly of 2D Crystalline Protein Arrays into Covalently Stacked 3D Bionanomaterials. *Biotechnol. Bioeng.* **2019**, *Under Review*.

- (219) Tajon, C. A.; Yang, H.; Tian, B.; Tian, Y.; Ercius, P.; Schuck, P. J.; Chan, E. M.; Cohen, B. E. Photostable and Efficient Upconverting Nanocrystal-Based Chemical Sensors. *Opt. Mater.* **2018**, *84*, 345–353. <https://doi.org/10.1016/j.optmat.2018.07.031>.
- (220) Purcell, E. M. Proceedings of the American Physical Society. *Phys. Rev.* **1946**, *69* (11–12), 674–674. <https://doi.org/10.1103/PhysRev.69.674>.
- (221) Ratchford, D.; Shafiei, F.; Kim, S.; Gray, S. K.; Li, X. Manipulating Coupling between a Single Semiconductor Quantum Dot and Single Gold Nanoparticle. *Nano Lett.* **2011**, *11* (3), 1049–1054. <https://doi.org/10.1021/nl103906f>.
- (222) Chen, A. Y.; Deng, Z.; Billings, A. N.; Seker, U. O. S.; Lu, M. Y.; Citorik, R. J.; Zakeri, B.; Lu, T. K. Synthesis and Patterning of Tunable Multiscale Materials with Engineered Cells. *Nat. Mater.* **2014**, *13* (5), 515–523. <https://doi.org/10.1038/nmat3912>.
- (223) Ding, B.; Deng, Z.; Yan, H.; Cabrini, S.; Zuckermann, R. N.; Bokor, J. Gold Nanoparticle Self-Similar Chain Structure Organized by DNA Origami. *J. Am. Chem. Soc.* **2010**, *132* (10), 3248–3249. <https://doi.org/10.1021/ja9101198>.
- (224) Ghosh, D.; Lee, Y.; Thomas, S.; Kohli, A. G.; Yun, D. S.; Belcher, A. M.; Kelly, K. A. M13-Templated Magnetic Nanoparticles for Targeted in Vivo Imaging of Prostate Cancer. *Nat. Nanotechnol.* **2012**, *7* (10), 677–682. <https://doi.org/10.1038/nnano.2012.146>.
- (225) Souza, G. R.; Christianson, D. R.; Staquicini, F. I.; Ozawa, M. G.; Snyder, E. Y.; Sidman, R. L.; Miller, J. H.; Arap, W.; Pasqualini, R. Networks of Gold Nanoparticles and Bacteriophage as Biological Sensors and Cell-Targeting Agents. *Proc. Natl. Acad. Sci.* **2006**, *103* (5), 1215–1220. <https://doi.org/10.1073/pnas.0509739103>.
- (226) Charrier, M.; Li, D.; Mann, V. R.; Yun, L.; Jani, S.; Rad, B.; Cohen, B. E.; Ashby, P. D.; Ryan, K. R.; Ajo-Franklin, C. M. Engineering the S-Layer of *Caulobacter Crescentus* as a Foundation for Stable, High-Density, 2D Living Materials. *ACS Synth. Biol.* **2019**, *8* (1), 181–190. <https://doi.org/10.1021/acssynbio.8b00448>.
- (227) Stuart, M. A. C.; Huck, W. T. S.; Genzer, J.; Müller, M.; Ober, C.; Stamm, M.; Sukhorukov, G. B.; Szleifer, I.; Tsukruk, V. V.; Urban, M.; et al. Emerging Applications of Stimuli-Responsive Polymer Materials. *Nat. Mater.* **2010**, *9* (2), 101–113. <https://doi.org/10.1038/nmat2614>.
- (228) Axpe, E.; Duraj-Thatte, A.; Chang, Y.; Kaimaki, D.-M.; Sanchez-Sanchez, A.; Caliskan, H. B.; Dorval Courchesne, N.-M.; Joshi, N. S. Fabrication of Amyloid Curli Fibers–Alginate Nanocomposite Hydrogels with Enhanced Stiffness. *ACS Biomater. Sci. Eng.* **2018**, *4* (6), 2100–2105. <https://doi.org/10.1021/acsbiomaterials.8b00364>.
- (229) Sun, F.; Zhang, W.-B.; Mahdavi, A.; Arnold, F. H.; Tirrell, D. A. Synthesis of Bioactive Protein Hydrogels by Genetically Encoded SpyTag-SpyCatcher

- Chemistry. *Proc. Natl. Acad. Sci.* **2014**, *111* (31), 11269–11274.
<https://doi.org/10.1073/pnas.1401291111>.
- (230) Gonzalez, M. A.; Simon, J. R.; Ghoorchian, A.; Scholl, Z.; Lin, S.; Rubinstein, M.; Marszalek, P.; Chilkoti, A.; López, G. P.; Zhao, X. Strong, Tough, Stretchable, and Self-Adhesive Hydrogels from Intrinsically Unstructured Proteins. *Adv. Mater.* **2017**, *29* (10), 1604743. <https://doi.org/10.1002/adma.201604743>.
- (231) Attard, P. Measurement and Interpretation of Elastic and Viscoelastic Properties with the Atomic Force Microscope. *J. Phys. Condens. Matter* **2007**, *19* (47), 473201. <https://doi.org/10.1088/0953-8984/19/47/473201>.
- (232) Nawaz, S.; Sánchez, P.; Bodensiek, K.; Li, S.; Simons, M.; Schaap, I. A. T. Cell Visco-Elasticity Measured with AFM and Optical Trapping at Sub-Micrometer Deformations. *PLOS ONE* **2012**, *7* (9), e45297. <https://doi.org/10.1371/journal.pone.0045297>.
- (233) Lau, P. C. Y.; Dutcher, J. R.; Beveridge, T. J.; Lam, J. S. Absolute Quantitation of Bacterial Biofilm Adhesion and Viscoelasticity by Microbead Force Spectroscopy. *Biophys. J.* **2009**, *96* (7), 2935–2948. <https://doi.org/10.1016/j.bpj.2008.12.3943>.
- (234) Alsteens, D.; Gaub, H. E.; Newton, R.; Pfreundschuh, M.; Gerber, C.; Müller, D. J. Atomic Force Microscopy-Based Characterization and Design of Biointerfaces. *Nat. Rev. Mater.* **2017**, *2* (5), 1–16. <https://doi.org/10.1038/natrevmats.2017.8>.
- (235) Ragazzon, M. R. P.; Gravidahl, J. T.; Vagia, M. Viscoelastic Properties of Cells: Modeling and Identification by Atomic Force Microscopy. *Mechatronics* **2018**, *50*, 271–281. <https://doi.org/10.1016/j.mechatronics.2017.09.011>.
- (236) Ashby, P. D. Gentle Imaging of Soft Materials in Solution with Amplitude Modulation Atomic Force Microscopy: Q Control and Thermal Noise. *Appl. Phys. Lett.* **2007**, *91* (25), 254102. <https://doi.org/10.1063/1.2824576>.
- (237) Sretenovic, S.; Stojković, B.; Dogsa, I.; Kostanjšek, R.; Poberaj, I.; Stopar, D. An Early Mechanical Coupling of Planktonic Bacteria in Dilute Suspensions. *Nat. Commun.* **2017**, *8* (1), 1–10. <https://doi.org/10.1038/s41467-017-00295-z>.
- (238) Gardel, M. L.; Shin, J. H.; MacKintosh, F. C.; Mahadevan, L.; Matsudaira, P.; Weitz, D. A. Elastic Behavior of Cross-Linked and Bundled Actin Networks. *Science* **2004**, *304* (5675), 1301–1305. <https://doi.org/10.1126/science.1095087>.
- (239) Norville, J. E.; Kelly, D. F.; Knight, T. F.; Belcher, A. M.; Walz, T. Fast and Easy Protocol for the Purification of Recombinant S-Layer Protein for Synthetic Biology Applications. *Biotechnol. J.* **2011**, *6* (7), 807–811. <https://doi.org/10.1002/biot.201100024>.
- (240) Schindelin, J.; Arganda-Carreras, I.; Frise, E.; Kaynig, V.; Longair, M.; Pietzsch, T.; Preibisch, S.; Rueden, C.; Saalfeld, S.; Schmid, B.; et al. Fiji: An Open-Source Platform for Biological-Image Analysis. *Nat. Methods* **2012**, *9* (7), 676–682. <https://doi.org/10.1038/nmeth.2019>.

- (241) Ashby, P. D.; Lieber, C. M. Ultra-Sensitive Imaging and Interfacial Analysis of Patterned Hydrophilic SAM Surfaces Using Energy Dissipation Chemical Force Microscopy. *J. Am. Chem. Soc.* **2005**, *127* (18), 6814–6818. <https://doi.org/10.1021/ja0453127>.
- (242) Caputo, R.; Palermo, G.; Infusino, M.; De, S. L. Liquid Crystals as an Active Medium: Novel Possibilities in Plasmonics. *Nanospectroscopy* **2015**, *1* (1). <https://doi.org/10.1515/nansp-2015-0003>.
- (243) Batson, P. E. Scanning Transmission Electron Microscopy. In *Treatise on Materials Science & Technology*; Elsevier, 1988; Vol. 27, pp 337–387. <https://doi.org/10.1016/B978-0-12-341827-2.50014-5>.
- (244) Ng, S. A.; Razak, K. A.; Aziz, A. A.; Cheong, K. Y. The Effect of Size and Shape of Gold Nanoparticles on Thin Film Properties. *J. Exp. Nanosci.* **2014**, *9* (1), 64–77. <https://doi.org/10.1080/17458080.2013.813651>.
- (245) Sundberg, P.; Karppinen, M. Organic and Inorganic–Organic Thin Film Structures by Molecular Layer Deposition: A Review. *Beilstein J. Nanotechnol.* **2014**, *5* (1), 1104–1136. <https://doi.org/10.3762/bjnano.5.123>.